MODELING OF STEEL HEATING AND MELTING PROCESSES IN INDUSTRIAL STEELMAKING FURNACES

by

Guangwu Tang

A Dissertation

Submitted to the Faculty of Purdue University

In Partial Fulfillment of the Requirements for the degree of

Doctor of Philosophy

School of Mechanical Engineering

West Lafayette, Indiana

May 2019

THE PURDUE UNIVERSITY GRADUATE SCHOOL
STATEMENT OF DISSERTATION APPROVAL

Dr. Chenn Q. Zhou, Chair
School of Mechanical Engineering

Dr. Jun Chen
School of Mechanical Engineering

Dr. Steven T. Wereley
School of Mechanical Engineering

Dr. Tom I. Shih
School of Aeronautics and Astronautics

Approved by:

Dr. Jay P. Gore
Head of the Departmental Graduate Program

To my parents and my wife, who made this possible.

ACKNOWLEDGMENTS

My greatest special thanks go to Prof. Chenn Q. Zhou. It is she who offered the opportunity for me to study at Purdue. No doubt she has enriched my knowledge and broadened my view the most in the past of my life. She has been set as an excellent role model for me in the field of research, and motivated me to pursue and love research. The support and care to my family from Prof. Zhou is also greatly appreciated during the past few years. I would like to thank Prof. Jun Chen, Prof. Steven T. Wereley, and Prof. Tom Shih for serving on my advisory committee and providing valuable suggestions and comments during the course of study. I would also like to acknowledge the late Prof. Sanford Fleeter, who served on my advisory committee for one year before his passing.

I also would like to thank colleagues at the Center for Innovation through Visualization and Simulation (CIVS) at Purdue University Northwest, including Mr. Bin Wu, Dr. Armin Silaen, Dr. Dong Fu, Dr. Tyamo Okosun, Mrs. Doreen Gonzalez-Gaboyan, Mr. Charles A Capek, Mr. John Moreland, Mr. Jichao Wang, Mr. Michael E Hoerter, Mr. Yuchao Chen, Mr. Haibo Ma, Mr. Xiang Liu and many others for their help and encouragement to me.

I would like to acknowledge support from the collaborators at Steel Dynamics Inc., AK Steel, ArcelorMittal, U.S. Steel, Stelco Inc., Praxair, Union Gas, Cliffs Natural Resources, NIPSCO, NUCOR, SSAB, and other supporters of the Steel Manufacturing Simulation and Visualization Consortium (SMSVC) throughout the course of this research. I also would like to acknowledge the help from Dengqi Bai (SSAB), Yufeng Wang (SSAB), Rick Bodnar (SSAB), Andrew Spencer (Steel Dynamics Inc.), Yury Krotov (Steel Dynamics Inc.), and Mike Riley (Praxair). I would also like to thank the project technical committee (PTC) members including Hamzah Alshawarghi (Praxair), Jianghua Li (AK Steel), Joe Maiolo (Praxair), John Lowry (Nucor), Michael Lowry (ArcelorMittal), and Sunday Abraham (SSAB).

I would like to thank the grace and love from God. I am grateful to my parents, sisters, my wife, and my son for their love and support. I also would like to acknowledge the help from my friends, Tim Chen, Daphne Chen, Christine Jensen, and Rob Jensen.

TABLE OF CONTENTS

LIST OF TABLES

LIST OF FIGURES

NOMENCLATURE

p	Static pressure, pascal
ρ	Density, kg/m^3
$\vec{F}$	External body force, N
$\vec{g}$	Gravity, m/s^2
$\vec{v}$	Velocity, m/s
t	Time, s
$\bar{\bar{\tau}}$	Stress tensor
μ	Molecular viscosity, kg/m·s
δ_{ij}	Stress tensor due to molecular viscosity
u_i	Velocity component along the direction x_i, m/s
u_j	Velocity component along the direction x_j, m/s
u_i'	Instant turbulence velocity on the direction x_i, m/s
u_j'	Instant turbulence velocity on the direction x_j, m/s
k	Turbulent kinetic energy, m^2/s^2
ε	Turbulent dissipation rate, m^2/s^3
I	Unit tensor
μ_t	Turbulence viscosity, kg/m·s
G_k	Generation of turbulence kinetic energy due to the mean velocity gradients
G_b	Generation of turbulence kinetic energy due to buoyancy
Y_M	Fluctuating dilatation in compressible turbulence
σ_k	Turbulent Prandtl number for k, 1.0
σ_ε	Turbulent Prandtl number for ε, 1.2 for realizable, 1.3 for standard
$C_{1\varepsilon}$	Constant, 1.44
C_2	Constant, 1.9
v	Kinematic viscosity, m^2/s
k_{eff}	Effective thermal conductivity, W/m-K
C_p	Specific heat, J/kg·K
Pr_t	Turbulent Prandtl number
$\vec{J}_j$	Diffusion flux of species j
E	Total energy, J
h_j	Sensible enthalpy of species j
S_h	Heat of chemical reaction, and any other volumetric heat sources, J
Y_j	Mass fraction of species j
$C_{p,j}$	Temperature-dependent constant pressure specific heat of species j, J/kg·K
$\vec{J}_i$	Diffusion flux term of species i
Y_i	Local mass fraction of species i
R_i	Net rate of production of species i by chemical reactions
$D_{i,m}$	Diffusion coefficient for species i in the mixture

$D_{T,i}$	Thermal diffusion coefficient, m^2/s
Sc_t	Turbulent Schmidt number, 0.7
Y_i^*	Mass fraction of species i within the fine structures after reacting over the time τ^*
Y_i^0	Mass fraction of species i in the fluid surrounding the fine structures
ξ^*	Mass fraction occupied by the fine structure regions
C_ξ	Volume fraction constant, 2.1377
τ^*	Time scale
a	Absorption coefficient, m^{-1}
n	Refractive index
σ_s	Scattering coefficient, m^{-1}
σ	Stefan-Boltzmann constant ($5.669 \times 10^{-8} \frac{W}{m^2K^4}$)
T	Local static temperature, K
Φ	Phase function
Ω'	Solid angle
$a_{\varepsilon,i}$	Emissivity weighting factor for the i^{th} fictitious gray gas
K_i	Absorption coefficient of the i^{th} gray gas, m^{-1}
P	Sum of the partial pressures of all absorbing gases, Pascal
S	Path length, m
$b_{\varepsilon,i,j}$	Emissivity gas temperature polynomial coefficients
V	Fluid volume, m^3
A	Total surface area of the fluid boundaries, m^2
$\vec{u}_{mesh}$	Mesh velocity of the moving mesh, m/s
Γ	Diffusion coefficient, m^2/s
S_{gu}	Source term for gas phase introduced by the scrap phase
u_g	Gas superficial velocity, m/s
$\emptyset$	Scrap porosity
ψ_j	Particle shape factor, 1
d_j	Particle diameter or scrap size, m
S_{gH}	Heat transfer rate between gas and solid scrap
h_j	Heat transfer coefficient, W/m^2-K
A_s	Scrap surface area, m^2
k_g	Constant, 0.0184
Pr_g	Prandtl number
Re_j	Reynolds number
A	Constant, 160.0
$f(w)$	Constant, 0.5
V_g	Gas velocity, m/s
k	Constant, 4.00×10^{-7}, g^2/cm^4-s
β	Liquid fraction of melted material
W	Weight gain, g
A_{mush}	Mushy zone constant, 100,000
α_g	Gas phase volume fraction
α_q	Solid phase volume fraction
H	Enthalpy, J
$T_{solidus}$	Solidus temperature, K
$T_{liquidus}$	Liquidus temperature, K

M_τ Turbulent Mach number

a Speed of sound, m/s

γ Constant, 1.4

R Gas constant, 287 J/kg·K

$C_{1\varepsilon}$ Constant, 1.44

$C_{2\varepsilon}$ Constant, 1.92

$H(x)$ Heaviside function

T_t Local total temperature, K

T_g Normalized local total temperature gradient

$M_{\tau 0}$ Constant, 0.1

$T(x, y, t)$ Temperature at time step t

x Slab longitudinal direction coordinate

y Gauge direction coordinate

$C_s(t)$ Temperature dependent specific heat of the slab

ρ_s Density of the slab

$K_s(t)$ Thermal conductivity of the slab

Δx Increment on x direction

Δy Increment on y direction

Δt Increment of time

$T_{i,j}^{t}$ Node temperature at time step t, K

$T_{i,j}^{t+\Delta t}$ Node temperature at time step t + Δt, K

G Slab thickness, m

$T(x, G, t)$ Top surface (y=G) temperature at time step t, K

f View factor

ε_s Emissivity of the slab

T_{itop} Top chamber furnace temperature, K

h_i The convective heat transfer coefficients, W/m^2-K

α Constant, 0.0841

β Constant, 0.6035

U_e Jet exit velocity, m/s

U_m Normalized velocity by the jet exit velocity

ρ_e Exit density, kg/m^3

ρ_a Ambient gas density, kg/m^3

D_e Diameter of jet exit, m

ABSTRACT

Author: Tang, Guangwu. Ph.D.
Institution: Purdue University
Degree Received: May 2019
Title: Modeling of Steel Heating and Melting Processes in Industrial Steelmaking Furnaces.
Major Professor: Chenn Q. Zhou

Steel heating and melting processes consume the majority of the energy used in advanced short-process steelmaking practices. Economic and environmental pressures from energy consumption drive the research to improve the furnace operation efficiency and energy efficiency. The goal of this research is to utilize computational fluid dynamics (CFD) modeling to provide useful tools and recommendations on the steel heating and melting practices in the steelmaking process. The steel slab reheating process, the steel scrap preheating process and the steel scrap melting process are studied.

A transient three-dimensional (3-D) CFD model was developed to simulate the flow characteristics, combustion process and multi-scale, multi-mode heat transfer inside the reheating furnace. The actual geometry of an operating industrial furnace was used and typical operating conditions were simulated. Specific walking speeds of slabs in production were modeled using a dynamic mesh model which is controlled by a user-defined function (UDF) solved using ANSYS Fluent. Fuel variations at different zones with respect to time were also considered. The model was validated with instrumented slab trials conducted at the SSAB Mobile (Alabama) mill. The temperature field in the furnace and the temperature evolution of a slab predicted by the CFD model are in good agreement with those obtained from the instrumented slab trials. Based on the simulation results, the slab reheating process and the temperature uniformity of a slab at discharge were able to be properly evaluated. In addition, a comprehensive two-dimensional (2-D) numerical heat transfer model for slab reheating in a walking beam furnace was developed using the finite difference method. An in-house code was developed. The model is capable of predicting slab temperature evolution during a reheating process based on real time furnace conditions and steel physical properties. The model was validated by using mill instrumented slab trials and production data. The results show that the temperature evolution predicted by the model is in good agreement with

that measured by the thermocouples embedded in the instrumented slab. Compared with 3-D CFD simulation of a reheating process, this 2-D heat transfer model used for predicting slab temperature evolution requires less computing power and can provide results in a few seconds. A graphical user interface was also developed to facilitate the input and output process. This is a very convenient and user-friendly tool which can be used easily by mill metallurgists in troubleshooting and process optimization.

CFD models for steel scrap preheating and melting processes by the combined effects of the heat source from both oxy-fuel combustion and electric arc were also developed. The oxy-fuel burners firing natural gas (NG) are widely used in EAF operation during the scrap preheating and melting stages. In order to understand the role of oxy-fuel combustion and potentially increase the energy input from NG while decreasing the electricity consumption, numerical simulation of scrap preheating by oxy-fuel combustion in an EAF was firstly conducted. A 3-D CFD model was developed with detailed consideration of gas flow, oxy-fuel combustion, heat transfer between gas and solid scrap and scrap oxidation. The model was validated by a small-scale experimental study and applied onto a real-scale EAF.

Scrap melting in bath is comprehensively studied with a CFD model developed to simulate the melting in bath process under given operating conditions. Two sub-models were developed for model integration: steel melting model and coherent jet model. The multiphase volume of fluid (VOF) model and the enthalpy-porosity technique are applied to describe the steel melting process. The coherent jet model calculates the gas jet momentum and is integrated into the flow model to calculate its effect on the fluid flow in the bath. The electric arc was treated as a heat flux to represent the heat transfer from the electric arc during the melting process. Model validations were conducted for each sub-model to ensure their accuracy. Parametric studies were also carried out to obtain useful information for real practice.

Overall, the CFD models developed in this research work have demonstrated value in improving energy efficiency in the energy-intensive steelmaking processes. The developed CFD models also provide insights for better understanding of the multi-physics processes.

CHAPTER 1. INTRODUCTION

1.1 Research Motivation

The steelmaking industry has played a key role in industrializing human culture, and steel consumption often reflects the strength of the economy. Despite competition from materials such as plastics, aluminum, composites, and even wood, steel has remained dominant on both a low cost and high-tonnage basis [1]. In general, the already well-developed steelmaking process continues to mature with all the new technologies. World-wide, the long process, or the integrated mill system, still dominates crude steel production. The process is shown in Figure 1. The typical integrated mill uses the blast furnace (BF) for producing molten iron and the basic oxygen furnace (BOF) to produce steel. Combined with other processes, the iron in the iron ore can be converted to different grades of steel. The other steelmaking process, called the short process, or the mini-mill system, is playing a more and more important role in the steelmaking industry nowadays. The short process uses the electric arc furnace (EAF) to produce steel directly from steel scraps. The process mainly uses electrical energy and chemical energy. For both processes, the liquid steel will go through the general casting and reheating process to produce final steel products as shown in Figure 1. The short process as shown in Figure 2 has the advantage of energy savings compared to the traditional long process. The energy consumption using the EAF process is 11.30 MBtu/ton [1], while the energy usage for the production of hot metal using the blast furnace is 20.08 MBtu/NTHM.

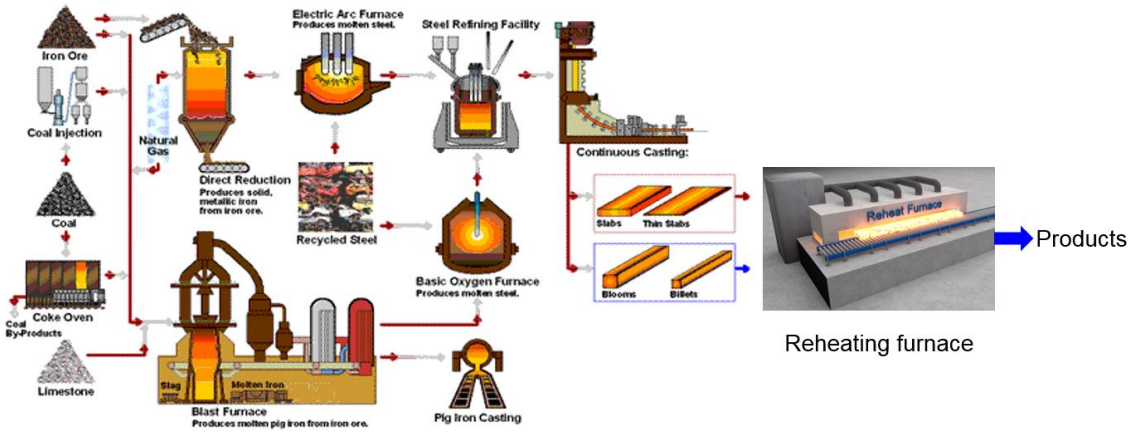

Figure 1. The steelmaking processes.

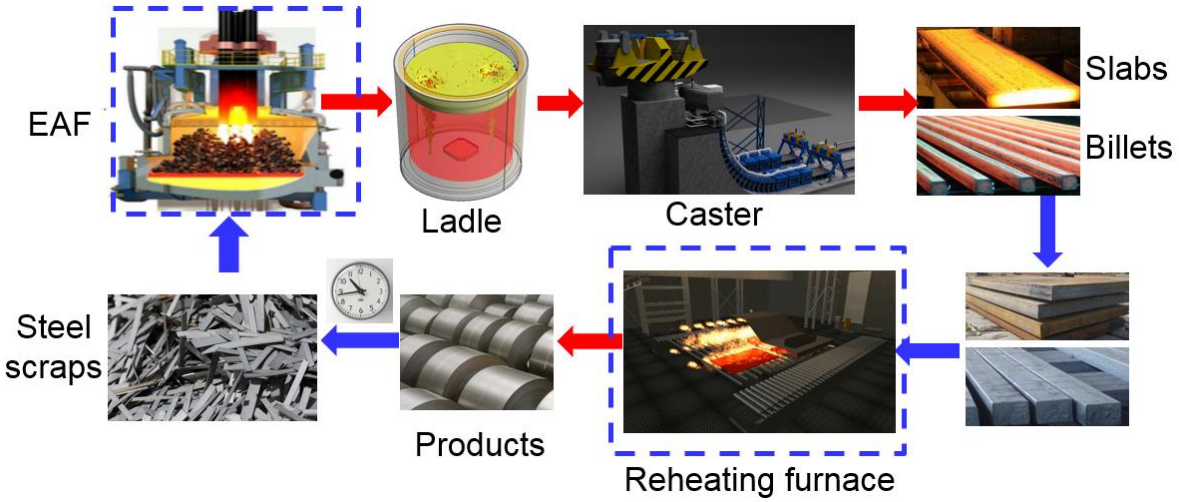

Figure 2. The steelmaking process in the mini-mill.

As shown in Figure 2, the short process of steelmaking uses the electric arc furnace to produce liquid steel from steel scraps. Further processing with the ladle, caster and reheating furnaces helps refine and shape the final products. From the energy consumption point of view, the whole process is a heating and cooling process on steel (slab, billet, scraps). The steel scraps are heated and melted inside the EAF to produce liquid steel. By using the continuous casting process, the liquid steel is then cooled and formed into different shapes such as slabs and billets. The slabs and billets are either further cooled down and then heated up later, or directly heated up after casting using the reheating furnace. The main energy consumption in the whole process is the process of heating and melting in the EAF and heating in the reheating furnace.

The steel industry consumes approximately 5.2% of the total energy used in the entire U.S. manufacturing sector. The share of U.S. steel production using EAF (the short process) is approximately 60%. About 87.4% of the produced steel went through hot rolling process using reheating furnace with various types [2]. Both the EAF and the reheating furnace consume vast amounts of energy. Around 155 EAFs operate in the U.S. with a production capacity of more than 77 million metric tons per year [3] with energy consumption of electricity alone ranging from 330 to 750 kWh/metric ton (approximately 1.6×10^{14} Btu/year). Electrical energy fulfills approximately 60% of an EAF's total energy requirement. The energy efficiency of EAF steelmaking is only 55 to 65%. Similarly, around 140 reheating furnaces operate in the U.S. and altogether consume

approximately $1.6x10^{14}$ Btu/year of natural gas alone. In order to improve the energy efficiency of the steelmaking short process, process optimization is the key. Due to the complexity of the process and harsh environment in steelmaking mills, numerical simulations have played an important role in optimizing the existing processes. This is acting as a primary motivation towards this research.

1.2 The Steel Slab Reheating Process in Reheating Furnaces

1.2.1 Reheating Furnace Process

Slab reheating is a key process in the production of high-quality steel products. The steel reheating process is typically required before the hot rolling process during steelmaking. The goal of using the reheating furnace is to heat up the steel slab to a target rolling temperature to reduce the stresses introduced during the rolling process. A schematic view of a generic steel slab reheating furnace is shown in Figure 3. The industrial reheating furnace generally consists of three zones: preheating zone, heating zone, and soaking zone. In each zone, different types of burners are used to provide heat for the heating process. Typically, natural gas with preheated air is input to form combustion in the furnace. The heat from combustion is then transmitted to the slabs, skids, furnace walls and supporting structures through radiation, convection and conduction heat transfer as shown in Figure 4. During the process, the steel slabs are charged at the charge door at a relatively low temperature compared to the target temperature, depending on the operation practice: cold charge, warm charge, hot charge. The slab then travels through the reheating furnace on the skid which is supported by the supporting structure. Depending on the type of the furnace (pusher type or walking beam), different movement mechanisms are applied. During the slab movement process, the heat released from the combustion is partially transferred into the steel slab through radiation, convection, and conduction. In general, the radiation heat transfer is dominant. And the three different zones play different roles in the slab reheating process. The preheating zone is using the combustion flue gas to heat up the steel slab mainly through radiation and convection. The heating zone plays an important role in elevating steel slab temperature to the target discharge temperature, while the soaking zone homogenizes the steel slab temperature to reduce the temperature difference between the highest temperature and the lowest temperature throughout the slab. The preheated steel slab with relatively homogenous temperature is then discharged from the discharge door.

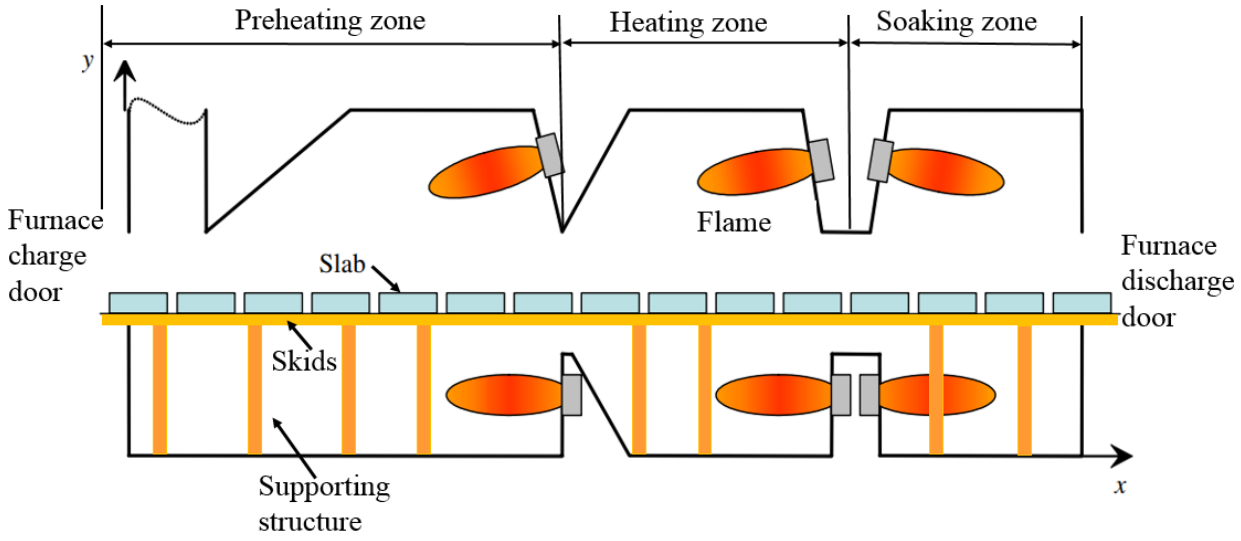

Figure 3. A schematic view of a generic steel slab reheating furnace.

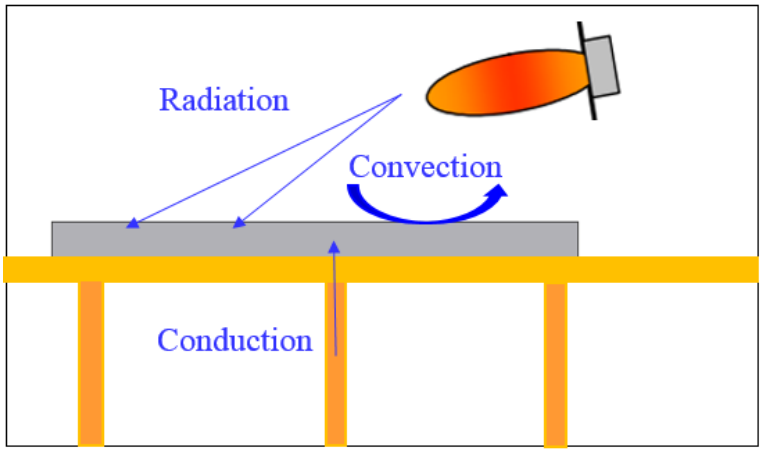

Figure 4. The heat transfer mechanisms in the reheating furnace.

A good reheating practice ensures not only a high furnace throughput but also a uniform temperature distribution within reheated slabs [4]. Walking beam reheating furnaces fired by natural gas are commonly employed in hot rolling steel mills. At a steel mill, many different steel grades are reheated for rolling on a daily basis, some of which can be hot or warm charged, while others must be cold charged into the reheating furnace. The target reheating temperature can also vary over a wide range depending on the specific product/thickness being rolled. The required furnace time will also vary depending on the temperature of the slab being charged (hot vs. warm vs. cold), and the need to dissolve alloy carbides/nitrides prior to rolling.

Overall, slab reheating is a very complicated process which often transitions from warm-to-cold charging, or from high-to-low slab discharge temperature and so on. This complexity not only increases the difficulty of ensuring that all slabs are reheated uniformly to the target temperature but also increases the intricacy of production planning. Very often, slab reheating is a bottleneck for many steel mills due to the difficulty of achieving an optimal balance between reheating quality and furnace throughput.

In the production of steel plates, slabs are heated up to a certain temperature, approximately 1500 K, prior to rolling. Ideally, the temperature gradient inside a reheated slab should be below 50 K/m before discharging from the slab reheating furnace [5,6]. In order to develop optimized reheating practices, it is necessary to understand the reheating furnace operation and develop suitable control logic for different reheating scenarios. The reheating furnace operation is a complex physical and chemical process which involves combustion, heat exchange among the furnace wall, flame, skids, slab movement, and slab internal heat conduction [7]. A good slab reheating furnace operation should have high thermal efficiency, high productivity, low emissions, and a well-controlled slab discharging temperature [8,9]. Numerical modeling and optimization methodologies have been applied to many industrial reheating furnaces to address these concerns.

1.2.2 Literature Review

The steel industry consumes approximately 5.2% of the total energy used in the entire U.S. manufacturing sector. Reheat furnaces consume around 70-80% of the total energy consumption of steel plant rolling mills, and are widely used to heat up steel to a target temperature for rolling, but must balance many influential factors to meet the target temperatures consistently and homogeneously, and maintain desired steel properties. All forms of semi-finished steels must be heated to a predetermined target temperature to reach a desired state of plastic deformation, but there are many different grades or types of traditional steel, new steel, and steel alloys, which often require different target temperatures, different heating rates, and varying levels of heating control precision (temperature windows) to maintain product quality. In addition, because reheat furnaces are “upstream” of the rolling mills, product quality is of particular importance since defective products can damage downstream equipment, resulting in losses from product re-work, wasted

energy resources, downtime, and equipment repair/replacement. Industrial experiments, also called the instrumental slab trials, are expensive and time-consuming.

Although the reheating furnace process has been well studied for many years and the process control is well performed in general, it is experiencing technical challenges such as low energy efficiency, and inconsistent productivity and product quality. Experimental study on the industrial-scale reheating furnace is a challenge due to the harsh environment and high cost. A limited number of instrumental slab trials have been conducted to measure the slab temperature throughout the whole reheating process. Most of the instrumental slab trials are intend to obtain data for control model calibration. With the fast development of computer technology and software, CFD has been widely used to model reheating furnaces for many different aspects to improve the furnace performance and minimize issues.

A number of studies have been conducted regarding the use of CFD for analyzing reheating furnace operations. The scope of modeling reheating furnaces can be divided into the following categories: furnace combustion modeling, heat transfer modeling including the slab heating process and the skid-mark effect, slab residence time optimization, thermal efficiency analysis, environmental effect investigations [10,11], and slab surface scale effects [12,13]. Numerical investigation of the reheating furnace flow and combustion is the basis for further study of the slab reheating characteristics. Hsieh et al. [14,15] investigated reheating furnace combustion without considering the transient slab heating process. They applied the probability density function (PDF) turbulence combustion model to the simulation of the combustion process. The discrete ordinates (DO) radiation model and weighted-sum-of-gray-gases model (WSGGM) were used to describe the radiation within the reheating furnace. Kim et al. [16,17] investigated the effect of heat transfer models on the prediction of steel slab temperature. Their research shows that heat transfer within a reheating furnace includes all modes, but the radiative heat transfer is dominant, accounting for over 90% of the total heat transfer. By applying the DO heat transfer model and the finite volume solution method, Kim was able to develop a heat transfer model which worked well for predicting the slab temperature in the reheating furnace. Singh [17] claimed that the skid supporting system has little effect on the temperature distribution of a slab. However, the effect of the water-cooled skid on the slab temperature distribution could be large, according to the research of Jang et al.

[18-21]. Kim et al. [19] studied the effects of different shapes of skid buttons on the slab temperature distribution. The results indicate that it is better to increase the exposure area of the skid button, which will increase the total heat transfer to the coolant and decrease the heat conduction between the parts, thereby reducing the severity of the skid marks on the slab. Jang et al. [22] developed an algorithm with a simplified conjugated-gradient method and a shooting method to optimize the heating pattern, thereby minimizing energy consumption. Their results indicate that the decrease in the preheating zone temperature will lead to a significant decrease in energy consumption. Other aspects, such as oxy-fuel combustion [23,24], and the effects of mill delay [25], were also addressed using CFD.

The slab reheating furnace is large and requires a large number of grids in the CFD model to capture the details of fluid flow, combustion, and heat transfer characteristics. Therefore, the models developed recently by some researchers employed some simplifications, such as dividing the reheating furnace into several zones and assuming constant temperature in each zone [18,26,27]. Some researchers also simplified the complex movement process [5,28,29]. However, these simplifications often introduced significant errors in the modeling. For example, in real reheating furnace operation, dynamic phenomena such as variation in slab walking speed, variation in fuel input, and different steel grades being heated, often occur. All of these can affect the furnace conditions such as velocity field, combustion process, and heat transfer characteristics. There are few studies dealing with a full-scale simulation of an industrial reheating furnace operation with these detailed dynamic phenomena.

Other researchers developed simplified models, such as heat transfer models focusing on a single slab to achieve high calculation efficiency. Chen et al. [30] developed a slab temperature model based on the finite difference method. By optimizing the reheating process, the total furnace residence time for a slab was reduced by 13 minutes on average, which corresponds to an increase in furnace throughput of 9.72%. However, the model used a zone method with a limited number of zones (6 in total) in the furnace, which may have resulted in inaccurate thermal boundary conditions. Jang et al. [20] developed a billet heat transfer model based on a 2D finite element method (FEM) model to obtain the temperature distribution of a billet during the reheating process. In this model, an optimization algorithm was proposed to minimize the difference between the

model outputs and the measurements. However, the model focused on radiative heat transfer and took into account the convective heat transfer by adjusting the emission factor. Jaklic et al. [31] developed an online simulation model for the slab reheating process in a pusher-type furnace. The model considered the exact geometry of the furnace and slabs and was validated by comparing the measured and calculated slab heating curves. However, the model simplified the furnace temperature field using a zone method and applied a constant convective heat transfer coefficient. These simplifications may have hampered the model's ability to recreate the furnace conditions, and therefore affected the accuracy of the model predictions.

Based on the literature review, the gap in reheating furnace research is how to achieve a high efficiency in production while maintaining high product quality. Process control level II models have been equipped in almost every reheating furnace operation. However, due to the complexity of changing operating conditions for different grades of steel, good order arrangements and production sequences are needed with the assistance of tools like numerical models. This research work is intended to help fill the gap.

1.2.3 Research Tasks and Contributions

In this study, a comprehensive transient CFD model was developed by taking into account the flow characteristics, combustion, all modes of heat transfer, and dynamic interactions. The CFD model provides a basic understanding of the combustion, furnace atmosphere, and slab reheating process. In addition, it can also generate heat transfer coefficients under various operating conditions. Since the CFD model requires a large computing capability which is unrealistic to be used in a steel mill, a two-dimensional (2-D) heat transfer model has been developed based on the 3-D CFD simulations. The model provides various I/O functions for users to input different conditions and output results. The integration of the CFD simulation results into the 2-D heat transfer model makes it possible for a mill engineer to use an ordinary computer to run simulations for troubleshooting and optimizing the slab reheating process.

The research undertaken in steel slab reheating processes has been conducted by completing the following six tasks:

Task 1: Develop a comprehensive CFD model for the slab reheating process in a reheating furnace.

Task 2: Conduct model validation with industrial measurement data.
Task 3: Investigate the slab reheating process for cold charge, warm charge, and hot charge conditions.
Task 4: Develop a 2-D (two-dimensional) heat transfer model to simulate the slab reheating process using finite difference method.
Task 5: Integrate the 3-D CFD model with 2-D heat transfer model.
Task 6: Conduct parametric studies to optimize the reheating process under different operation scenarios.

Through conducting this research, the following contributions have been made in the research area of steel slab reheating process:

1. Applied dynamic mesh model onto simulation of steel slab moving in reheating furnace.
2. Conducted comprehensive model validation with industrial experimental data.
3. Developed in-house code to simulate the steel slab reheating process with real-time input from industrial sensors.

1.3 The Steel Scrap Heating and Melting Processes in Electric Arc Furnaces

1.3.1 Electric Arc Furnace Process

The EAF is used to produce steel from steel scraps using electricity and chemical energy. Worldwide, the steel scrap consumption has been increasing in the past 70 years as shown in Figure 5. The steel and foundry sectors consume approximately one-third of the world's steel scraps [32,33]. In the United States, the share of U.S. steel production using EAF is approximately 60%, and it is expected to reach 69% by 2040 [34]. Worldwide, the crude steel production by the EAF process increased dramatically during the past 60 years and it is expected to increase in the next 30 years as shown in Figure 6. The survey conducted by Madias et al. [35] showed that the greatest number of the EAFs are located in North America as shown in Figure 7. The EAF steelmaking process is an energy-intensive process that consumes vast amounts of electrical and chemical energy. Raw materials and operating practices affect EAF efficiency and productivity. Raw materials charged into EAFs have changed since 1995, and scrap accounts for around 75% of the metallic for EAFs worldwide. The availability to meet higher value-added steel grades is difficult

to achieve through scrap alone. Productivity and energy consumption are strongly dependent on alternative scrap materials [36] such as Direct-Reduced Iron (DRI), Hot Briquetted Iron (HBI), pig iron, and hot metal. Worldwide, scrap covers around 75% of the metallic, DRI/HBI covers around 15% and 10% by pig iron and hot metal [37]. Due to changes in raw materials, new research can help explore the changes expected to occur in the EAF in productivity and efficiency.

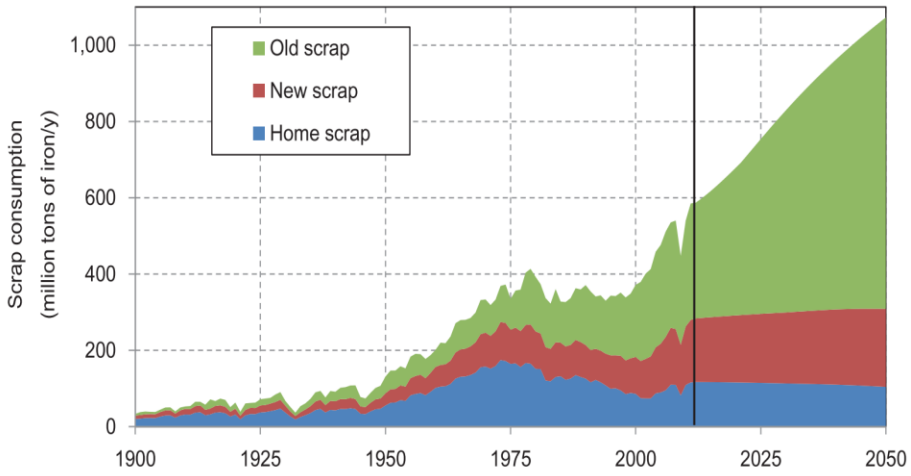

Figure 5. Scrap consumption in steel and foundry sectors [32].

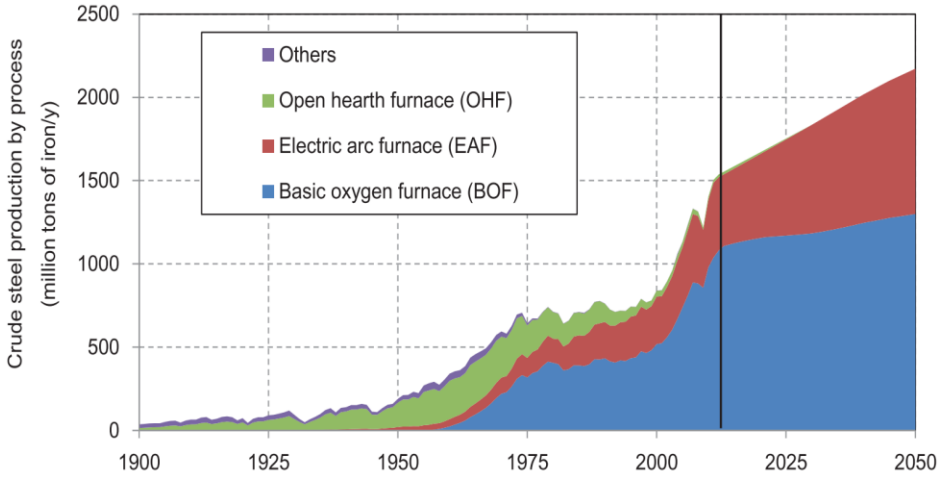

Figure 6. Crude steel production by processes [32].

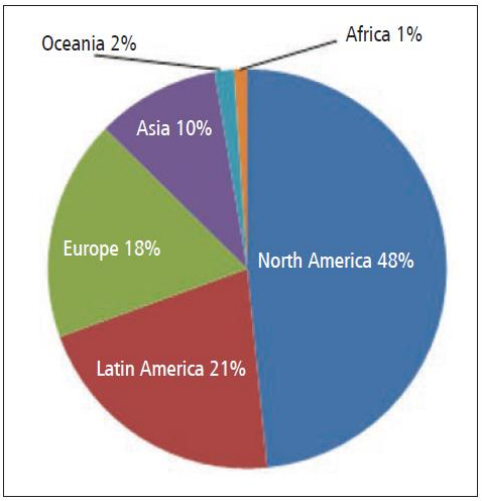

Figure 7. EAF distribution by region [35].

The EAF is categorized in to direct current (DC) and alternating current (AC) two types based on the way of inputting electricity current. While both of the two types are employed in modern steelmaking, AC EAFs are receiving more attention in general as they vastly outnumber DC EAFs (see Figure 8). And newer designed furnaces such as the Consteel EAFs and the twin shell EAFs are including scrap preheating process as shown in Figure 8. A general AC EAF process is shown in Figure 9. Typically, the EAF process is a batch process. In the batch process, the operating cycle is called “heats”, which consists of melting and refining stages. As shown in Figure 9, depending on the target steel grade to be made, the first step in the production is to prepare buckets of scrap to be charged into the furnace. The general criteria for preparing the scrap bucket is to ensure proper melt-in chemistry and good melting conditions. Steel bucket is used to load different types of steel scraps into the EAF during the charging process. Most EAFs are designed to have a minimum of two charges. Some of the EAFs charge molten iron during the two bucket scrap charges. After scrap charging, the melting process starts. The melting process inside the EAF also includes several stages. In modern EAFs, oxy-fuel burners are included to assist the melting by electrical energy through the electric arc. The oxy-fuel combustion uses natural gas as the main fuel source. Heat transfer from the flame radiation, convection and conduction to the steel scraps. In some operations, oxygen is injected via either a consumable pipe lance or the primary oxygen jet (in the coherent jet burner) to react with the hot scrap and burns iron to generate intense heat for cutting the scrap. The electrical power input from the graphite electrodes consists of a few stages. An intermediate voltage tap is selected at the beginning to ignite the arc and until the

electrodes bore into the scrap. About 15 % of the total charged scrap is melted during the initial bore-in process. After the electrodes bore-in sufficiently into the scrap, long arc can be used to enhance the melting process without damage to the panel and roof. The main melting phase will continue until a flat bath condition is formed. At this stage, melting is still continuing for the un-melted scrap in the liquid bath. The convective heat transfer between the liquid steel and the scrap determines the melting rate. Generally, agitation of the liquid bath will enhance the melting. Meanwhile, the refining stage starts with the injection of supersonic oxygen jet into the steel bath for decarburization reaction and slag foaming. The purpose of the steel refining is to remove phosphorus, sulfur, aluminum, silicon, manganese, and carbon from the steel. When the desired steel composition and temperature are achieved, the heat is ready for tapping. Overall, the modern EAF process involves complex practices to make new steel out of steel scraps. The typical process time is about 40 minutes in many practices nowadays. The EAF process also involves complex physics and chemical phenomena in terms of heat and mass transfer.

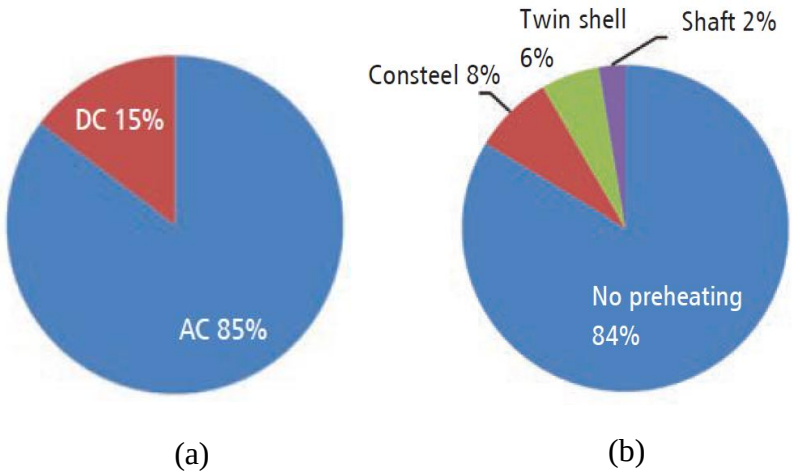

Figure 8. EAF distributions, (a) Furnace types, (b) Scrap preheating process [35].

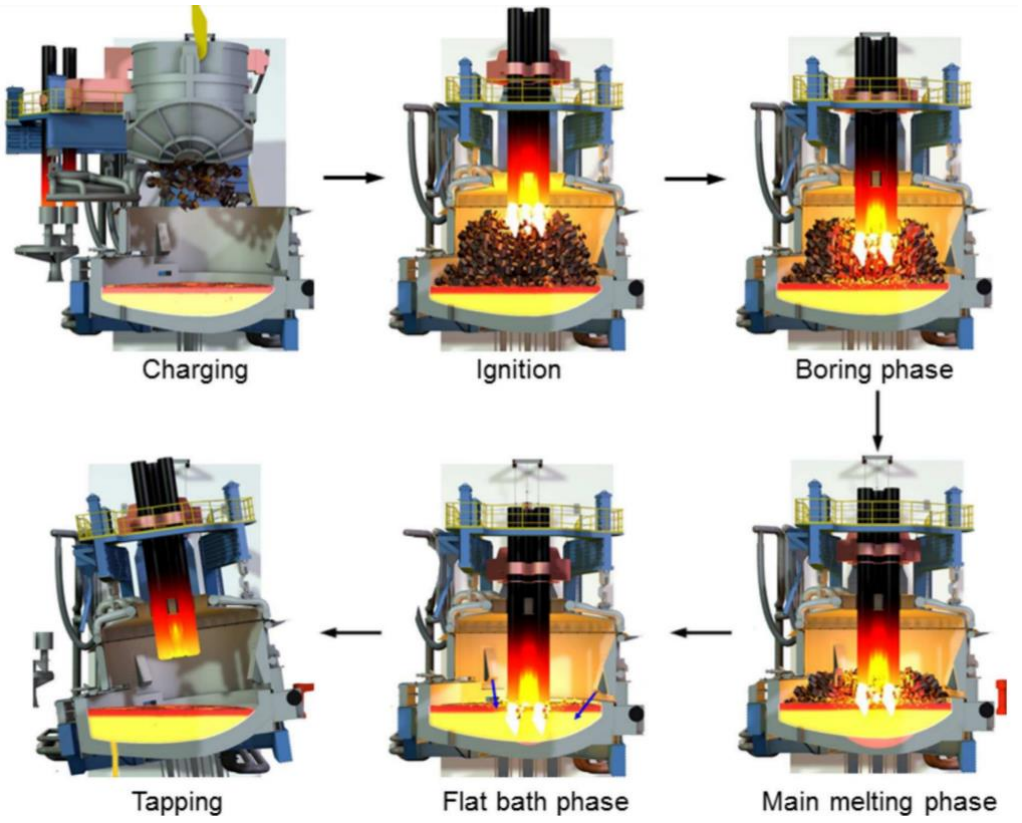

Figure 9. A typical AC EAF process [38].

Due to the advantages of energy saving and short process time, the EAF has played a more and more important role in the overall crude steel product worldwide. New research and development are also paying more and more attention in further optimizing the process. There have been many advances in technology that are used in the EAF operation. The primary goal of these technologies is to increase productivity to reduce the cost of steel production. The energy consumption for EAF steelmaking is in the range of 380-400 kWh/ton. Table 1 shows the typical energy balance in modern EAF practices. The latest technologies can be summarized below:

- Oxy-fuel burners
- Scrap preheating
- Supersonic oxygen lancing
- Slag foaming practices and carbon/lime injection
- Post-combustion in EAF freeboard
- EAF bath stirring
- Continuous scrap charging

Table 1. A typical energy balance in modern EAF.

Inputs	
Electricity	65%
Burners	5%
Bath reactions	30%
Outputs	
Steel	57%
Slag	10%
Cooling water losses	10%
Off-gas losses	20%
Miscellaneous losses	3%

The steel scrap heating and melting processes use the majority of the energy input in EAF. In order to reduce energy consumption in this process, gaining an in-depth understanding of the heat and mass transfer during the scrap heating and melting process is key. Therefore, among the goals of this research is to understand the fundamental heat and mass transfer process during scrap heating and melting processes using CFD.

1.3.2 Literature Review

The research attention paid in the EAF area is growing nowadays along with the development of computer technologies. Many tools have been developed to assist operators, field engineers and process researchers to further improve the EAF process such as empirical models [39,40] including the MSA BOSS model for scrap blending, iEAF model [41] for furnace off-gas measurement, dynamic model [42] for process modeling, mathematical models [33,43,44] for process optimization, and CFD models [46-55]. Empirical models and some thermodynamic models have been used in process optimization, and some are for process control. CFD models are mostly employed to understand the complex physical phenomena occurring in the EAF. With the development of computer hardware and software, many CFD models have been developed for the EAF process due to its advantage of capturing detailed physics and chemistry phenomena. Due to the complexity of the EAF process which involves multi-physics and chemistry, the current CFD models are either focusing on a specific problem or a part of the process.

Although the challenges faced by CFD simulations of the EAF process are huge, some phenomena have been studied using specific models. Distinct CFD models have focused on different components of the EAF process, such as the furnace cooling system [56], gas burners, injectors, scraps, and melt and slag movements [38]. These models are effective when applied to a specific component study. From a whole EAF process modeling perspective, further development of those models is needed to improve the flexibility of application. For example, numerical models reported for simulating scrap melting in the EAF are mostly with significant simplifications. And there is no CFD model for scrap melting by electric arc and oxy-fuel combustion for real EAFs. Only the heat transfer to the scrap pile had been simulated [38]. Scrap preheating by oxy-fuel combustion in a small-scale furnace has been studied by Mandal and Iron [57,58] with both experiment and numerical simulation. The scrap was treated as a porous medium and the combustion process was simplified to include an energy source at the burner inlet to represent the combustion. The CFD model developed has been validated by experimental data, and thus has the potential to be used in real furnace simulation for scrap preheating. In order to conduct process modeling for the typical EAF operation using CFD, the fundamental knowledge regarding the physics and chemistry occurred in the EAF is critical to explore such as scrap properties, combustion, electric arc, all modes of heat transfer, multiphase flow, in bath chemical reactions, and so on.

Steel scraps are used in the EAF as primary raw materials. There are a lot of different scrap types as regards the size, shape and chemical compositions. Typical scrap types are busheling, bundles, and shredded scraps. Figure 10 shows the appearances and properties of four different types of steel scraps [57]. The porosity profile of the scrap bed for each type was measured by Mandal [59] as shown in Figure 11. A summary of scrap bulk density, specific surface area, and other properties for the different types of steel scraps shows that defining reliable data can be a challenge for mathematical modeling [38]. In the scrap melting process, different scenarios with a different number of phases and heat transfer mechanisms are noticed. But in general, it can be categorized into two types, directly and indirectly, in terms of how the energy gets to the location of the melting process. For direct scrap melting, the combustion flame, and electric arc are directly interacting with solid scrap. The main heat transfer is through convection and radiation. In this part, the mechanism has not been fully understood yet, especially when the electric arc is involved. For the indirect scrap melting, the energy is conveyed by the superheated molten steel. The heat transfer

is through convection and conduction. The phase change and interface behavior between steel scrap and molten steel are critical for mathematical modeling. During the EAF melting process, the direct melting and indirect scrap melting may happen at the same time during most with hot heel practices.

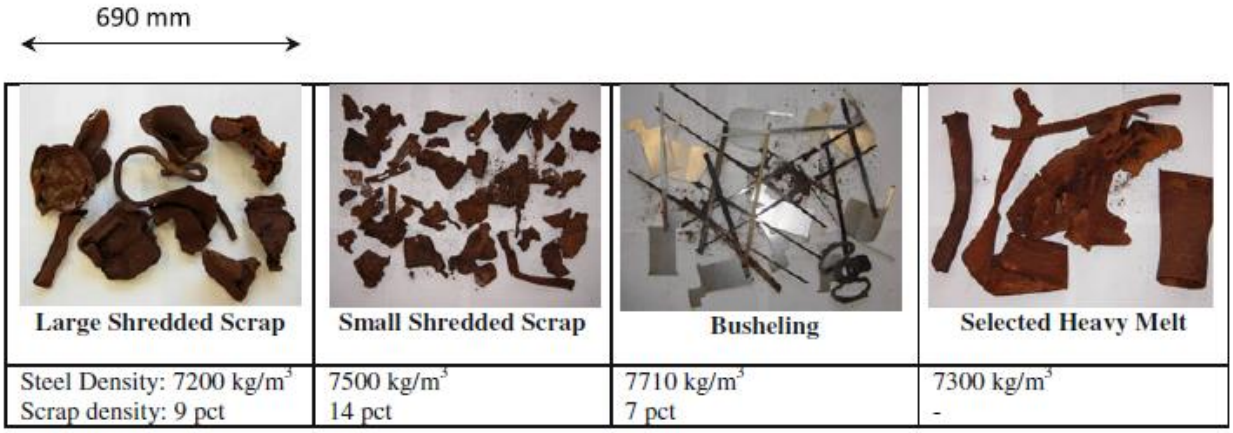

Figure 10. Typical steel scraps and properties [57].

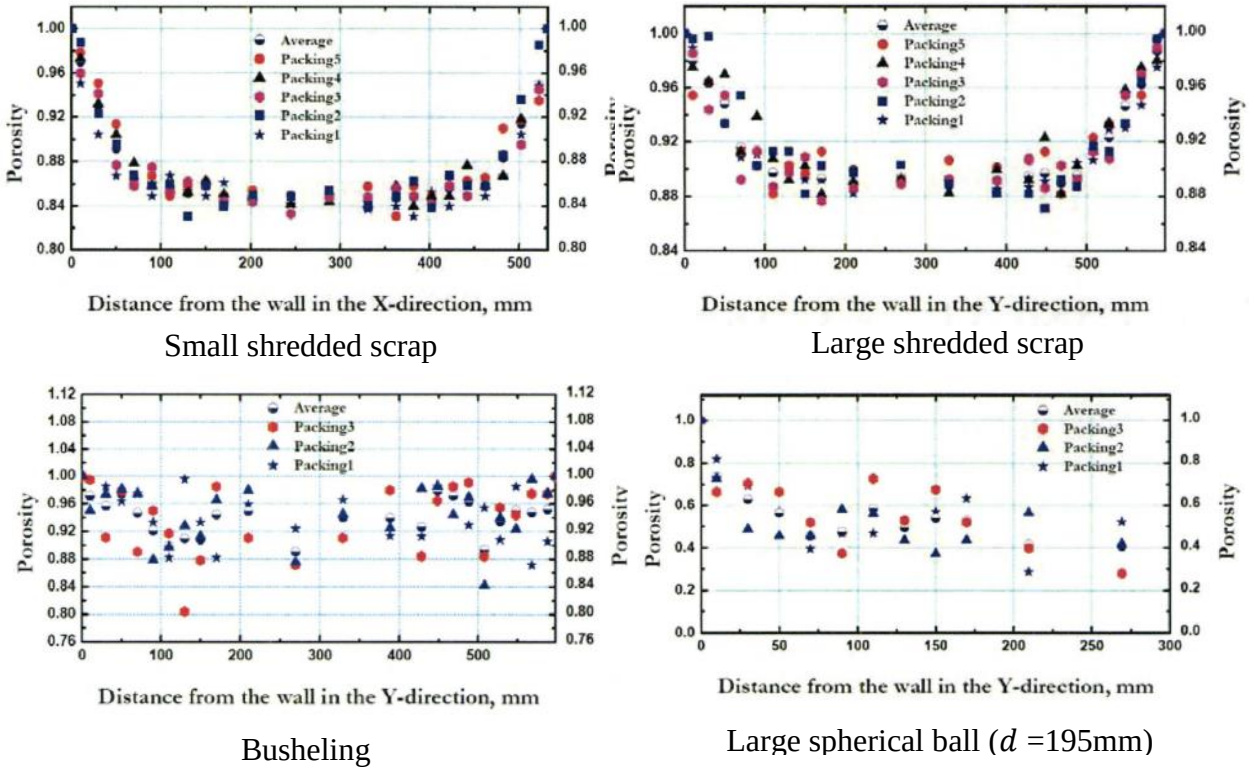

Figure 11. Porosity profile of different types of steel scraps [59].

Electrical and chemical energy melt steel scrap and iron alternatives in the EAF process. The improvement in energy efficiency is critical for the reduction of production costs. Besides scraps, electricity, natural gas and oxygen consumption constitute the highest conversion cost in making steel. Oxy-fuel burners are widely used in EAFs to assist electrical melting. The oxy-fuel burners are not only used to melt the scrap located far away from the electrodes but to de-carburize and clean the molten steel. Typical productivity increases are in the range of 5 to 20 percent when using the oxy-fuel burners [57,58]. In order to optimize the energy input, a complete understanding of the furnace environment during operation is needed. Combustion models and electrode heating effects have been reported in the literature [51,52,60]. However, including both phenomena in a single model, is seldom done. As the role of oxy-fuel burners in the EAF process is critical, it is important to take into account burner details during furnace environment modeling. Research has been undertaken to explore oxy-fuel burner combustion in the EAF by many researchers. Alam et al. [53] developed a CFD model to investigate the supersonic coherent jet properties in the EAF. A simplified 2-D framework with a transient approach was used, and one-step natural gas combustion mechanism was applied. The CFD model was validated with literature-reported experimental results. The model was then enhanced by taking the environmental temperature into consideration [61]. However, the transient approach requires longer computational time, which limited the usage of this model. A steady-state CFD model for conventional supersonic jet has been reported [62]. The steady-state conventional supersonic jet CFD model was validated with both experimental and isentropic theory calculation.

Several research articles present their work on modeling the EAF process including scrap preheating [59,63], scrap melting, multiphase flow with chemical reactions, fuel combustion and heat transfer. A scrap preheating technology is recently applied in newer designed EAFs such as Consteel EAFs [63], shaft EAFs and twin-shell EAFs shown in Figure 12 [64]. It is reported that the scrap preheating can save 0.016 to 0.2 GJ/ton-steel. However, only a few research studies [59,63] have provided results on scrap preheating in a lab-scale experiment. Investigation of scrap melting above bath by the electric arc and the oxy-fuel combustion using numerical simulation has not been reported.

Several studies have been carried out to investigate steel melting in liquid steel baths. Arzpeyma et al. [45] developed a mathematical model for analyzing in bath scrap melting in the EAF. CFD and FEA were used to solve the flow and electromagnetic forces. Li et al. [46,65] conducted both experimental study and numerical simulation on the scrap melting process. The phase field method was used to track the interface between solid and liquid during the scrap melting process. Steel scrap melting by using single-bar, two-bar, and multi-bar with different spacing and initial temperatures were studied. Numerical simulation was conducted to understand the fundamentals of scrap melting in the liquid steel bath, and a phase-field model was developed and validated with the experimental results. The phenomenon of the solidified shell that forms immediately after the steel was immersed in the liquid steel bath was revealed using numerical simulation. Melting process modeling was also reported in other industries [47]. Zhou et al. [47] used the population balance model (PBM) to simulate the aluminum scrap movement in a rotary furnace. A simplified scrap melting sub-model was used to reduce computational cost. Carmona et al. [49] developed a numerical model to simulate the aluminum melting furnace with a plasma torch heat source. The aluminum melting time was calculated using the enthalpy-porosity method [66,67] implemented in ANSYS Fluent. Kim et al. [48] also modeled the melting process of phase change materials using the enthalpy-porosity method and the multiphase VOF model. The critical point in modeling of scrap melting in steel bath is to track the interface of melted and un-melted steel scrap. Three methods have been used to describe the interface behavior during the scrap melting process, they are empirical and classical method [68,69], phase field method [70], and enthalpy-porosity method [48,66,67]. Overall, the phase field method and the enthalpy-porosity method have better predictions accuracy compared to empirical and classical method. The enthalpy-porosity method is computationally cheaper than the phase field method.

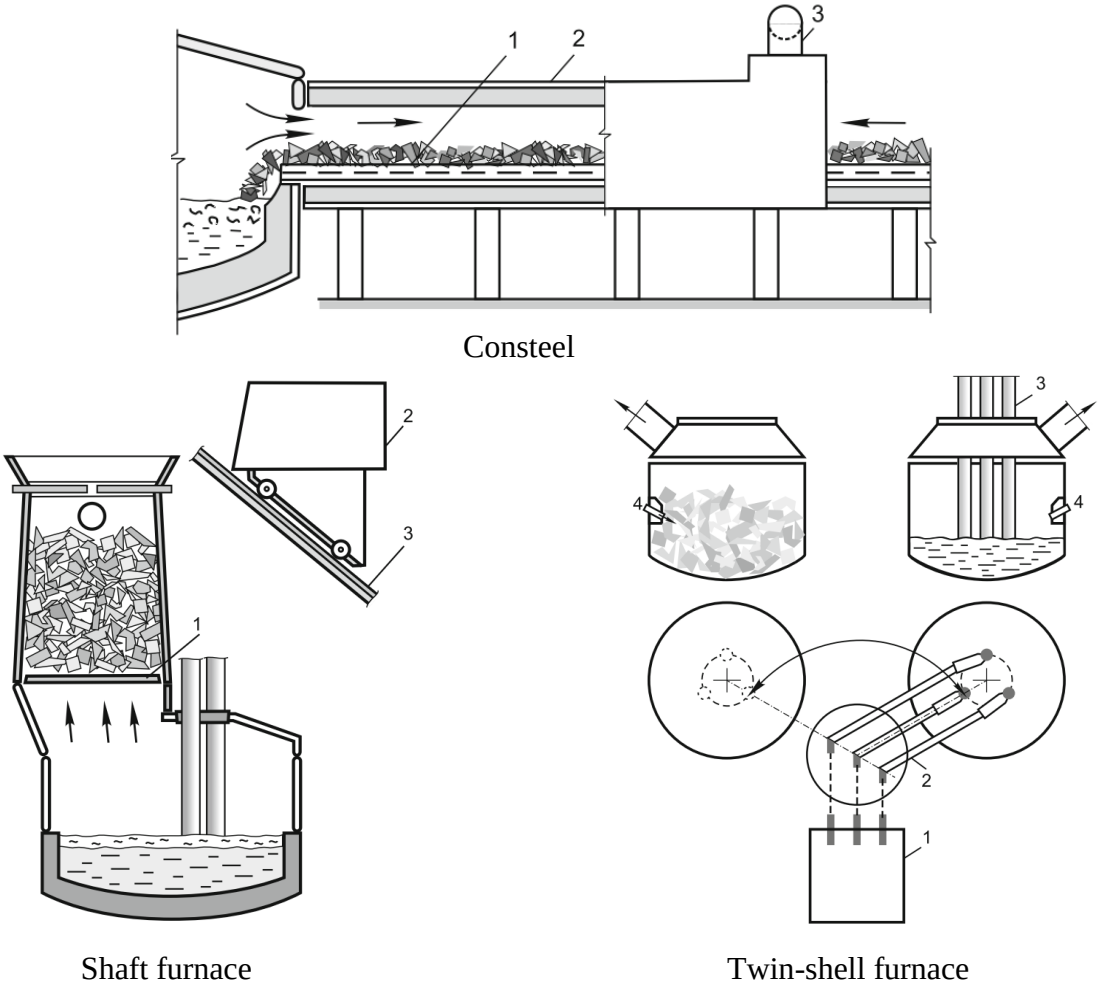

Figure 12. EAF processes with scrap preheating [64].

Energy input in EAF is mainly from the electric arc and the chemical energy within the materials and from the burners. Although effort has been made to improve the chemical energy input such as injecting more natural gas, while reducing the energy input from the electricity to save cost, the electricity input in modern EAFs is still more than 60% of the total energy input. In order to optimize the energy input in EAF, it is critical to understand the heat transfer phenomena in the EAF, especially the heat transfer between the electric arc and scrap. Electric arc has been extensively studied in the welding industry [71-75]. Majority of the mathematical or numerical models focused on the DC arc. Research work has also been conducted on the DC arc and its interaction with anode piece where the melting of the anode material is considered [76]. However, research work on the AC arc interaction with the multi-piece solid materials like the steel scrap has not been reported. Very limited research work exists on the modeling of 3D AC arc using CFD.

Rehmet et al. [77,78] developed a 3D AC arc CFD model and validated the CFD model with experimental work. The arc behavior for a 200 Volt electricity potential was simulated using the MagnetoHydroDynamic (MHD) model. The arc profiles were recorded using a high-speed camera and compared with the numerical simulation. However, the details of high-voltage AC electric arc used in the EAF have not been reported or simulated. Simplifications of the arc as an energy source are normally applied. Gonzalez et al. [50] developed a mathematical model to investigate the effect of arc length on fluid flow and mixing in EAF.

Combustion of fuels such as natural gas and coal is another important energy input in the EAF operation. Attention is always paid to the combustion efficiency [52] and environmental concerns [79]. Yigit et al. [52] developed a CFD model to simulate the carbon combustion in the EAF to evaluate the temperature field and species distributions in an industrial EAF with a flat bath assumption. Post-combustion is a method used in EAF to utilize the chemical energy in the CO and H_2 evolving off of the steel bath through the injection of oxygen. With the post-combustion technology, the produced combustible gases (CO and H_2) during the scrap melting are combusted inside the EAF instead of in the off-gas ductworks. A significant amount of potential chemical energy can be transferred into the steel scrap and liquid metal. Li and Fruehan [51] studied the post-combustion in EAFs using CFD. Their study showed that the CO generation rate is approximately 1.5 kmol per ton of steel, which corresponding to an energy release of 425 MJ by complete combustion. The heat transfer efficiency is higher when a low-temperature scrap pile exists in the furnace, and air ingress in the EAF will reduce the post-combustion ratio and heat transfer efficiency.

Modeling of the multiphase flow characteristics among oxygen jet, slag and steel are also reported [54,55]. During the transition from scrap melting in bath to steel refining, the coherent jet is used to stir the molten steel bath to promote melting and decarburize the liquid steel. Most current EAF operations use the oxy-fuel burners to provide a coherent jet to introduce oxygen into the molten steel bath and provide stirring power. In general, deeper penetration, less splashing, higher flow rate, more intensive mixing, and minimal maintenance needs are desirable. The conventional supersonic jets using converging-diverging nozzles can provide an exit velocity of oxygen typically ranging from Mach 2.0 to Mach 2.3. The potential core length by using the supersonic

jets ranges from 20 De to 35 De, where De is the exit diameter of the converging-diverging nozzle. During the jet installation, the distance to the steel bath should be within the potential core length to achieve deeper penetration and less splashing. Therefore, the limitations of the supersonic jet are obvious due to the short potential core length. The coherent jet technology was introduced by Praxair in the 1970s for oxygen injection in electric arc furnaces [80]. The potential core length of the jet can be significantly increased through a flame envelope or flame shroud that maintains the coherency of the supersonic jet. The potential core length of the coherent jet can exceed 50 De with optimum flame conditions.

Research has been conducted on the flow properties and combustion characteristics in the coherent jet both experimentally and numerically. Anderson et al. [81] conducted experimental work to measure the coherent jet axial velocity using reactive gases such as oxygen, and non-reactive gases such as nitrogen and argon, as the primary supersonic jet. The experiments showed that with the flame shroud, the potential core length could be extended to about 50 times the jet diameter. Alam et al. [53] developed a CFD model to simulate the properties of coherent jet flow and combustion. That CFD model uses a modified k-epsilon turbulence model based on a study of the conventional supersonic jet. [61] The eddy dissipation (ED) combustion model with simplified one-step methane-oxygen reaction mechanism was applied to simulate the combustion process. Validation of the CFD model was conducted by comparing the jet axial velocity with the measurements obtained by Anderson et al. [81] Wei et al. [61,84] also studied the coherent jet with CO_2 and O_2 mixed injection simulation. The eddy dissipation concept (EDC) combustion model was applied and used GRI-Mech 3.0 mechanisms to calculate the methane-oxygen combustion. The model constants in the standard k-epsilon turbulence model were also adjusted to fit the correlation between experimental data and simulation results. Liu et al. [85,86] conducted both experimental and numerical studies on the coherent jet with a primary focus on the effects of ambient and preheated oxygen temperatures. The study indicated that the higher gas temperature can prolong the potential core length for both coherent and conventional jets. Liu et al. [87] also studied the effects of CH_4 flow rate on the flow field and stirring ability of the coherent jet. The results indicated that the increase of CH_4 flow rate will increase the coherent jet potential core length when the volume flow rate of CH_4 is less than 10% of the primary oxygen volume flow rate.

Flow behavior and combustion characteristics in a flame-shrouded coherent jet are very complicated. Among the numerical models reported in the literature, there is no complete agreement on key sub-models and model parameters. Use of an appropriate turbulence model is critical since both of the standard turbulence models (k-epsilon turbulence model and k-omega turbulence model) were developed at room/ambient temperature. Alam et al. [53,61,87,88] use model modifications to account for the temperature fluctuations or gradient effects for both conventional supersonic jets and coherent jets. However, Wei et al. [82,84] and Liu et al. [85,86] use the standard k-epsilon turbulence model and standard k-epsilon model with modification of the model constants. Selection of the combustion model reaction mechanism is another critical factor that will affect the prediction of jet flow properties. Detailed combustion mechanisms such as the GRI-Mech 3.0 mechanisms are preferred for greater accuracy. However, the computational expenses will limit the use of the model for industrial applications. Alam et al. [53]use a one-step CH_4-O_2 combustion reaction, while Wei et al. [82,84] and Liu et al. [85,86] use GRI-Mech 3.0 for CH_4-O_2 combustion reactions. In the coherent jet, the shrouding fuel combusted with the oxygen directly which formed an oxy-fuel combustion. Since the oxy-fuel combustion is different from the traditional air-fuel combustion in terms of numerical modeling. The combustion reaction mechanisms and the radiation model for oxy-fuel combustion have to be carefully identified. No research has been reported in the coherent jet study considered the oxy-fuel combustion characteristics. Most of the CFD models use the chemical reaction mechanisms and radiation model used for air-fuel combustion. In addition, the effects of ambient temperature on coherent oxygen jet flow properties have not been investigated. At the steelmaking temperature conditions, the effects of fuel input on the potential core length are also of great interest to researchers and field engineers.

1.3.3 Research Tasks and Contributions

In order to develop CFD models to simulate the steel scrap melting process in an EAF, the general melting process has been simplified as Figure 13 shows. Assuming there is no hot heel initially in the furnace before the scrap charging, the process consists of four stages: the scrap preheating by oxy-fuel combustion, electrodes bore-in, melting stage 1, and melting stage 2. Due to the complexity of having direct and indirect melting at the same stage, this study will develop the

scrap melting above bath and scrap melting in bath models separately. Iterations between melting above bath model and melting in bath model may be conducted in the future research.

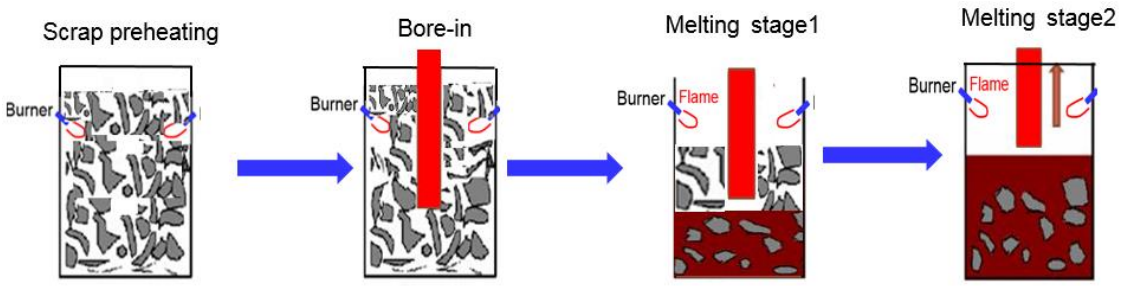

Figure 13. General melting process without hot heel practice.

The detailed research tasks on the model developed are listed below:

Task 1: Develop a CFD model to simulate the oxy-fuel combustion and gas scrap heat transfer.

Task 2: Develop a CFD model for scrap melting in bath.

Task 5: Develop a coherent jet model to calculate the jet profile and the corresponding stirring effect during the scrap melting process in bath.

Task 6: Integrate the coherent jet model and scrap melting in bath model to investigate the scrap melting process in industrial EAF.

Through conducting this research, the following contributions have been made in the research area of steel scrap melting process:

1. Developed a scrap oxidation model.
2. Developed and validated an coherent jet model and a scrap melting in bath model.
3. Conducted model integration of the coherent jet model and the scrap melting in bath model.

1.4 Objectives

The primary research objectives for this research on the steel slab reheating process are:

1. To develop a comprehensive CFD model for the steel slab reheating process in industrial reheating furnaces.

2. Use the model to simulate 3-D turbulent combusting flows in the reheating furnace under typical operating conditions to understand the furnace flow properties and slab heating characteristics.
3. To validate the model with industrial experiments.
4. To develop a high efficiency, user-friendly tool to optimize the steel slab heating process and integrate with sensor measurement data to produce real-time output.
5. To provide guidance and suggestions for production.

The primary objectives for research into steel scrap heating and melting processes are:

1. To develop and validate a CFD model for steel scrap heating in industrial EAFs.
2. To provide a fundamental understanding of preheating process in EAFs.
3. To apply the model to real furnace operation and evaluate the effects of different operating parameters.
4. To develop a CFD model to investigate the scrap melting in bath in EAF operation.

1.5 Organization

This dissertation contains three numerical models focusing on modeling the steel heating and melting processes in industrial steelmaking furnaces. The three models are the steel slab reheating CFD model, the steel scrap preheating CFD model and the steel scrap melting in bath CFD model. The computational models were developed in order of complexity. First, the primary model was developed based on a steel slab reheating process. The steel scrap preheating model is then developed based on the steel slab reheating CFD model. The contents of each chapter are specified as the following:

Chapter 1 gives an introduction of the research included in this dissertation. Detailed descriptions on the process and literature review are both conducted. The objective, specific research tasks and contributions from this study are also defined.

Chapter 2 lists all the three CFD models with detailed model assumptions and model equations. Various sub-models were also introduced with details.

Chapter 3 presents the research on using the developed steel slab reheating CFD model to simulate the furnace flow properties, combustion and slab reheating process in an industrial reheating furnace. Both a comprehensive 3-D CFD model and a 2-D heat transfer model are introduced with model validation and model applications.

Chapter 4 presents the research on applying the developed steel scrap preheating CFD model to investigate the scrap preheating process in an industrial EAF. Simulation conditions, model validation, and parametric studies are provided.

Chapter 5 presents the research on using the developed steel scrap melting in bath CFD model to study the scrap melting bath process in an industrial EAF. The research on the important sub-models was detailed and useful conclusions were drawn.

Chapter 6 lists all the conclusions from this research work in this dissertation. The future work for these models are further discussed.

CHAPTER 2. CFD MODELS

The steel slab reheating, steel scrap preheating and melting processes in industrial steelmaking furnaces typically involve gas flow, combustion, multi-mode heat transfer, and phase change. Therefore, the modeling of steel reheating or preheating and melting processes will be subjected to modeling the gas flow and combustion process along with heat transfer and phase change. In this chapter, the general combustion process of natural gas used in industrial steelmaking furnaces is modeled using the EDC model. The heat transfer involving conduction, convection, and radiation are also modeled in detail. The following model description consists of a steel slab reheating CFD model, a steel scrap preheating CFD model, and a steel scrap melting in bath CFD model.

2.1 CFD Model for Steel Slab Reheating

2.1.1 Model Description and Assumptions

In this CFD model, detailed turbulent combustion flow with heat and mass transfer was included. The realizable k-ε turbulence model [89] was applied to predict the flow turbulence. The species transport model was employed to take account of the natural gas combustion with the EDC turbulence combustion model [90] enabled to calculate the combustion reactions. In theory, the heat transfer in a reheating furnace includes several modes, but radiation is dominant. Work done by Kim et al. [15,19], and Singh et al. [16,17,91,92] indicates that the DO radiation model [93] and WSGGM are appropriate to be used to predict the radiation within a reheating furnace. Following these studies, the DO radiation model was adopted to take account of the dominant heat transfer flux, while the WSGGM was used to describe the radiation heat transfer in the combustion gas medium in the present model. The WSGGM has been widely used in industrial reheating furnace simulations since the furnace atmosphere is highly concentrated in CO_2 and H_2O. Man Young Kim's [16] study also indicated that the gray absorption coefficient was similar to the one obtained from the WSGG non-gray model. The slab dynamic movement was realized by using the dynamic mesh model with a UDF code developed to control the specific slab walking speed according to the real operating condition.

The following general assumptions were made in this model:

1. The slab moving speed uses an averaged value for each minute, and the vertical movement of the slab is not included.
2. The fuel input is defined using the hourly average due to limitations on plant data recording.
3. The scale formation and its effect on the heat transfer are neglected.

2.1.2 Governing Equations

The mass conservation equation is:

$$\frac{\partial \rho}{\partial t} + \nabla \cdot (\rho \vec{v}) = 0 \tag{1}$$

The momentum conservation equation is defined as:

$$\frac{\partial}{\partial t}(\rho \vec{v}) + \nabla \cdot (\rho \vec{v} \vec{v}) = -\nabla p + \nabla \cdot (\bar{\bar{\tau}}) + \rho \vec{g} + \vec{F} \tag{2}$$

where p is the static pressure, $\rho \vec{g}$ and $\vec{F}$ are the gravitational body force and external body force, ρ is the fluid density, $\vec{v}$ is the fluid velocity having x, y and z components, and $\bar{\bar{\tau}}$ is the stress tensor which is given by

$$\bar{\bar{\tau}} = \mu \left[(\nabla \vec{v} + \nabla \vec{v}^T) - \frac{2}{3} \nabla \cdot \vec{v} I \right] \tag{3}$$

where μ is the molecular viscosity, I is the unit tensor, and the second term on the right hand side is the effect of volume dilation. By the long-time averaged method, Equation (2) can be converted to a Reynolds-averaged Navier-Stokes (RANS) equation as follows:

$$\frac{\partial}{\partial t}(\rho u_i) + \frac{\partial}{\partial x_j}(\rho u_i u_j) = -\frac{\partial p}{\partial x_i} + \frac{\partial}{\partial x_j}\left[\mu \left(\frac{\partial u_i}{\partial x_j} + \frac{\partial u_j}{\partial x_i} - \frac{2}{3} \delta_{ij} \frac{\partial u_l}{\partial x_l} \right) \right] + \frac{\partial}{\partial x_j}\left(-\rho \overline{u_i' u_j'} \right) \tag{4}$$

In Equation (4), the Reynolds stresses may be related to the velocity gradient by the Boussinesq hypothesis as follows:

$$-\rho\overline{u_i'u_j'} = \mu_t\left(\frac{\partial u_i}{\partial x_j}+\frac{\partial u_j}{\partial x_i}\right)-\frac{2}{3}\left(\rho k+\mu_t\frac{\partial u_k}{\partial x_k}\right)\delta_{ij} \quad (5)$$

where δ_{ij} is the stress tensor due to molecular viscosity.

Turbulence modeling is achieved with the realizable k-ε turbulence model. As the average Reynolds number for flow within the reheating furnace is high, the entirety of the flow domain is in the turbulent regime. The gas flow pattern in the reheating furnace shows high turbulence intensity characteristic as its vortex mixing mechanism. This turbulence phenomenon can be solved by time-averaged velocity scalar. The gas flow conditions in this study are calculated based on the Reynolds-averaged Navier-Stokes (RANS) equations. The averaged Reynolds stresses term can be solved through the conservation of kinetic energy and dissipation rate. The realizable k-ε turbulence model is used due to its ability to model flow with strong streamline curvature, vortices, and rotation. The standard wall function was used for the near-wall treatment. The turbulence energy (k) expressed below:

$$\frac{\partial}{\partial t}(\rho k)+\frac{\partial}{\partial x_i}(\rho k u_i)=\frac{\partial}{\partial x_j}\left[\left(\mu+\frac{\mu_t}{\sigma_k}\right)\frac{\partial k}{\partial x_j}\right]+G_k+G_b-\rho\varepsilon-Y_M+S_K \quad (6)$$

$$\mu_t = c_\mu\rho\frac{k^2}{\varepsilon} \quad (7)$$

The generation of kinetic energy and buoyancy force attribution are:

$$G_k = -\rho\overline{u_i'u_j'}\frac{\partial u_j}{\partial x_i} \quad (8)$$

$$G_b = \beta g_i\frac{\mu_t}{Pr_t}\frac{\partial T}{\partial x_i} \quad (9)$$

The turbulent dissipation rate (ε)

$$\frac{\partial}{\partial t}(\rho\varepsilon)+\frac{\partial}{\partial x_j}(\rho\varepsilon u_j)=\frac{\partial}{\partial x_j}\left[\left(\mu+\frac{\mu_t}{\sigma_\varepsilon}\right)\frac{\partial\varepsilon}{\partial x_j}\right]+\rho C_1 S\varepsilon-\rho C_2\frac{\varepsilon^2}{k+\sqrt{\nu\varepsilon}}+C_{1\varepsilon}\frac{\varepsilon}{k}C_{3\varepsilon}G_b+S_\varepsilon \quad (10)$$

where the equations are given on x_j direction, σ_k and σ_ε are the turbulent Prandtl numbers for k and ε, 1.0, 1.2, μ_t is the turbulence viscosity, G_k is the generation of turbulence kinetic energy due to the mean velocity gradients, G_b is the generation of turbulence kinetic energy due to buoyancy, and Y_M represents the contribution of the fluctuating dilatation in compressible turbulence to the overall dissipation rate, which is zero in this model. S_K and S_ε are user-defined source terms, which is 0 in this model. C_1 = max(0.43,$\frac{\eta}{\eta+5}$), $\eta = s\frac{k}{\varepsilon}$, $s=\sqrt{2S_{ij}S_{ij}}$, $S_{ij} = \frac{1}{2}(\frac{\partial u_j}{\partial x_i} + \frac{\partial u_i}{\partial x_j})$, C_2 and $C_{1\varepsilon}$ are constants, 1.9 and 1.44, respectively.

The energy equation can be represented as:

$$\frac{\partial}{\partial t}(\rho E) + \nabla \cdot [\vec{v}(\rho E + p)] = \nabla \cdot \left[k_{eff}\nabla T - \sum_j h_j \vec{J}_j + \left(\bar{\bar{\tau}}_{eff} \cdot \vec{v}\right)\right] + S_h \quad (11)$$

where k_{eff} is the effective conductivity ($k + \frac{C_p \mu_t}{Pr_t}$) and $\vec{J}_j$ is the diffusion flux of species j. The first three terms on the right-hand side of the equation represent energy transfer due to conduction, species diffusion, and viscous dissipation respectively. S_h includes the heat of chemical reaction, and any other volumetric heat sources. E is defined as:

$$E = h - \frac{p}{\rho} + \frac{v^2}{2} \quad (12)$$

where sensible enthalpy h is defined for incompressible flows as

$$h = \sum_j Y_j h_j + \frac{p}{\rho} \quad (13)$$

where Y_j is the mass fraction of species j, and h_j is defined as

$$h_j = \int_{298.15K}^{T} C_{p,j} dT \quad (14)$$

where $C_{p,j}$ is the constant pressure specific heat of species j.

The species transport model was used to define the species and to calculate the species conservation and transportation. The local mass fraction of each species Y_i can be solved by the convection-diffusion equations. The conservation equation of each species can be expressed by

$$\frac{\partial}{\partial t}(\rho Y_i) + \nabla * (\rho \bar{v} Y_i) = -\nabla * \vec{J}_i + R_i \quad (15)$$

where R_i is the net rate of production of species *i* by chemical reactions. $\vec{J}_i$ is the diffusion flux term of species *i*, which arises due to gradients of concentration and temperature, under which the diffusion flux is given as follow:

$$\vec{J}_i = -(\rho D_{i,m} + \frac{\mu_t}{Sc_t})\nabla Y_i - D_{T,i}\frac{\nabla T}{T} \quad (16)$$

where $D_{i,m}$ is the diffusion coefficient for species i in the mixture, $D_{T,i}$ is the thermal diffusion coefficient, and Sc_t is the turbulent Schmidt number, which is 0.7.

The detailed Arrhenius chemical reaction kinetics of air-natural gas combustion can be incorporated in turbulent flames through the EDC model [94]. The EDC model relies on the Kolmogorov cascade of energy dissipation on all length scales in turbulence flow. The chemical reactions and molecular mixing were assumed to be associated with turbulence dissipation occurring in the fine structure of the flow. The source terms in the conservation equation for the mean species *i are* modeled as follows:

$$R_i = \frac{\rho(\xi^*)^2}{\tau^*\left[1-(\xi^*)^3\right]}(Y_i^* - Y_i) \quad (17)$$

where $Y_i^*$is the mass fraction of species i within the fine structures after reacting over the time τ^*, Y_i is the Favre-averaged mass fraction of species i obtained from

$$Y_i = (\xi^*)^3 Y_i^* + (1-(\xi^*)^3)Y_i^0 \quad (18)$$

where Y_i^0 represents the mass fraction of species i in the fluid surrounding the fine structures, and ξ^* the mass fraction occupied by the fine structure regions can be expressed as:

$$\xi^* = C_\xi(\frac{v\varepsilon}{k^2})^{1/4} \tag{19}$$

where C_ξ is a volume fraction constant and the value is 2.1377, C_T is the time scale constant, 0.4082. The reactions are assumed to occur in the fine structures over a residence time scale τ^*.

$$\tau^* = C_\tau(\frac{v}{\varepsilon})^{1/2} \tag{20}$$

Natural gas combustion happens right after mixing with combustion air in the reheating furnace and a high-temperature combustion flame will supply heat for the slab reheating process. The radiation heat transfer has a great effect on the temperature distributions. According to the literature [90,95], the DO radiation model has been widely used to simulate the steel slab reheating process. It solves the radiative transfer equation (RTE) for a finite number of discrete solid angles. Each angle is associated with a vector direction $\vec{s}$ fixed in the Cartesian system, and is treated as a field equation which can be described as:

$$\nabla \cdot (I(\vec{r}, \vec{s})\vec{s}) + (a + \sigma_s)I(\vec{r}, \vec{s}) = an^2\frac{\sigma T^4}{\pi} + \frac{\sigma_s}{4\pi}\int_0^{4\pi} I(\vec{r}, \vec{s}')\Phi(\vec{s} \cdot \vec{s}')d\Omega' \tag{21}$$

where $\vec{r}$ is position vector, $\vec{s}$ is the direction vector, and $\vec{s}'$ is the scattering direction vector, a is absorption coefficient, n is refractive index, σ_s is scattering coefficient, σ is Stefan-Boltzmann constant (5.669 x 10^{-8} $W/m^2 \cdot K^4$), I is radiation intensity, which depends on the position, $\vec{r}$ and the direction $\vec{s}$, T is local temperature, Φ is phase function, Ω' is solid angle. In this study, the implementation of the DO model in ANSYS Fluent is called the finite-volume scheme. Each octant of the angular space 4π at any spatial location is discretized into $N_\emptyset$ and N_θ solid angles. N_θ is equal to 4 and $N_\emptyset$ is equal to 8 with 32 discretized angular components of the radiation intensity. $\emptyset$ and θ are the polar and azimuthal angles.

The gas radiative properties was calculated using the WSGGM. The WSGGM is a reasonable compromise between the oversimplified gray gas model and a complete model which takes into account particular absorption bands [93]. The emissivity over the distance S can be presented as:

$$\varepsilon = \sum_{i=0}^{I} a_{\varepsilon,i}(T)\ (1 - e^{-K_i PS}) \tag{22}$$

where $a_{\varepsilon,i}$ is the emissivity weighting factor for the *i*th fictitious gray gas, the bracketed quantity is the *i*th fictitious gray gas emissivity, K_i is the absorption coefficient of the *i*th gray gas, P is the sum of the partial pressures of all absorbing gases, and S is the path length.

The absorption coefficient for i=0 is assigned a value of zero to account for windows in the spectrum between spectral regions of high absorptions ($\sum_{i=0}^{I} a_{\varepsilon,i} < 1$) and the weighting factor for i=0 is evaluated as:

$$a_{\varepsilon,0} = 1 - \sum_{i=0}^{I} a_{\varepsilon,i} \tag{23}$$

The temperature dependence of the emissivity weighing factor can be approximated by the function:

$$a_{\varepsilon,i} = \sum_{j=0}^{J} b_{\varepsilon,i,j} T^{j-1} \tag{24}$$

where $b_{\varepsilon,i,j}$ is the emissivity gas temperature polynomial coefficient [93]. The coefficients $b_{\varepsilon,i,j}$ and K_i are varying with PS and T. When 0.001 $\leq PS \leq$ 10.0 atm-m and 600 $\leq T \leq$ 2400K, the coefficients are provided by Smith et al. [96] When T > 2400K, the coefficients are provided by Coppalle and Vervisch [97].

The absorption a can be estimated as:

$$a = -\frac{\ln(1-\varepsilon)}{s} \tag{25}$$

where ε (the emissivity for the WSGGM) can be computed using Equation (22).

The path length S was set equal to the mean beam length, which is expressed as:

$$S = 3.6\frac{V}{A} \tag{26}$$

where V is the fluid volume, m^3, A is the total surface area of the fluid boundaries, m^2.

The slab movement was modeled using the dynamic mesh model to account the heat transfer between the gas medium and the solid slabs. In the transient simulation, the steel slabs are moving from the slab charging door to the discharging door. The moving speed is generally varying with time according to the furnace real operating condition. In this study, the steel slab vertical movement was neglected. The horizontal movement was modeled using the dynamic mesh model. In the CFD model, a UDF was used to realize a detailed control of the slab moving speed towards the discharging door. In the UDF, the slab moving speed was specified based on the slab location change. In real operation, the slab locations were tracked every minute by the operation model. The averaged velocity within each minute was calculated and used in the CFD model. With respect to dynamic meshes, the integral form of the conservation equation for a general scalar $\emptyset$, on an arbitrary control volume V, whose boundary is moving can be expressed as:

$$\frac{\partial}{\partial t}\int_V \rho\,\emptyset\,dV + \int_{\partial V} \rho\,\emptyset(\vec{u} - \vec{u}_{mesh})d\vec{A} = \int_{\partial V} \Gamma\,\nabla\emptyset d\vec{A} \tag{27}$$

where ρ is the fluid density, $\vec{u}$ is the flow velocity vector, $\vec{u}_{mesh}$ is the mesh velocity of the moving mesh, Γ is the diffusion coefficient, ∂V is to represent the boundary of the control volume V. In this study, $\vec{u}_{mesh}$ is specified by using a UDF. During the mesh moving, the spring-based smoothing method was applied to adjust the mesh of a zone with a moving boundary. The interior nodes of the mesh move based on defined velocity, but the number of nodes and their connectivity does not change.

The CFD simulations in the present work were performed by using the commercial software package ANSYS Fluent 16.2 [93,98,99]. The Finite Volume Method (FVM) [99] was used to solve the partial differential equations by discretizing the equations using an upwind differencing

scheme over the finite volumes. The SIMPLE algorithm was used to adjust the pressure and velocities after each iteration when solving the gas continuity and momentum equations. In the full-scale furnace simulations, the computational grid exceeds 10 million and the calculations were conducted on the High-Performance Computer (HPC) at Purdue University Northwest. Each transient slab reheating process needs approximately 168 hours to simulate 2 hours of furnace operation by using 80 processors.

2.2 CFD Model for Steel Scrap Preheating

2.2.1 Model Description and Assumptions

The EAF utilizes chemical energy in the process to reduce the electricity consumptions. Oxy-fuel burners firing natural gas have been widely used in industrial EAFs. A variety of complex phenomena take place within EAF during the scrap preheating process: oxy-fuel combustion, gas/scrap heat transfer, scrap oxidation, and scrap melting. In this model, the solid scrap is treated as a porous media. The oxy-fuel combustion was modeled with a detailed calculation of flame temperature, species distributions. The scrap oxidation was considered and it contributes heat to the scrap phase.

The following general assumptions were made in this model:

1. The scrap melting phenomenon is simplified by converting solid to liquid at the melting point.
2. The scrap porosity is uniform in the industrial furnace simulation.
3. The scrap initial temperature is using a mass-weighted-averaged value by considering the physical heat from the hot heel and charged hot metal.

2.2.2 Governing Equations

The scrap preheating CFD model was established based on the detailed physics and chemistry occurring during the EAF operation. The model considers gas flow, oxy-fuel combustion, multi-mode heat transfer including the heat exchange between gas and solid scrap, scrap oxidation, and scrap melting. Numerical simulation was conducted using the commercial software ANSYS Fluent.

The scrap phase was treated as a porous medium and its governing equations were input into ANSYS Fluent using the user-defined scalar (UDS). Gas momentum sink due to the porous medium is considered using a UDF. The energy source terms for both gas and solid phases are added using UDFs. The UDFs are solved together with other terms in the governing equations. The EDC model was used to calculate the propane-oxygen and natural gas-oxygen combustion reactions with the appropriate chemical reaction mechanism. The DO radiation model was used to model the dominant heat transfer flux, and a modified WSGGM for oxy-fuel combustion [100] was used to describe the radiation heat transfer in the combustion gases. The modified WSGGM for oxy-fuel combustion is implemented using a UDF. The governing equations were solved in transient conditions.

The gas phase governing equations used for steel scrap preheating model in this study are as follows:
The mass conservation equation is:

$$\frac{\partial \rho}{\partial t} + \nabla \cdot (\rho \vec{v}) = 0 \tag{28}$$

The momentum conservation equation is:

$$\frac{\partial}{\partial t}(\rho \vec{v}) + \nabla \cdot (\rho \vec{v} \vec{v}) = -\nabla p + \nabla \cdot (\bar{\bar{\tau}}) + \rho \vec{g} + \vec{F} + S_{gu} \tag{29}$$

where p is the static pressure, $\rho \vec{g}$ and $\vec{F}$ are the gravitational body force and external body force, respectively, and S_{gu} is a source term introduced by the scrap phase.

The momentum exchange between the gas phase and the solid scrap is described by an Ergun-type equation [101]. The source term for gas velocity in the x-direction is given as Equation (30), and the source term for gas velocity in the y-direction is similar.

$$S_{gu,i} = -\left(\frac{\mu}{\alpha} u_{g,i} + C_2 \frac{\rho_g |u_{g,i}|}{2} u_{g,i}\right) \tag{30}$$

where

$$\alpha = \frac{(\psi_j d_j)^2 \emptyset^3}{150(1-\emptyset)^2} \tag{31}$$

$$C_2 = 3.5 \frac{(1-\emptyset)}{(\psi_j d_j)\emptyset^3} \tag{32}$$

S_{gu} is the source term for the momentum equation of the gas phase, N/m^3, u_g is gas superficial velocity m/s, $\emptyset$ is scrap porosity, ψ_j is particle shape factor, 1, d_j is particle diameter, m, ρ is the fluid density, kg/m^3, $\vec{v}$ is the fluid velocity having *x*, *y* and *z* components, and $\bar{\bar{\tau}}$ is the stress tensor which is given by

$$\bar{\bar{\tau}} = \mu \left[(\nabla \vec{v} + \nabla \vec{v}^T) - \frac{2}{3} \nabla \cdot \vec{v} I \right] \tag{33}$$

where μ is the molecular viscosity, I is the unit tensor, and the second term on the right-hand side is the effect of volume dilation. By the long-time averaged method, Equation (29) can be converted to a Reynolds-averaged Navier-Stokes (RANS) equation as follows:

$$\frac{\partial}{\partial t}(\rho u_i) + \frac{\partial}{\partial x_j}\left(\rho u_i u_j\right) = -\frac{\partial p}{\partial x_i} + \frac{\partial}{\partial x_j}\left[\mu\left(\frac{\partial u_i}{\partial x_j} + \frac{\partial u_j}{\partial x_i} - \frac{2}{3}\delta_{ij}\frac{\partial u_l}{\partial x_l}\right)\right] + \frac{\partial}{\partial x_j}\left(-\rho\overline{u_i' u_j'}\right) \tag{34}$$

In Equation (34), the Reynolds stresses may be related to the velocity gradient by the Boussinesq hypothesis as follows:

$$-\rho\overline{u_i' u_j'} = \mu_t\left(\frac{\partial u_i}{\partial x_j} + \frac{\partial u_j}{\partial x_i}\right) - \frac{2}{3}\left(\rho k + \mu_t \frac{\partial u_k}{\partial x_k}\right)\delta_{ij} \tag{35}$$

where δ_{ij} is the stress tensor due to molecular viscosity. The realizable k-ε turbulence model is used with the standard wall function is used for the near-wall treatment.

The energy equation is:

$$\frac{\partial}{\partial t}(\rho E) + \nabla \cdot [\vec{v}(\rho E + p)] = \nabla \cdot \left[(k_{eff} + k_r)\nabla T - \sum_j h_j \vec{J}_j + \left(\bar{\bar{\tau}}_{eff} \cdot \vec{v}\right)\right] + S_h \quad (36)$$

where k_{eff} is the effective conductivity and $\vec{J}_j$ is the diffusion flux of species j. The first three terms on the right-hand side of the equation represent energy transfer due to conduction, species diffusion, and viscous dissipation, respectively. S_h includes the heat of chemical reaction, and any other volumetric heat sources. E is defined as:

$$E = h - \frac{p}{\rho} + \frac{v^2}{2} \quad (37)$$

where sensible enthalpy h is defined for incompressible ideal gases as

$$h = \sum_j Y_j h_j + \frac{p}{\rho} \quad (38)$$

where Y_j is the mass fraction of species j, and h_j (the sensible enthalpy for species j) is defined as

$$h_j = \int_{298.15K}^{T} C_{p,j} dT \quad (39)$$

where $C_{p,j}$ is the constant pressure specific heat of species j.

K_r is the radiative thermal conductivity [102,103], can be expressed as:

$$K_r = \frac{8\sigma T_j^3}{a+2\sigma_s} \quad (40)$$

$$a = 1.5\varepsilon(1-\emptyset)/d_j \quad (41)$$

$$s = 1.5\ (2-\varepsilon)(1-\emptyset)/d_j \quad (42)$$

where a is the absorption coefficient, σ_s is the scattering coefficient, T_j is the scrap temperature, $\emptyset$ is scrap porosity, d_j is the scrap size, σ is the Stefan-Boltzmann constant, and ε is emissivity.

The modified WSGGM [100] was applied to calculate gas mixture emissivity in the oxy-fuel combustion. Due to the fact that the WSGGM [96] was developed for traditional air-fuel combustion radiative gas properties calculation, it is difficult to naturally accommodate different combustion situations. It is known that much higher concentrations of CO_2 and H_2O are generated in the oxy-fuel combustion compared to air-fuel combustion, and the radiation heat transfer is strongly promoted [104]. The gaseous radiative properties are affected accordingly. The WSGGM was developed based on the air-fuel combustion atmosphere to calculate the gaseous radiative properties and will neglect the radiation effects of high CO concentrations. Many new WSGGMs [100,105-107] were developed to address the gas radiative properties for oxy-fuel combustion. The modified WSGGM [108] covers both the air-fuel and the oxy-fuel combustion scenarios and is used for calculating the in-flame radiation for oxy-fuel combustion in this study. It has a similar calculation efficiency compare to the WSGGM which is a reasonable compromise between the oversimplified gray gas model and a complete model that takes into account particular absorption bands. The emissivity over the distance S can be presented as:

$$\varepsilon = \sum_{i=0}^{I} a_{\varepsilon,i}(T)\ (1 - e^{-K_i PS}) \tag{43}$$

where $a_{\varepsilon,i}$ is the emissivity weighting factor for the *i*th fictitious gray gas, the bracketed quantity is the *i*th fictitious gray gas emissivity, K_i is the absorption coefficient of the *i*th gray gas, P is the sum of the partial pressures of all absorbing gases, and S is the path length.

$$a_{\varepsilon,i} = \sum_{j=1}^{J} b_{\varepsilon,i,j}\left(\frac{T_g}{T_{ref}}\right)^{j-1} \text{ i=1,000, } I,\ a_{\varepsilon,i}>0 \tag{44}$$

$$a_{\varepsilon,0} = 1 - \sum_{i=0}^{I} a_{\varepsilon,i} \tag{45}$$

where I = 4, J = 4, T_{ref} = 1200 K, $b_{\varepsilon,i,j}$ is the emissivity gas temperature polynomial coefficients. The modified WSGGM use values for K_i and $b_{\varepsilon,i,j}$ are listed in Yin et al. [100] The model was implemented using a UDF and compiled into ANSYS Fluent.

The absorption coefficient a can be estimated as:

$$a = -\frac{\ln(1-\varepsilon)}{S} \tag{46}$$

where ε (the emissivity for the modified WSGGM) can be computed using Equation (43). The beam length s is determined as:

$$S = 3.6\frac{V}{A} \tag{47}$$

where V is the volume of the domain, A is the total surface area of the volume.

The heat transfer between the gas and solid scrap is described as Equation (48), and the heat transfer coefficient proposed by Wakao et al. [109] and Mandal [59] are used to account for the porous bed effects on the heat transfer coefficient of a single particle. Re_j is the particle Reynolds number based on particle diameter and superficial gas velocity.

$$S_{gH} = h_j A_s (T_j - T_g) \tag{48}$$

$$\frac{h_j d_j}{k_g} = 2 + 1.1 {Re_j}^{0.6} {Pr_g}^{1/3} \ (T_j \leq 1373\text{K}) \tag{49}$$

$$h_j A_s = A * f(w) \frac{{V_g}^{0.9} {T_j}^{0.3}}{{d_j}^{0.75}} (T_j > 1373\text{K}) \tag{50}$$

where, S_{gH} is the heat transfer rate between gas and solid scrap, h_j is the heat transfer coefficient, A_s is the scrap surface area, k_g is a constant, 0.0184, Pr_g is Prandtl number (ratio of the kinematic

viscosity to thermal diffusivity), 0.5, Re_j is Reynolds number, A is constant, 160.0, $f(w)$ is constant, 0.5, V_g is gas velocity.

The species transport model was used to define the species in the gas mixture and to calculate the species conservation and transportation during the steel scrap preheating process. The model equation can be found in section 2.1.2. The oxy-propane combustion mechanisms and kinetics are listed in Table 2 [110].

Table 2. Oxy-propane reaction mechanisms and kinetics (units in kg, m, s, kcal, mol and K).

Mechanisms	Reaction	Reaction order	A	b	E
JL					
R1	$C_3H_8+1.5O_2 \rightarrow 3CO+4H_2$	$[C_3H_8]^{0.5}[O_2]^{1.25}$	4×10^{11}	0	30.0
R2	$C_3H_8+3H_2O \rightarrow 3CO+7H_2$	$[C_3H_8][H_2O]$	3×10^{8}	0	30.0
R3	$H_2+0.5O_2 \rightarrow H_2O$	$[H_2]^{0.25}[O_2]^{1.5}$	8.5×10^{15}	-1	40.0
R3r	$H_2O \rightarrow H_2+0.5O_2$	$[H_2]^{-0.75}[O_2][H_2O]$	2.52×10^{19}	-1.5	99.2
R4	$CO+H_2O \rightarrow CO_2+H_2$	$[CO][H_2O]$	2.75×10^{9}	0	20.0
R4r	$CO_2+H_2 \rightarrow CO+H_2O$	$[CO_2][H_2]$	9.268×10^{10}	0	28.1
Three-step					
R1	$C_3H_8+1.5O_2 \rightarrow 3CO+4H_2$	$[C_3H_8]^{0.5}[O_2]^{1.25}$	4×10^{11}	0	30.0
R2	$H_2+0.5O_2 \rightarrow H_2O$	$[H_2][O_2]^{0.5}$	1.8×10^{13}	0	35.1
R2r	$H_2O \rightarrow H_2+0.5O_2$	$[H_2O]$	5.337×10^{16}	-0.5	94.3
R3	$CO+0.5O_2 \rightarrow CO_2$	$[CO][O_2]^{0.5}[H_2O]^{0.5}$	1.3×10^{11}	0	30.0
R3r	$CO_2 \rightarrow CO+0.5O_2$	$[CO_2][H_2O]^{0.5}$	1.213×10^{16}	-0.5	97.1

Scrap oxidation reaction is also considered as the following mechanism:

$$Fe\ (s)+\frac{1}{2}O_2(g)=FeO\ (s), \Delta H_f^{298}=-270.16\ kJ/mol \tag{51}$$

Based on the steel oxidation model developed for steel slab oxidation in the reheating process [111], this scrap oxidation rate for EAF scrap oxidation is calculated based on the rate constant and species concentrations defined as:

$$(\frac{W}{A})^n = kt \cdot ([Fe][O_2])^n \tag{52}$$

where k ranges from 4.00×10^{-7} g^2/cm^4-s to 6.67×10^{-7} g^2/cm^4-s [112], the term $\frac{W}{A}$ is weight gain per unit area, t is time, $[Fe]$ is steel concentration in the local cell, $[O_2]$ is oxygen concentration in the local cell.

The general transport equation for the scrap phase is given as Equation (53). The transient term for solid scrap phase is included to consider the change of scrap molar density, enthalpy, and concentrations. In this study, since the scrap oxidation is simplified, only species Fe and FeO are considered. Due to the assumption that the scrap movement is not considered, the flux term F_i is zero in Equation (53). The diffusion term for the scrap molar density transportation equation is zero due to its solid form [113]. However, in the scrap enthalpy transportation equation, the thermal diffusivity is considered.

$$\frac{\partial(\rho_s \emptyset_s)}{\partial t} + \frac{\partial}{\partial \mathrm{x}_i}\left(F_i \emptyset_s - \Gamma_k \frac{\partial \emptyset_s}{\partial \mathrm{x}_i}\right) = S_s \tag{53}$$

The general variables for the scrap phase are listed in Table 3.

Table 3. General variables for solid scrap phase.

Scalar	$\emptyset_s$	ρ_s	F_i	Γ_k	S_s
Scrap Molar Density	1	1	0	0	0
Scrap Enthalpy	H_s	ρ_s	0	Γ_k	S_{gH}
[Fe] concentration	Z_{Fe}	ρ_s	0	0	$-S_R$
[FeO] concentration	Z_{FeO}	ρ_s	0	0	S_R

The realizable k-ε turbulence model has been applied to model the turbulence of gas flow.

The CFD simulations were conducted by using the commercial software package ANSYS Fluent 18.2. The SIMPLE algorithm was used to adjust the pressure and velocities after each iteration when solving the gas continuity and momentum equations.

2.3 CFD Model for Steel Scrap Melting

2.3.1 Model Description and Assumptions

When simulating the steel scrap melting in the liquid steel bath, the heat transfer from the liquid steel to the steel scrap is the key. During the melting process, it involves the multiphase flow, heat transfer and phase change.

The following assumptions were made in the development of the scrap melting in bath model:

1. The scrap was treated as individual pieces with given shape and size.
2. The heat coming from the electric arc was treated as a heat flux from the contact surface of the electrode.
3. The electromagnetic force introduced by the AC electrodes is neglected.
4. The coherent jet interaction with liquid steel bath is simplified as momentum transfer.

2.3.2 Governing Equations

2.3.2.1 Melting in Bath Sub-model

As the focus of this simulation is to simulate the time-dependent melting process of steel scrap in EAF, the non-isothermal condition is defined and no chemical reactions are considered. The VOF multiphase flow model was employed to calculate the phase distributions and interactions. The k-ε turbulence model was used to describe the turbulence properties. The enthalpy-porosity method is used to model the steel scrap melting. The equations solved in this model are as follows:
The mass conservation equation is:

$$\frac{\partial \rho}{\partial t} + \nabla \cdot (\rho \vec{v}) = S_m \tag{54}$$

The momentum conservation equation is:

$$\frac{\partial(\rho\vec{v})}{\partial t} + \nabla \cdot (\rho\vec{v}\vec{v}) = -\nabla_p + \nabla \cdot (\bar{\bar{\tau}}) + \rho\vec{g} + S_u \tag{55}$$

where p is the static pressure, $\rho\vec{g}$ is the gravitational body force, and $\bar{\bar{\tau}}$ is the stress tensor, given by

$$\bar{\bar{\tau}} = \mu\left[(\nabla\vec{v} + \nabla\vec{v}^T) - \frac{2}{3}\nabla \cdot \vec{v}I\right] \tag{56}$$

where μ is the molecular viscosity, I is the unit tensor, and the second term on the right-hand side is the effect of volume dilation.

The source term S_u modifies the balance of the equation on the completion of melting phase change. In the enthalpy-porosity method, the melting interface is tracked based on a quantity called the liquid fraction. The mushy zone is defined where the liquid fraction lies between 0 and 1, which is modelled as a porous medium.

$$S_u = \frac{(1-\beta)^2}{(\beta^3+\varepsilon)} A_{mush}\vec{\mathrm{v}} \tag{57}$$

where β is the liquid fraction, ε is a small number to prevent division by zero. A_{mush} is the mushy zone constant.

The standard k-ε turbulence model, which is based on model transport equations for the turbulence kinetic energy (k) and its dissipation rate (ε), is applied. Due to the mushy zone assumption when considered the melting phase change, the source terms S_K and S_ε can be defined as:

$$S = \frac{(1-\beta)^2}{(\beta^3+\varepsilon)} A_{mush}\emptyset \tag{58}$$

where $\emptyset$ represents the turbulence quantity S and ε.

Since the air phase and liquid steel phase co-exist in the EAF during melting in bath, the VOF formulation is used, which relies on the fact that two or more fluids or phases are not interpenetrating. For each additional phase, a new variable is introduced such as the volume fraction of the phase in the computational cell. In each control volume, the sum of volume fractions of all phases is unity. The fields for all variables and properties are shared by the phases and represent volume-averaged values, as long as the volume fraction of each of the phases is known at each location. Thus the variables and properties in any given cell are either purely representative of one of the phases, or representative of a mixture of the phases, depending upon volume fraction values.

$$\alpha_g + \alpha_q = 1 \tag{59}$$

where α_q is the q^{th} fluid's volume fraction in the cell, whern

• $\alpha_q = 0$: the cell is empty (of the q^{th} fluid).

• $\alpha_q = 1$: the cell is full (of the q^{th} fluid).

• $0 < \alpha_q < 1$: the cell contains the interface between the q^{th} fluid and one or more other fluids.

The volume-fraction-averaged density:

$$\rho = \alpha_g \rho_g + \alpha_q \rho_q \tag{60}$$

The volume-fraction-averaged viscosity:

$$\mu = \alpha_g \mu_g + \alpha_q \mu_q \tag{61}$$

The variable α_g satisfies Equation (62):

$$\frac{\partial}{\partial t}(\alpha_g) + \nabla \cdot (\alpha_g \vec{v}) = 0 \tag{62}$$

In the enthalpy-porosity method, the energy equation is written as:

$$\frac{\partial}{\partial t}(\rho H) + \nabla \cdot (\rho \vec{v} H) = \nabla \cdot (k \nabla \mathrm{T}) \ + S \tag{63}$$

where H is enthalpy, ρ is density, $\vec{v}$ is fluid velocity. The enthalpy of the material is computed as the sum of the sensible enthalpy, h and the latent heat, ΔH.

$$H = h + \Delta H \tag{64}$$

$$h = h_{ref} + \int_{T_{ref}}^{T} C_p dT \tag{65}$$

where h_{ref} is reference enthalpy, T_{ref} is reference temperature, C_p is specific heat at constant pressure.

The liquid fraction β can be defined as:

$$\begin{aligned} &\beta = 0 \quad if\ T < T_{solidus} \\ &\beta = 1 \quad if\ T > T_{solidus} \\ &\beta = \frac{T - T_{solidus}}{T_{liquidus} - T_{solidus}} \quad if\ T_{solidus} < T < T_{liquidus} \end{aligned} \tag{66}$$

The latent heat content can be written in terms of the latent heat of material, L:

$$\Delta H = \beta L \tag{67}$$

2.3.2.2 Coherent Jet Sub-model

The standard k-epsilon turbulence model was applied with modifications on both the turbulence viscosity and compressibility. A UDF was developed to implement the modifications. The species transport model was employed to model species transportation due to flow and natural gas combustion, with the EDC model to account for the turbulence combustion reactions. The DO radiation model was used to model the radiation heat transfer flux, and the modified WSGGM was

used to describe the radiation heat transfer in the combustion gases. The governing equations were solved in steady-state conditions.

The mass conservation equation is:

$$\nabla \cdot (\rho \vec{v}) = 0 \tag{68}$$

The momentum conservation equation is defined as:

$$\nabla \cdot (\rho \vec{v} \vec{v}) = -\nabla p + \nabla \cdot (\bar{\bar{\tau}}) + \rho \vec{g} + \vec{F} \tag{69}$$

where p is the static pressure, $\rho \vec{g}$ and $\vec{F}$ are the gravitational body force and external body force, ρ is the fluid density, $\vec{v}$ is the fluid velocity having *x*, *y* and *z* components, and $\bar{\bar{\tau}}$ is the stress tensor, given by

$$\bar{\bar{\tau}} = \mu \left[(\nabla \vec{v} + \nabla \vec{v}^T) - \frac{2}{3} \nabla \cdot \vec{v} I \right] \tag{70}$$

where μ is the molecular viscosity, I is the unit tensor, and the second term on the right-hand side is the effect of volume dilation. By the long-time averaged method, Equation (69) can be converted to a Reynolds-averaged Navier-Stokes (RANS) equation as follows:

$$\frac{\partial}{\partial t}(\rho u_i) + \frac{\partial}{\partial x_j}(\rho u_i u_j) = -\frac{\partial p}{\partial x_i} + \frac{\partial}{\partial x_j}\left[\mu \left(\frac{\partial u_i}{\partial x_j} + \frac{\partial u_j}{\partial x_i} - \frac{2}{3} \delta_{ij} \frac{\partial u_l}{\partial x_l} \right) \right] + \frac{\partial}{\partial x_j}\left(-\rho \overline{u_i' u_j'} \right) \tag{71}$$

In Equation (71), the Reynolds stresses may be related to the velocity gradient by the Boussinesq hypothesis as follows:

$$-\rho \overline{u_i' u_j'} = \mu_t \left(\frac{\partial u_i}{\partial x_j} + \frac{\partial u_j}{\partial x_i} \right) - \frac{2}{3} \left(\rho k + \mu_t \frac{\partial u_k}{\partial x_k} \right) \delta_{ij} \tag{72}$$

where δ_{ij} is the stress tensor due to molecular viscosity.

The energy equation is:

$$\frac{\partial}{\partial x_i}[u_i(\rho E + p)] = \frac{\partial}{\partial x_j}\left[k_{eff}\frac{\partial T}{\partial x_i} - \sum_j h_j \vec{J}_j + \left(\bar{\bar{\tau}}_{eff} \cdot \vec{v}\right)\right] + S_h \quad (73)$$

$$k_{eff} = k + \frac{c_p \mu_t}{\mathrm{Pr}_t} \quad (74)$$

where k_{eff} is the effective conductivity and $\vec{J}_j$ is the diffusion flux of species j. The first three terms on the right-hand side of the equation represent energy transfer due to conduction, species diffusion, and viscous dissipation, respectively. Pr_t is the turbulent Prandtl number, which is 0.85 as default in ANSYS Fluent. Alam et al. [53] use 0.5 as suggested by D. C. Wilcox [114]. It is suggested that for free shear layers, values on the order of 0.5 for the turbulent Prandtl number are more appropriate. Categorically, conventional supersonic jets are free shear flows, which are not bounded by solid surfaces. The turbulent Prandtl number used should be on the order of 0.5. However, for the coherent jet, the flame shroud prevents the free shear to a certain extent. Therefore, the turbulent Prandtl number should be larger than 0.5 yet smaller than 0.9. In this model, the turbulent Prandtl number used for the supersonic jet without a flame shroud is 0.5, and 0.85 for the supersonic jet with a flame shroud. S_h includes the heat of chemical reaction. E is defined as:

$$E = h - \frac{p}{\rho} + \frac{v^2}{2} \quad (75)$$

where sensible enthalpy h is defined for ideal gases as

$$h = \sum_j Y_j h_j \quad (76)$$

where Y_j is the mass fraction of species j, and h_j is defined as

$$h_j = \int_{298.15K}^{T} C_{p,j} dT \quad (77)$$

where $C_{p,j}$ is the temperature-dependent constant-pressure specific heat of species j.

Due to the high Reynolds number (1.5×10^6) in the coherent jet flow, the standard k-epsilon turbulence model was used. The standard wall function was used for the near-wall treatment. This turbulence phenomenon can be solved by using a time-averaged velocity scalar. The transport equation for the turbulence kinetic energy (k) is expressed below:

$$\frac{\partial}{\partial x_i}(\rho k u_i) = \frac{\partial}{\partial x_j}\left[\left(\mu + \frac{\mu_t}{\sigma_k}\right)\frac{\partial k}{\partial x_j}\right] - \rho\overline{u_i' u_j'}\frac{\partial u_j}{\partial x_i} - \rho\varepsilon - \rho\varepsilon M_\tau^2 \tag{78}$$

where μ_t is the turbulence viscosity. For High-Mach-number flows, the compressibility affects turbulence through dilatation dissipation. According to Sarkar [115], the compressibility effects were added as the last term in the turbulence kinetic energy conservation equation. M_τ is the turbulent Mach number defined as:

$$M_\tau = \frac{\sqrt{2k}}{a} \tag{79}$$

where a is the acoustic velocity (m/s), defined as:

$$a = \sqrt{\gamma RT} \tag{80}$$

The conservation equation for the turbulent dissipation rate (ε) is defined as:

$$\frac{\partial}{\partial x_i}(\rho\varepsilon u_i) = \frac{\partial}{\partial x_j}\left[\left(\mu + \frac{\mu_t}{\sigma_\varepsilon}\right)\frac{\partial \varepsilon}{\partial x_j}\right] - C_{1\varepsilon}\frac{\varepsilon}{k}\rho\overline{u_i' u_j'}\frac{\partial u_j}{\partial x_i} - \rho C_{2\varepsilon}\frac{\varepsilon^2}{k} \tag{81}$$

where the equations are given on the x_i direction. σ_k and σ_ε are the turbulent Prandtl numbers for k and ε, with values of 1.0 and 1.3, respectively; and $C_{1\varepsilon}$ and $C_{2\varepsilon}$, are constants and their values are 1.44 and 1.92, respectively.

The definition of the turbulent viscosity μ_t is given below:

$$\mu_t = C_\mu \rho \frac{k^2}{\varepsilon} \tag{82}$$

where the C_μ equals 0.09 in the standard k-epsilon turbulence model. In this study, the C_μ was modified according to Alam et al. [53] which was derived originally from the literature [116], which is shown below:

$$C_\mu = \frac{0.09}{C_T} \tag{83}$$

$$C_T = 1 + \frac{1.2{T_g}^{0.6}}{1+f(M_\tau)} \tag{84}$$

where T_g is the normalized local total temperature gradient, which is the function of k and ε:

$$T_g = \frac{|\nabla T_t|(k^{\frac{3}{2}}/\varepsilon)}{T_t} \tag{85}$$

where T_t is the local total temperature (K). The function $f(M_\tau)$ related to the turbulent Mach number was considered:

$$f(M_\tau) = ({M_\tau}^2 - {M_{\tau 0}}^2)H(M_\tau - M_{\tau 0}) \tag{86}$$

$H(x)$ is the Heaviside function, and $M_{\tau 0}$ is a constant equal to 0.1. To realize the k-epsilon turbulence model correction on C_μ, a UDF code was developed using C language and compiled to ANSYS Fluent.

The detailed Arrhenius chemical reaction kinetics of natural gas combustion can be incorporated in turbulent flames through the EDC model [117]. The chemical reactions and molecular mixing were assumed to be associated with turbulence dissipation occurring in the fine structure of the flow. The source terms in the conservation equation for the mean species, *I*, are modeled as:

$$R_i = \frac{\rho(\xi^*)^2}{\tau^*\left[1-(\xi^*)^3\right]}(Y_i^* - Y_i) \tag{87}$$

where Y_i^* is the mass fraction of species i within the fine structures after reacting over the time τ^*. Y_i is the Favre-averaged mass fraction of species i calculated from:

$$Y_i = (\xi^*)^3 Y_i^* + (1 - (\xi^*)^3) Y_i^0 \tag{88}$$

where Y_i^0 represents the mass fraction of species i in the fluid surrounding the fine structures, and ξ^* is the length fraction of the fine scales:

$$\xi^* = C_\xi \left(\frac{v\varepsilon}{k^2}\right)^{1/4} \tag{89}$$

where C_ξ is a volume fraction constant with a value of 2.1377, and v is kinematic viscosity. The reactions are assumed to occur in the fine structures over a residence time scale τ^*.

$$\tau^* = C_\tau \left(\frac{v}{\varepsilon}\right)^{1/2} \tag{90}$$

where C_T is the time scale constant, 0.4082.

The methane-oxygen combustion reaction mechanism used in this simulation is a 28-step model proposed by Jazbec et al. [118]

CHAPTER 3. MODELING OF STEEL SLAB REHEATING

Applied research utilizing CFD modeling to optimize the steel slab reheating process in a reheating furnace has been performed. Comprehensive numerical modeling and validation on an industrial walking beam slab reheating furnace were conducted. A transient three-dimensional (3-D) CFD model was developed to simulate the flow characteristics, combustion process, and multi-mode, multi-scale heat transfer inside the reheating furnace. The actual geometry of the furnace was used and typical operating conditions were simulated. Specific walking speeds of slabs in production were modeled using a dynamic mesh model which is controlled by a UDF solved using ANSYS Fluent. Fuel variations in different zones with time were also considered. The model was validated with instrumented slab trials conducted at the SSAB Mobile mill. The temperature field in the furnace and the temperature evolution of a slab predicted by the CFD model are in good agreement with those obtained from the instrumented slab trials. Based on the simulation results, the slab reheating process and the temperature uniformity of a slab at discharge were able to be properly evaluated.

Due to the fact that comprehensive 3-D CFD simulation is computationally expensive for large-scale industrial reheating furnaces, a simplified 2-D heat transfer model was developed to overcome the challenge of computational cost while also fully utilizing the 3-D CFD simulation results. A customized 2-D heat transfer model for the slab reheating process has also been developed based on the finite difference method. The simulation results from the 3-D CFD model provide detailed heat transfer boundary conditions for the 2-D heat transfer model. It also provides various I/O functions for users to input different conditions and output results including connections to real-time sensors such as thermocouples. Instrumented slab trials were conducted under typical operating conditions of the furnace and the results were used to calibrate the 2-D model. By comparing the slab temperatures measured from the instrumented slab trials and those predicted using the models, it was demonstrated that the 3-D CFD and 2-D heat transfer models predict the reheating process reasonably well (within 10% error). The proposed methodology is fairly easy to be used by mill engineers for troubleshooting and optimizing of the slab reheating process. The research process of conducting comprehensive modeling of the slab reheating process in industrial reheating furnaces is shown in Figure 14.

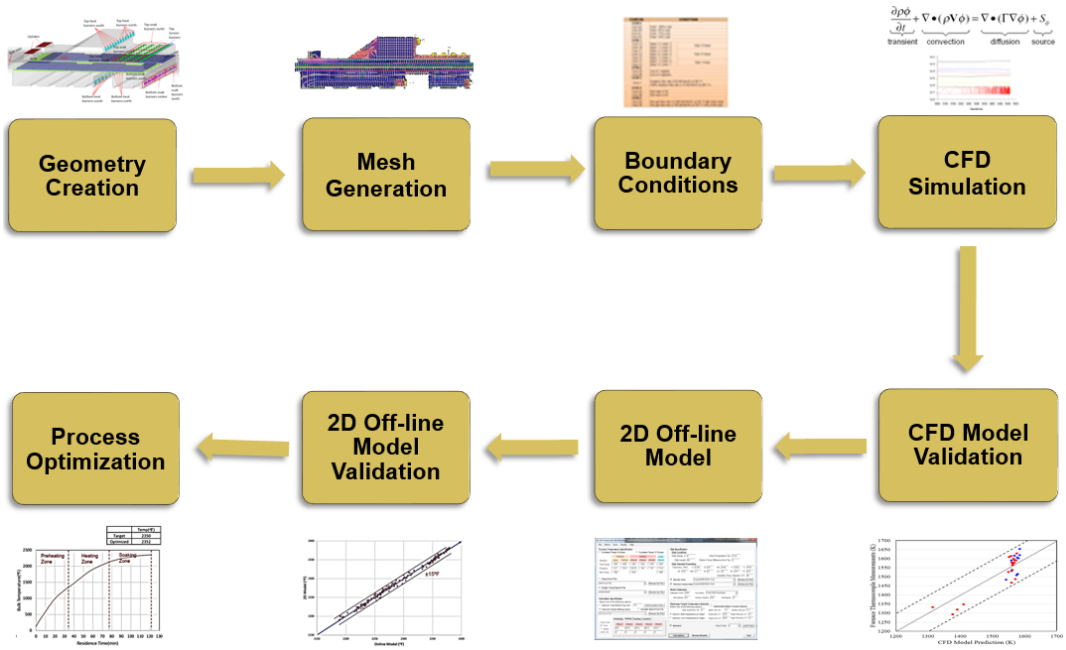

Figure 14. Research process of comprehensive modeling of the slab reheating process.

As shown in Figure 14, development of 3-D CFD model was conducted first to gain a fundamental understanding of the full-scale furnace operation. Then, model validation was carefully conducted with industrial measurement data on both furnace conditions and slab temperature. Based on the validated 3-D CFD model, the slab reheating process for cold charge, warm charge, and hot charge conditions were investigated. The convective heat transfer coefficient is then exported from the 3-D CFD model to the developed 2-D heat transfer model. After an in-depth validation of the developed 2-D heat transfer model, the 2-D heat transfer model is used to optimize the steel slab reheating process under different operation conditions. To simulate a slab reheating process using 2-D heat transfer model only takes a few seconds in terms of computational time, which significantly improved the efficiency of model prediction. The 3-D simulation can be used to investigate various aspects such as local temperature deviations which can not be captured by the 2-D heat transfer model.

3.1 Simulation Conditions

3.1.1 Model Geometry

A detailed geometric model was developed based on the drawings of the walking beam reheating furnace, as shown in Figure 15. From left to right (or from the charge door to the discharge door), the furnace can be divided into three temperature zones: preheating, heating, and soaking. Detailed burner geometries are included and the burner locations are also illustrated in Figure 15(a). Burners are mainly located in the heating and soaking zones, with no burners in the preheating zone. Burners are installed on both top and bottom sides of the furnace, which are grouped as Top Heat North, Top Heat South, Bottom Heat North, Bottom Heat South, Top Soak North, Top Soak Center, Top Soak South, Bottom Soak North, Bottom Soak Center, Bottom Soak South, and Top Screen. The total element number used for the simulation is 8.3 million. The details of the mesh near the burners, in the slab and in the moving zone are shown in Figure 15(b).

Fuel and air are evenly distributed to the burners inside a group. However, the fuel flow rate could vary from group to group depending on the heating condition. Steel slabs are charged from the left side into the furnace and travel toward the discharge door of the furnace on the right through the walking beams. To ensure optimum reheating, a ΔT between the slab bulk temperature at the exit of the heating zone and the targeted discharge temperature is used to control the slab movement. The soaking zone is mainly used to obtain a fully soaked slab with a homogenized temperature close to the aimed discharge temperature. The curved skids are also included in the geometry with a simplified form based on the real size of the skid and the cooling water pipes.

3.1.2 Boundary Conditions

In the simulations, natural gas was supplied as fuel. The fuel and combustion air mass flow rates and compositions are listed in Tables 4 and 5. During production, the fuel input varies with time. Hourly averaged fuel consumption was used to reduce the complexity of changing boundary conditions. In natural gas, methane is approximately 96%. A two-step reaction mechanism was applied for methane-air reaction to obtain more detailed species concentrations, while a one-step reaction mechanism was used for ethane-air combustion due to the small percentage as listed in Table 6. The furnace wall was treated as an adiabatic [15,21,31] wall with 0.75 emissivity [16].

The slab boundary is using the coupled wall condition, which takes the convective and radiative heat transfer. The slab wall emissivity is 0.5. The skid boundary condition is using a constant heat flux which is calculated from the absorbed energy of the cooling water. The charge door and discharge door were closed in the same condition as the furnace wall.

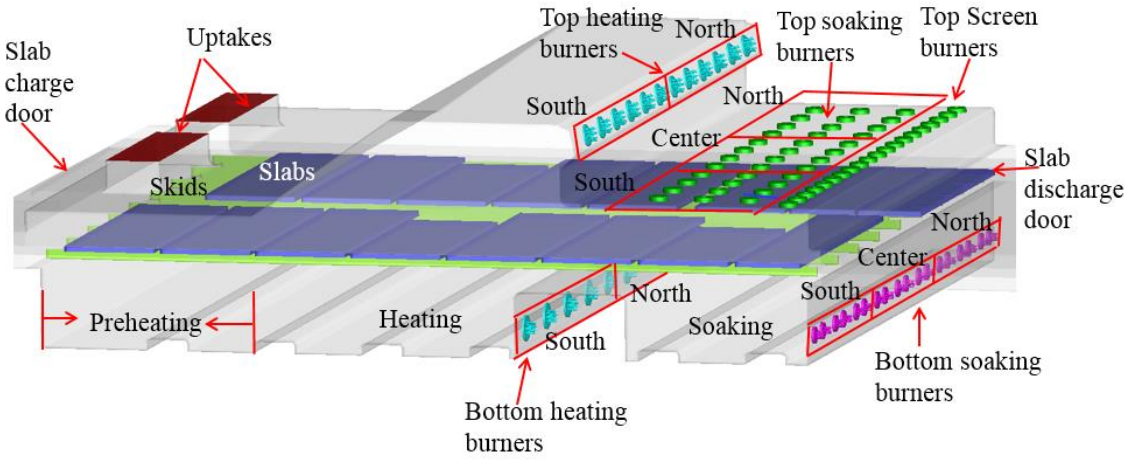

(a)

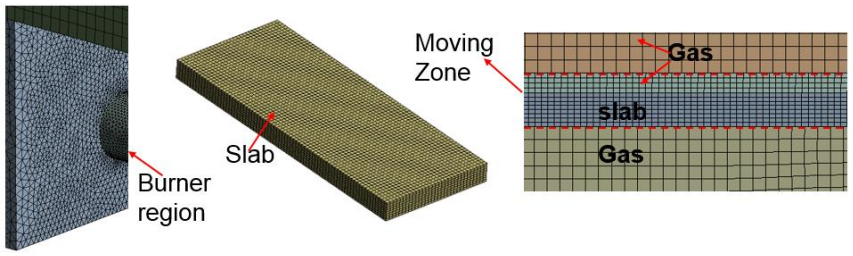

(b)

Figure 15. (a) Computational domain, (b) Mesh.

Table 4. Fuel and air consumption at different time period.

	Hourly average1 (1-36 min)		**Hourly average 2 (37-96 min)**		**Hourly average 3 (97-120 min)**	
Burners	Gas flow (kg/s)	Air flow (kg/s)	Gas flow (kg/s)	Air flow (kg/s)	Gas flow (kg/s)	Air flow (kg/s)
Top North Heat	0.36	5.92	0.35	5.71	0.29	4.92
Top South Heat	0.31	5.08	0.33	5.55	0.22	3.62
Bottom North Heat	0.19	3.29	0.43	7.33	0.15	2.72
Bottom South Heat	0.18	3.38	0.52	8.91	0.19	3.33
Top North Soak	0.00	0.29	0.01	0.25	0.01	0.27
Top Center Soak	0.00	0.24	0.01	0.24	0.00	0.25
Top South Soak	0.10	1.70	0.05	0.78	0.10	1.76
Bottom North Soak	0.00	0.24	0.01	0.24	0.00	0.25
Bottom Center Soak	0.10	1.63	0.11	1.83	0.15	2.57
Bottom South Soak	0.01	0.47	0.07	1.12	0.14	0.23
Screen Zone	0.01	0.31	0.10	1.57	0.10	1.54

Table 5. Fuel and air compositions.

Species	**Air (mol)**	**Fuel Gas (mol)**
O_2	21%	
N_2	79%	0.65%
H_2O		
CO_2		1.12%
CO		0.01%
C_2H_6		2.25%
CH_4		95.97%

Table 6. Reaction mechanisms and kinetics.

Reactions	**Pre-exponential Factor A [1/s]**	**Activation Energy E [J/mol]**
$CH_4 + 3/2\ O_2 \rightarrow CO + 2\ H_2O$	5.012×10^{11}	2.0×10^{8}
$CO + ½\ O_2 \rightarrow CO_2$	2.239×10^{12}	1.7×10^{8}
$CO_2 \rightarrow CO + ½\ O_2$	5.0×10^{8}	1.7×10^{8}
$C_2H_6 + 7/2\ O_2 \rightarrow 2\ CO_2 + 3\ H_2O$	6.186×10^{9}	1.256×10^{8}

3.1.3 Initial Conditions

The results of the mill instrumented slab trials were used to validate the numerical model by comparing the model predictions with measurements. The transient scheme was used. Simulation started at a certain time for a given mill trial. This is considered to be the initial condition for the numerical simulation. An example case is shown in Figure 16. There were sixteen slabs in the

reheating furnace and the trial slab was outside of the furnace, waiting to be charged. Two rows of slabs were charged into the reheating furnace alternatively one by one. The trial slab was charged after slabs B1 and B2 were charged. All of the slabs were lined up based on a real production scenario with specific slab length, width, initial temperature, steel grade, and positions. Based on the initial slab temperature, the furnace temperature was first calculated in the steady state as the initial furnace temperature as shown in Figure 17, after which the transient dynamic reheating process started. The initial slab temperature inside the furnace is defined based on the production calibrated level 2 model prediction.

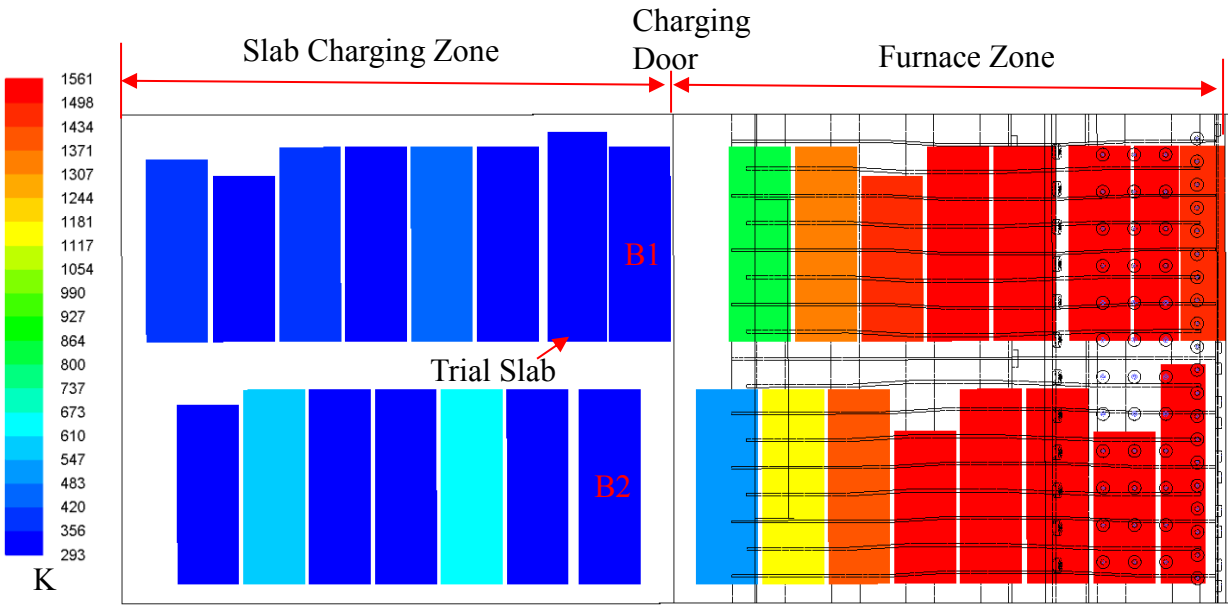

Figure 16. Initial slab line-up and temperature on the slab.

Since the CFD model was constructed based on a 3-D domain, the velocity and temperature contours on any plane (or cross-section) inside the furnace can be viewed. As an example, the velocity and temperature contours on three longitudinal cross-sections are shown in Figure 17. The center cross-section is at the middle width of the reheating furnace, while the north and south cross-sections are at the quarter width of the furnace on the north side and south side of the furnace, respectively. It can be seen from the velocity contours in Figure 17(a) that the operation of the reheating furnace exhibits a high turbulence and fast gas interaction characteristics. It can also be seen that the high-velocity zones are near the burners due to the combustion process. For instance, the velocity contour on the center cross-section shows high velocity flows near the bottom burners

in both the heating and soaking zones. The velocity contour on the south cross-section shows high-velocity combustion flow near the top burners in the heating zone. The temperature contours showed in Figure 17(b) illustrate the temperature evolution inside the furnace from the preheating zone to the soaking zone. It can be seen that the temperature distributions in the later heating zone and soaking zone are more uniform compared to that in the preheating zone.

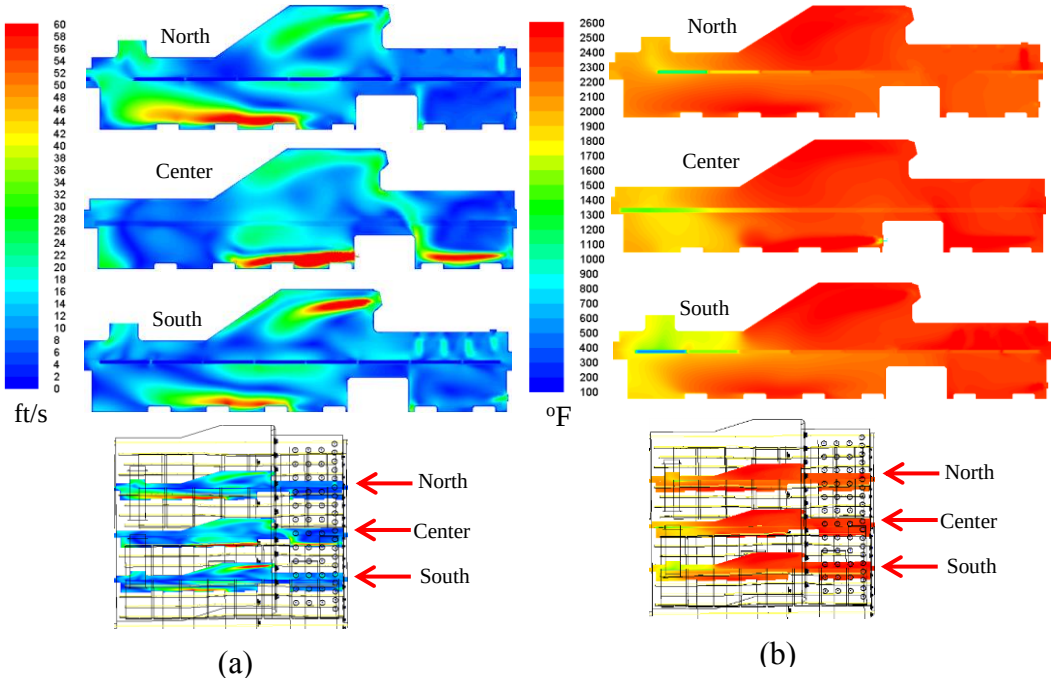

Figure 17. Contours on different longitudinal cross-sections of the reheating furnace, (a) Velocity, (b) Temperature.

There are 28 thermocouples in the reheating furnace which are used to monitor the furnace temperature in different zones as shown in Figure 18(a). All thermocouples colored in blue are on the bottom side of the furnace (the side below the slabs in the furnace) and the thermocouples colored in red are on the top side of the furnace (the side above the slabs in the furnace). Each thermocouple records a temperature every half minute at its corresponding location

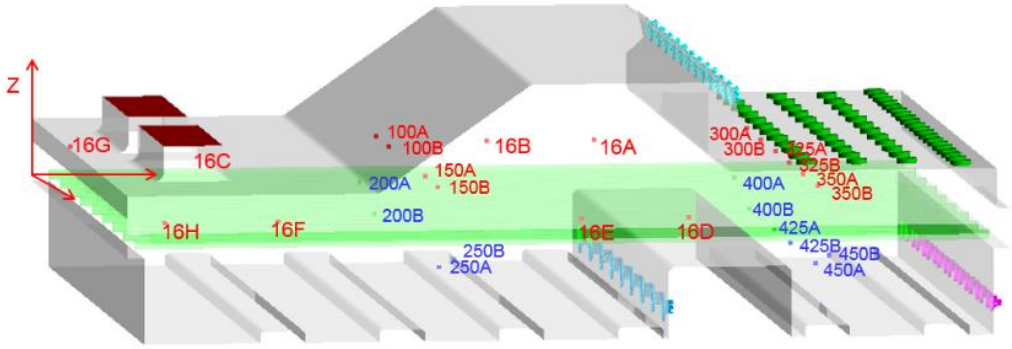

(a)

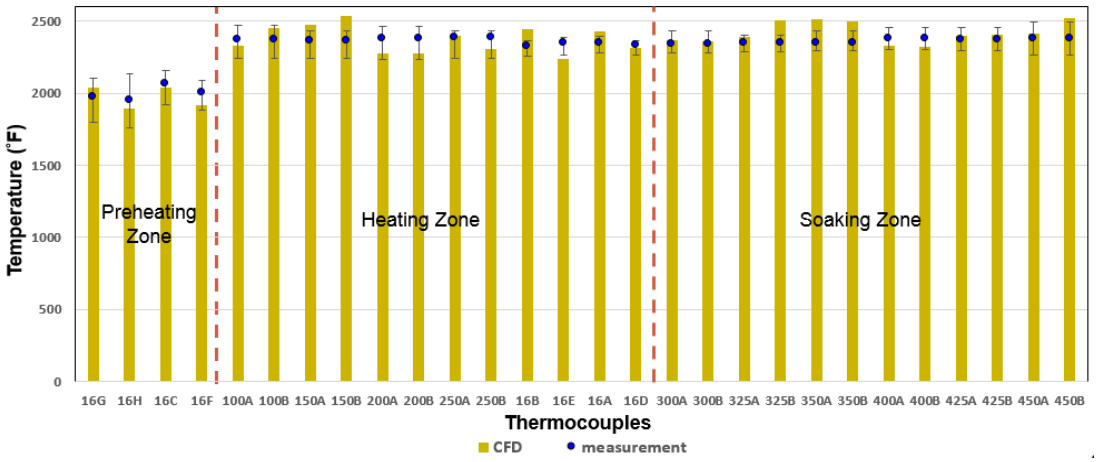

(b)

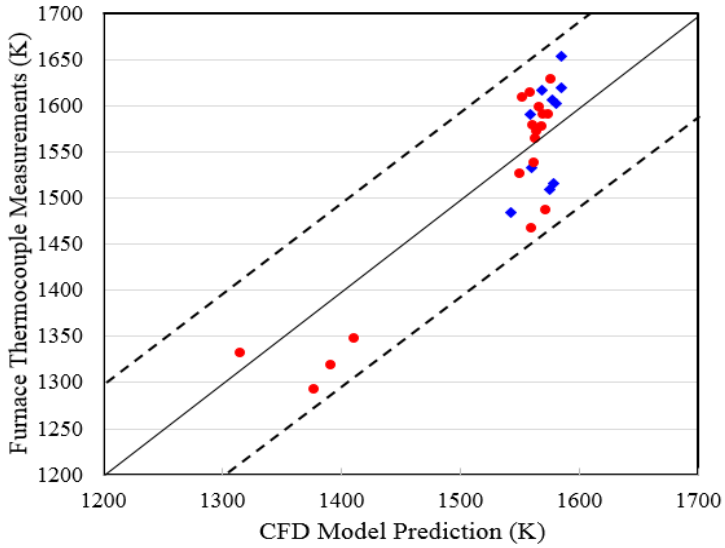

(c)

Figure 18. Furnace temperature, (a) Furnace thermocouples' location, (b) Comparisons between CFD prediction and measurements, (c) Parity plot.

In Figure 18(b), a comparison between the CFD predictions and thermocouple measurements is presented according to the sequential locations of the thermocouples in the furnace from the charging door to the discharge door. The bars represent the furnace temperature predicted by the CFD model, and the points are the average values of the furnace temperatures over a period of time simulated. The error bars on the blue points represent the temperature variations over the same period of time simulated. It can be seen from the figure that most of the CFD predicted values are close to the thermocouple measurements, which validates the CFD model developed for the reheating furnace. A parity plot comparison between the CFD predictions and the average thermocouple measurements from individual thermocouples in the furnace over the period of trial time is shown in Figure 18(c). In this figure, the solid diagonal line represents the 1:1 match between the CFD predictions and the thermocouple measurements. The maximum difference between the CFD predictions and the measurements is within 100 K.

3.1.4 Material Properties

The thermal properties of the steel are required to calculate the heat transfer for a given steel grade. The thermal properties of the steel used for the instrumented slab trials are shown in Figure 19. In the furnace, slabs are supported by skids. The heat transfer between the skids and slabs is important and was taken into account in the heat transfer model. The skid thermal properties are shown in Figure 20 [119].

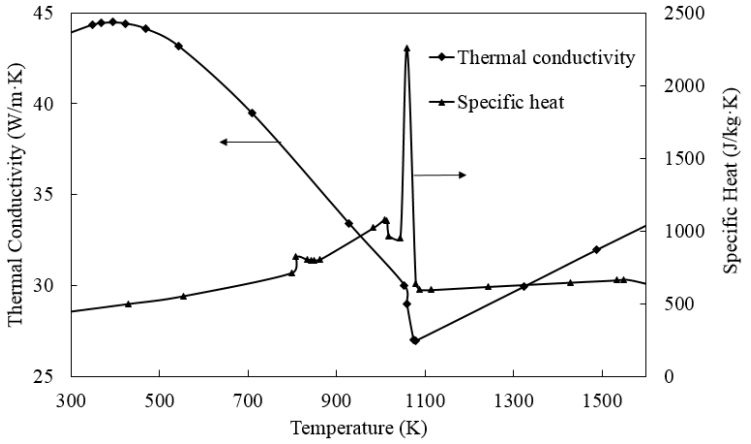

Figure 19. Thermal properties of the steel used for the mill instrumented slab trials.

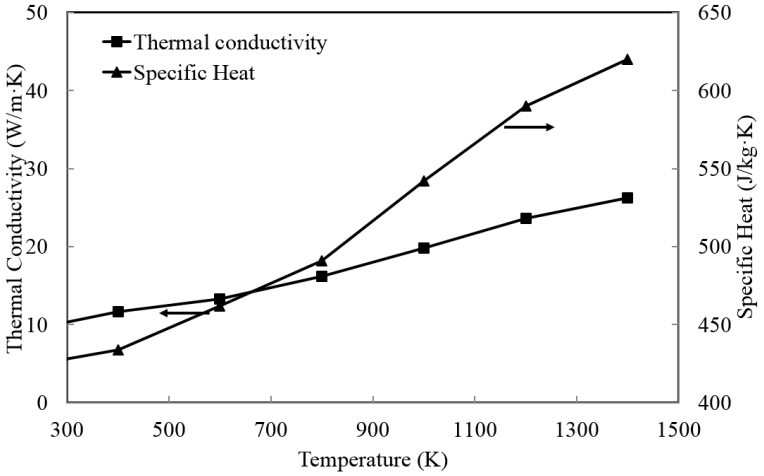

Figure 20. Thermal properties of the skids.

3.1.5 Slab Walking Speed

The time the trial slab spent in each furnace zone is based on the slab movement through the reheating furnace. In the CFD model, the moving slabs were treated as a dynamic mesh zone with defined moving velocity, with the rest of the geometry domain remaining still during computation. As shown in Figure 21(a), the moving zone bottom is the slab/skid interface and the zone height is 0.3m, which contains the solid slab zones and the gas zone. The mesh size in the moving zone is smaller than the mesh in the gas zone to make sure the mass and heat transfer from the gas to the steel slabs are correct. The dynamic travel speed of the instrumented slab was defined by using a UDF in the dynamic mesh model according to the actual travel speed of the slab during the reheating process. The speed profile of the instrumented slab is shown in Figure 21(b). It can be seen from the figure that the instrumented slab was moving at different speeds through the reheating furnace. The residence times were 23, 70, and 27 minutes in the preheating zone, heating zone, and soaking zone, respectively. The total furnace residence time was 120 minutes.

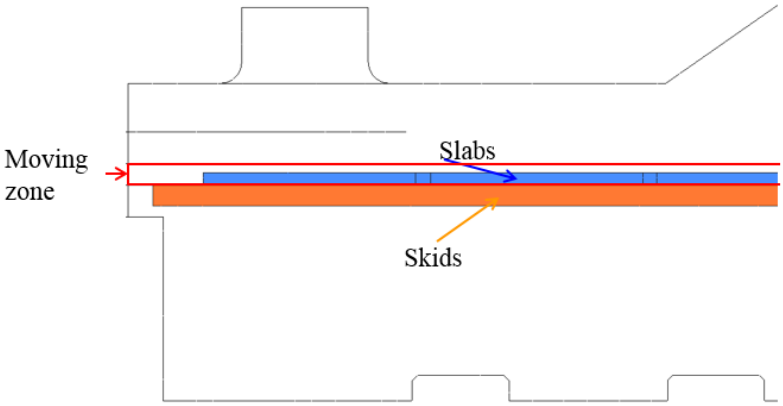

(a)

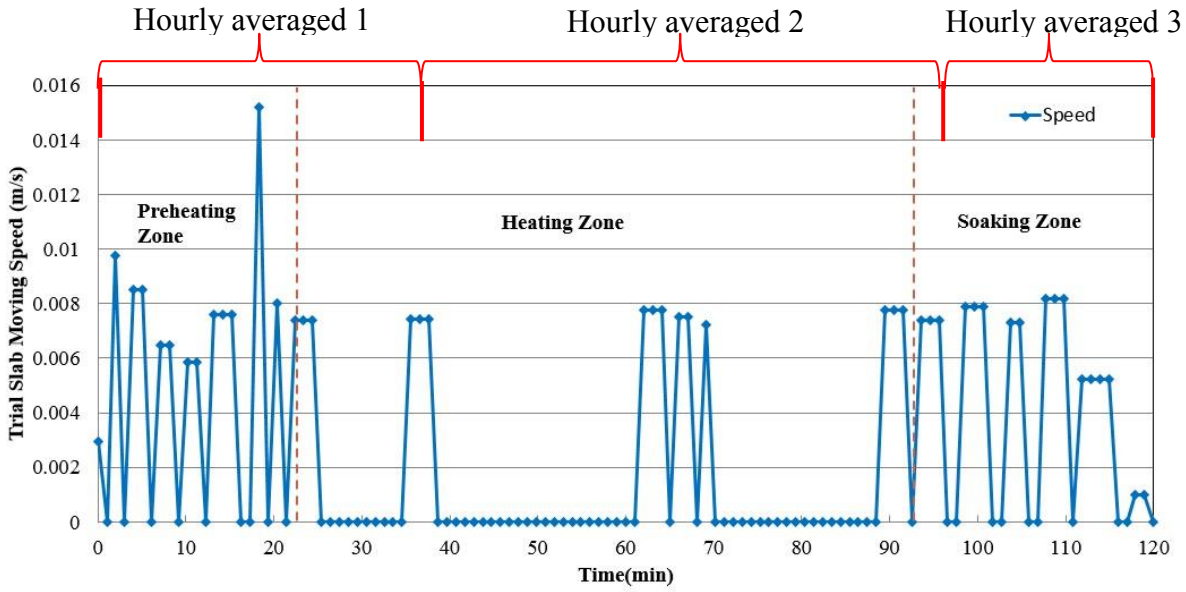

(b)

Figure 21. Slab movement, (a) Moving zone, (b) Moving speed.

3.2 Results and Discussions

3.2.1 Validation

The instrumented slab was cold charged with a target discharge temperature of 1561 K. The trial procedure and slab moving speed in the reheat furnace during the trial have been described in the previous sections. The slab temperatures between-skid and over-skid were measured by the embedded thermocouples and captured by the Datapaq unit attached to the trial slab over the period of trial time. By applying the same moving speed, total furnace residence time, and transient boundary conditions, the numerical model predicted the temperature evolution of the trial slab over

the same period of time. For the purpose of comparison, the slab temperatures at the same locations measured by the thermocouples (the Datapaq unit) and predicted by the numerical model will be compared.

Instrumented slab trials were conducted under typical operating conditions at the SSAB Mobile mill to assess the validity of the CFD model. A full-size slab approximately 6 inches thick, 96 inches wide and 340 inches long (see Figure 22a) was prepared for the trials. Thermocouples were installed in the slab to measure the temperatures at different locations inside the slab during a reheating process. The thermocouples were connected to a data collection device (Datapaq) which was placed in a water-cooled box wrapped with insulation material. The slab temperatures recorded by the Datapaq unit were extracted later and compared with the predictions from the CFD model.

As shown in Figure 23, a total of six thermocouples in two groups were placed in the slab at two different locations to cover the areas of over-skid (thermocouples #1, #2, and #3), and the areas between-skid (thermocouples #4, #5, and #6). For each group, one thermocouple was placed near the slab top surface, one at the slab mid-thickness, and one near the slab bottom surface to capture the temperatures through the slab thickness. All the thermocouples were inserted about 15 inches in from the slab narrow face to ensure that the measurements represent the slab inner temperatures. The position of the instrumented slab in the roller line and alignment with the furnace skid is shown in Figure 22(b). The yellow strip on the slab top surface marks the location of the thermocouples which were aligned with one of the skids in the furnace.

(a) (b)

Figure 22. Instrumented slab trial experiment, (a) Charging, (b) Alignment.

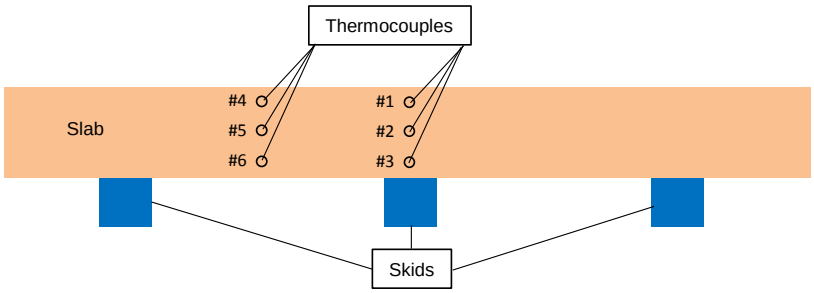

Figure 23. Thermocouple installation diagram for the instrumental trial slab.

Thermal snapshots showing the trial progression are presented in Figure 24. The position of the trial slab in the furnace at each stage is located by either red or blue arrows in the figure. The snapshots in Figure 24 are top views of the furnace at a different stage of the reheating process. Slabs move from left to right. The total furnace residence time for the trial slab is 120 minutes. At the beginning of the trial (t = 0 min), the instrumented slab was cold charged into the reheating furnace. The slab was walked through the furnace at various speeds. At t = 20 min, the trial slab walked into the heating zone where the heating rate starts to increase. The slab temperature at this moment was about 811 K. The slab temperature increased rapidly while it walked through the heating zone. The slab temperature reached 1477 K before it entered the soaking zone (t = 80 min). In the soaking zone, the heating rate decreased and a thermal homogenization process is the main event.

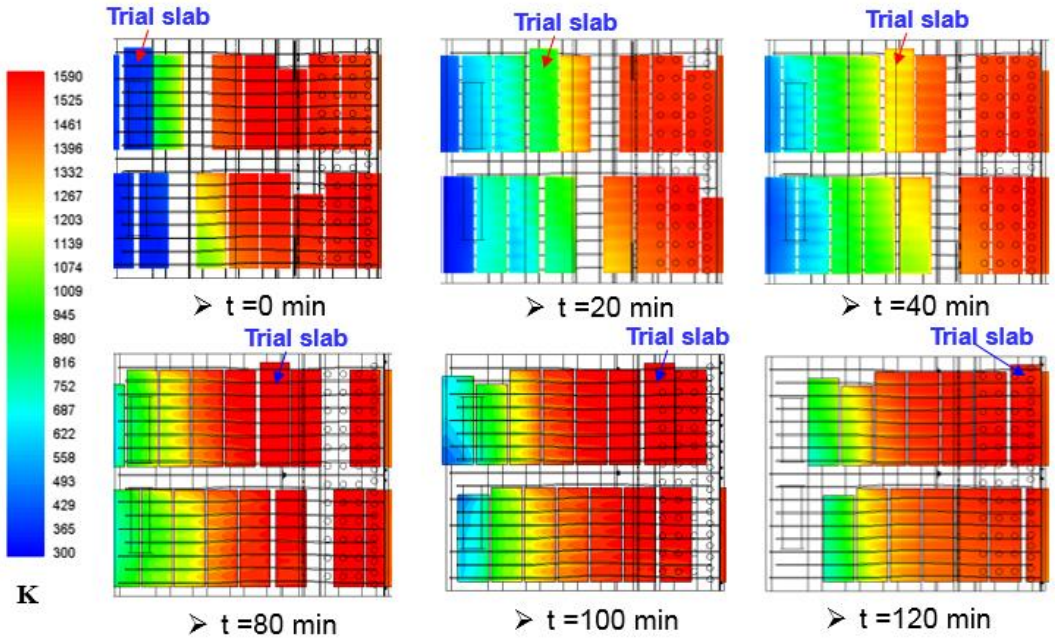

Figure 24. Snapshots of trial progression.

The detailed comparisons between the CFD simulation and experimental measurements on the slab temperature at all the measurement locations are in good agreement as shown in Figure 25. A more detailed comparison is presented in Table 7. The data shows that the six temperatures measured from two different locations (between-skid and over-skid) vary in a very narrow range, indicating a uniformly heated slab. In general, the temperature on the top surface of the slab is slightly higher than that on the bottom surface possibly due to the skid mark effect. For the between-skid temperatures, the CFD predictions are in good agreement with the measurements. However, for the temperatures over-skid, the CFD model produced slightly under-predicted values (the negative ΔT values in Table 7), especially at the location where the slab had direct contact with a skid. This small discrepancy could be reduced if the boundary condition for the heat transfer between skid and slab can be determined more accurately. Overall, the slab bulk temperatures (the average value of the six temperatures) at discharge are in good agreement between the CFD prediction (1540.4 K) and the measurement (1553.2 K). These values are also close to the aim discharge temperature (1560.9 K), indicating that the reheating process produced a fully reheated slab.

Table 7. Comparison of slab discharge temperature between measurement and CFD prediction.

	#1 (over-skid top)	#2 (over-skid core)	#3 (over-skid bottom)	#4 (between-skid top)	#5 (between-skid core)	#6 (between-skid bottom)	Bulk
Datapaq (K)	1557.6	1555.4	1547.6	1555.4	1552.6	1550.9	1553.2
CFD (K)	1546.5	1534.3	1526.5	1555.9	1548.2	1535.4	1540.4
ΔT (K)	-11.1	-21.1	-21.1	0.5	-4.4	-15.5	-12.8
% Error	0.71	1.36	1.36	0.03	0.28	1.00	0.82

Note: ΔT = CFD model predicted temperature – Datapaq measurement

To indirectly access the validity of the CFD model, slab bulk temperatures predicted by the CFD model and those predicted by the mill online model under the same furnace conditions are compared in Figure 26. It can be seen that the prediction obtained from the CFD model developed from the present work closely matches that calculated by the mill online model. Based on the results presented in Figures 25 and Figure 26, it is clear that the evolution of slab temperature during a reheat process goes through three different stages. At the early stage of reheating, i.e. reheating in the preheating zone and the first half of the heating zone, a fairly stable heating rate is experienced by the slab. At the late stage of heating (the slab moves closer to the exit of the heating zone), the heating rate decreases while the slab bulk temperature keeps increasing. At the stage where the slab enters the soaking zone, the heating rate decreases to a very low level. The slab temperature profile levels off and the reheating becomes a homogenization process through which a uniformly heated slab is ensured at discharge.

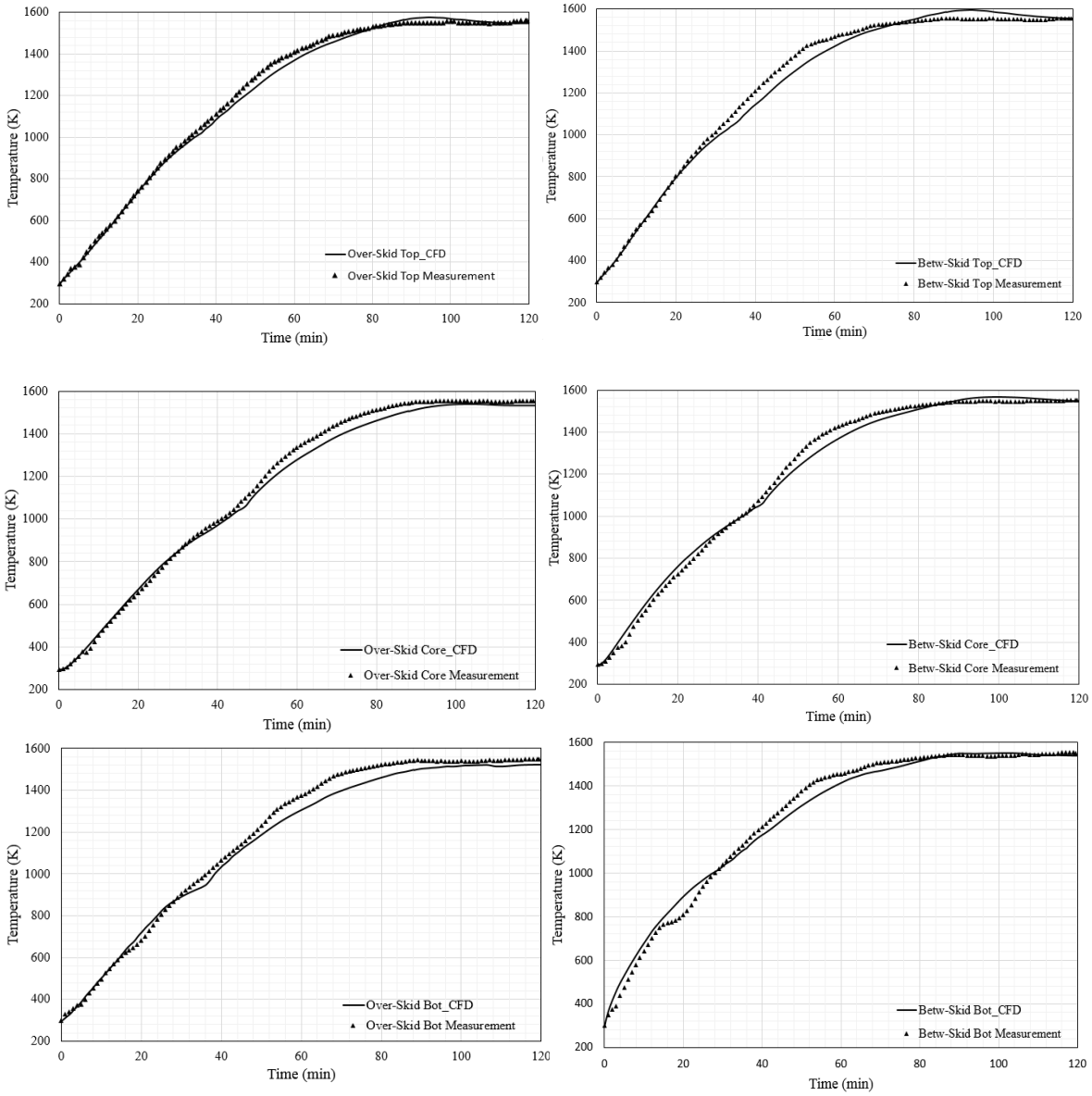

Figure 25. Comparisons of slab temperature profiles between the CFD predictions and thermocouple measurements.

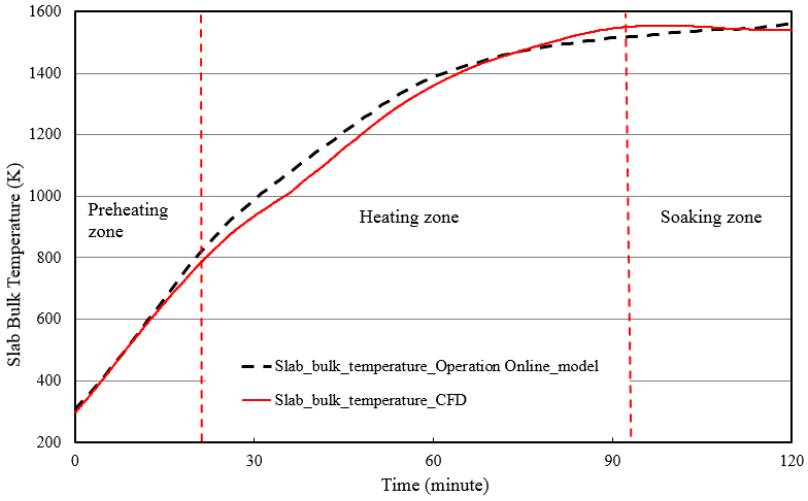

Figure 26. Comparisons of slab bulk temperature profiles between the CFD model and the mill online model.

To further compare the CFD model with the mill online model, eight more cases with different operation conditions, including both hot charge and cold charge, were simulated. The slab bulk temperatures predicted by the CFD model and the mill online model are plotted in Figure 27. The maximum difference between the predictions by the two models is about 36 K. Based on this and the comparison with the instrumented slab trial results presented in Figure 25, it is evident that the CFD model developed in the present work performs reasonably well for the slab dynamic heating process in a walking beam reheating furnace.

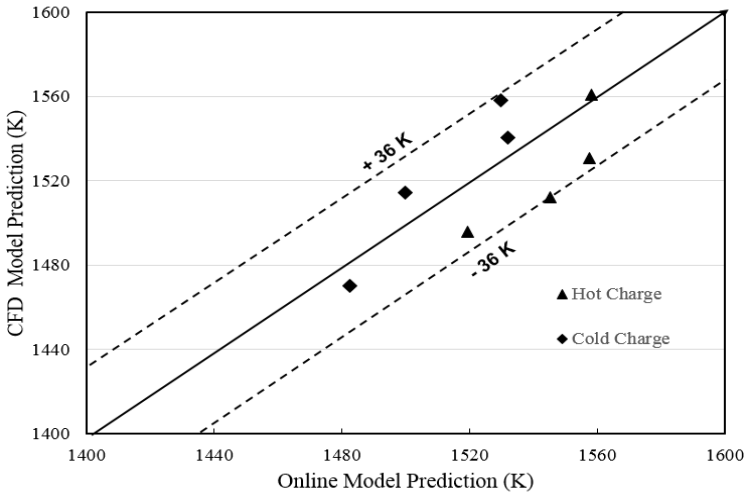

Figure 27. Comparisons of slab bulk temperature at discharge between the CFD model and mill online model predictions.

3.2.2 Temperature Distribution in Slab

It is important to know the temperature distribution in a slab being heated so that the mill operator can decide if a slab can be discharged or not at the end of reheating. This is usually controlled by two ΔTs, one is the temperature difference between the hottest spot and the coldest spot in a slab, and the other is the difference between the slab bulk temperature and the aim discharge temperature. The former is a measure of temperature uniformity inside the slab, while the latter is a measure of the readiness for the discharge of the slab. With the CFD simulation, the detailed temperature distribution on the slab surface and inside the slab during the entire reheating process can be clearly revealed. As shown in Figure 28, the temperature evolution on the slab surface during a two-hour reheating is demonstrated. At the start of the process (t = 0 min), a cold slab was charged into the reheating furnace. As the slab moved toward the heating zone, the front edge of the slab got heated first and had the highest temperature. Due to the large temperature differential between the areas over-skid and between-skid, the skid marks on the slab can be clearly seen, as shown by the temperature maps of t = 20 min and t = 40 min in Figure 28. The skid marks can still be seen at t = 80 min although they become weaker. The slab entered the soaking zone at t = 93 min. After a few minutes soaking in this zone, the slab temperature became more uniform and the skid marks gradually diminished. It can also be seen from the temperature map of t = 20 min, the effect of skid is more pronounced on one side than the other along the slab length (or across the furnace width). This is due to an unbalanced fuel flow in the furnace.

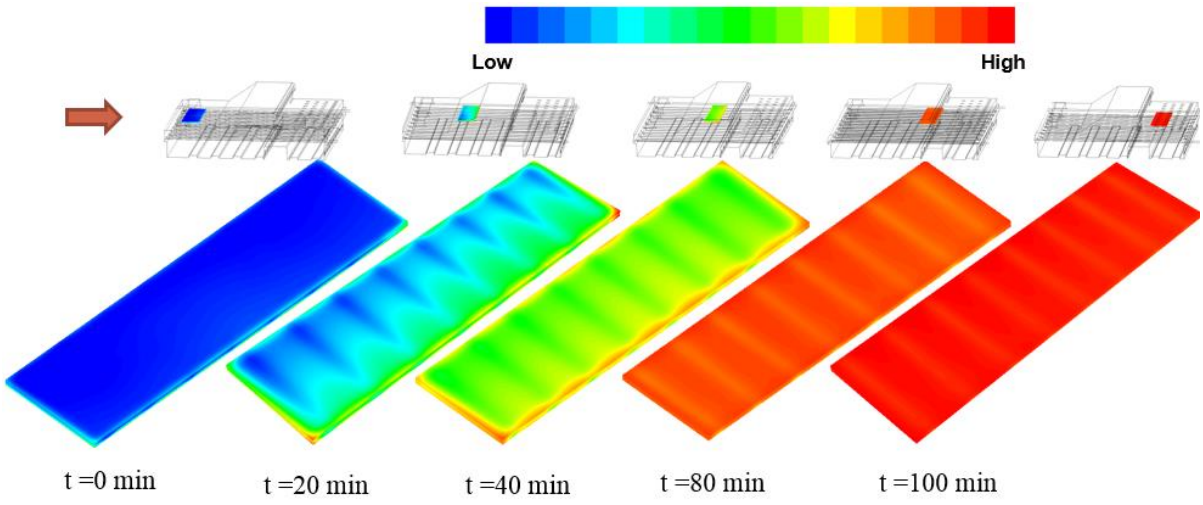

Figure 28. Slab temperature evolution.

Another important temperature distribution is the temperature profile through the slab thickness. A low core temperature at the slab mid-thickness would lead to high mill loads during hot rolling. As shown in Figure 29, the temperature profiles along the slab thickness (at the slab center location) at different times are plotted. In the beginning, the slab was charged at room temperature. When the slab was walked through the preheating and heating zones, the temperature difference between the slab center point and the top and bottom surfaces first increased and then decreased. During the heating process, the slab surface temperature was higher than the temperature inside the slab. After 100 minutes, the temperature distribution became uniform throughout the slab thickness.

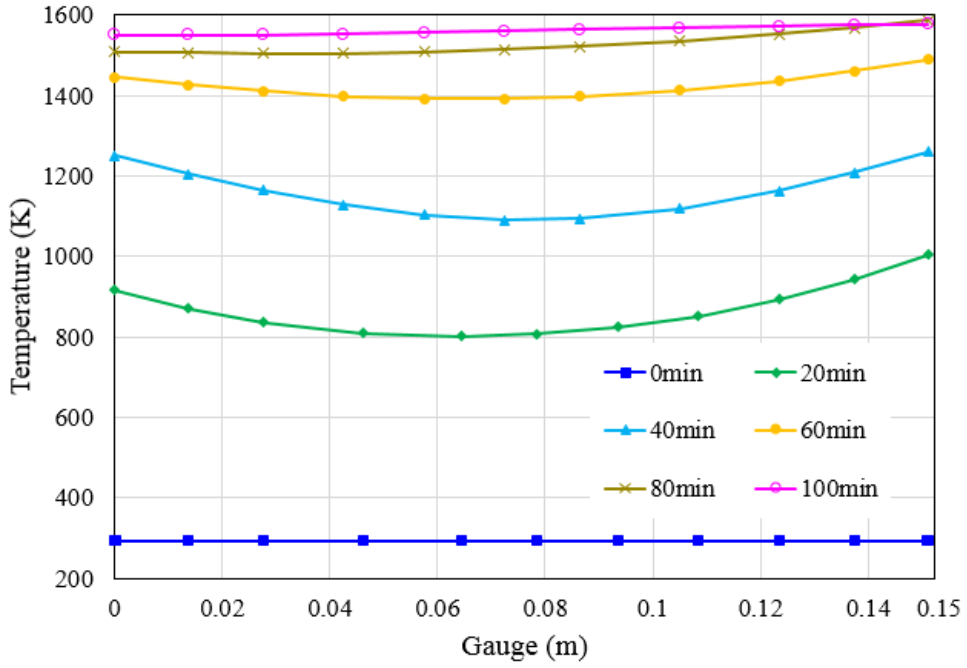

Figure 29. CFD prediction of temperature distribution along slab thickness at slab center location.

The effect of the skids on slab surface temperature is further demonstrated in Figure 30. In this simulation, the slab bottom surface temperature was analyzed by plotting the temperature distribution on the slab bottom surface along the slab length. The temperature distribution on the slab bottom surface indicates that the skid marks have a relatively lower temperature. It can also be seen that the temperature difference between the areas with and without skid marks remains high (approximately 100K) until the slab reaches the soaking zone, which indicates that proper

soaking time is required to reduce the skid mark effect. During the slab travel process, the main heat transfer into the steel slab is through radiation as shown in Figure 31.

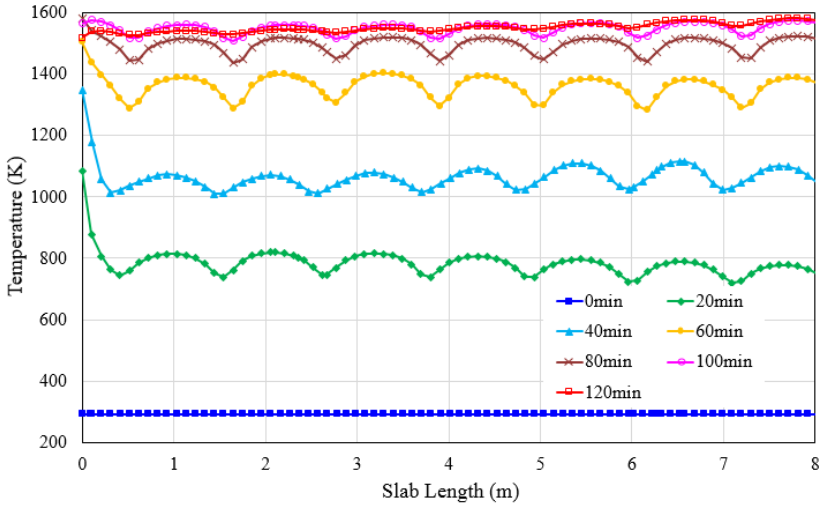

Figure 30. Temperature distribution along the slab length on the bottom surface.

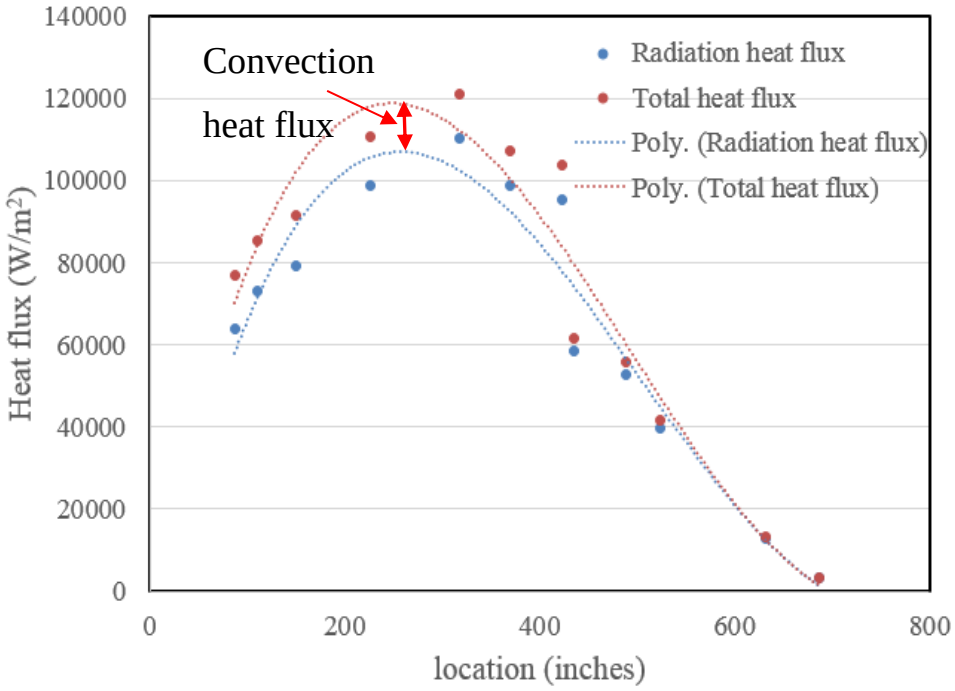

Figure 31. Heat flux due to different modes of heat transfer in the furnace along slab movement direction.

3.3 2D Heat Transfer Model

3.3.1 Model Description

In the 2-D heat transfer model [119], the transient heat conduction process in the slab can be expressed by the following equation:

$$C_s(t)\rho_s \frac{\partial T(x,y,t)}{\partial t} = \frac{\partial}{\partial x}\left(K_s(t)\frac{\partial T(x,y,t)}{\partial x}\right) + \frac{\partial}{\partial y}\left(K_s(t)\frac{\partial T(x,y,t)}{\partial y}\right) \quad (91)$$

where $T(x, y, t)$ is the temperature at time step t, x is slab longitudinal direction coordinate, y is slab thickness direction coordinate, $C_s(t)$ is the specific heat of the steel, ρ_s is the density of the steel, and $K_s(t)$ is the thermal conductivity of the slab.

The finite difference method was used to discretize the two-dimensional heat transfer equation. In order to solve the unsteady non-linear heat transfer problem, the explicit method was applied to the nodes, which were created by dividing the slab slice into smaller sections. The discretization on the internal nodes can be expressed as Equation (92). The boundary conditions at the top boundary nodes, bottom surface nodes, left edge nodes and right edge nodes can be expressed as Equation (93) to Equation (96).

$$\rho_s C_s(t)\Delta x\Delta y \frac{T_{i,j}^{t+\Delta t} - T_{i,j}^{t}}{\Delta t} = -K_s(t)\Delta x\left[\frac{2T_{i,j}^{t} - T_{i,j+1}^{t} - T_{i,j-1}^{t}}{\Delta y}\right] - K_s(t)\Delta y\left[\frac{2T_{i,j}^{t} - T_{i+1,j}^{t} - T_{i-1,j}^{t}}{\Delta x}\right] \quad (92)$$

where Δx, Δy, Δt are an increment of x coordinate, y coordinate and time, $T_{i,j}^{t}$ is node temperature at time step t, and $T_{i,j}^{t+\Delta t}$ is node temperature at time step $t + \Delta$t.

$$K_s(t)\frac{\partial T(x,G,t)}{\partial y} = f\varepsilon_s\sigma\left[{T_{itop}}^4 - T(x,G,t)^4\right] + h_i(T_{itop} - T(x,G,t)) \quad (93)$$

$$K_s(t)\frac{\partial T(x,0,t)}{\partial y} = f\varepsilon_s\sigma\left[{T_{ibot}}^4 - T(x,0,t)^4\right] + h_i(T_{ibot} - T(x,0,t)) \quad (94)$$

$$K_s(t)\frac{\partial T(0,y,t)}{\partial x} = f\varepsilon_s\sigma\left[{T_{iedg}}^4 - T(0,y,t)^4\right] + h_i(T_{iedg} - T(0,y,t)) \quad (95)$$

$$K_s(t)\frac{\partial T(L,y,t)}{\partial x} = f\varepsilon_s\sigma\left[{T_{iedg}}^4 - T(L,y,t)^4\right] + h_i(T_{iedg} - T(L,y,t)) \quad (96)$$

where G is slab thickness, $T(x, G,\ t)$ is top surface (y=G) temperature at time step t, and f is view factor; for the top surface, f=1, while for the bottom surface, f is determined by the geometric effects introduced by the skid structures. Therefore, f values for bottom surface nodes, skid nodes and shadow nodes are calculated based on reference [120]. σ is Stefan-Boltzmann constant, ε_s is emissivity of the slab, L is the length of the steel slab, T_{itop} is the top chamber furnace temperature (i = 1,2,3, representing the preheating zone, heating zone and soaking zone, respectively), T_{ibot} is the bottom chamber furnace temperature, $T_{iedg} = \frac{1}{2}(T_{itop} + T_{ibot})$, h_i is the convective heat transfer coefficients, which is calculated using the validated 3-D CFD model.

3.3.2 Simulation Domain

During reheating, the material flow inside the reheating furnace is shown in Figure 32(a). Slabs travel through three different zones, a preheating zone, a heating zone, and a soaking zone, from the furnace charging side to the discharge side. Slabs are 6 inches thick and in various lengths. They are charged into the reheating furnace in an orientation with the width direction parallel to the charging direction. The computational geometry used in the 2-D model is a slice of the steel slab along its length as shown in Figure 32(b). The 2-D slice is divided into 1" × 2" rectangles which are also called grids. The nodes on the divided grids are the points containing temperature values through the numerical iterations. Boundary conditions are applied to the boundary nodes such as surface nodes, edge nodes and corner nodes shown in Figure 32(b). The skid nodes represent the skid structure, which is used for supporting and transporting the slabs throughout the furnace. Conduction heat transfer occurs between skids and slabs. Because the skids have an effect on the nearby contact region when introducing radiation heat transfer between combustion flames and slabs, the shadow nodes were introduced to take account these effects. In this model, special treatments on the skid nodes and the shadow nodes near the skids are applied by using correction factors to take into account of the effect of skid temperature boundary condition on the heat flux

in the skid contact area and its geometric effect on the radiation heat flux near the skid nodes. During a reheating process, the computational geometry (the slab longitudinal cross-section) moves through the reheating furnace. As an example to show the effect of the skids on the slab temperature distribution, the model calculated temperature profiles along the slab length at different stages during a two-hour reheating are shown in Figure 33.

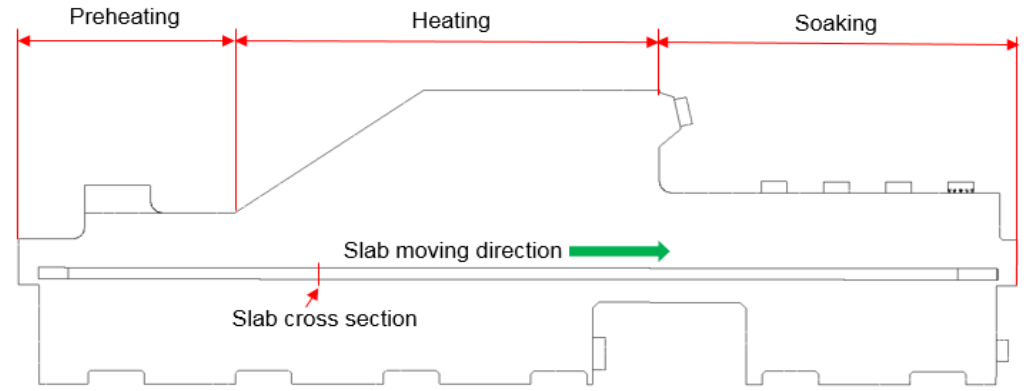

(a)

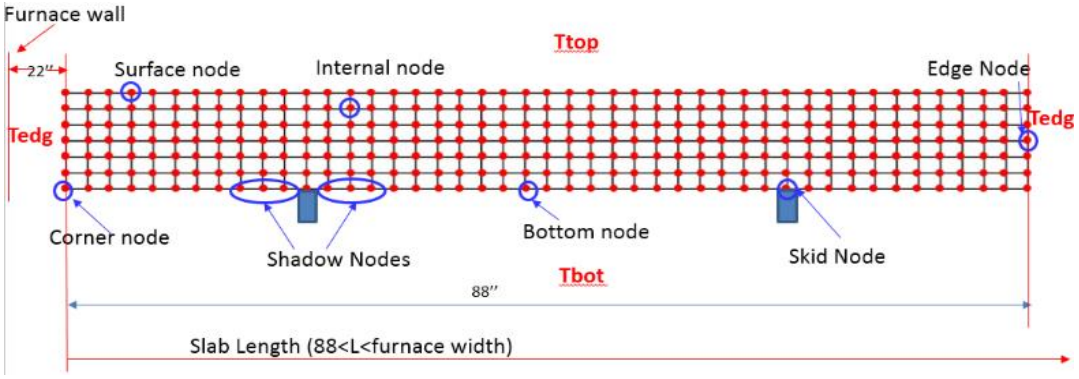

(b)

Figure 32. Computational domain, (a) Reheating furnace, (b) Slab cross section.

It can be seen from the temperature profiles presented in Figure 33 that at the early stages of reheating, skids have a noticeable effect on the slab temperature. The slab temperatures at the locations where the slab is in contact with the skids are lower than the temperatures at the locations where the slab is in between the skids. This difference becomes smaller when the slab progressively moves into the soaking zone. Eventually, the temperatures throughout the slab body are equalized in the soaking zone.

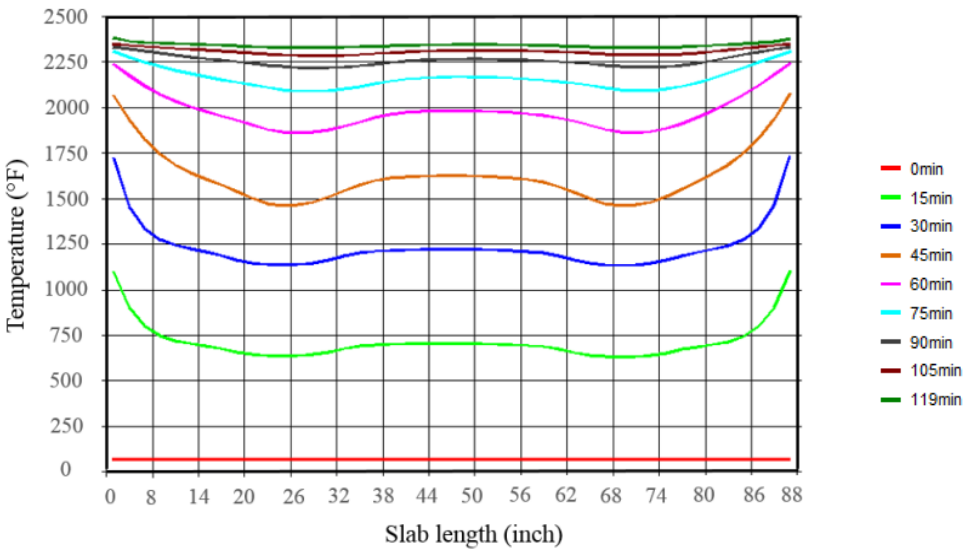

Figure 33. Temperature profiles along the slab length.

The flow chart of the slab reheating calculation is shown in Figure 34. The furnace and slab conditions are the inputs to the 2-D heat transfer solver. The furnace temperatures in different zones can be user-defined values or from the furnace thermocouple readings. The specific user input interface was developed to provide users with different options to determine the furnace conditions as the heat transfer boundary conditions for calculations. Slab geometry, slab charging temperature, and steel grades with specific thermal properties, such as thermal conductivity and specific heat, can be determined based on real-time production situations. In addition, the model is also capable of handling non-constant walking speeds of a slab during reheating. With all these furnace conditions and slab conditions inputs, the 2D heat transfer model will calculate the slab temperature evolution and slab temperature profile at different locations, such as slab temperature through the slab thickness and along the slab length.

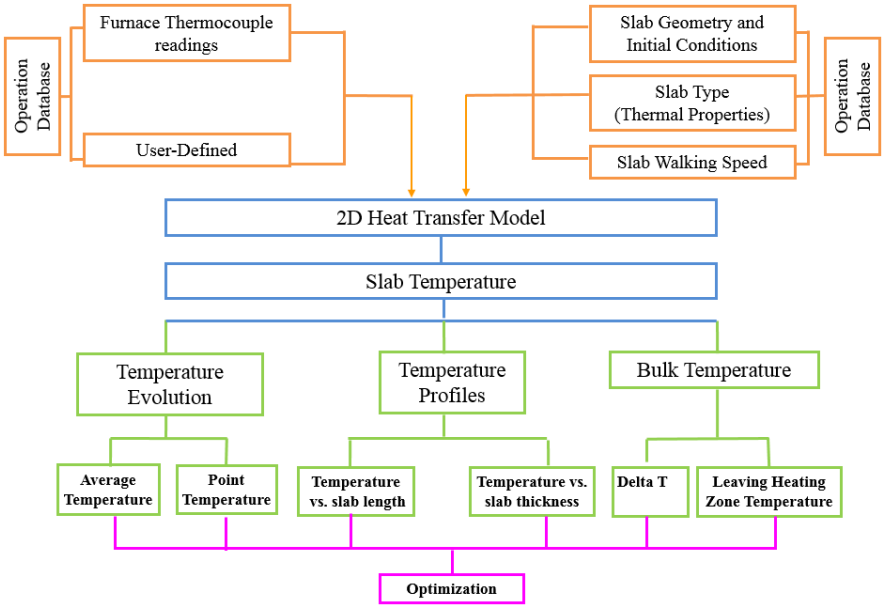

Figure 34. Flowchart of the slab reheating simulation in 2-D heat transfer model.

3.3.3 Model Validation

It is clear that there are multiple transitions throughout the reheating process. The radiation and convection heat transfer coefficients are varying with locations. Radiation heat transfer coefficient is only dependent on the gas temperature field. However, it is difficult to measure the convective heat transfer coefficient between the steel slab and the hot gas inside the furnace. The developed 3-D comprehensive CFD model provides the details of the convective heat transfer coefficient based on the typical operating condition. By tracking the trial slab through the whole reheating process, the convective heat transfer coefficient between the trial slab and the hot furnace gas at different locations was obtained, as shown in Figure 35.

The heat transfer coefficient in the reheating furnace ranges from approximately 12 to 30 $W/m^2 \cdot K$ under the furnace operating conditions. It is also shown that the convection heat transfer is higher in the heating zone than in the preheating and soaking zones. It has to be mentioned that the convective heat transfer coefficient profile is slightly different for each slab traveling through a certain location during the reheating process. But the average value at a certain location under certain operation conditions is representative. The averaged convective heat transfer coefficient profile predicted by the CFD model was used in the 2-D heat transfer model under certain operating conditions.

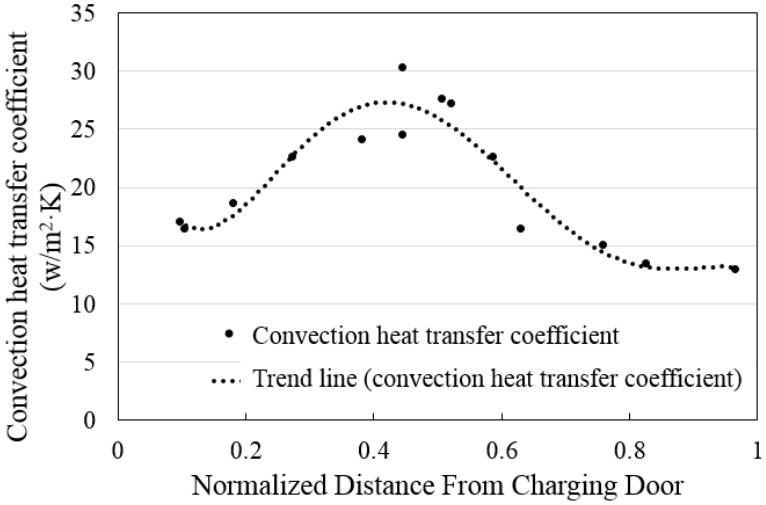

Figure 35. Convective heat transfer coefficient at different positions in the reheating furnace.

To demonstrate the accuracy of the 3-D CFD model and the 2-D heat transfer model, the slab temperature profiles (average of six thermocouple readings) obtained from the instrumented slab trial and those calculated using the 3-D CFD and 2-D heat transfer models are presented in Figure 36 and Figure 37. For the 3-D CFD simulation, the same walking speed, total furnace residence time, and transient boundary conditions in the instrumented slab trial were used. For the simulation using the 2-D heat transfer model, the convective heat transfer coefficient obtained from the 3-D CFD calculation was used. It can be seen from the slab temperature profiles presented in Figure 36 that the predictions obtained from both models are in good agreement with that obtained from the instrumented slab trial.

Further comparison between the measurements obtained from the instrumented slab trial and predictions obtained from the models is shown in Table 8. In the table, the slab temperatures at six locations in the slab are compared. The maximum difference between the 3-D CFD model predictions and measurements is 26 K. The maximum difference between the 2-D heat transfer model predictions and measurements is 15 K. These differences represent less than 2% error, suggesting that the models are capable of predicting the reheating process accurately.

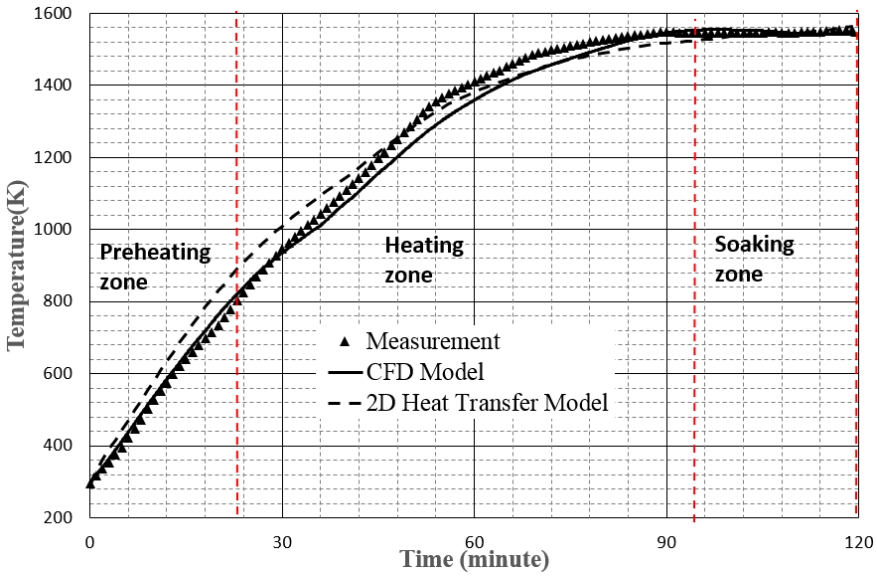

Figure 36. Comparisons of slab temperature profiles between the measurement and model predictions.

The reheating furnace is controlled by an online Level II model which monitors slab temperatures through the thermocouples installed in the reheating furnace and controls the slab movement and fuel and air flow rates according to multiple set points defined under certain operating conditions. At the end of reheating, slabs will be discharged if the difference between the model predicted slab bulk temperature and aim discharge temperature is within a specified value.

In order to compare the present offline 2-D model with the online Level II model, a total of 210 reheating cases were studied, and the results are shown in Figure 38. The selected cases covered both cold and hot charging conditions with aim discharging temperatures ranging from 1478K to 1561K. For the 2-D heat transfer model calculations, the furnace temperatures measured by the thermocouples installed in the different zones of the furnace were used to define the thermal boundary conditions. With specific slab thermal properties and walking speeds, slab discharge temperatures at discharge for individual slabs were calculated. It can be seen from the data presented in Figure 38 that the differences between the offline and online model predictions are within ± 10K.

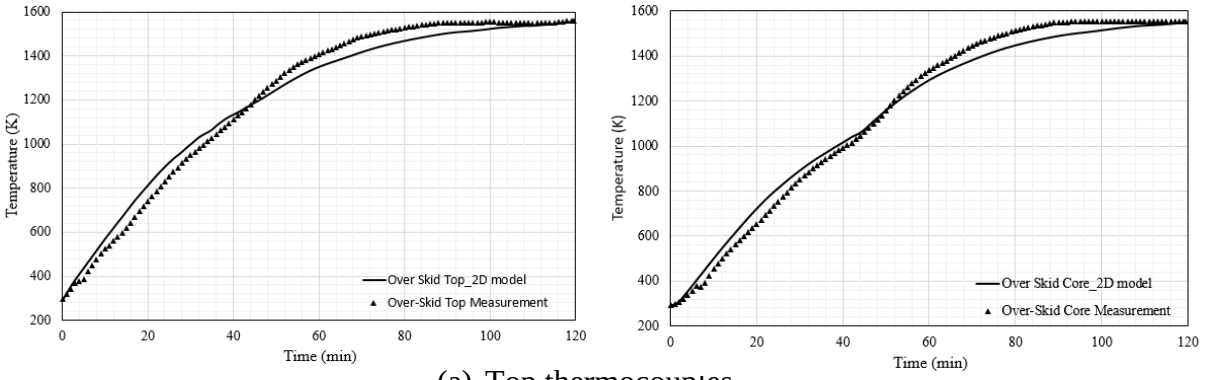

(a) Top thermocouples

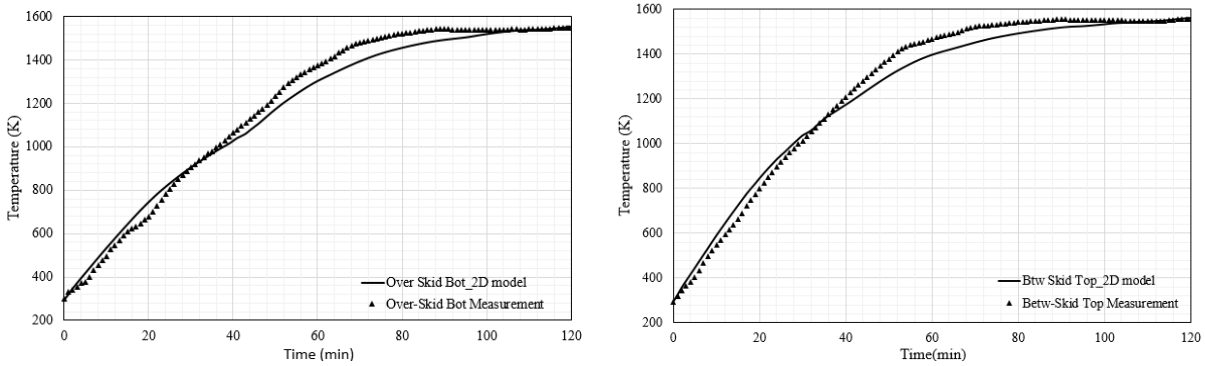

(b) Core thermocouples

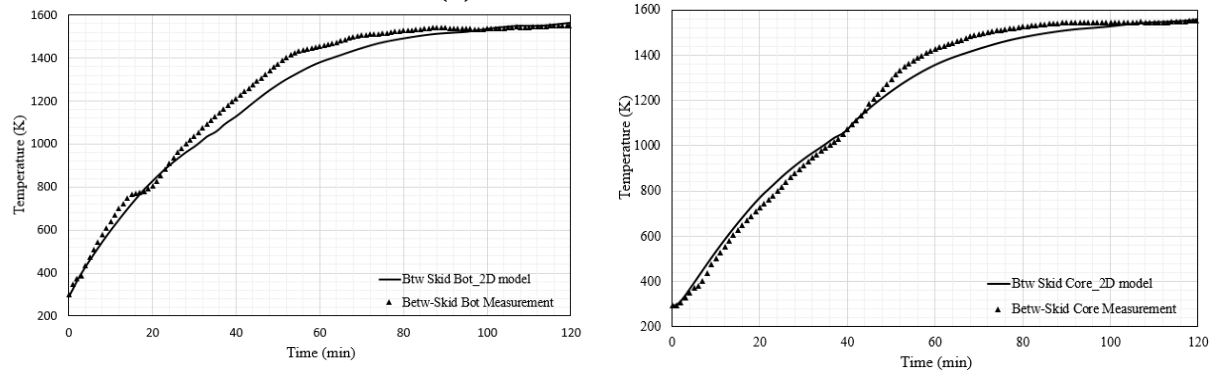

(c) Bottom thermocouples

Figure 37. Thermocouple measurements vs. 2D model predictions.

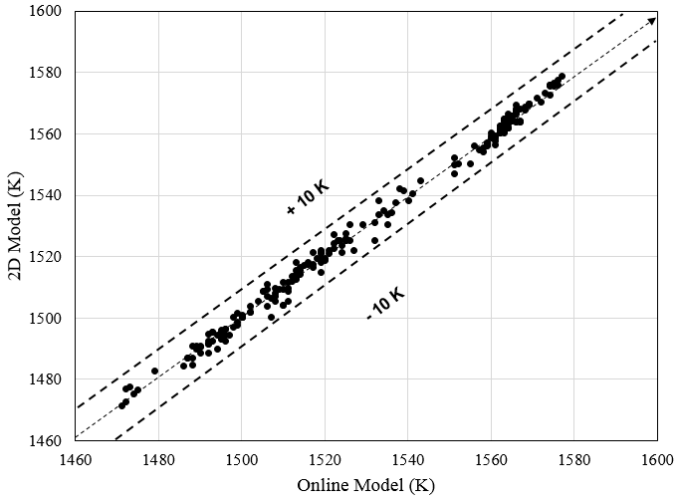

Figure 38. Discharge temperature comparison between the offline and online model predictions.

Table 8. Comparisons of slab discharge temperature between measurements and model predictions.

	#1	#2	#3	#4	#5	#6
Measurement (K)	1558	1555	1548	1555	1553	1551
3D CFD Model (K)	1546	1534	1522	1556	1548	1536
Difference (K)	12	21	26	1	4	15
% Error	0.77	1.35	1.68	0.06	0.26	0.97
2D Heat Transfer Model (K)	1556	1550	1555	1562	1558	1566
Difference (K)	2	5	7	7	5	15
% Error	0.13	0.32	0.45	0.45	0.32	0.97

3.3.4 Model Application

One of the primary goals of this work was to develop an offline model (2-D heat transfer model) which can be used by mill engineers to simulate the slab reheating process, thereby optimizing the process to obtain a good balance between the reheating quality and furnace throughput. Due to a large number of grids in the 3-D CFD model to capture the slab temperature, the computational time for the instrumental slab trial simulation is more than a week using HPC. By using the 2-D heat transfer model, the simulation calculation of the instrumental slab trial can be completed within 10 seconds. Therefore, the 2D model is a more practical tool for mill engineers to use in reheating furnace troubleshooting or optimizing the slab reheating process. The 2D heat transfer model was used to predict the slab temperatures for a group of slabs. Since the data from the

instrumented slab trials is limited, the slab reheating data generated from the mill online model was used to compare with that obtained from the 2-D heat transfer model. As shown in Figure 39, the maximum difference between the two sets of data is less than 4 K, which is very small.

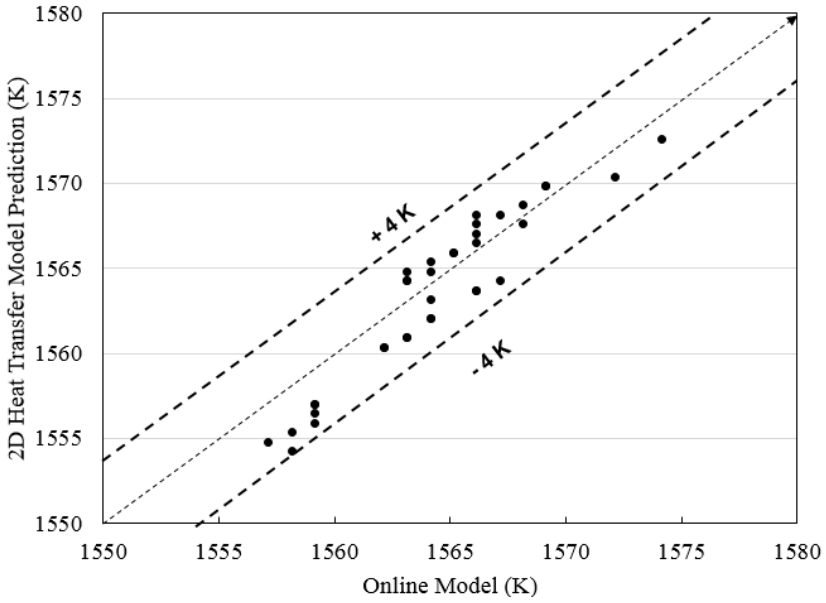

Figure 39. Comparisons of slab temperature between 2-D heat transfer model and mill online model.

One of the important measures on reheating quality is the temperature uniformity in a slab when it is discharged, specifically, the difference in temperature between the hottest spot and coldest spot inside a heated slab, ΔT. Based on a large number of simulations using the 2-D heat transfer model, it was found that the slab temperature uniformity, ΔT, is a function of the slab bulk temperature at the exit of the heating zone, as shown in Figure 40. It is clearly demonstrated in Figure 40 that the ΔT at discharge decreases with increasing slab bulk temperature at the exit of the heating zone. This is because the heating zone is the primary zone for raising the slab temperature since a large number of high powered burners are located in this zone. The soaking zone is mainly used to homogenize slab temperature, and the heating rate in this zone should be low. If the bulk temperature of a slab leaving the heating zone is significantly lower than the aim discharge temperature, the furnace tends to increase the heating rate in the soaking zone to raise the slab bulk temperature. This will result in a large ΔT between the slab surface and core, leading to a poorly thermally homogenized slab.

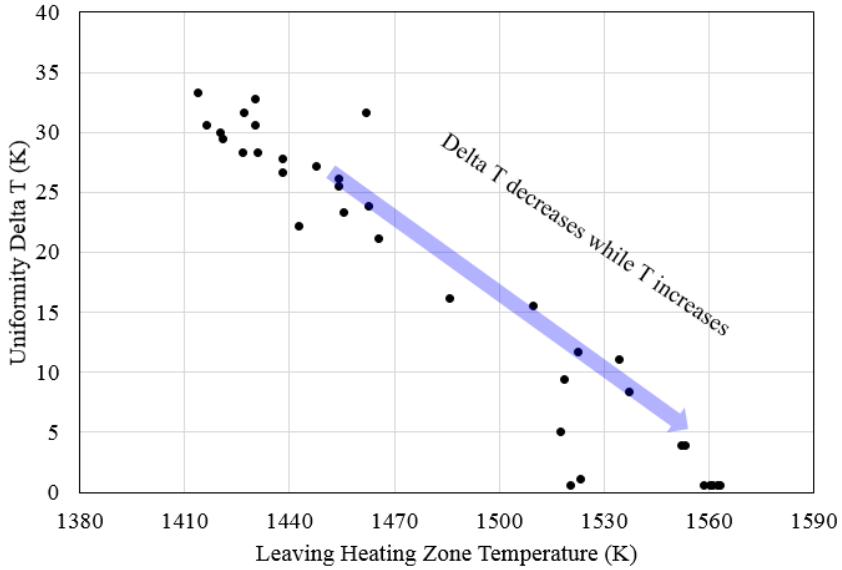

Figure 40. Relationship between slab temperature uniformity ΔT and slab bulk temperature leaving the heating zone.

3.4 Summary

In the present work, a comprehensive 3-D CFD model involving turbulence interacting flow, combustion, heat transfer and a dynamic operating condition was developed for an industrial walking beam slab reheating furnace. The CFD model offers detailed descriptions of the complicated combustion and heat transfer processes. The furnace temperature was properly predicted based on actual operating boundary conditions, and the model was validated through comparisons of data with an instrumented slab trial and the operating online model. The current model is capable of predicting the temperature distribution inside the reheating furnace and also the temperature distribution inside a slab being heated. The model provides reasonable predictions and can be used to identify potential production issues and to optimize the furnace operation.

A comprehensive 2-D heat transfer model for slab reheating in a walking beam furnace was developed using the finite difference method. The model is capable of predicting slab temperature evolution during a reheating process based on real-time furnace conditions and steel physical properties. The model was validated by using mill instrumented slab trials and production data. The results show that the temperature evolution predicted by the model is in good agreement with measurements by the thermocouples embedded in the instrumented slab. Compared with 3-D CFD

simulation of a reheating process, this 2-D heat transfer model used for predicting slab temperature evolution requires significantly less computing power and can provide results in a few seconds. This is a very convenient and user-friendly tool which can be used easily by mill metallurgists in troubleshooting and process optimization.

.

CHAPTER 4. MODELING OF STEEL SCRAP PREHEATING

In this study, numerical simulation on the scrap preheating process in an industrial twin-shell EAF has been conducted. The model development is directly based on the real operation process used by Steel Dynamics, Inc. The real operating conditions are available for model development. The direct validation with industrial data is a challenge due to the difficulty of obtaining measurement data. Along with the model development, validation studies are conducted with data from experimental work reported in the literature. This chapter contains all the detailed information about simulation conditions, validation, real furnace simulation results. This work will be continued within the Steel Manufacturing Simulation and Visualization Consortium (SMSVC).

4.1 Simulation Conditions

4.1.1 Model Geometry

A geometric model was developed based on the drawings of the electric arc furnace provided by Steel Dynamics Inc., as shown in Figure 41. The bottom part of the EAF is steel and slag zones. There are five burners above the slag zone, which are used to combust natural gas to provide heat during the scrap melting process and inject oxygen jets at supersonic speed to stir the molten steel bath and remove carbon during the refining stage. The detailed burner configuration is shown in Figure 42. The supersonic oxygen jet is used to provide oxygen at a velocity up to Mach 2. The secondary oxygen and the fuel inlets are used to provide combustion gases to form combustion flame. The electrodes are also considered, with detailed electrode tips at the bottom and electrode gap at the top roof. The exhaust gas outlet is also considered.

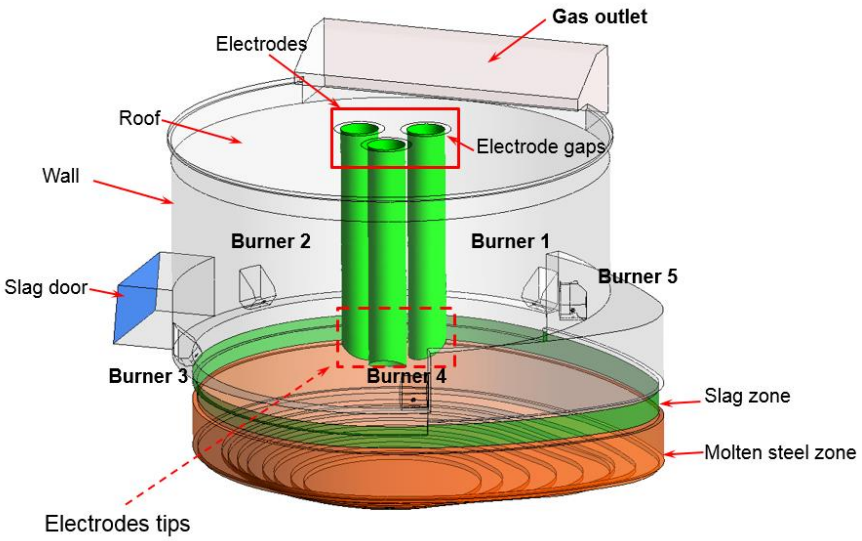

Figure 41. EAF computational domain.

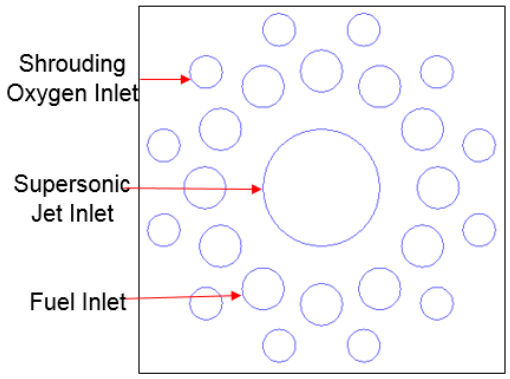

Figure 42. Oxy-fuel burner configuration.

4.1.2 Boundary Conditions

The boundary conditions for the combustion simulation are based on the standard EAF operation. The slag door is open or closed depends on the use of door lance. It is typically closed to reduce ingression of air to save energy. A uniform heat flux is used for the top roof and the side wall. The electrode gaps and the exhaust gas outlet are treated as a pressure outlet with an external pressure of 1 atm. Heat flux can be defined on the tips of the electrodes to consider the heat transfer from electrodes arc to the liquid steel and the furnace atmosphere. Table 9 lists the burner boundary conditions including fuel input, oxygen flow rate. Electrodes cooling water is 30 gallons/min.

Table 9. The typical oxy-fuel burner boundary conditions.

Burners	**Lance mode**	**Burner Mode**
NG (scfm)	113	74
Primary Oxygen (scfm)	910	100
Secondary Oxygen (scfm)	116	74
Temperature (°F)	80	80

The oxy-fuel burner operates at different operating conditions during the melting and refining stages. In the melting stage, the typical burner mode is used while in the refining stage, the lance mode is used. The boundary conditions for the scrap preheating are shown in Table 10. In the current model, the slag door is closed. A uniform heat transfer coefficient is used for the top roof and the side wall. Since the electrodes are not used during the scrap preheating, the heat flux is defined as zero on the tips of the electrodes.

Table 10. Boundary conditions for scrap preheating.

Boundaries	Velocity (m/s)	Temp. (K)	Heat flux (W/m^2)
Natural Gas Inlet	142.49	300	
Oxygen Inlet	288.70	300	
Supersonic Oxygen Inlet	235.59	300	
Surround Wall			-67343.13
Top Wall			-139081.7

During the EAF operation, the steel scrap was charged into the furnace with various types. The charged scrap occupies most of the EAF volume with overall porosity about 0.8 to 0.9. Normally, the oxy-fuel burners are buried in the steel scrap, as shown in Figure 43(a). In order to simplify the problem and establish the CFD model, and to allow for refined conditions, later on, a uniform scrap size was used with an average porosity of 0.85, as shown in Figure 43(b).

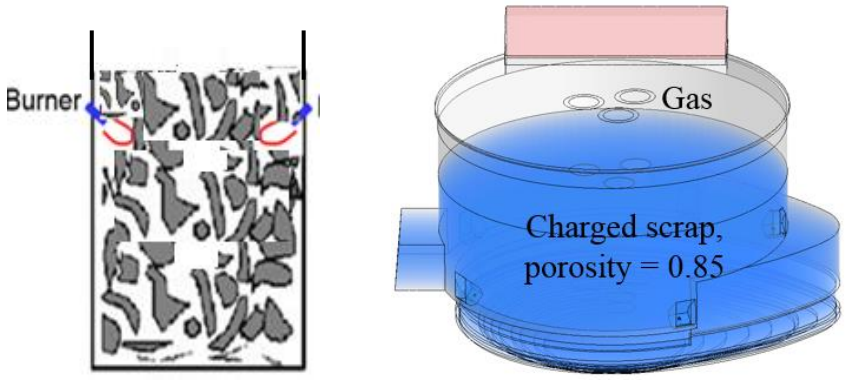

(a) (b)

Figure 43. (a) Schematic of scrap preheating, (b) Initial scrap in EAF.

4.2 Model Validation

4.2.1 Oxy-fuel Combustion

Oxy-fuel combustion is widely used in EAF operation. The oxy-fuel burners are now standard equipment on many electric arc furnaces. The oxy-fuel burners provide combustion flame for scrap preheating and melting in the melting stage, while it provides a supersonic coherent oxygen jet during the refining stage. In order to predict the scrap temperature in the EAF during the scrap preheating and melting stages, correctly modeling the oxy-fuel combustion process is a key step. Since the oxy-fuel combustion is significantly different from the air-fuel combustion, both the chemical mechanisms and radiation heat transfer model have to be carefully considered [104]. Compared to traditional air-fuel combustion, the oxy-fuel combustion generates higher CO concentrations in the near-burner region due to the CO_2 reaction with hydrogen and hydrocarbons. For oxy-propane combustion, four different mechanisms [110] were used: Jones and Lindstedt (JL), three-step, four-step, and six-step. For oxy-natural gas combustion, revised multi-step combustion mechanisms [121] were proposed to be used in CFD modeling. The Westbrook and Dryer two-step mechanisms (WD) [122] and the revised WD [121], the JL four-step mechanism [123] and the revised JL [121] are listed in Table 11. In addition, radiative heat transfer in oxy-fuel combustion is strongly promoted due to a higher concentration of CO_2, H_2O species and in-flame soot compared to air-fuel combustion. Since the combustion environments of air-fuel and oxy-fuel combustion make no difference in solving the radiative transfer equations, efforts on developing models to more accurately calculate gaseous radiative properties for oxy-fuel

combustion have been made. Based on the WSGGM [96] developed for air-fuel combustion, the modified WSGGMs [100,124,125] were developed for oxy-fuel combustion. Among the new modified WSGGMs, the one proposed by Yin et al. [100] can accommodate different combustion environments including both oxy-fuel and air-fuel combustions. It also accounts for the species concentration variations in a flame and the impacts of participating species other than H_2O and CO_2 [126].

Table 11. Methane global combustion mechanisms.

	Reaction	Reaction order	A	b	E
WD					
WD1	$CH_4+1.5O_2 \rightarrow CO+2H_2O$	$[CH_4]^{0.7}[O_2]^{0.8}$	5.012×10^{11}	0	2×10^{8}
WD2	$CO+0.5O_2 \rightarrow CO_2$	$[CO][O_2]^{0.25}[H_2O]^{0.5}$	2.239×10^{12}	0	1.7×10^{8}
WD2r	$CO_2 \rightarrow CO+0.5O_2$	$[CO_2]$	5.0×10^{8}	0	1.7×10^{8}
WD revised					
WD1	$CH_4+1.5O_2 \rightarrow CO+2H_2O$	$[CH_4]^{0.7}[O_2]^{0.8}$	5.03×10^{11}	0	2×10^{8}
WD2	$CO+0.5O_2 \rightarrow CO_2$	$[CO][O_2]^{0.25}[H_2O]^{0.5}$	2.24×10^{6}	0	4.18×10^{7}
WD2r	$CO_2 \rightarrow CO+0.5O_2$	$[CO_2][H_2O]^{0.5}[O_2]^{-0.25}$	1.10×10^{13}	-0.97	3.28×10^{8}
JL					
JL1	$CH_4+0.5O_2 \rightarrow CO+2H_2$	$[CH_4]^{0.5}[O_2]^{1.25}$	7.82×10^{10}	0	1.2552×10^{8}
JL2	$CH_4+H_2O \rightarrow CO+3H_2$	$[CH_4][H_2O]$	3.0×10^{8}	0	1.2552×10^{8}
JL3a	$H_2 + 0.5O_2 \leftrightarrow H_2O$	$[H_2]^{0.5}[O_2]^{2.25}[H_2O]^{-1}$	4.45×10^{15}	-1	1.6736×10^{8}
JL3b	$H_2 + 0.5O_2 \leftrightarrow H_2O$	$[H_2]^{0.25}[O_2]^{1.5}$	1.21×10^{15}	-1	1.6736×10^{8}
JL4	$H_2O+CO \leftrightarrow CO_2+H_2$	$[CO][H_2O]$	2.75×10^{9}	0	8.36×10^{7}
JL revised					
JL1	$CH_4+0.5O_2 \rightarrow CO+2H_2$	$[CH_4]^{0.5}[O_2]^{1.25}$	4.4×10^{11}	0	1.26×10^{8}
JL2	$CH_4+H_2O \rightarrow CO+3H_2$	$[CH_4][H_2O]$	3.0×10^{8}	0	1.26×10^{8}
JL3	$H_2 + 0.5O_2 \leftrightarrow H_2O$	$[H_2][O_2]^{0.5}$	5.69×10^{11}	0	1.465×10^{8}
JL4	$H_2O+CO \leftrightarrow CO_2+H_2$	$[CO][H_2O]$	2.75×10^{9}	0	8.36×10^{7}

In this study, oxy-natural gas combustion was simulated using CFD. Different combustion mechanisms for oxy-fuel combustion were used and compared including WD, revised WD, JL, revised JL, 28-step [118], and GRI-Mech 3.0. The 28-step chemical reaction mechanism is listed in Table 12. The revised WSGGM proposed by Yin et al. [100] was implemented by developing a UDF. In order to validate the oxy-natural gas combustion CFD model, a validation process has been conducted. The experimental work was conducted by Lallemant et al. [127] the in-flame measurements were conducted to obtain data on flow properties and reactions. In current research

work, numerical simulations were performed to compare the simulation results with the measurements. Yin et al. [104,108,126] also conducted similar validation process. The computational domain was developed based on the experimental furnace setup as shown in Figure 44.

Table 12. The 28-step methane-oxygen (air) combustion mechanisms [118].

	Reactions	$k=AT^b \exp(Ea/RT)$		
		A (mol cm s K)	b	Ea (cal/mol)
1	$OH + H_2 = H_2O + H$	2.14E+08	1.52	3449
2	$H + O_2 = OH + O$	1.00E+14	0	14,850
3	$H+ O_2 +M = HO_2 + M$ (RH_2O=12, RH_2 =1.82, RO_2=0.6)	2.60E+15	0	-1350
4	$OH + HO_2 = H_2O + O_2$	2.89E+13	0	-497
5	$H + HO_2 = H_2 + O_2$	4.28E+13	0	1411
6	$O + HO_2 = O_2 + OH$	3.25E+13	0	0
7	$OH + OH = O + H_2O$	4.33E+03	2.7	-2485
8	$O + O +M = O_2 + M$	1.89E+13	0	-1788
9	$HO_2 + HO_2 = H_2O_2 + O_2$	4.20E+14	0	12,000
10	$H_2O_2 +M = OH + OH + M$	1.21E+17	0	45,507
11	$CH_4 + O_2 = CH_3 + HO_2$	3.97E+13	0	56,900
12	$CH_4 + O = CH_3 + OH$	6.90E+08	1.56	8485
13	$CH_4 + OH = CH_3 + H_2O$	1.60E+06	2.1	2,460
14	$CH_4 + H = CH_3 + H_2$	1.33E+04	3	8034
15	$CH_4 + HO_2 = CH_3 + H_2O_2$	9.04E+12	0	24,640
16	$CH_3 + O_2 = CH_3O +O$	1.32E+14	0	31,400
17	$CH_3 + O_2 = CH_2O + OH$	3.31E+11	0	8942
18	$CH_3 + H = CH_4$	2.11E+14	0	0
19	$CH_3 + HO_2 = CH_3O +OH$	1.81E+13	0	0
20	$CH_3O +M = CH_2O + H +M$	4.30E+17	0	27,820
21	$CH_2O + O_2 = HO_2 + HCO$	6.03E+13	0	40,658
22	$CH_2O + O = HCO + OH$	3.60E+13	0	3460
23	$CH_2O + OH = HCO + H_2O$	3.43E+09	1.18	-447
24	$CH_2O + H = HCO + H_2$	2.28E+10	1.05	3279
25	$HCO + O_2 = HO_2 + CO$	3.31E+12	0	0
26	$CO + O_2 = CO_2 +O$	1.26E+13	0	47,060
27	$CO + OH = CO_2 +H$	1.51E+07	1.3	-758
28	$CO + HO_2 = CO_2 + OH$	5.80E+13	0	22,934

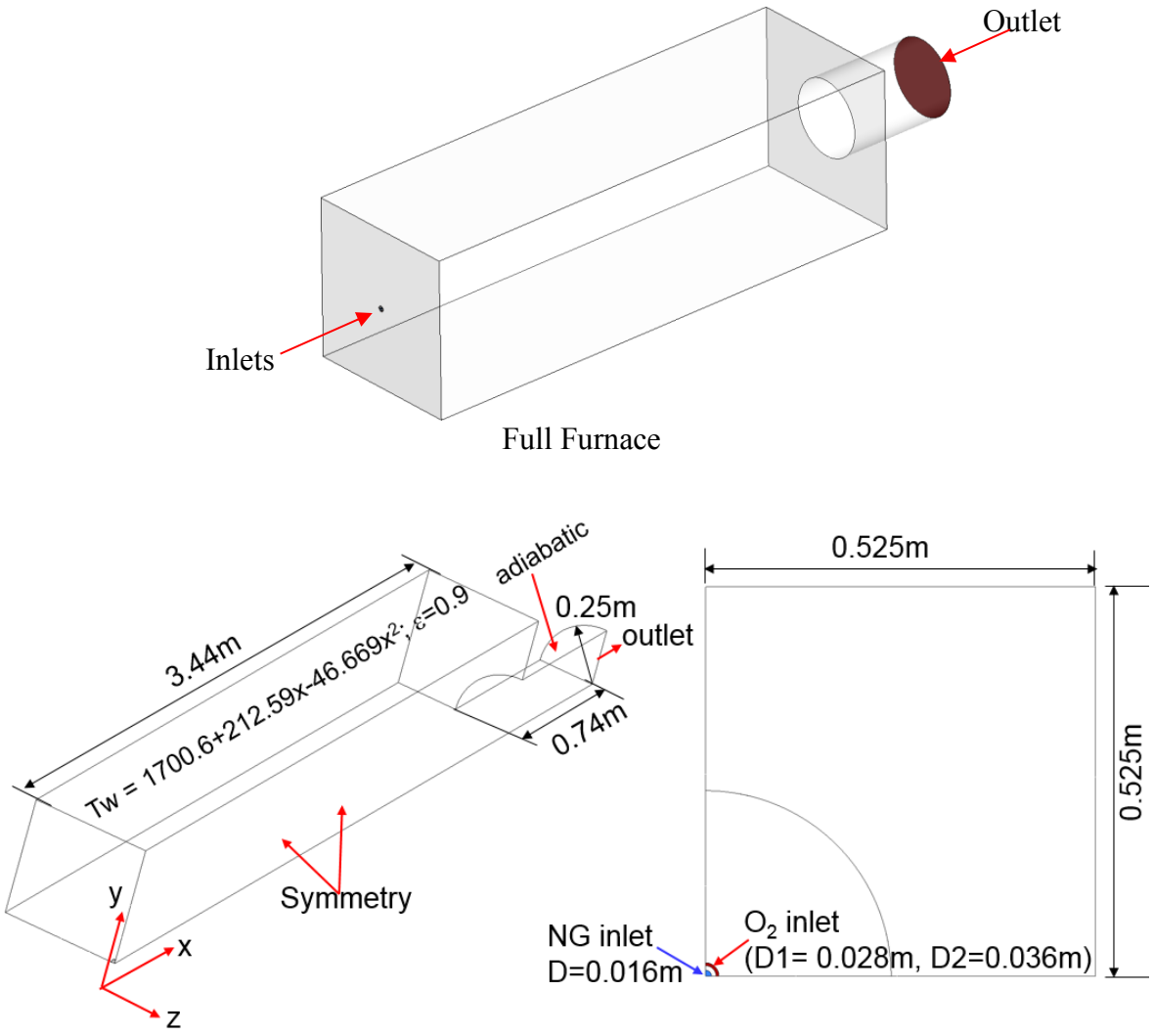

Figure 44. Computational domain for oxy-natural gas combustion validation.

The experimental furnace is a 0.8 MW oxy-fuel combustion furnace. The natural gas (NG) jet issued from the burner center enters the furnace with shrouded oxygen gas issued from the outer annulus as shown in Figure 44. The furnace exhaust outlet is located downstream of the combustion gas flow. The total length of the furnace is about 4.18 m long and the width is 1.05 m. Due to the symmetrical shape of the furnace, one-fourth of the whole furnace is used as the computational domain. The detailed dimensions and wall boundary conditions are shown in Figure 44. The fuel and oxidant compositions are listed in Table 13. The natural gas mass flow rate is 63 kg/h at room temperature. The oxygen mass flow rate is 224.5 kg/h at room temperature.

Table 13. Fuel and oxidant compositions.

Species	Natural gas inlet	Oxygen inlet
O_2	0.0021	1
C_2H_6	0.0799	
CH_4	0.86	
CO_2	0.0179	

Mesh independence study was conducted to ensure the simulation results are not affected by the computational grids. The very fine mesh was used around the burner inlets, while relatively coarse mesh was adopted for the near furnace wall region. The region that connects the very fine mesh and relatively coarse mesh region is a mesh with gradually changed sizes as shown in Figure 45. Three different mesh numbers: coarse mesh (0.6 million cells), medium grid (1 million cells) and fine mesh (2 million cells) were used. The temperature profiles along the radial direction at 0.82 m downstream of the burner were compared for three different mesh levels as shown in Figure 46. It can be seen from the comparison that the medium mesh and the fine mesh predict the same results, while the coarse mesh over-predicts the gas temperature. Therefore, the medium mesh is adopted for other numerical simulation.

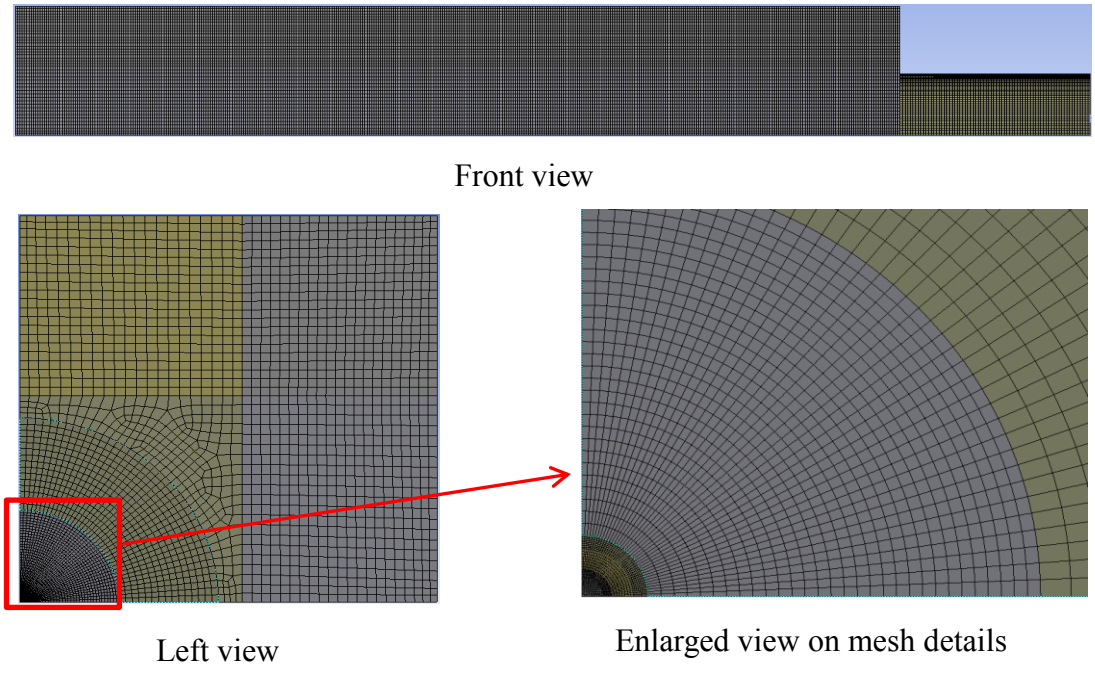

Figure 45. Mesh details for oxy-natural gas combustion model validation geometry.

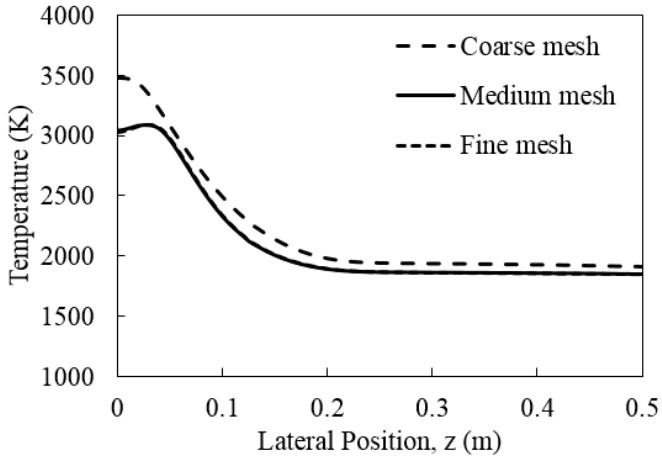

Figure 46. Mesh independence study.

Numerical simulation was conducted based on the developed CFD model for the oxy-fuel combustion in the 0.8MW oxy-fuel combustion experimental furnace. In terms of the chemical reaction mechanisms and gas radiation model, the 28-step oxy-natural gas combustion reaction mechanisms and the modified WSGGM [100] were used. The CFD model predicted velocity, temperature, species mole fractions are plotted in Figure 47. In order to compare the simulation results with measurements, the CFD predicted results on three different lines were plotted, where the three locations, 0.82 m, 1.42 m and 2.21 m downstream of the burner, are shown in Figure

47(h). The comparisons of model prediction and experimental measurements on the lines (x=0.82 m, 1.42 m and x= 2.21 m) are shown in Figure 48, Figure 49 and Figure 50, respectively.

Due to the burner configuration, the natural gas injected from the center of the burner mixes with the shrouded oxygen. The natural gas jet velocity reaches a maximum of 132 m/s as shown in Figure 47 (a). The combustion reactions start at the jet turbulence mixing region and the highest combustion flame temperature reaches 2858 K. The oxygen and the natural gas are provided for the oxy-fuel combustion burner at a stoichiometric ratio. After reaching a steady state, the O_2 is consumed and the major species in the furnace is CO_2. High concentrations of CO and H_2 exist in the combustion flame region and further react to other products. The use of the 28-step chemical reaction mechanisms for oxy-natural gas combustion allows the model to predict other species and radicals such as CO, H_2, and OH.

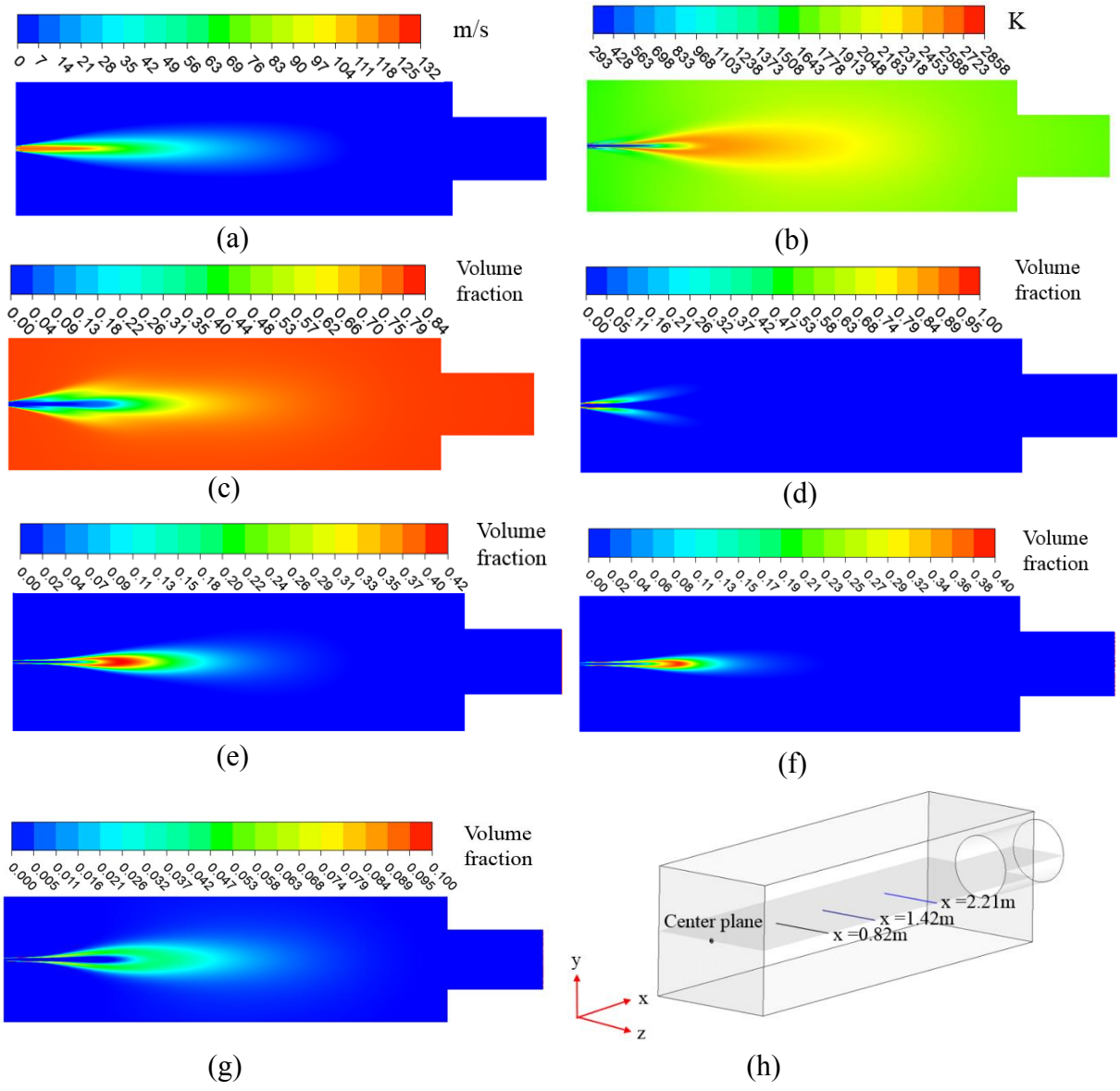

Figure 47. Flow properties in the 0.8MW oxy-fuel combustion furnace, (a) velocity, (b) temperature, (c) CO_2 volume fraction (dry), (d) O_2 volume fraction (dry), (e) CO volume fraction (dry), (f) H_2 volume fraction (dry), (g) OH volume fraction (dry), (h) Plotted plane and measurement locations.

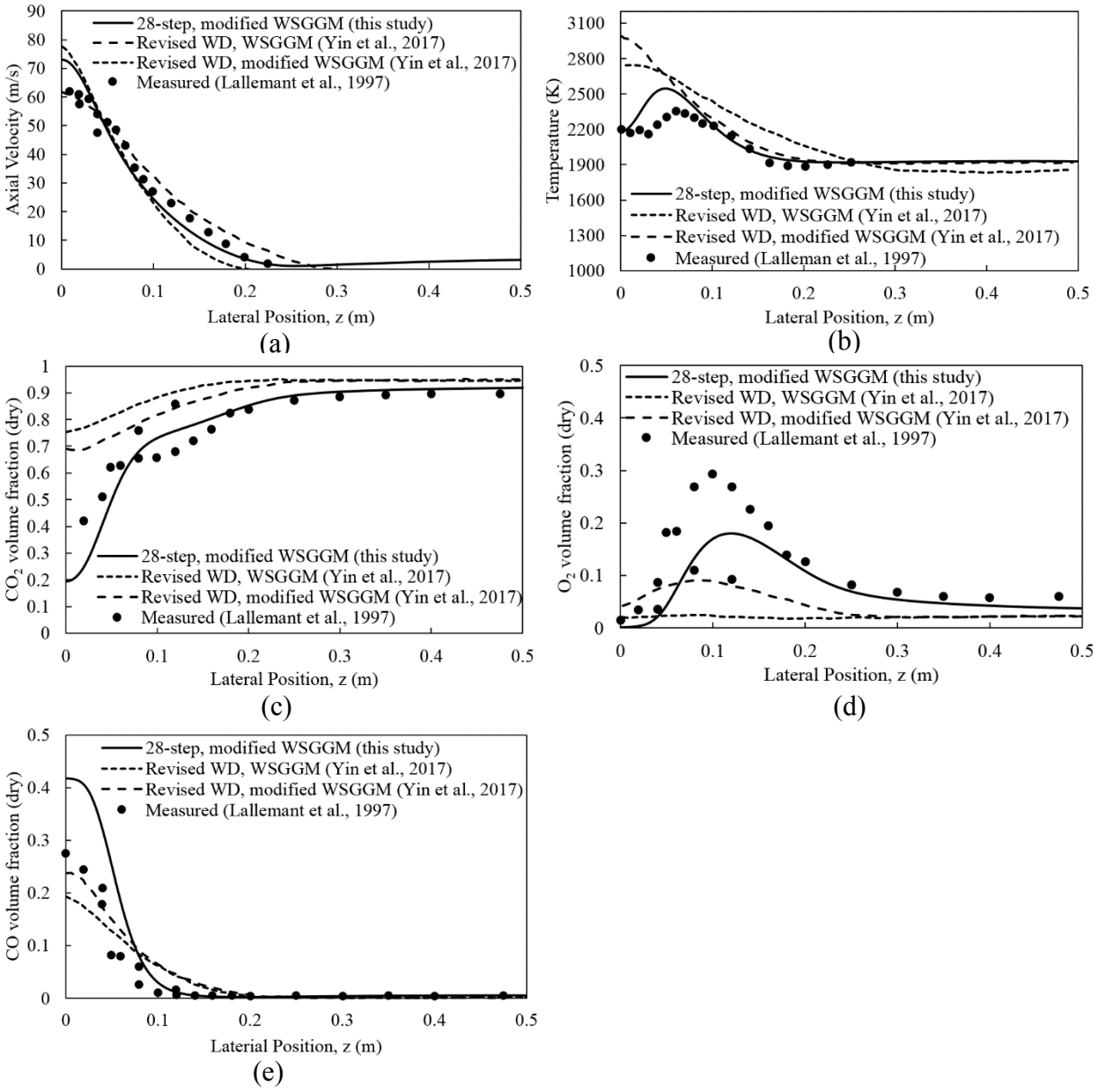

Figure 48. Comparisons of model prediction results and measurements at 0.82 m downstream of the burner, (a) velocity, (b) temperature, (c) CO_2 volume fraction (dry), (d) O_2 volume fraction (dry), (e) CO volume fraction (dry).

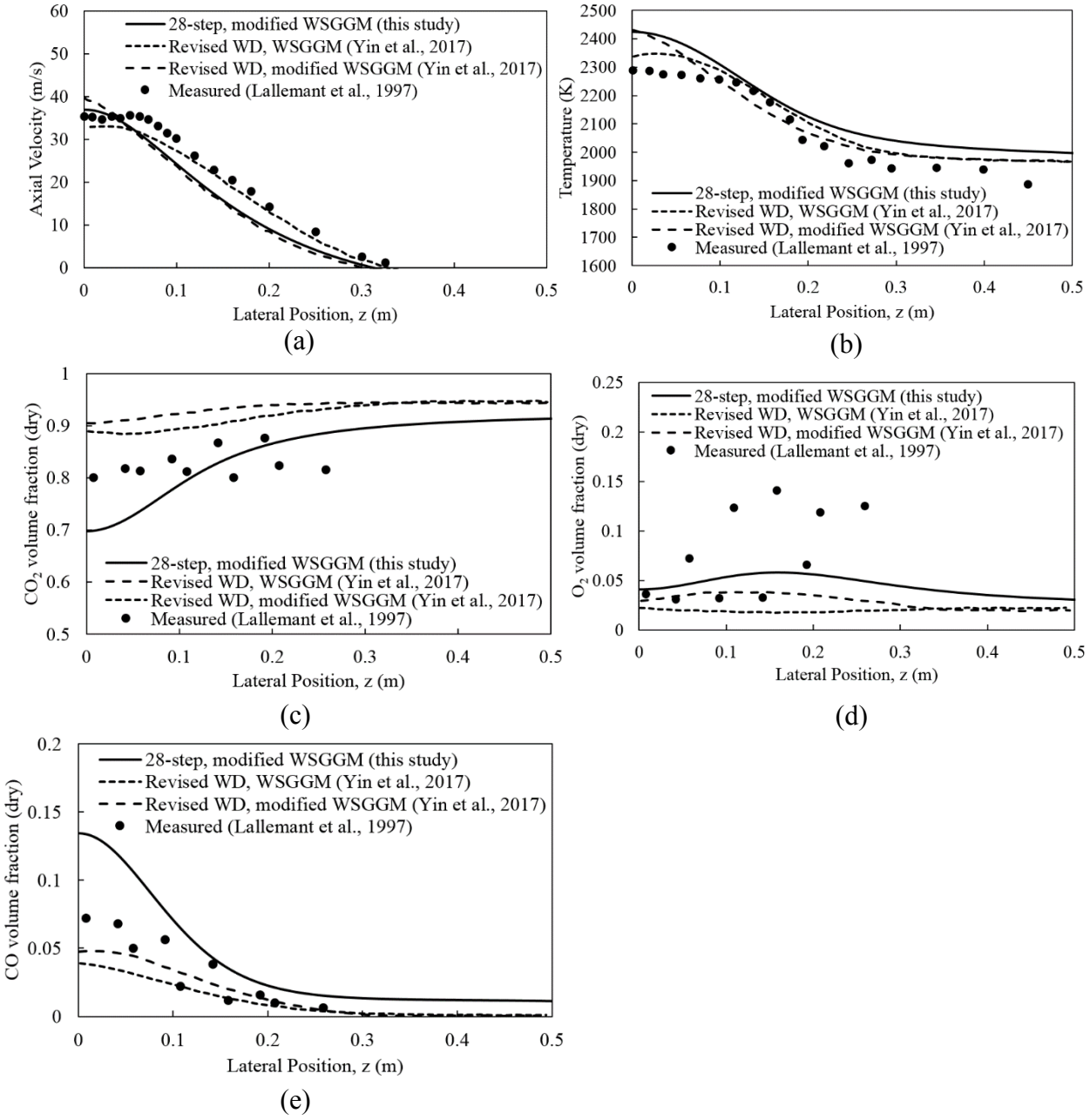

Figure 49. Comparisons of model prediction results and measurements at 1.42 m downstream of the burner, (a) velocity, (b) temperature, (c) CO_2 volume fraction (dry), (d) O_2 volume fraction (dry), (e) CO volume fraction (dry).

According to Figure 48, the comparisons are made among the current CFD model predictions, the experimental measurements and the CFD model prediction by Yin et al. [108] It can be seen that the revised WD combined with WSGGM model provides the best agreement on the velocity profile compared to experimental measurements. However, for the temperature profile, CO_2

volume fraction (dry) and the O_2 volume fraction (dry), the 28-step reaction mechanism combined with the modified WSGGM agrees with the measurements the best. The 28-step combined with modified WSGGM over-predicts the CO volume fraction (dry) when the lateral position less than 0.08m. Overall, both the current CFD model and the CFD model used by Yin et al. [108] predict the combustion characteristic of the oxy-fuel combustion fairly well. It can be seen that the 28-step reaction mechanism combined with the modified WSGGM model provides better predictions on the temperature, CO_2 and O_2 volume fractions.

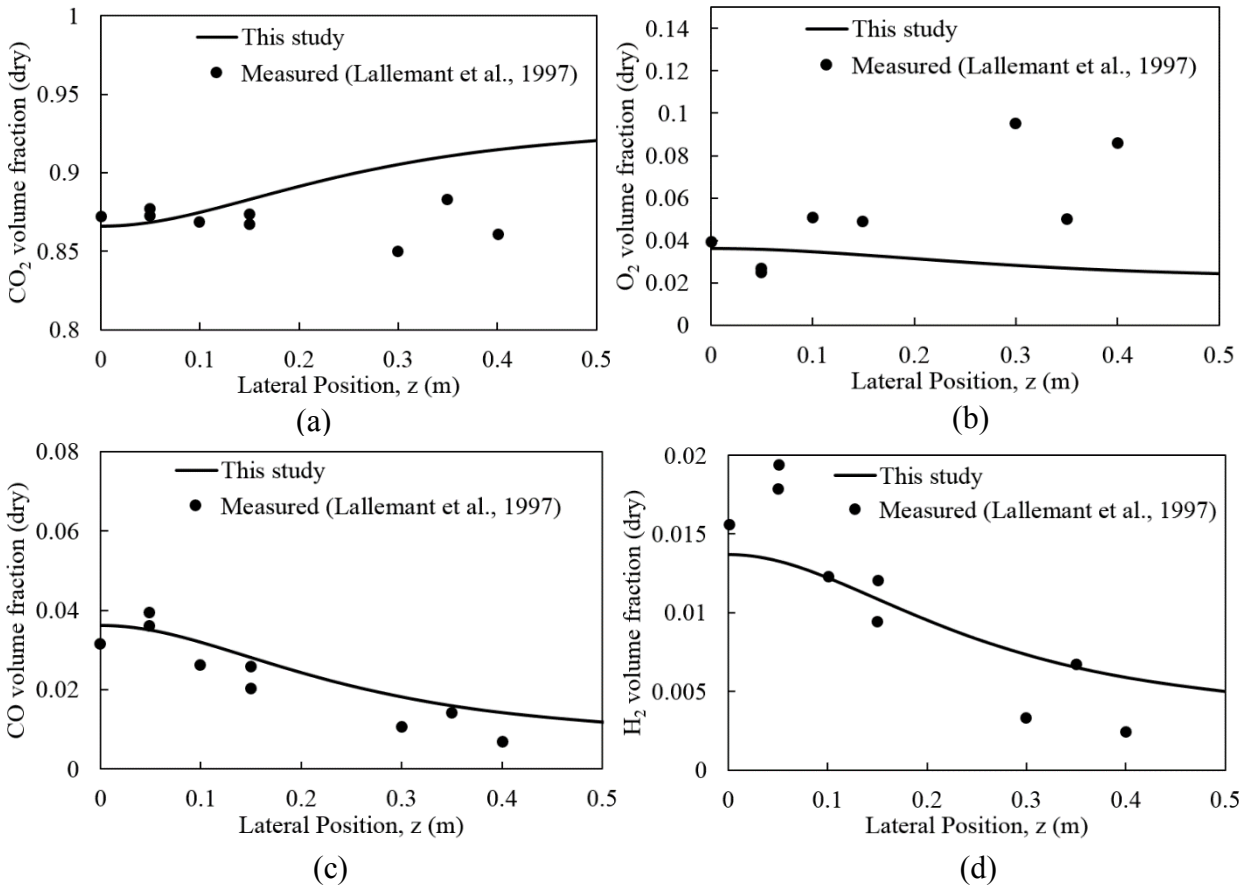

Figure 50. Comparisons of current CFD model predictions with measurements at 2.21 m downstream of the burner, (a) CO_2 volume fraction (dry), (b) O_2 volume fraction (dry), (c) CO volume fraction (dry), (d) H_2 volume fraction (dry).

At the locations (x=1.42m and x=2.21 m) further downstream of the burner, agreements between the CFD model predictions and the experimental measurements are still can be seen in Figure 49 and Figure 50. In Figure 49, all the CFD models over-predict the temperature profile similar to the results at x=0.82 locations. It is reported that the quality of the measured temperatures has

relatively large error compared to the measurements of velocity and species due to the use of water-cooled suction pyrometer. [108] Similar to the comparisons at location x=0.82 m, the current CFD model predictions have a better agreement on CO_2 and O_2 species volume fractions while it over-predicts the CO volume fraction compared to other CFD models and measurements. As shown in Figure 50, the current CFD model predicted species volume fractions have a good agreement with the experimental measurements in the flame region (the lateral direction $z < 0.2$ m).

Overall, the current CFD model for the oxy-fuel combustion is carefully developed with detailed consideration of mesh independence, turbulence, combustion mechanisms, and radiation model. It is capable of predicting the flow field and chemical reactions during the oxy-fuel combustion. The experimental measurements provide evidence that the CFD model performs reasonably well. Due to the challenges of obtaining high-quality measurement data, discrepancies between CFD and measurements are still not negligible. Further studies are needed for both experimental and numerical work.

Research work has been conducted to find appropriate chemical reaction mechanisms for oxy-fuel combustion in EAF. In general, more detailed chemical reaction mechanisms will produce more accurate in-flame chemistry and flame temperature. However, industrial applications using more complicated chemical reaction mechanisms are always limited by the computational time which associated with the furnace geometry and time scales. The effects of oxy-fuel combustion reaction mechanisms on the flame properties are further studied using four different chemical reaction mechanisms: revised WD two-step, revised JL four-step, 28-step and the GRI-Mech 3.0. The temperature contours on the oxy-fuel combustion furnace center plane predicted by the four different chemical reaction mechanisms are shown in Figure 51.

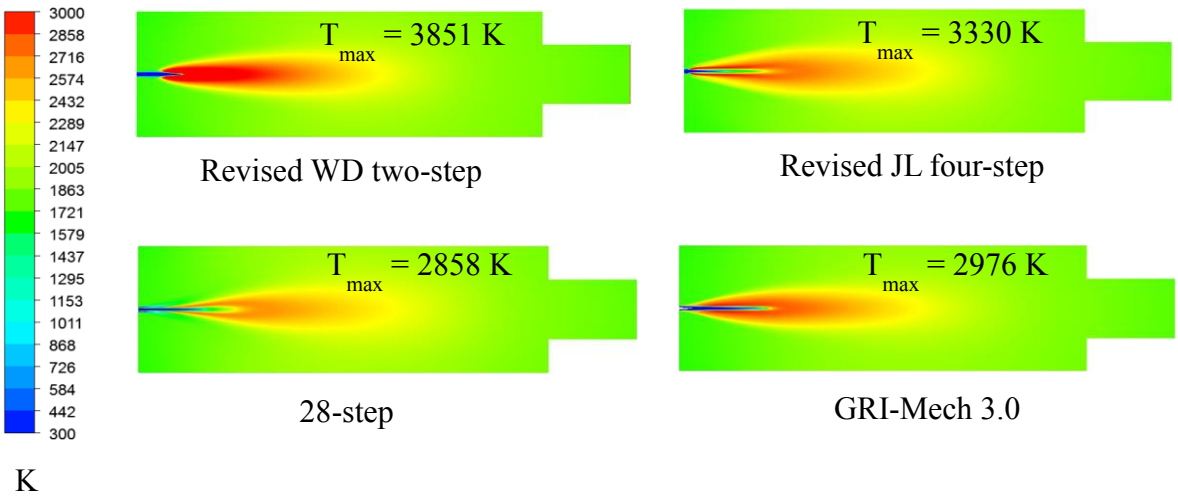

Figure 51. Model predictions of temperature contours on the furnace center plane using different combustion mechanisms.

As shown in Figure 51, the choice of chemical reaction mechanisms can affect the combustion temperature field significantly. The highest flame temperature predicted by the revised WD two-step chemical reaction mechanism is 3851 K which is significantly larger than the adiabatic flame temperature of oxy-natural gas combustion (T_{max}= 3042 K at stoichiometry) [104]. By using the improved revised JL four-step chemical reaction mechanism, the highest flame temperature is reduced to 3330 K. Improve the complexity of the chemical reaction mechanisms, the highest flame temperature is reduced below 3000 K. The high temperature flame zones are different by using different chemical reaction mechanisms. The comparisons shown in Figure 52 demonstrate the difference of flow properties and reactions chemistry in the flame region using different chemical reaction mechanisms.

It can be seen in Figure 52 that the choice of different reaction mechanisms have little effect on the flow velocities. However, the temperature profiles at the x=0.82 m line are affected by chemical reaction mechanisms greatly. The 28-step and GRI-Mech 3.0 agree with experimental measurements better than revised WD two-step and revised JL four-step. For CO_2, O_2 and CO volume fractions (dry), the 28-step chemical reaction mechanisms case agrees the best with measurements. Therefore, in terms of chemical reaction mechanism, the 28-step reaction mechanism can provide reasonably accurate results on oxy-fuel combustion regarding both temperature and chemistry. It is computationally relatively more expensive than the revised WD

two-step and the revised JL four-step chemical mechanisms, but still more affordable for industrial scale EAF simulations than the full-step reaction mechanism (GRI-Mech 3.0). In industrial EAF applications, it is recommended to use the 28-step chemical reaction mechanism for a high accuracy requirement. The revised JL four-step is also applicable for obtaining quick simulation results with reasonable accuracy.

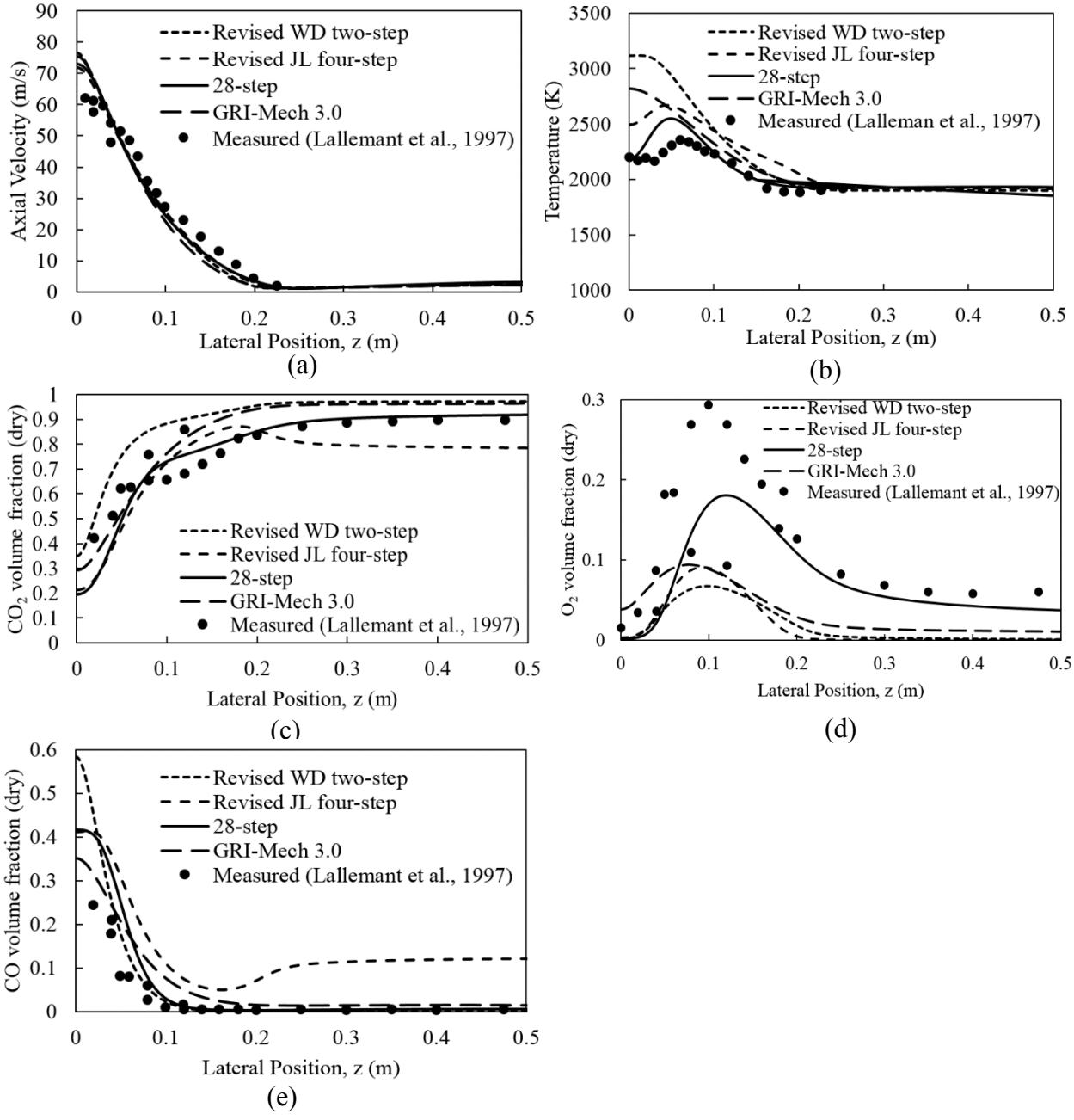

Figure 52. Model prediction of flow velocity, tempeature and species volume fractions at 0.82 m downstream of the burner using different combustion mechanisms.

4.2.2 Gas-Scrap Heat Transfer

It is difficult to measure the scrap temperature inside an EAF during operation. In order to validate the CFD model, small-scale experimental results [59] were used to compare with the simulation. The experiment was conducted to measure the efficiency of scrap heating by a propane-oxygen burner. The volume of the experimental furnace is in the order of 1 m^3 volume as shown in Figure 53(a). The propane-oxygen burner was used in the lower part of the furnace, with burner power of 8.3 kW. The thermocouples are installed at different locations in the furnace without contacting the steel scrap. In the beginning, the furnace was purged with argon gas. During the experiment, steel scraps are placed in the furnace at room temperature. Then the propane-air burner starts to heat the steel scrap and the temperature measurements by the thermocouples were recorded. The scrap preheating model was applied to simulate the scrap preheating process by propane-oxygen combustion. The computational domain was developed based on the detailed dimensions of the experimental furnace as shown in Figure 53 (b). The oxy-fuel burner power used is 8.3 kW. The scrap used for this simulation is the small shredded scrap. The mixed propane-oxygen was put into the furnace through a 4 mm diameter lance. More details can be found in the literature [59] used for comparison.

A numerical simulation was performed based on the real conditions used in the lab-scale experimental study. The simulation results shown in Figure 54 demonstrate the process of scrap heating in the experimental furnace. The propane-oxygen gas mixture was ignited and put into the scrap piles. Due to the high temperature of oxy-fuel combustion, the density of the combustion flue gas is significantly reduced and flows upwards through the steel scraps to the top exit as indicated in Figure 54 (a). The combustion flame temperature of the propane-oxygen combustion can reach up to 4000 K as shown in Figure 54 (b). The corresponding highest gas velocity reaches 61 m/s. Due to the heat transfer from the hot combustion flue gas to the cold scrap, the scrap temperature increased most in the flame region as shown in Figure 54 (c). Quantitative comparisons are shown in Figure 55. The measurement at point2 (0.166 m, 0, 0.478 m) was chosen to compare.

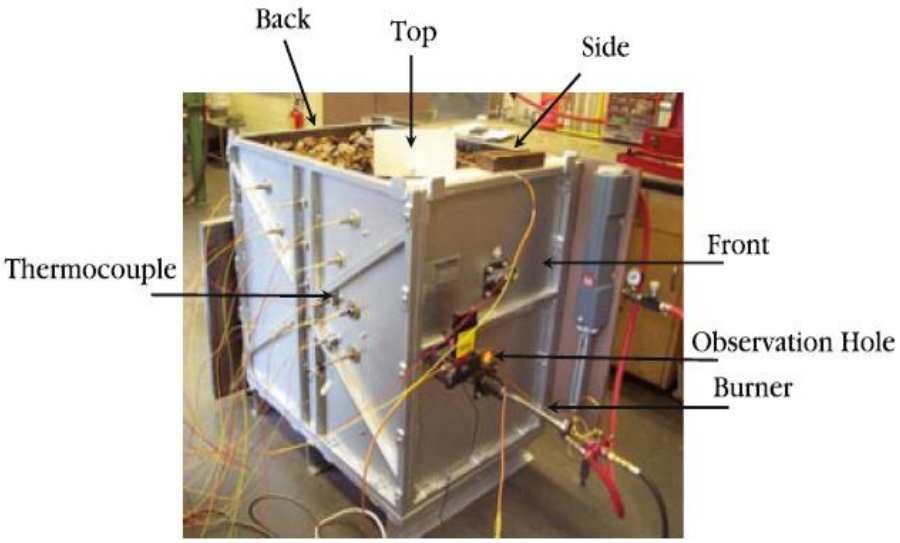

(a)

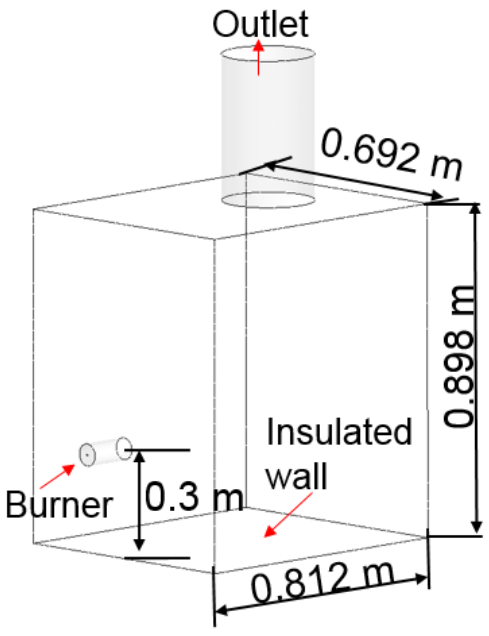

(b)

Figure 53. (a) Experimental setup [59], (b) Computational domain.

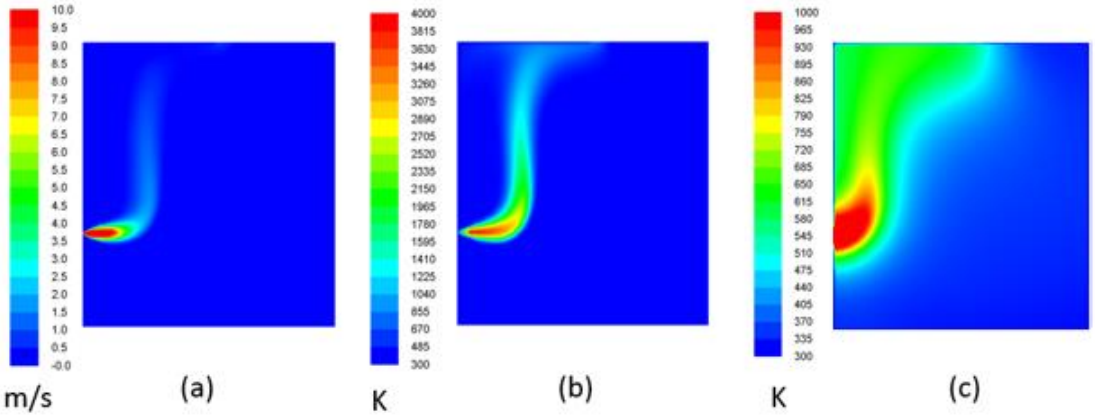

Figure 54. Simulation results of (a) Gas velocity, (b) Gas temperature, and (c) Scrap temperature at t= 60 min.

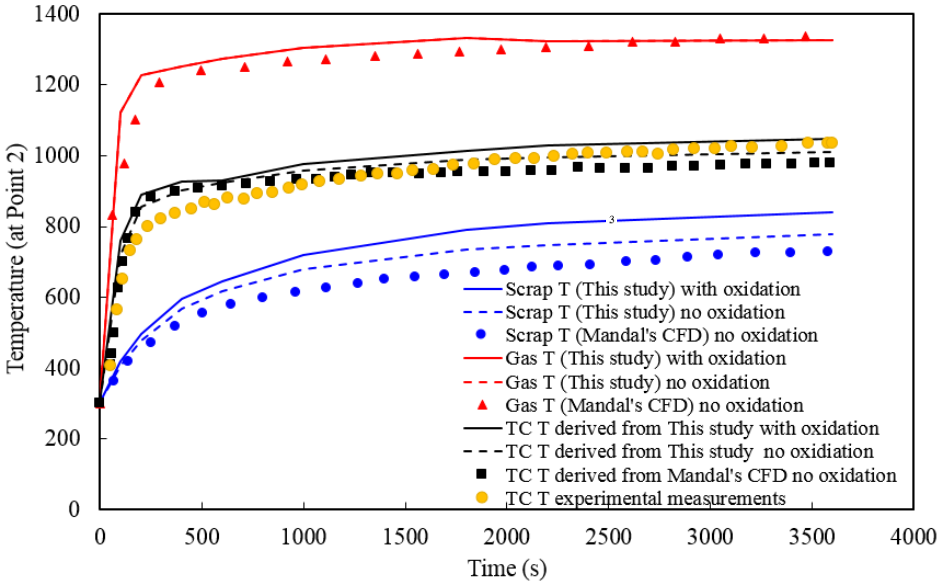

Figure 55. Comparisons of temperatures at a measured point between CFD and measurements.

According to Figure 55, the gas temperature, scrap temperature, and the thermocouple (TC) temperature are compared between CFD simulation and experimental measurements. The TC measured temperature is neither the gas temperature nor the scrap temperature. Based on the assumption that the thermocouple temperature is changing slowly, a quasi-steady state thermocouple temperature can be calculated based on gas temperature, scrap temperature using the energy balance equation.

$$\mathrm{hA}\left(T_f - T_{th}\right) = F_{th-sc}\mathrm{A}\,\varepsilon\,\sigma\,\left({T_{th}}^4 - {T_{sc}}^4\right) \tag{97}$$

where h, A, T_f, T_{th}, F_{th-sc}, ε, σ, T_{sc} are the heat transfer coefficient between gas and scrap, the area of the thermocouple, the fluid temperature, the thermocouple temperature, the shape factor, the thermocouple emissivity, the Stefan-Boltzmann constant and the scrap temperature.

The comparison in Figure 55 shows three groups of data set, the scrap temperature, gas temperature, TC temperature. Each group consists of a CFD simulation of scrap preheating with oxidation and without oxidation. The TC temperature group also consists of experimental measurements. It can be seen that this study over-predicts the scrap temperature compared with Mandal's CFD under no oxidation conditions. When the oxidation is considered, the scrap temperature is even higher due to the fact that the oxidation reaction is exothermic. In the numerical model, the scrap oxidation occurs in the steel scrap, therefore, 100% of the heat release contributes to the scrap phase. When compare the gas temperature in Figure 55, the effects of oxidation on the gas temperature change is minimal. Both CFD of this study and Mandal's CFD show in good agreement on the trend and quantitatively. The TC temperature comparison indicates that the CFD simulations have a similar trend of scrap temperature change with respect to time. However, the CFD models are over-predicting the scrap temperature at the beginning stage. In general, the TC temperature will be higher due to the oxidation effects. The comparisons of the TC temperature predicted by this study with the measurements are shown in Figure 55.

In experimental work, the small shredded scrap may subject to reuse. As shown in Figure 56, the average percentage error of without oxidation is 5.6% which is lower than the 7.6% for with oxidation. It indicates that the effect of oxidation will increase the difference when compared to the experiment. Therefore, the oxidation during the experiment was not significant. However, in real EAF operation, the effects of oxidation is significant due to the fact that oxygen supply is over stoichiometric and furnace temperature is high. The effects of oxidation in the experimental furnace were studied. The scrap temperature and oxidized scrap distributions are shown in Figure 57. Figure 58 shows the quantitative change of scrap temperature due to the oxidation effect.

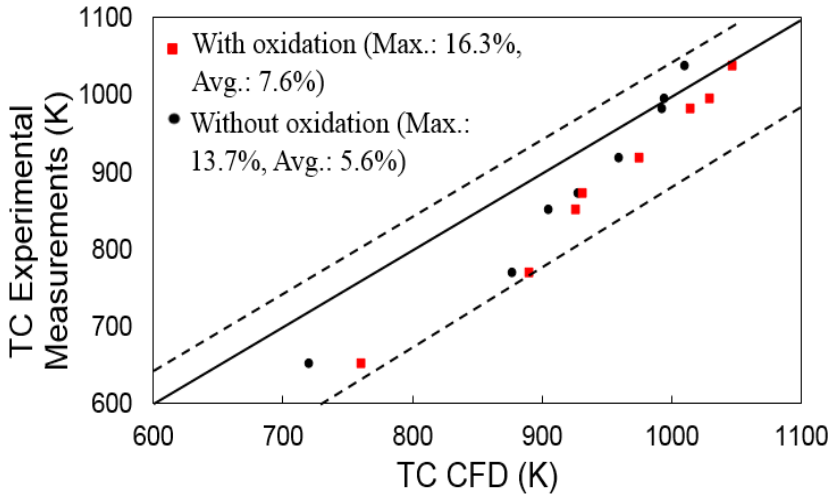

Figure 56. Comparison of CFD and experiment on TC temperature.

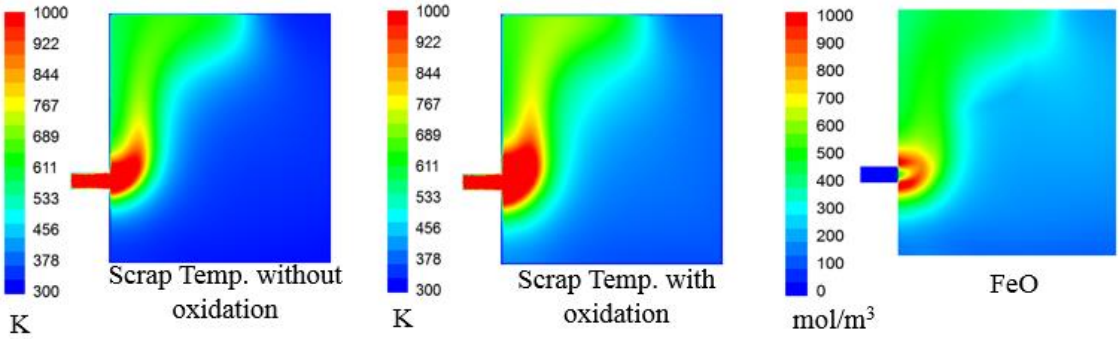

Figure 57. Effects of oxidation on scrap temperature distribution.

It can be seen that the scrap oxidation reaction increases the scrap temperature. In this simulation conditions, the oxidation reaction occurred mostly in front of the burner where the scrap temperature and oxygen concentrations are higher than any other places. Quantitatively, the oxidation could potentially increase the scrap temperature by about 7.9% compared to no oxidation.

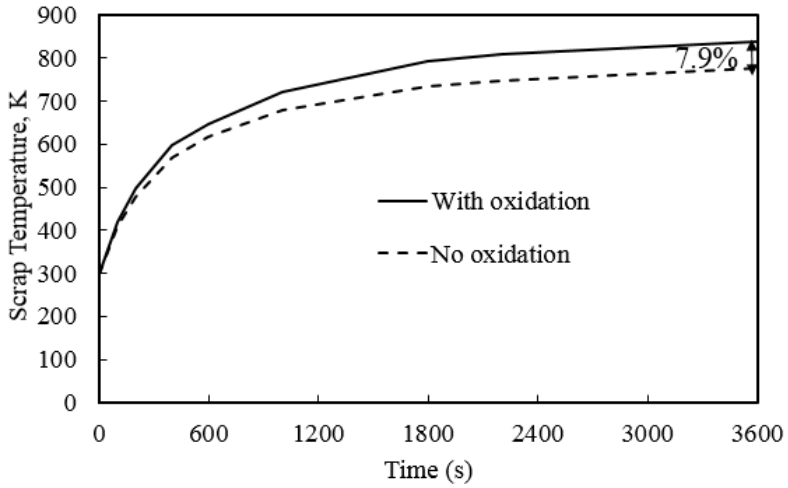

Figure 58. Effects of oxidation on scrap temperature at the measurement point.

4.3 Results and Discussions

4.3.1 Oxy-fuel combustion in EAF

Based on the process, after the furnace discharge of the molten steel, the oxy-fuel burner that fires natural gas is still on duty to preheat the furnace for the next charging process. Since the scrap preheating is a transient process, obtaining accurate initial conditions for the furnace is important. Therefore, the empty furnace with oxy-fuel combustion was simulated to act as the initial condition for the scrap preheating simulation. The steady-state calculation was performed and the temperature and velocity distributions, on planes cut through an oxy-fuel burner, are shown in Figure 59.

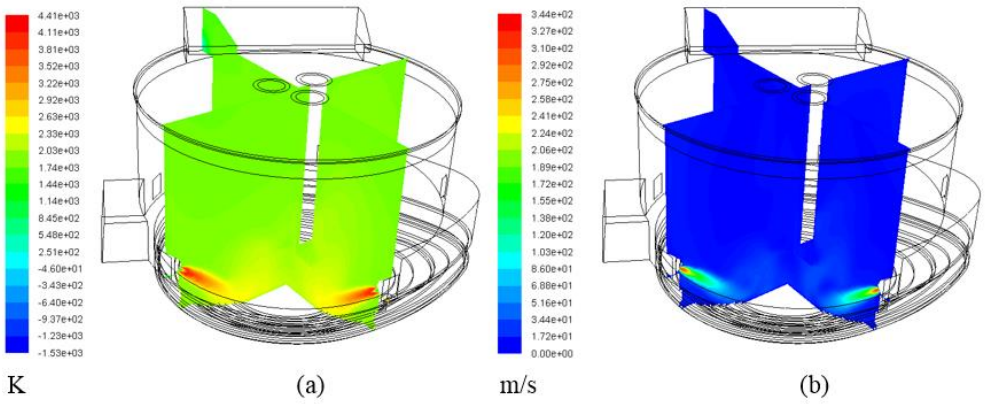

Figure 59. Furnace flow properties, (a) Temperature, (b) Velocity.

Figure 59 shows the simulation results for a steady-state empty furnace with combustion used to predict initial gas temperature distribution in the furnace before charging the scrap. Two vertical cross-sections cutting through the centers of burner 1 and burner 2 were made to show the temperature and velocity distribution inside the furnace. The highest temperature generated by CH_4 with pure oxygen combustion is close to 3014 K. The high-temperature gas hits the bottom surface of the furnace with an average speed of 86 m/s, heating the entire furnace from the bottom to top. During the scrap charging process, the furnace roof opens to the atmosphere. Due to the high-velocity jet in the furnace, the up-moving high-temperature flue gas will lead to air ingression into the furnace. As shown in Figure 60, the furnace temperature dropped significantly during the charging process. The average predicted temperature used as the initial temperature for the preheating is around 1440 K.

Scrap charging starts once a stable gas temperature distribution is obtained. In this study, total charged scrap mass is 143,290 kg occupying a volume of 127 m^3. Other major initial conditions for charged scrap are given in Table 14. Note that the flat surface for the charged scrap with 0.85 porosity is assumed, and the phase change of the scrap when reaching the melting point is ignored first. The hot heel and hot metal were considered. By taking the physical heat from the hot heel and hot metal into consideration, the average initial scrap temperature is 611 K.

Table 14. Initial conditions for charged scrap in preheating.

Variable	Values
Scrap amount (kg)	143,290
Scrap density (kg/m^3)	7500
Scrap porosity	0.85
Total charged scrap volume (m^3)	127.36
Charged scrap temperature (K)	300

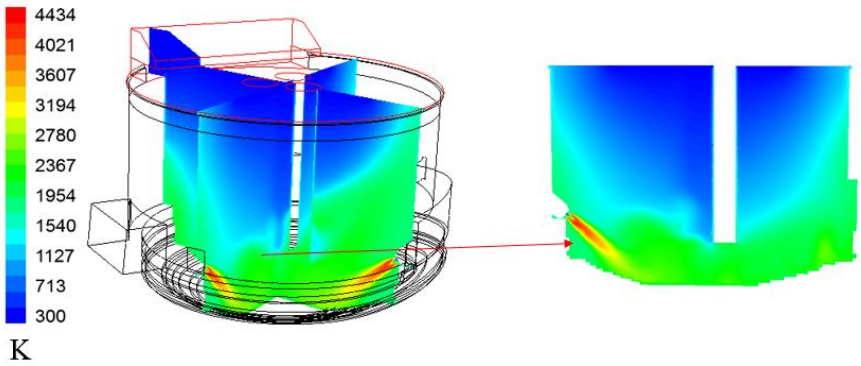

Figure 60. Furnace temperature estimation at charging stage.

4.3.2 Gas-scrap Heat Transfer

The temperature profile variation over time for scrap preheating is shown in Figure 61. Major heating comes from the combustion gas and is transferred to the scrap around the burner inlets, further heating up the surrounding scrap to all scrap in the furnace. After 15 minutes of heating time, the average temperature increase is around 300 K as shown in Figure 62. The red region represents the melted scrap, with temperatures above the melting point, which appears near the five burners. Since the phase change of the scrap when reaching the melting point is ignored, as long as the temperature in the scrap phase is above 1800 K, the occupied volume will be counted as melted scrap for further calculation.

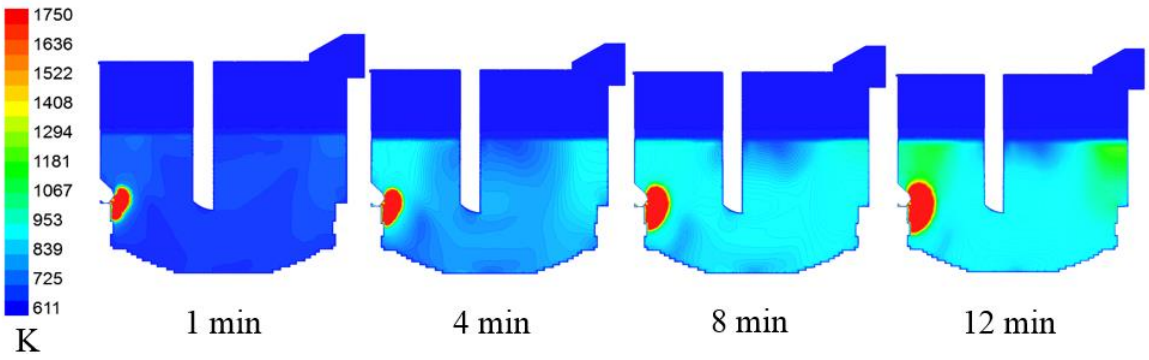

Figure 61. Scrap temperature during preheating.

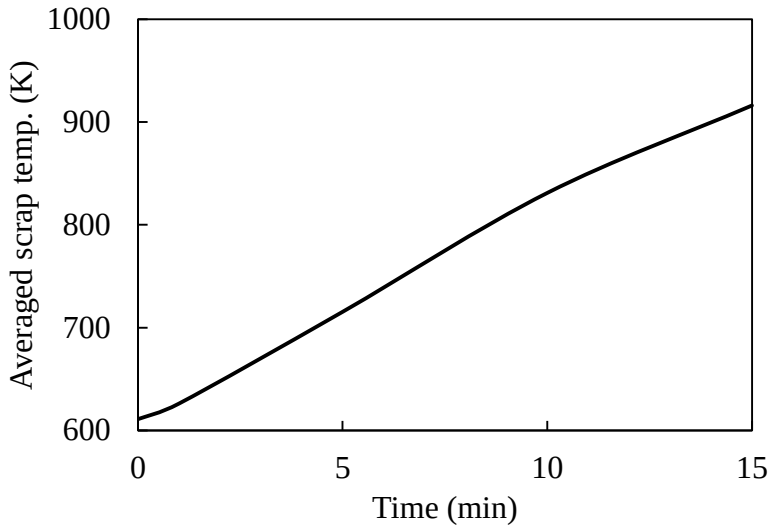

Figure 62. CFD prediction of averages scrap temperature in EAF during scrap preheating.

4.4 Summary

A 3-D CFD model for scrap preheating process by the oxy-fuel combustion in EAFs has been developed. The model provides a detailed consideration of gas flow, oxy-fuel combustion, scrap oxidation and multi-mode heat transfer between gas and solid scrap. The CFD model has been validated against the measurement data obtained from a small-scale experimental furnace. The effects of scrap oxidation on the scrap preheating are investigated. The results indicate that scrap oxidation could increase scrap temperature by up to 7.9% in the experimental furnace. The model can be applied to industrial EAFs to optimize scrap preheating process.

A three-dimensional CFD model has been developed with detailed consideration of furnace geometry, oxy-fuel burner configuration, natural gas combustion, gas scrap heat transfer, and scrap oxidation. The model has been validated against the experimental and numerical simulation done by Mandal [59]. This model was applied to an industrial EAF to study the effects of using the oxy-fuel burner to preheat the steel scraps before the arcing process. The simulation results show that the average scrap temperature would increase about 300 K during a 15-minute preheating using 2.5 MW burner power with five burners in the EAF. This model will be further developed for scrap melting by modeling both oxy-fuel burners and the electric arc.

CHAPTER 5. MODELING OF STEEL SCRAP MELTING

Modeling of scrap melting in EAF is an important but difficult task. Scrap melting consumes the majority of the energy with electricity consumption ranges from 330 to 750 kWh/metric ton. Process optimization on the scrap melting process using a CFD model would have significant impacts on the energy efficiency and operational efficiency. The scrap melting process modeling is a challenge mainly due to the fact that the scraps used in steel industry are in irregular shapes and not following the continuum descriptions in terms of the flowing properties. The scrap melting in a generic industrial EAF operation is complicated. The solid scrap in the furnace could be melted by the electric arc, oxy-fuel combustion flame, and liquid steel depends on the location.

In terms of the physics occurred during the EAF scrap melting process, it can be summarized in three different scenarios: melting above bath, melting in bath and combined melting process as shown in Figure 63. Some practices in EAF operation start with the melting above bath process, such as the low hot heel (hot heel is molten steel left from previous heat) practice. Some other practices start with the combined melting process when a large amount of hot heel is reused. Start with melting in bath practices are also applied in some industrial EAFs such as the Consteel EAFs. Nowadays, the majority of the EAFs are using the practices with only a small percentage of furnace capacity as a hot heel. Therefore, the generic scrap melting process starts from melting above bath and gradually steps into the combined melting process and finally ends with melting in bath. During the electrodes bore-in period in the scrap melting above bath stage, the electric arc melts the scrap around of it. It is estimated that about 15 percent of the scrap was melted during this bore-in process. The melted liquid steel mostly will be solidified during the dripping process due to the low temperature of steel scrap beneath it. It is quite challenging to model this process due to the dynamic movements and complicated physics which consists of the electric arc, multi-mode heat transfer, multiphase flow and phase change. The combined melting process involves both scrap melting above bath and scrap melting in bath. The transition from scrap melting above bath to the combined melting process is also difficult to define and therefore it is difficult to model. For scrap melting in bath, the steel scraps immersed into the liquid steel bath and melted by the liquid steel through conduction and convection heat transfer, which is relatively easier to model. In this study, the numerical modeling process was performed for scrap melting in bath. During the course

of the study, a scrap melting above bath model is also under development for the purpose of simulating the entire melting process, which is not reported in this thesis.

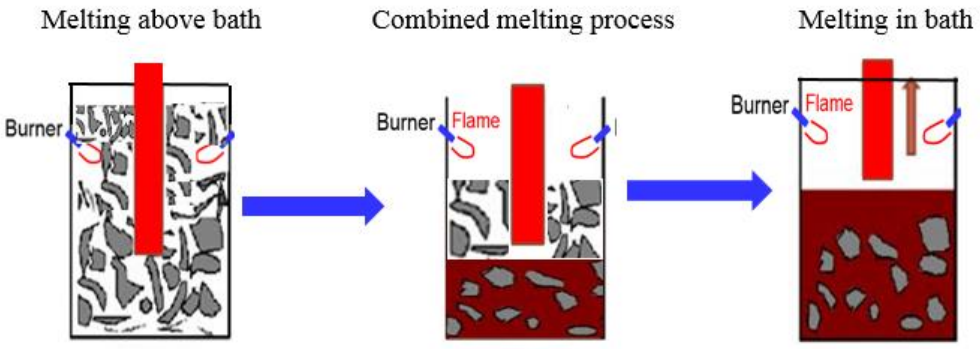

Figure 63. Scrap melting process in EAF.

5.1 Model Geometry

When the flat bath condition formed, the un-melted steel scrap will be immersed in the liquid steel bath. The melting process is through the conduction and convection heat transfer between liquid steel and the solid scrap. Meanwhile, the electric arc is supplying the heat. The top EAF freeboard starts the supersonic coherent jet to stir the steel bath. The combustion on the top freeboard also provides heat to prevent the heat loss through the slag to the furnace gas. In order to simplify the modeling process, the furnace geometry was divided into the top freeboard part and the bottom liquid bath part. In this case, the simulation of freeboard combustion and the liquid multiphase flow can be completed separately with data transfer between the two parts. Figure 64 shows the geometry of freeboard and liquid bath, which is separated by the gas/slag interface.

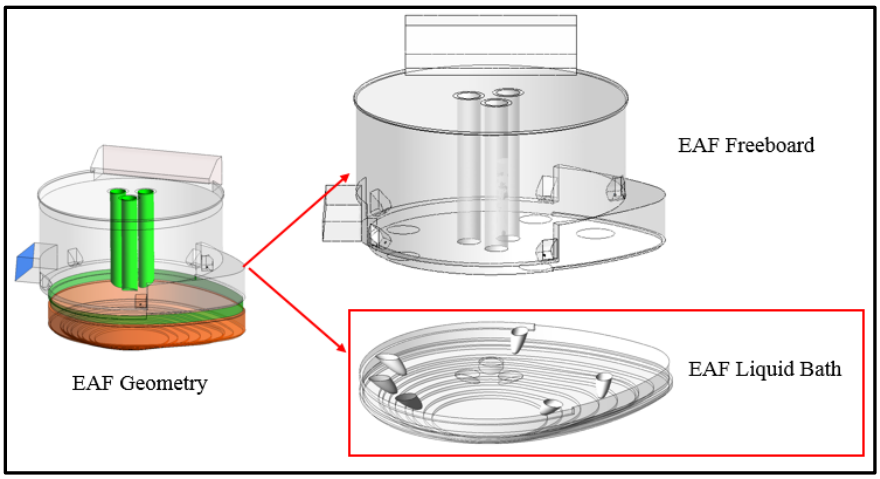

Figure 64. Scrap melting in bath geometry.

During the melting in bath stage, the supersonic coherent jet was used to stir the steel bath. The gas penetration depth can be calculated based on the oxygen jet flow rate. The stirring is also considered by defining the cavity shape and momentum transfer based on the approach used by Memoli et al. [128,129]

5.2 Simulation Conditions

Obtaining real operation condition for scrap melting in bath is difficult due to the challenges of tracking scrap locations and temperature. The current operating condition used for the scrap melting in bath modeling is partially determined based on engineering practice evaluations. The simulation conditions are listed in Table 15.

Table 15. Initial conditions for scrap melting in bath.

Parameters	Values
Density (kg/m^3)	7750
Viscosity (kg/m-s)	0.003
Total mass (kg)	160,000
Steel temperature (K)	1850
Scrap temperature (K)	1000
Electrodes heat flux (W/m^2)	2.9E7
Steel/slag interface temperature (K)	1900

5.3 Results and Discussions

It is difficult to obtain industrial measurements on the in-bath flow field and scrap size and temperature information during the operation. In order to provide accurate simulation results, the validation process has been conducted for each important sub-models along with parametric studies to provide useful knowledge for practices in many aspects. During the scrap melting in bath stage, the major phenomena need to be considered in the model are heat transfer the electric arc, forced convection from the coherent jet, multiphase flow in bath and scrap melting. The heat transfer from the electric arc is simplified using a heat flux as suggested by Arzpeyma et al. [45] The coherent jet model was developed to investigate the effects of various oxygen and fuel input during this stage. The scrap melting in bath model was developed to calculate the multiphase flow and the melting process of steel scraps.

5.3.1 Scrap Melting in Bath

The developed scrap melting sub-model was first validated by comparing the simulation results with experimental data from literature [130]. Li et al. [130] developed an experimental apparatus including a preheating furnace and an induction furnace as shown in Figure 65. In the experiment, a cold or a preheated steel bar was put into the molten steel bath for a certain time and then pulled out and quenched to measure the diameter. The steel bar melting process was investigated by measuring the diameter change along with the time. The steel bar melting profile and melting time can be determined under various conditions. Single-bar, two-bar and multi-bar arrangements were investigated. The purpose of the experiment is to identify correlations between the melting time and operation parameters such as scrap (steel bar represents scrap) size, temperature, and porosity. The computational geometry used for numerical simulation was developed based on the experimental setup as shown in Figure 65. More details about the experimental conditions can be found in the literature [130].

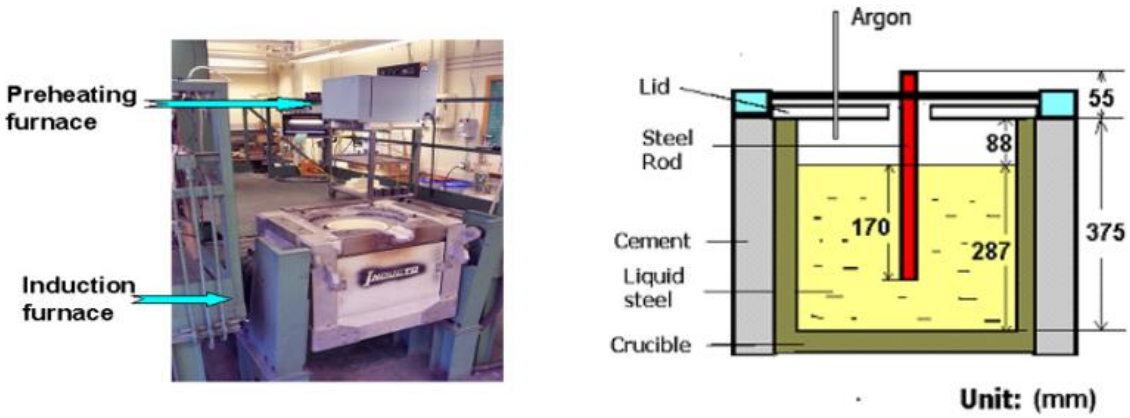

Figure 65. Experimental setup [130].

5.3.1.1 Model Geometry

The simulation domain was developed based on the experimental setup including the induction furnace and the steel bar. The detailed dimensions and the steel bar position are shown in Figure 66. The single steel bar is placed at the center of the induction furnace with 170 mm length into the molten steel.

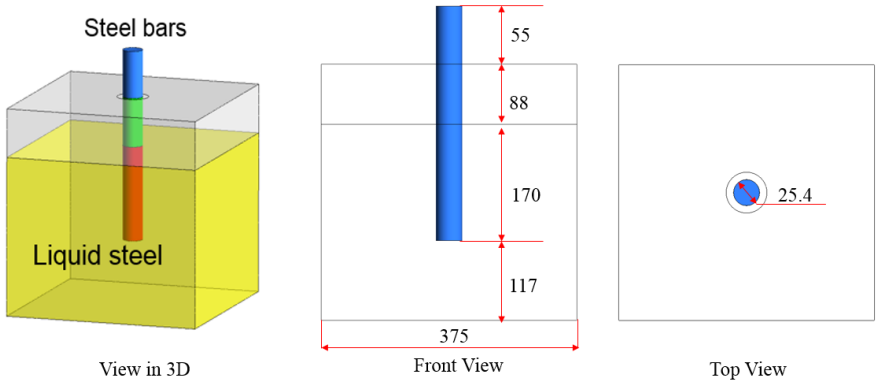

Figure 66. Computational domain (Unit: mm).

5.3.1.2 Simulation Conditions

The used steel bar and liquid steel in the experiment have the same thermal properties. The 1018 low carbon steel was used and the material properties including thermal properties are shown in Table 16 and Figure 67.

Table 16. Material Properties of 1018 low carbon steel [131].

Properties	Values
Density (kg/m^3)	7750
Viscosity (kg/m-s)	0.003
Latent heat (J/kg)	272000
Solidus temperature (K)	1600
Liquidus temperature (K)	1793

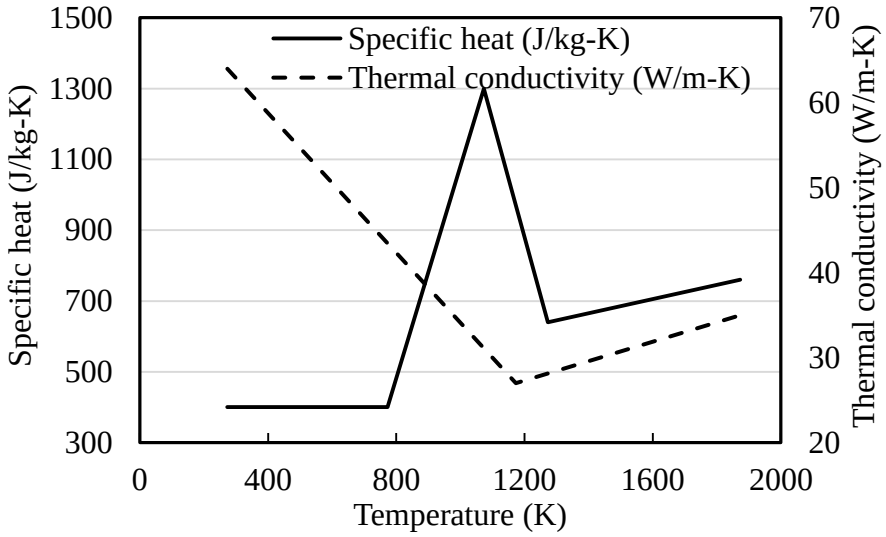

Figure 67. Thermal properties of 1018 low carbon steel [131].

The induction furnace wall was treated as an adiabatic wall which is made of refractory. The top outlet was set as a pressure outlet with normal pressure and temperature. The initial temperature of the molten steel bath and steel bar are 1913K and 298K, respectively.

5.3.1.3 Simulation Results

Mesh independence study is performed to reduce the influence of the number of grids on the computational results. For a more accurate solution, a finer mesh size is preferred. But in general, the finer mesh is more computationally expensive. Mesh independence study was conducted by comparing two different mesh sizes. In this simulation, the structured mesh was used. Two different meshes were created with 1 million and 2 million cells. Mesh refinement was used at the

interface between the gas and liquid steel phase for both meshes. The initial temperature of the melting bar was set at 1073K to save computational time. The single steel bar melting process predicted using the two meshes are shown in Figure 68.

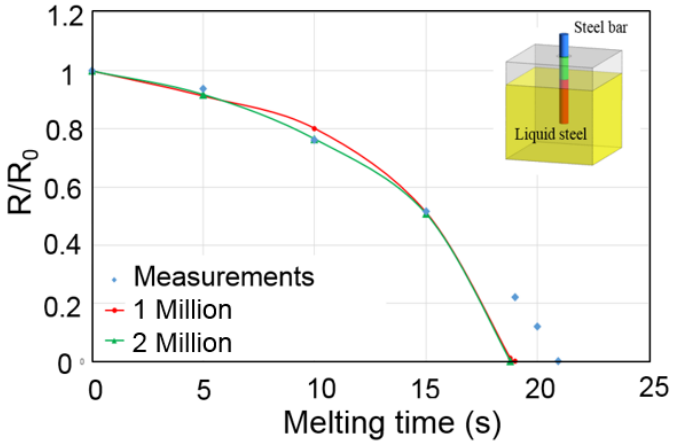

Figure 68. Mesh independence study.

According to Figure. 68, the melting time using the two different mesh are approximately 19 seconds, which shows a good agreement with the experiment. By analyzing the melting curves, the results of the two different mesh are very similar. Therefore, the mesh with 1 million cells is used to conduct the numerical simulation with reduced computation time.

Firstly, the one single steel bar melting process was investigated. The single steel bar is in a cylindrical shape with a diameter of 25.4 mm. The initial temperature of the molten steel bath and steel bar are 1913K and 298K, respectively. The liquid fraction contours of the steel bar with respect to time during the melting process is shown in Figure 69.

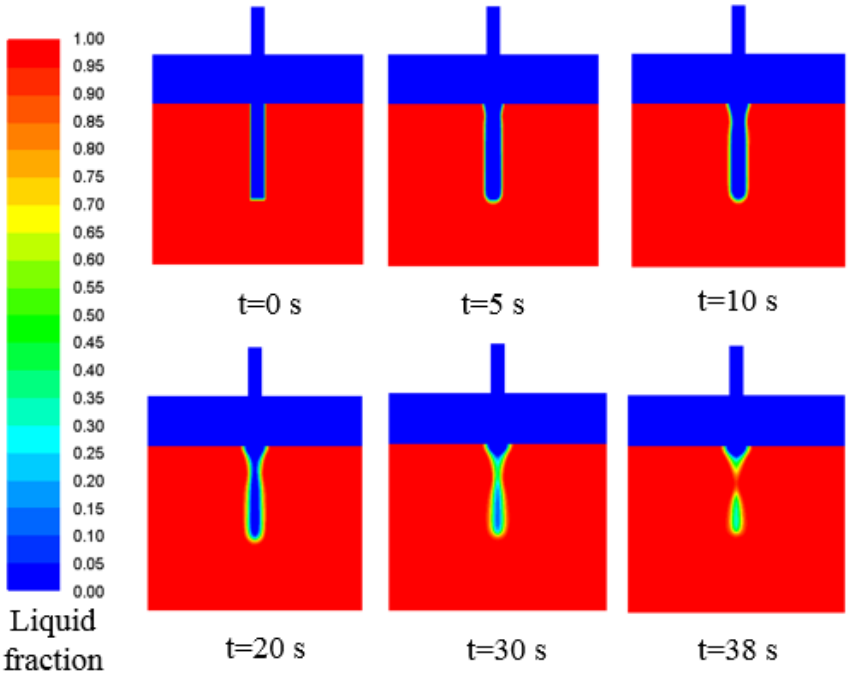

Figure 69. Steel bar liquid fraction with respect to time.

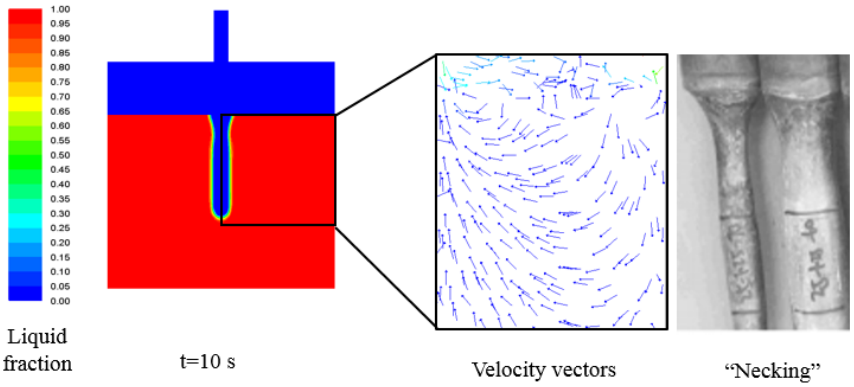

Figure 70. Effects of natural convection on melting shape.

As shown in Figure 69, the low-temperature steel bar in the high-temperature molten steel will first solidify the surrounded molten steel and form a solid shell. Once the solidified shell melted, the steel bar is gradually melted by the high-temperature molten steel. In the beginning, the heat transfer between the cold steel bar and the molten steel decreases the molten steel temperature around the cold steel bar to the level that below the solidification point. With the increase of the cold steel bar temperature, the temperature of the solidified steel shell around the cold steel bar also gradually increases. When the steel shell temperature exceeds the material liquidus temperature, the steel bar starts melting in the molten steel bath. In this simulation, the formed

solid steel shell around the cold (298 K) steel bar starts to melt after about 10s and finished melting process around the 20s. After the 20s, the steel bar gradually melts with a necking effect due to the natural convection created by the temperature difference. A “necking” phenomena were observed during the single steel bar melting process in experiment as shown in Figure 70. The “Necking” phenomena are caused by natural convection due to the temperature difference. The validation of the single bar melting process is shown in Figure 71. Overall, the comparisons between the simulation results and experimental measurements are in good agreement with an 8% average error. Therefore, the CFD model using the enthalpy-porosity method and the VOF approach is appropriate in modeling the steel bar melting process in a multiphase system. This modeling approach will be extended and applied to predict the scrap melting in bath process in the EAF.

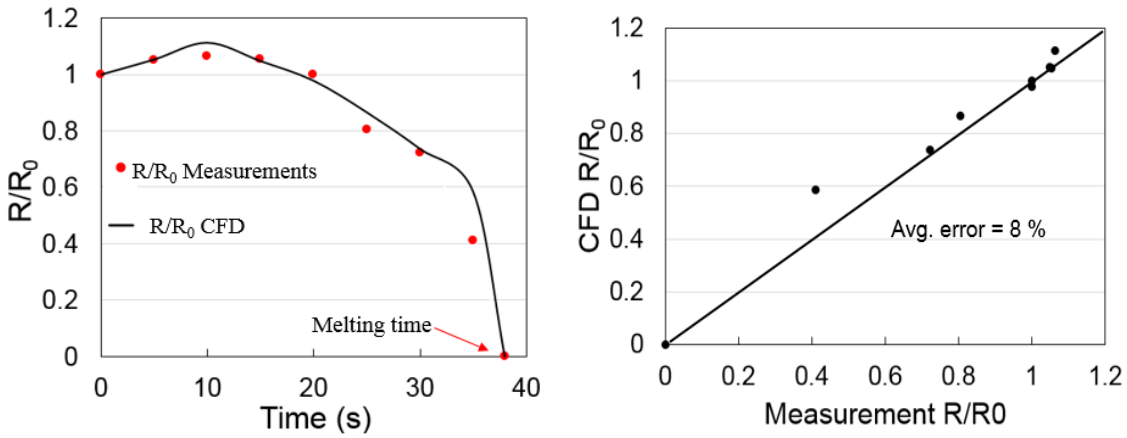

(a) Melting process (b) CFD vs. Exp.

Figure 71. Steel bar melting process and validation.

5.3.1.4 Parametric Studies

Effects of preheating temperature

Steel scrap melting in bath process involves a wide range of steel scrap temperature. For the steel scraps have already preheated by either the electric arc or combustion gases will have a high temperature before being immersed into a steel bath. However, for scraps away from the electric arc and combustion gases will have a low temperature. In general, higher scrap temperature will reduce the melting time and shorten the process time. The occurrence of incidence like un-melted

scrap during furnace tapping is annoying to operators, which also affects the steel compositions and operation efficiency.

Numerical simulation was performed to investigate the effects of initial bar temperature on the melting process. Figure 72 demonstrates the steel bar melting process with three different steel bar initial temperature: 298K, 673K and 1073K. The change of the steel bar diameter at the middle section of the immersed part was used to demonstrate the melting process, which was defined by the ratio of the steel bar diameter to the original steel bar diameter with respect to time.

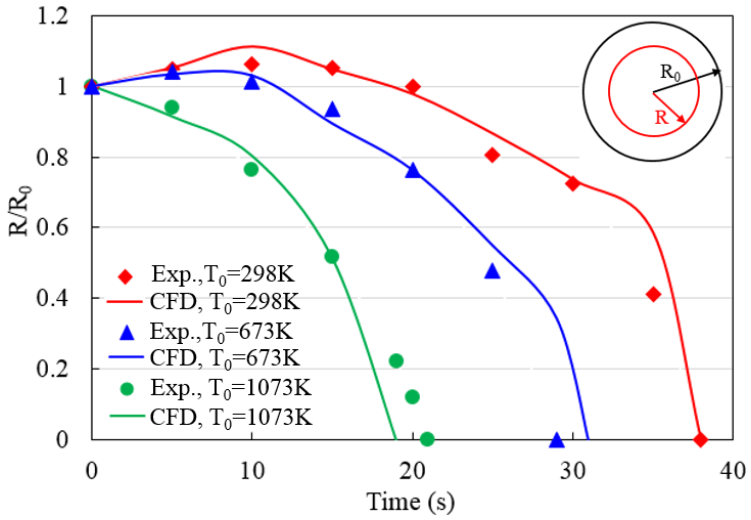

Figure 72. Single steel bar melting process under different initial temperature.

Figure 72 indicates that when the initial temperature of the steel bar was 298K, a solidified steel shell was formed and the thickness of the shell increased and reached its highest value at approximately 10s. After about 19s, the steel bar started melting. The melting of the bar completed at approximately 37s. When the initial temperature of the steel bar increased to 673K, the thickness of the formed steel shell decreased. The steel bar started melting at about 13s and completed at 32s. When the initial temperature of the steel bar further increased to 1073K, no steel shell was formed. Instead, the steel bar directly melted by the molten steel and completed the melting process at 19s. It can be seen from the simulation results that the steel bar initial temperature has a significant effects on the steel bar melting in bath process. The higher the initial scrap temperature,

the shorter melting time in general. The experimental results were plotted using discrete points. Overall, the simulation results show a good agreement with the experiment.

Effects of spacing between two steel bars

As indicated by the single bar melting simulation, the solidification process during the melting caused by the low initial temperature will reduce the melting efficiency. If multiple bars or scraps stay close with low initial temperature would potentially form a big piece of scrap, which is difficult to be melted. When there are two steel bars melting together in a high-temperature molten steel bath, the spacing between the bars affects the melting process and determines the complete melting time. The numerical simulation of the melting process was conducted under different spacing and different initial temperature of the bars. The computational domain is modified slightly with two steel bars in the domain as shown in Figure 73. Six different scenarios are investigated in terms of the spacing between two steel bars: 1.27 mm, 2.54 mm, 3.81 mm, 5.08 mm and 6.35 mm. For each spacing condition, the effect of the steel bar temperature is also investigated as shown in Figure 74.

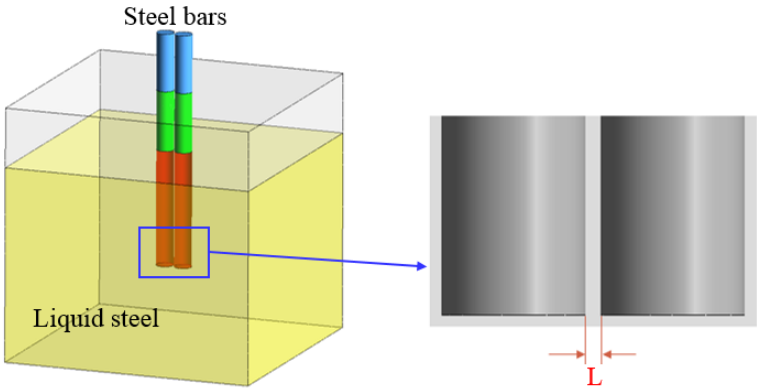

Figure 73. Computational domain for two steel bar melting simulation.

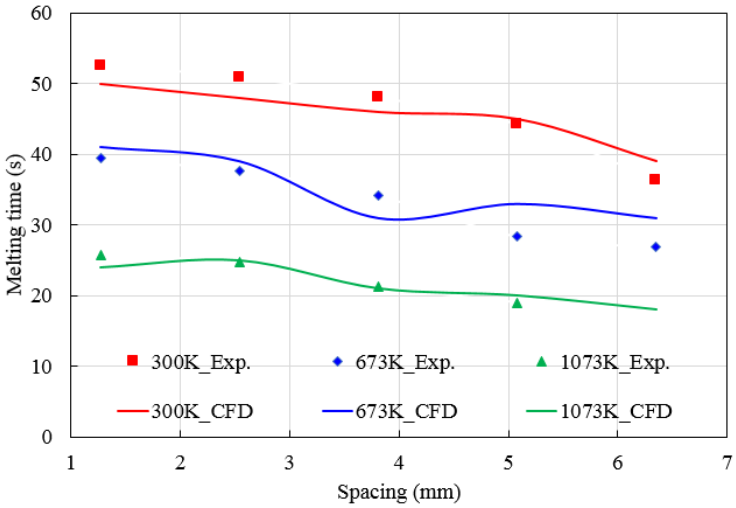

Figure 74. Effects of spacing on two steel bar melting process.

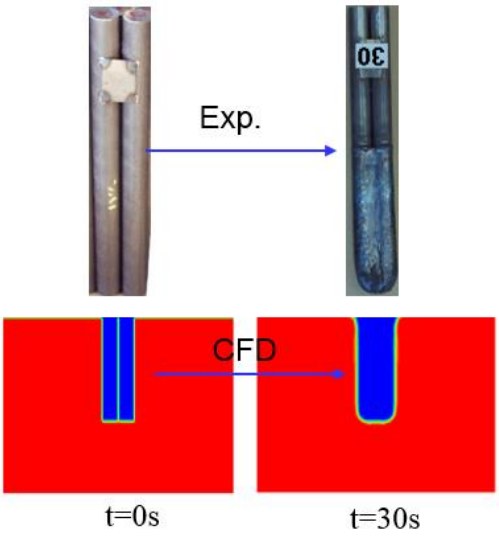

Figure 75. Steel iceberg phenomena during two steel bar melting (1.27 mm spacing).

Figure 74 indicates that with the increase of the steel bar spacing, the melting time of the two steel bar decreased. When the spacing between the two steel bar is larger than 6 mm, the melting time is close to the single bar cases, which indicates that the melting of each steel bar is completed independently. However, when the spacing is 1.27 mm, the melting time is approximately 50 seconds, which is longer than the single bar melting time. It can be seen that during the two steel bar melting process, the formation of the iceberg when the spacing is small will affect the melting time as shown in Figure 75. When the spacing is small, the iceberg formed and the two steel bars began melting together as one bar in a larger effective diameter. In addition, the melting time

decreases with the increase of the initial temperature of the steel bar. Overall, the Root Mean Squared Error (RMSE) between the simulation results and the measurements is 0.065, which indicates a good agreement between simulation and experiment.

Both the one steel bar melting and two steel bar melting simulations provide a basic understanding on the heat transfer and melting process. However, it is difficult to give guidance to real EAF operation since the scrap pieces located in the liquid steel bath has very complicated geometry and spacing. The multiple pieces of the steel scraps in the EAF bath formed complicated solid-liquid interphase like a porous medium. The porosity of the scrap will affect its melting process. Therefore, a multiple steel bar melting process was conducted to study the effects of porosity on the melting process. The computational domain for multiple steel bar melting process is shown in Figure 76.

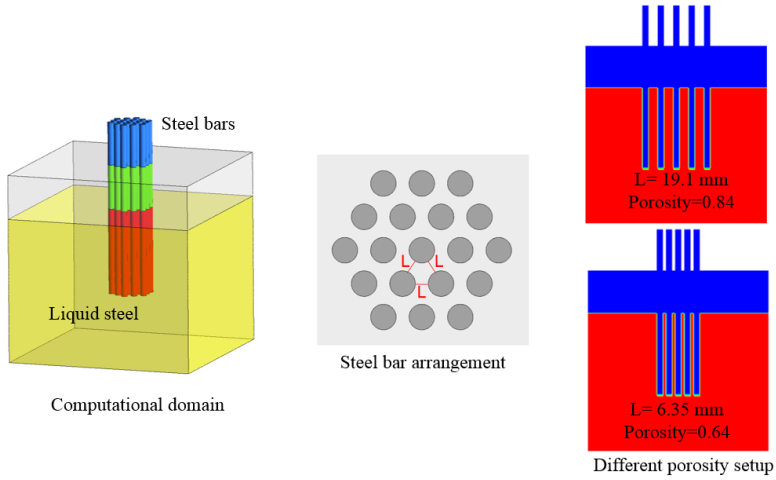

Figure 76. Computational domain for multiple steel bar melting.

Totally 19 steel bars were used to develop the computational domain for the multiples steel bar melting process. The single steel bar diameter is 12.7 mm. Based on the different spacing, the corresponding porosity can be calculated. The effect of porosity on the steel bar melting process is shown in Figure 77.

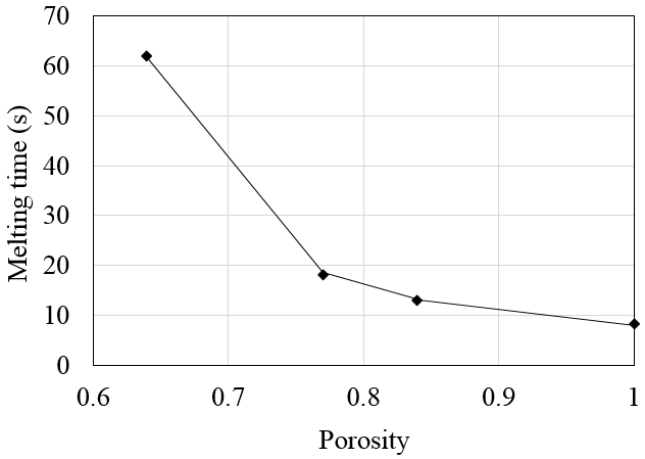

Figure 77. Effects of porosity on steel bar melting in bath.

According to Figure 77, the porosity has a significant effect on the multiple bar melting time. The melting time reduces significantly when the porosity increases from 0.64 to 0.77. Similar to the two steel bar melting process, when the porosity is low, the steel bars tend to agglomerate and formed a large steel chunk. Therefore, design appropriate charging profile for different types of scraps to avoid low scrap porosity (<0.77) is recommended.

In summary, A CFD model for steel melting in multiphase flow system was developed. The CFD model uses the enthalpy-porosity method and the VOF method can describe the important phenomena during the scrap melting in bath process. The overall validation shows that the CFD predictions agrees with the experimental measurements on both melting time and steel bar diameters. The results also indicate that,

1. Increase the steel initial temperature will reduce the formed shell thickness and increase the melting efficiency
2. The small spacing between steel bars or steel scraps will increase the melting time due to steel iceberg phenomena.
3. Increase steel scrap porosity to larger than 0.77 in bath to avoid significant agglomeration is suggested.

5.3.2 Coherent Jet Simulation

Coherent jet is widely used in industrial EAFs to increase the depth of oxygen jet penetration for better oxygen efficiency and stirring of the liquid steel. A coherent jet is defined when the

supersonic jet is shrouded by a flame envelope, which leads to a higher potential core length (the length up to which the axial jet velocity equals the exit velocity at the nozzle) as shown in Figure 78. The axial velocity of a conventional supersonic jet exits the converging-diverging nozzle will remain its initial velocity for a certain distance and then decrease quickly due to the gas entrainment. The coherent jet is designed to reduce or delay the gas entrainment so that the potential core length can be extended longer. The oxy-fuel burner provides the coherent jet in EAF, fuel and secondary oxygen ports are designed and arranged around the converging-diverging nozzle as shown in Figure 79. The formed combustion flame has two functions to help extend the jet length, one is decreasing the turbulence mixing, and the other is decreasing the gas entrainment due to the low density caused by the high temperature.

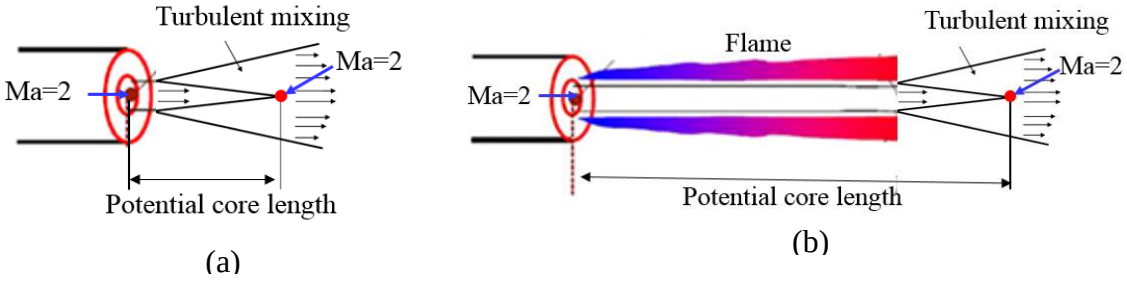

Figure 78. Jet flow mechanisms, (a) Supersonic jet, (b) Coherent jet.

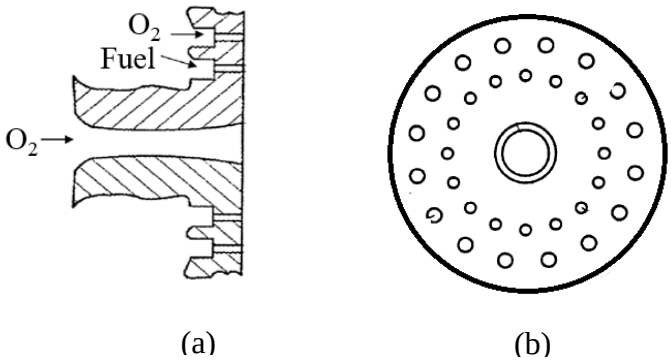

Figure 79. A coherent jet design [81].

The coherent jet acts as the main stirring power during the steel refining stage. Oxy-fuel burner operating conditions are changing depends on the amount of oxygen required during the refining stage. In order to accurately define boundary conditions for the scrap melting in bath simulation,

a coherent jet model is developed to investigate the jet velocities under various operating conditions.

5.3.2.1 Model Geometry

The computational geometry is shown in Figure 80. The burner configuration is developed based on the burner configuration used by Anderson et al. [81] In their experiment. The geometric model is a cylindrically shaped vessel that starts from the exit of the converging-diverging nozzle where the converging-diverging nozzle geometry is neglected. The geometric model uses a diameter of 40 De (De is the supersonic jet exit diameter) and 105 De in length. The coherent jet burner tip consists of totally 33 ports, including three different types of gas injection ports: one primary oxygen inlet, 16 fuel inlets, and 16 secondary oxygen inlets.

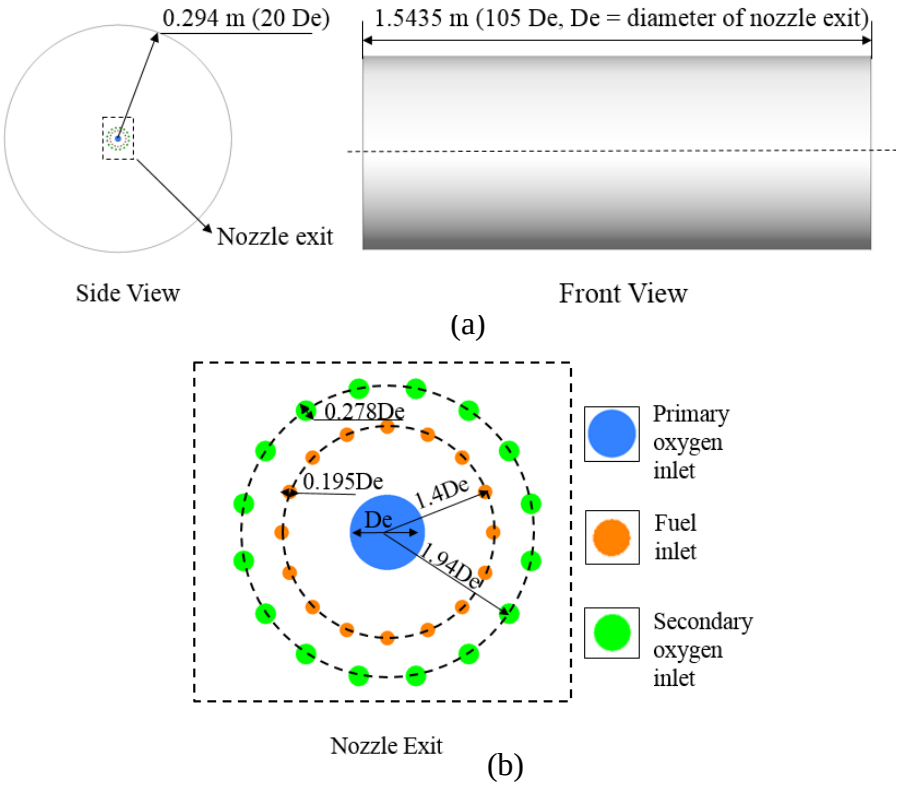

Figure 80. Coherent jet simulation geometry details, (a) Front and side view, (b) Nozzle exit.

5.3.2.2 Simulation Conditions

The primary oxygen jet inlet supplies the supersonic oxygen jet to stir the steel bath, while the fuel and secondary oxygen inlets are used to form combustion envelopes to shroud the supersonic jet for increasing the coherent jet potential core length. More information about the boundary conditions can be found in Table 17.

Table 17. Boundary conditions for the coherent jet simulation.

Name of Boundary	Boundary conditions	Values
Primary oxygen inlet (Pressure inlet)	Stagnation pressure	929,000 Pa
	Mach number	2.1
	Total temperature	294 K
	Oxygen mass fraction	100%
Fuel inlet (Mass flow inlet)	Mass flow rate	0.006383 kg/s
	CH_4 mass fraction	100%
	Static temperature	288.6 K
Secondary oxygen inlet (Mass flow rate)	Mass flow rate	0.01277 kg/s
	Oxygen mass fraction	100%
Wall	No slip, fixed temperature	298K
Outlet (Pressure outlet)	Static pressure	101,325 Pa

5.3.2.3 Simulation Results

Mesh independence study

A mesh independence study was conducted to avoid the numerical error introduced by the grids. Three different grid levels: coarse grid (1.2 million cells), medium grid (1.9 million cells) and fine grid (2.37 million cells) are used. The axial velocity profiles for all three grids levels are plotted as shown in Figure 81. It can be seen that compared to the fine grid, the coarse grid under-predicts the coherent jet axial velocity profile, while the medium grid closely predicts results. The variation between the medium grid and the fine grid is within approximately 1%, which is negligible. In this study, the medium grid is adopted for numerical simulations.

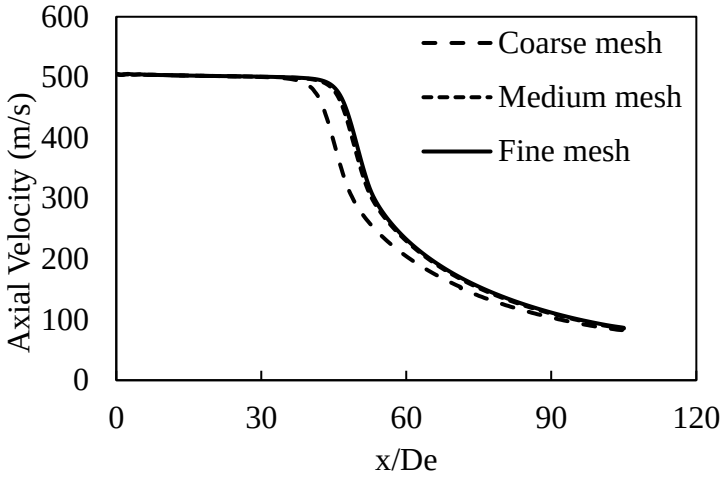

Figure 81. Grids independence study.

Model validation

The experiment conducted by Anderson et al. [81] is used to validate the developed coherent jet CFD model. Numerical simulations of the coherent jet with given experimental conditions of both with combustion flame shroud and without combustion flame shroud were conducted. The comparisons of the coherent oxygen jet axial flow velocity between the CFD model prediction and the experimental measurements are shown in Figure 82.

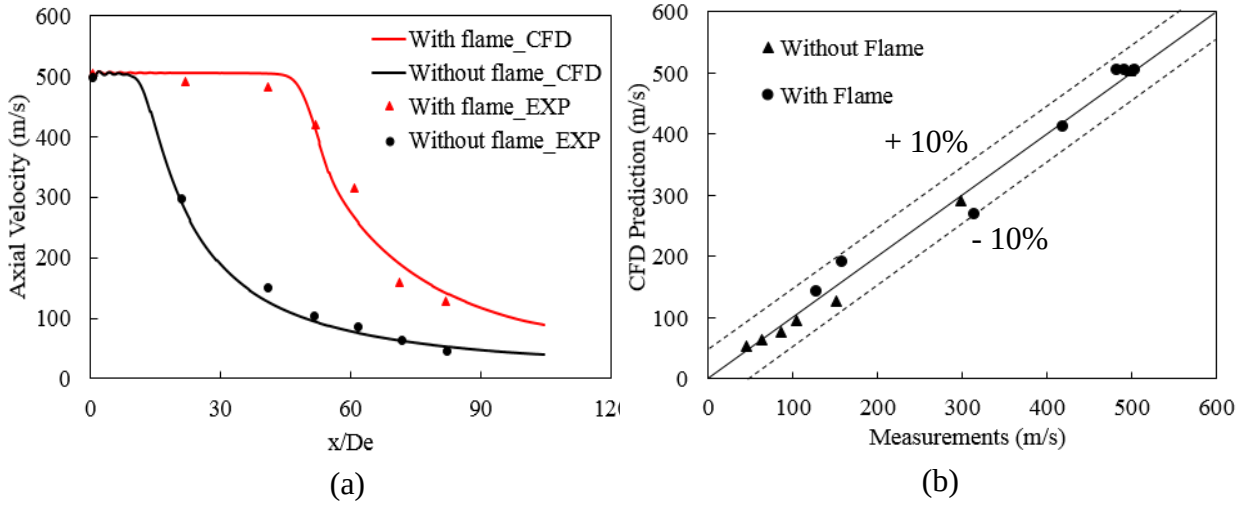

Figure 82. Axial velocity profile along the jet axis with and without flame, (a) Comparison, (b) Parity plot.

As shown in Figure 82 (a), the axial velocity profiles are plotted under two simulation conditions: with and without combustion flame shroud. At the conditions of without combustion flame shroud, the oxygen jet is a conventional supersonic jet, which remains at its initial velocity (from the nozzle exit) on the axis for approximately 12 De and then the axial velocity gradually reduces to subsonic. Compared to the measurements indicated by the points plotted in Figure 82 (a), the CFD model prediction shows a good agreement with experiment for all seven measurement points; the average percentage error calculated is 7.7%. With flame shroud, the Mach 2.1 high-velocity jet can maintain its initial velocity for a longer distance than the jet without the flame shroud. Due to the effects of combustion, the air entrainment is blocked by the combustion flame. When the flame was introduced and shrouded the supersonic oxygen jet, the coherent jet length (the length up to which the axial jet velocity equals the 92% of exit velocity at the nozzle) extended to approximately 47 De. As shown in Figure 82 (a), the axial velocity profiles correspond well to all seven measurement points. Compared to the measurements, the average difference is 8.1%. There is no significant expansion shockwave noticed in this simulation, due to the assumption that the converging-diverging geometry is neglected while the boundary conditions were calculated at the nozzle exit. For simulations including the converging-diverging nozzle geometry, an expansion shockwave will be noticed. [85,86] However, based on the coherent jet design, the energy loss due to the expansion/compression shockwave can be neglected. Therefore, the validation shows that the CFD predictions are in good agreement with the measurements.

Due to the limited measurement data on coherent jet axial temperature profile, further validation was conducted on conventional supersonic oxygen jet. In the experiment conducted by Sumi et al. [132], a combustion furnace was built to provide high-temperature field. Both the axial velocity and the axial temperature for a conventional supersonic oxygen jet were measured under three different ambient temperature conditions: 285K, 772K, and 1002K. The coherent jet and the supersonic jet under higher ambient temperature share a similar physics, which is a supersonic gas jet shrouded by high ambient temperature gases. Therefore, the coherent jet model should be able to predict the supersonic gas jets into higher ambient temperature conditions. In this further validation, numerical simulations were conducted for each ambient temperature condition to compare the CFD model prediction and the measurements.

The computational domain used for this study is shown in Figure 83. The nozzle configuration is the same as the one used by Sumi et al. [132] in their experiment. The converging-diverging nozzle supplies the supersonic oxygen jet. The geometry starts from the exit of the converging-diverging nozzle where the converging-diverging nozzle geometry is neglected. More information about the boundary conditions can be found in Table 18. The computational domain is axisymmetric. Therefore, a two-dimensional computational grid was used. The boundary conditions at the converging-diverging nozzle exit are calculated using the isentropic flow theory. In Sumi et al.'s experiment, the ambient temperature was controlled using combustion to study the effects of ambient temperature on the supersonic jet axial velocity profiles. The ambient gas compositions are different at different temperature conditions. Table 19 lists the ambient gas compositions which are used in the current study. The comparison of the supersonic oxygen jet axial flow velocity between the simulation and the experimental measurements is shown in Figure 84. The static temperature at different locations along the jet axis is also compared between CFD prediction and experimental measurements as shown in Figure 85.

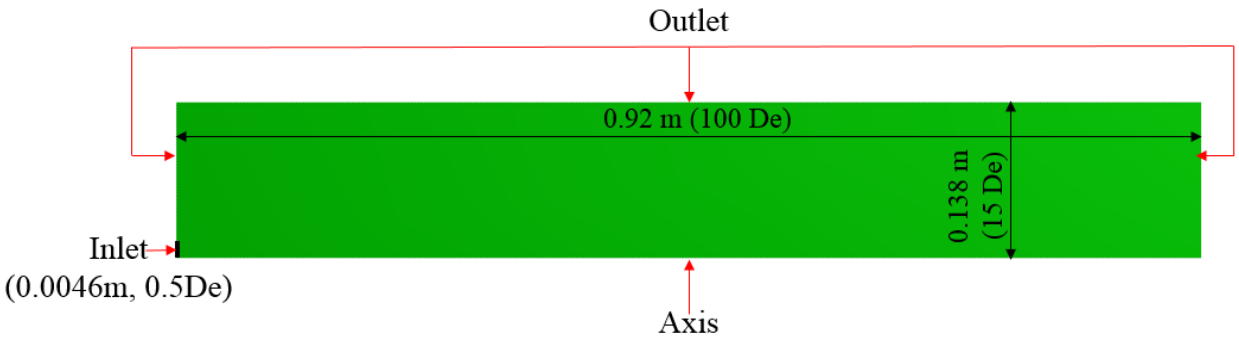

Figure 83. Computational domain.

Table 18. Boundary conditions.

Name of Boundary	Boundary conditions	Values
Inlet (Pressure inlet)	Stagnation pressure	497,695 Pa
	Mach number	1.72
	Total temperature	285 K
	Oxygen mass fraction	100%
Outlet (Pressure outlet)	Static pressure	100,000 Pa

Table 19. Ambient gas compositions.

Ambient T(K)	O_2 (%)	N_2 (%)	CO_2 (%)
285	54	46	0
772	85	9	6
1002	88	3	9

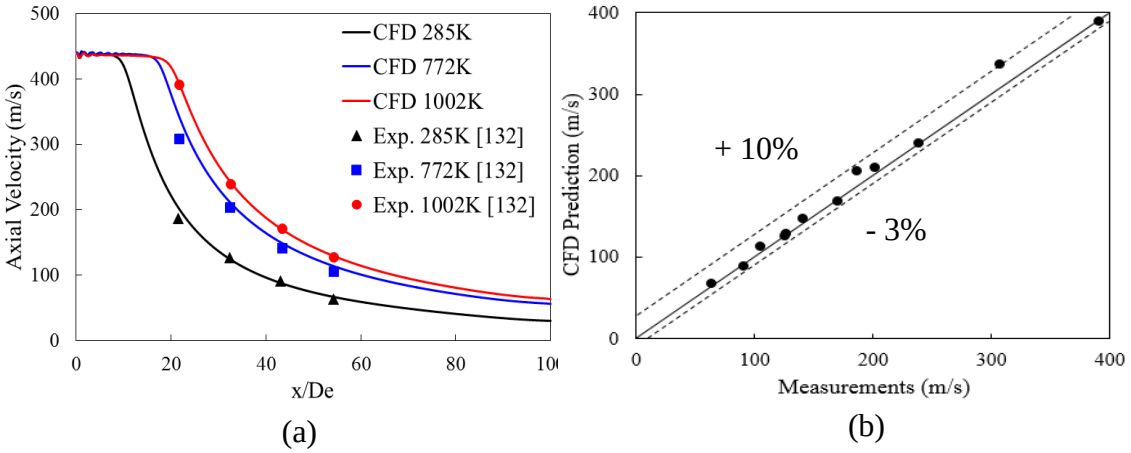

Figure 84. Axial velocity profile along the jet axis with different ambient temperature, (a) Comparison, (b) Parity plot.

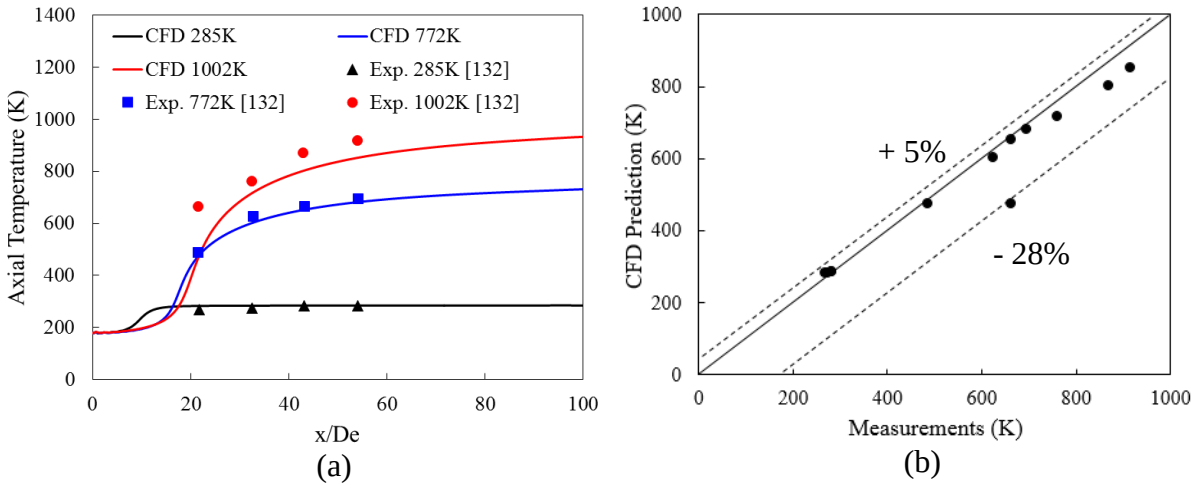

Figure 85. Axial static temperature profile along the jet axis with different ambient temperature, (a) Comparison, (b) Parity plot.

According to Figure 84, the supersonic oxygen jet velocity at the converging-diverging nozzle exit is approximately 451 m/s. The measurements indicate that with the increase of ambient temperature, the supersonic oxygen jet axial velocity remains at its initial velocity for a longer distance. The following factors contribute to this phenomenon: (a) a higher ambient gas

temperature equates to a lower ambient gas density, so that the gas entrainment in the turbulence mixing region is reduced; (b) the temperature effects will reduce the turbulence viscosity and therefore will reduce gas entrainment and increase the jet potential core length; (c) the higher ambient temperature will increase the turbulence kinetic energy in the shear layer. The comparisons of supersonic oxygen jet axial velocity profiles between CFD model prediction and measurements show good agreement on all the measurement data points as shown in Figure 84 (a). The error between the CFD model prediction and the measurements is within 10% as shown in Figure 84 (b). The average error between CFD and measurements is 3.12%. Similar comparisons on the supersonic oxygen jet axial temperature profiles were also conducted. The CFD model predictions on the supersonic oxygen jet axial temperature at 285 K and 772 K ambient temperature conditions show good agreement with the experimental measurements as shown in Figure 85 (a). However, the CFD-model-predicted supersonic oxygen jet axial temperature under 1002 K ambient temperature condition has larger discrepancies compared to measurements. The maximum difference is 28% for only one point as shown in Figure 85 (b). The average error between CFD and measurements is 5.63%. The overall comparisons show that the CFD model predictions have a good agreement with the experiment.

Empirical models were reported in the literature regarding the relationship between the axial velocity profile or potential core length and ambient conditions. Ito and Muchi [133] proposed an empirical model to calculate the jet axial velocity change with the ambient and location as written in Equation (98). When the U_m equals 1, the formula for the length of the potential core length is shown in Equation (99). Allenmand et al. [134] also proposed an empirical equation for calculating the jet potential core length at different ambient conditions as written in Equation (100). The supersonic oxygen jet axial velocity profile predicted by the CFD model was compared with the empirical model used by Sumi et al. [132] which was proposed by Ito and Muchi [133]. In the empirical model (Equation (98)), the value of constants α and β are calculated as 0.0841 and 0.6035 by Sumi et al. [132], respectively. The empirical equation builds a relationship between the jet velocity and the ambient conditions. The U_m is the normalized velocity by the jet exit velocity U_e, ρ_e is the exit density which can be calculated using isentropic theory, while $\rho_a$is the ambient gas density which is determined by the ambient gas compositions and temperature. The term x/D_e indicates the location of the jet. Theoretically, with the constant value of α and β, the U_m has a

fixed relationship with $\sqrt{\frac{\rho_e}{\rho_a}}\frac{x}{D_e}$. Figure 86 shows the plot of jet velocity field as a function of jet location and ambient properties ($\sqrt{\frac{\rho_e}{\rho_a}}\frac{x}{D_e}$).

$$-\frac{1}{2\ln(1-U_m)} = \alpha\sqrt{\frac{\rho_e}{\rho_a}}\frac{x}{D_e} - \beta\ ;\ (U_m = \frac{U}{U_e}) \tag{98}$$

$$\frac{x}{D_e} = \frac{(\beta/\alpha)}{\sqrt{\frac{\rho_e}{\rho_a}}} \tag{99}$$

$$\frac{x}{D_e} = \sqrt{\frac{\rho_e}{\rho_a}}[4.2 + 1.1\left(M_e^2 + 1 - \frac{T_e}{T_a}\right)] \tag{100}$$

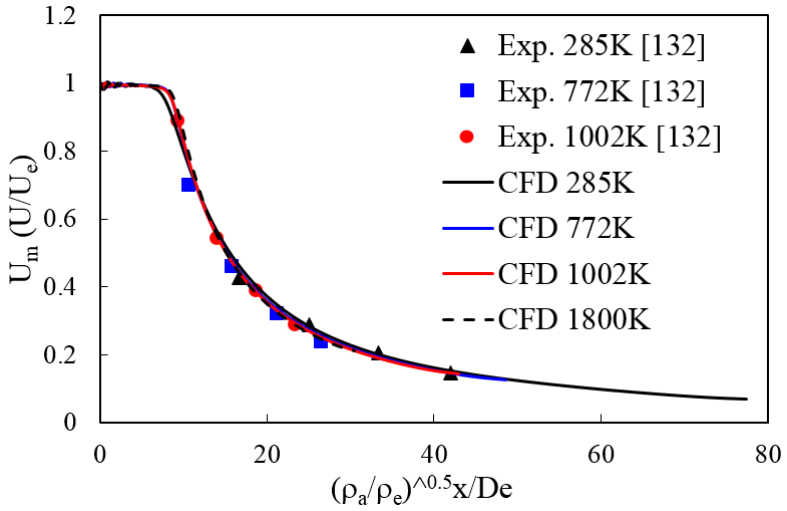

Figure 86. Normalized velocity profile along jet axis under different ambient temperature conditions.

According to Figure 86, both experimental measurements by Sumi et al. and numerical simulation results of three different ambient temperature conditions, 285 K, 772 K, and 1002 K, align very closely. An extra simulation of the supersonic jet at 1800 K ambient temperature condition was conducted and plotted in Figure 86, which also lines closely with the other temperature conditions. It indicates that the empirical model can predict the supersonic oxygen jet axial velocity profiles under different ambient temperature conditions. It also helps validate the developed CFD model

and suggests that both the CFD model and the empirical model can be used to predict supersonic jet characteristics at high ambient temperature.

The supersonic oxygen jet potential core length calculated from the CFD model and the two different empirical models under four different ambient temperature conditions, 285 K, 772 K, 1002 K, and 1800 K, are plotted in Figure 87. The detailed values and comparisons are listed in Table 20.

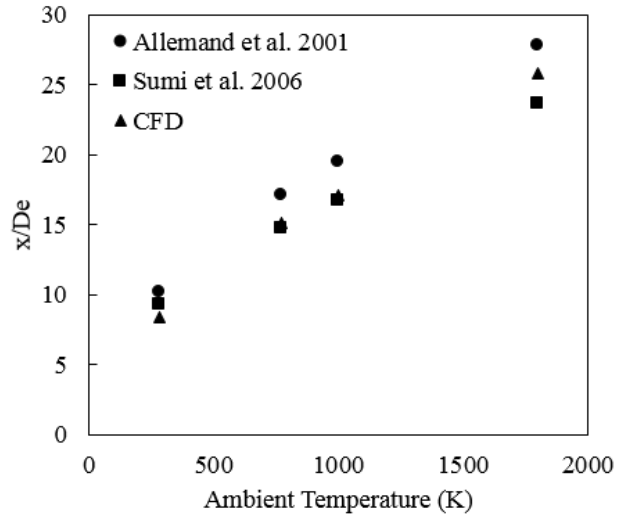

Figure 87. Comparisons of supersonic oxygen jet potential core length at different ambient temperatures using CFD and other empirical models.

Table 20. Supersonic oxygen jet potential core length using different models.

Ambient Temperature (K)	x/De (Allenmand et al. 2001)	x/De (Sumi et al. 2006)	CFD	% difference compared to Allenmand et al. 2001	% difference compared to Sumi et al. 2006
285	10.16	9.28	8.41	17.22	9.37
772	17.06	14.75	15.08	11.60	2.23
1002	19.43	16.69	17.07	12.15	2.28
1800	27.77	23.6	25.79	7.13	5.79

According to Figure 87, the supersonic oxygen jet potential core length increases with the ambient temperature. Generally, the jet potential core length predicted by the empirical model used by Sumi et al. [132] is smaller than the prediction by the empirical model of Allemand et al. [134] The CFD

predictions in this study are closer to the empirical model used by Sumi et al. [132] Table 20 shows the comparisons of jet potential core length predicted by the CFD model and the empirical models. The percentage of difference shows that the maximum percentage difference is less than 10% compared to Sumi et al. [132], while it is less than 20% compared to Allemand et al. [134]

Coherent jet properties

Based on the validated coherent jet model, the flow properties of the coherent jet were studied. The temperature and velocity distributions for the simulated coherent jet are shown in Figure 88. The gas density and flow Mach number are shown in Figure 89. The coherent jet species mass fraction distributions are shown in Figure 90. The detailed flame profile predicted using the EDC combustion model with the 28-step methane-oxygen combustion reaction mechanism is shown in Figure 91.

According to Figure 88, the shroud fuel and oxygen form a combustion flame around the supersonic jet. The combustion flame provides high-temperature gas flow which travels along with the supersonic jet. Heat transfer occurs between the hot gas generated from combustion and the relatively colder supersonic jet (T_t=294K). In the high-temperature combustion flame region, the turbulence viscosity is small and thus the gas entrainment by the supersonic jet is reduced. Heat transfer between the supersonic jet and combustion gas is also weak. However, away from the combustion flame, the supersonic gas jet entrainment enhances the heat transfer between the supersonic jet and the combustion gases. Eventually, the high-temperature combustion gas and the supersonic gas jet merge into one stream of high temperature flow. Due to the surrounding high-temperature combustion gases, the supersonic gas jet remains at its exit velocity for a long distance and then dissipates as shown in Figure 88 (b). The compressed gas density in the coherent jet potential core length region reached approximately 2.5 kg/m, while the gas density around the supersonic jet is very low due to the high combustion temperature as shown in Figure 89 (a). In correlation with the supersonic jet velocity, the supersonic jet Mach number remains 2.1 for a certain distance and then is gradually reduced to subsonic.

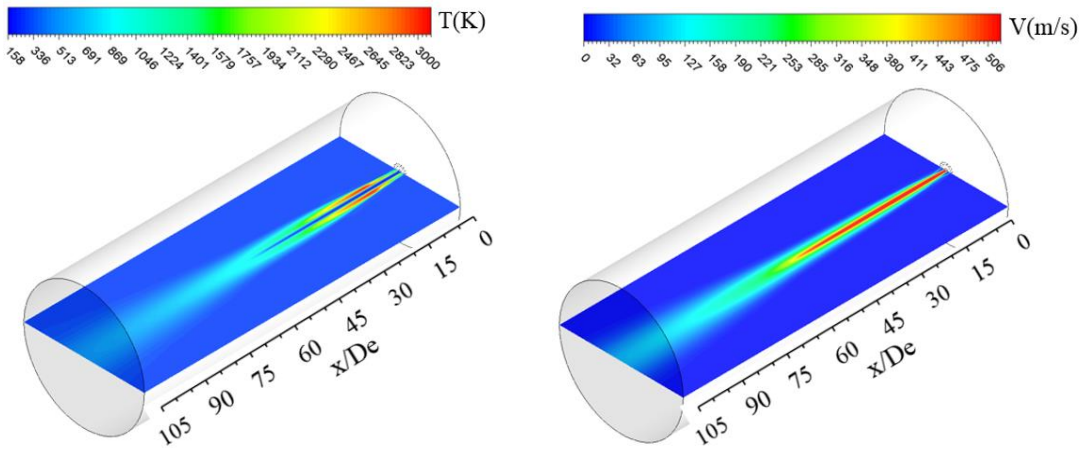

(a) (b)

Figure 88. Coherent jet temperature and velocity distribution, (a) Temperature, (b) Velocity.

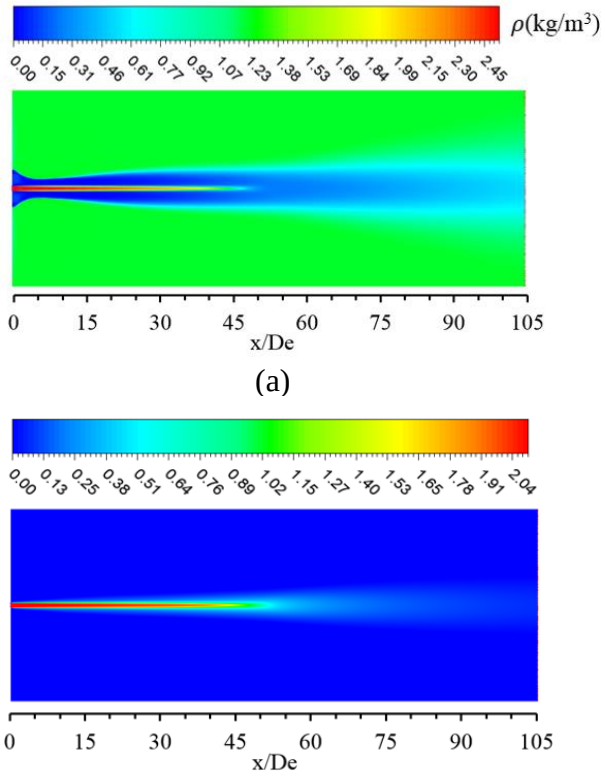

Figure 89. Coherent jet gas properties, (a) Gas density, (b) Mach number.

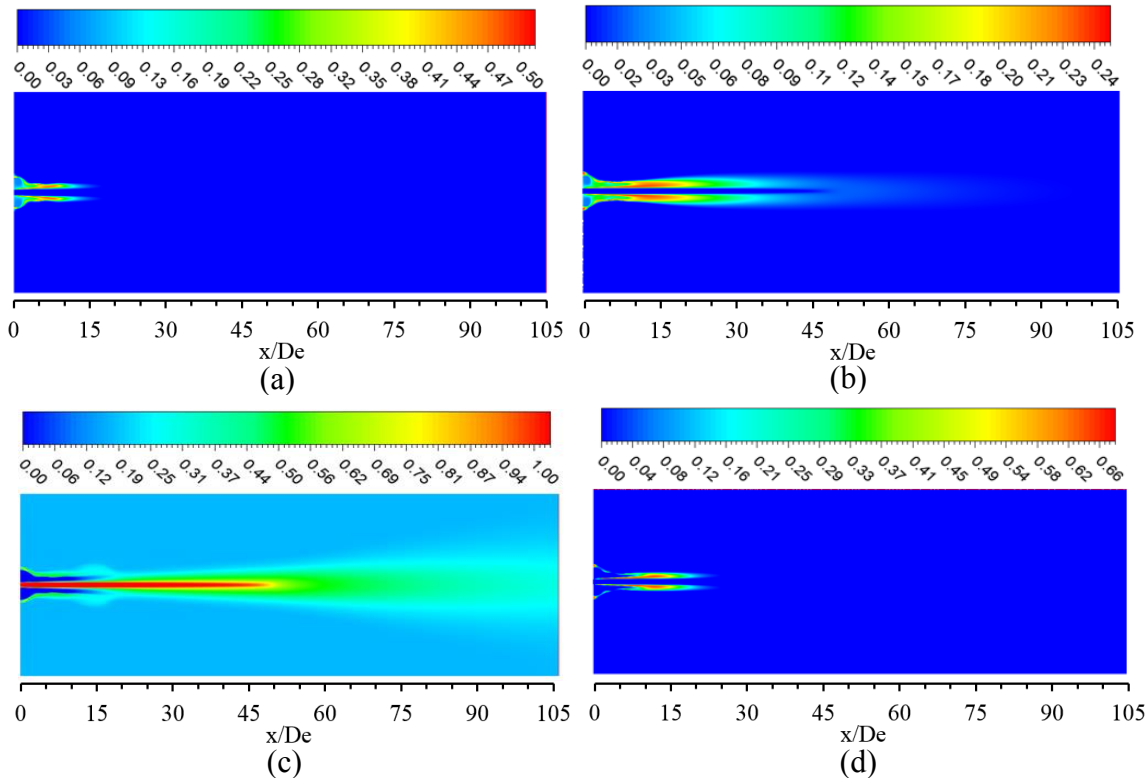

Figure 90. Coherent jet species mass fraction distribution, (a) CO, (b) CO_2, (c) O_2, (d) OH.

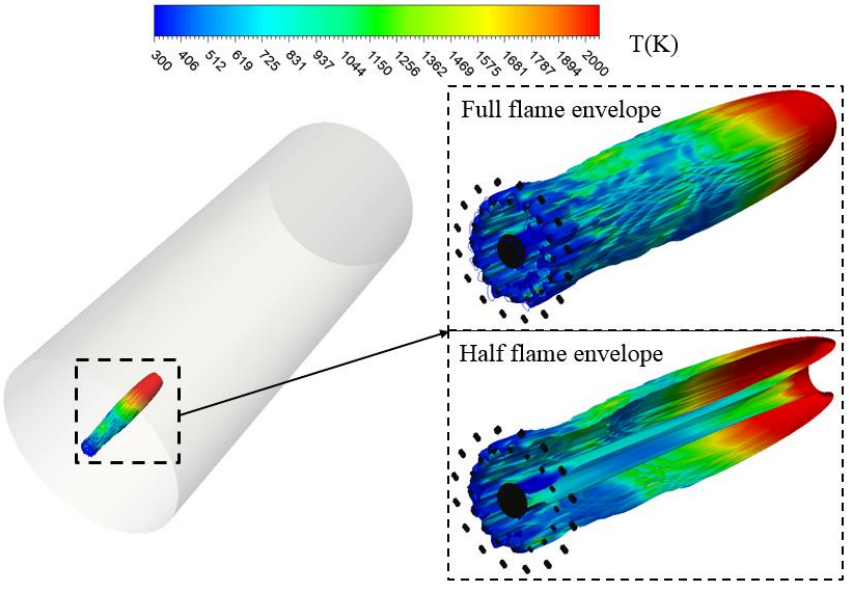

Figure 91. Coherent jet flame profile.

It can be seen from Figure 88 and Figure 89 that a favorable potential core length can be achieved using combustion flame shrouded coherent jet. The combustion flame plays three major roles in

achieving long potential core length: first, the combustion flame helps to destroy entrainment eddies; second, it reduces the gas entrainment by reducing the ambient gas density; and third, combustion flue gases as high-temperature shrouding gases reduce the turbulence viscosity to prolong the jet in the turbulence mixing zone (air entrainment zone). By using the EDC combustion model and the 28-step methane-oxygen combustion reaction mechanism, the simulation results show that the CO species mainly stays in the highest temperature zone at the very beginning of the flame region, while the CO_2 species distributes throughout the whole flame region and in the combustion flue gas as shown in Figure 90. The CFD-predicted methane-oxygen combustion flame temperature is approximately 3000 K. The combustion flame can be described using the CO mass fraction of 2500 ppm. [135] Based on the species concentration predicted using the developed CFD model, the combustion flame profile is illustrated in Figure 91. The fuel injected from the 16 fuel ports formed a combustion flame envelope that covers the supersonic jet for a length of about 0.36 meters (24.4 De).

5.3.2.4 Parametric Studies

Effects of k-epsilon turbulence model modification

Due to complex flow and heat transfer phenomena in the coherent jet, the standard turbulence models (both k-epsilon turbulence model and k-omega turbulence model) developed at room/ambient temperature fail to predict the coherent jet flow properties accurately. It is verified that both the k-epsilon turbulence model and k-omega turbulence model fail to predict the observed decrease in spreading rate with increasing Mach number for the compressible mixing layer [114]. For the k-epsilon turbulence model, Sarkar [136] and Zeman [137] developed models for the k equation to correct the deficiency of the prediction on the compressible mixing layer. Generally, neglecting the dilatation dissipation will over-predict the spreading rate with increasing Mach number for compressible flow mixing. The large temperature gradient will also affect the turbulence mixing. Therefore, there are two major reasons for model modification: 1) compressibility effects: the reduction of growth rate of the mixing layer with increasing convective Mach number cannot be captured by the standard turbulence models, 2) temperature gradient effects: in non-isothermal flows, the large temperature fluctuations affect the growth rate of the mixing layer, which is not considered in standard turbulence models. Based the work done by Sarkar et al. [115] and Abdol-Hamid et al. [116] both the compressibility effects and the

temperature gradient effects are included in this model. Sarkar [136] proposed a simple correction for dilatation dissipation by adding a term in the k equation in the standard k-epsilon two-equation turbulence model. Abdol-Hamid et al. [116] proposed to use the total temperature gradient to correct the turbulence viscosity term constant. It also has the advantages of only correcting the shear layer where the total temperature gradients exist, while for the boundary layer, the standard model will be applied. In this model, the effects of turbulence model modifications (both compressibility effects and temperature gradient effects) on the coherent jet properties are studied. The axial velocity profiles of the coherent jet with and without k-epsilon turbulence model modifications are compared and shown in Figure 92.

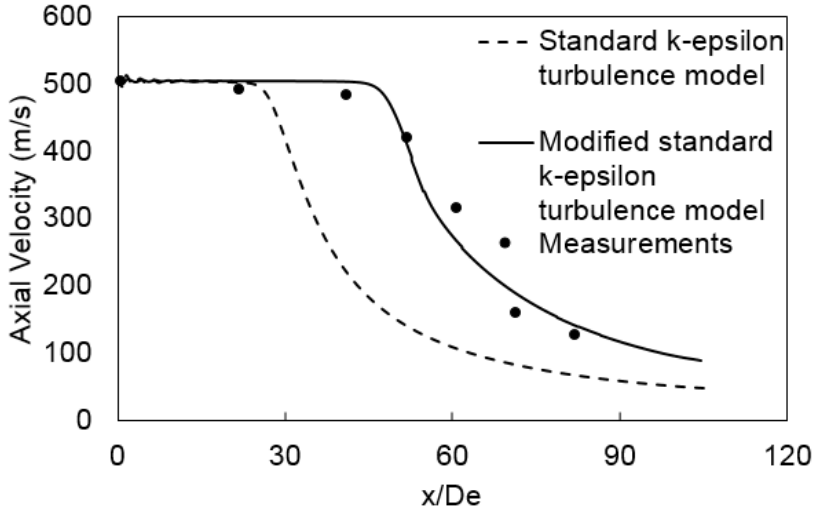

Figure 92. Effects of k-epsilon turbulence model modification on the coherent jet axial velocity.

As shown in Figure 92, without the modifications (both compressibility and temperature gradient effects) on the k-epsilon turbulence model, the potential core length of the coherent jet is approximately 29 De, which is significantly under-predicted. The effects of compressibility by dilatation dissipation and temperature gradient are studied as shown in Figure 93. The coherent jet axial velocity profiles with and without the modification proposed by Sarkar [115] are shown in Figure 93 (a). The coherent jet axial velocity profiles with and without the temperature gradient modification are shown in Figure 93 (b).

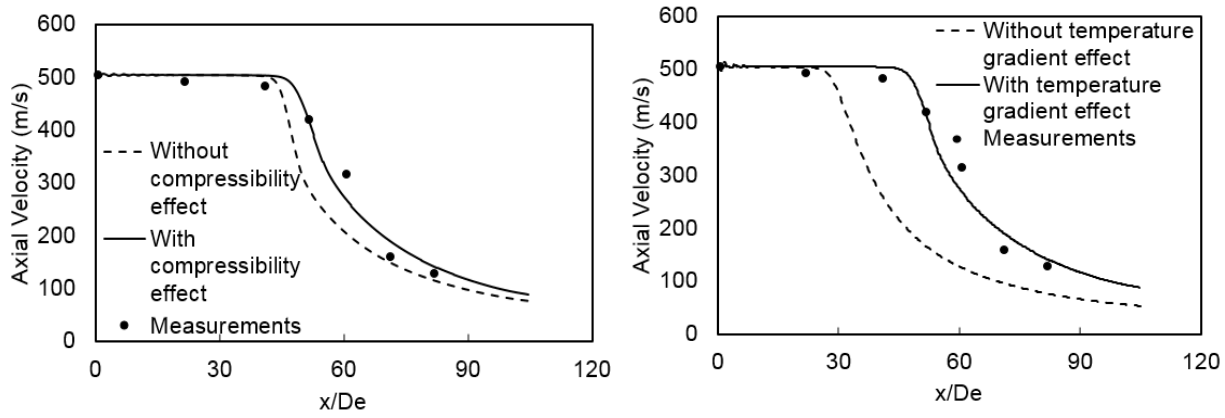

Figure 93. Coherent jet axial velocity profiles, a) Effects of compressibility, b) Effects of temperature gradient.

According to Figure 93, the compressibility effects have a certain extent of impact on the jet velocity profile. The coherent jet length will be reduced when the compressibility effects are neglected, where the spreading rate is over-predicted. The difference of coherent length predicted by the CFD model with and without compressibility effects is about 4.2 De (47.9 De – 43.7 De). Compared to the effects of compressibility, the effects of the temperature gradient in the coherent jet have a more significant impact on the coherent jet length as shown in Figure 93 (b). It can be seen that without the modification of the temperature gradient in the k-epsilon turbulence model, the potential core length of the coherent jet is reduced from 47.9 De to 26.3 De. Therefore, model modifications for the standard k-epsilon turbulence model to include both the compressibility effects and temperature gradient effects are necessary for coherent jet simulation.

Effects of ambient temperature

Coherent jets are mostly used in EAF steelmaking process. Depending on the location of the jet installed in the furnace, the ambient temperature of the jet will be different. Based on the physics of the coherent jet design, a high ambient temperature will reduce the ambient gas density and the turbulence viscosity, which will increase the coherent jet length. A high ambient temperature will also affect the combustion process through the heat transfer between the combustion flame and ambient gases. In order to understand the effects of ambient temperature on the coherent jet length, a parametric study on ambient temperatures has been conducted. The coherent jet velocity and

temperature contours under different ambient temperature conditions are shown in Figure 94. The coherent jet axial velocity and the coherent jet length under different ambient temperature conditions are shown in Figure 95.

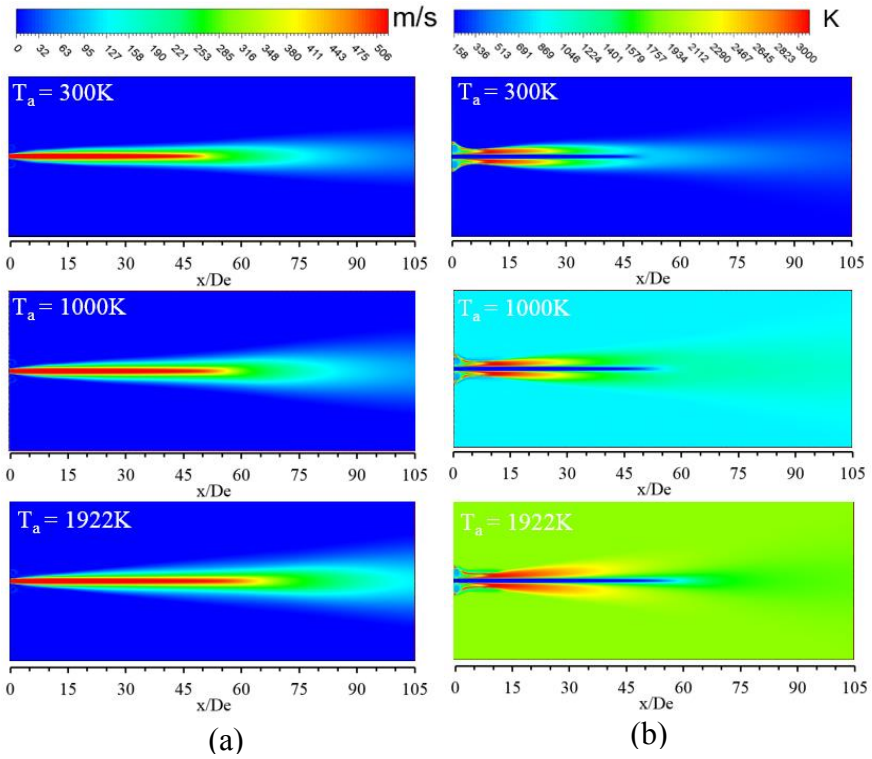

Figure 94. Coherent jet velocity and temperature contours under different ambient temperature, (a) velocity, (b) temperature.

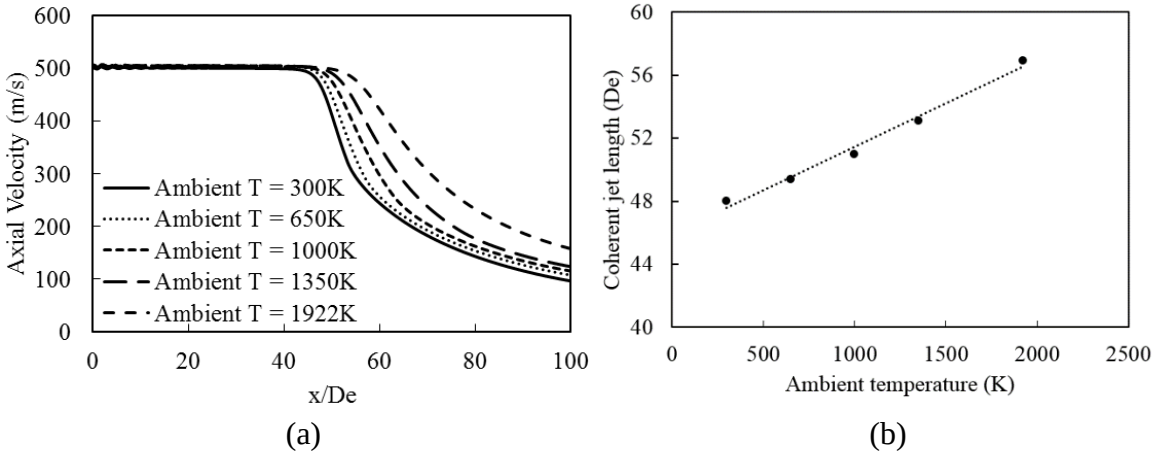

Figure 95. Effects of ambient temperature on the coherent jet axial velocity profiles and coherent jet length, (a) Axial velocity, (b) Coherent jet length.

As shown in Figure 94, the velocity contours indicate that with an increase in ambient temperature, the coherent jet length increases. The temperature contours indicate that the ambient temperature will also affect the high-temperature combustion flame region. With an increase in the ambient temperature, the high-temperature combustion flame zone becomes longer and more dissipated from the jet axis. The jet axial velocity profiles shown in Figure 95 (a) demonstrate that with an increase in the ambient temperature, the coherent jet length increase. With an ambient temperature increase from 300 K to 1922 K, the coherent jet length increases linearly with the ambient temperature as shown in Figure 95 (b).

Effects of CH_4 flow rate

As the difference between the conventional supersonic jet and the coherent jet is the combustion flame envelope formed by the charged fuel and oxygen, the fuel input plays an important role in maintaining the long coherent jet potential core length. In real EAF operation, a reduction of shrouding fuel is not typically applied as it could lead to the loss of jet coherency which could create significant splashing. In this part, the effects of fuel input on the coherent jet potential core length have been studied under 1922 K ambient temperature condition. The velocity and temperature contours of the coherent jet at different fuel input conditions are shown in Figure 96. The axial jet velocity profiles for different CH_4 flow rates are shown in Figure 97. The coherent jet lengths of the coherent jet under different fuel flow rates are shown in Figure 98.

The ratio of fuel volume flow rate to the primary oxygen volume flow rate is used to determine the optimum fuel input for coherent jets. According to Figure 96, the velocity and temperature contours were compared under three different fuel/primary oxygen volume flow rate ratios: 1.3%, 6.5%, and 7.9%. It can be seen that the coherent jet experienced difficulties in forming shrouding combustion flame at the low fuel rate condition. The fuel/primary oxygen volume flow rate ratio for the baseline case condition is 5.6%. When the fuel/primary oxygen volume flow rate ratio exceeds 6.5%, the combustion flame shape changes slightly and the velocity contours shows similar velocity distributions.

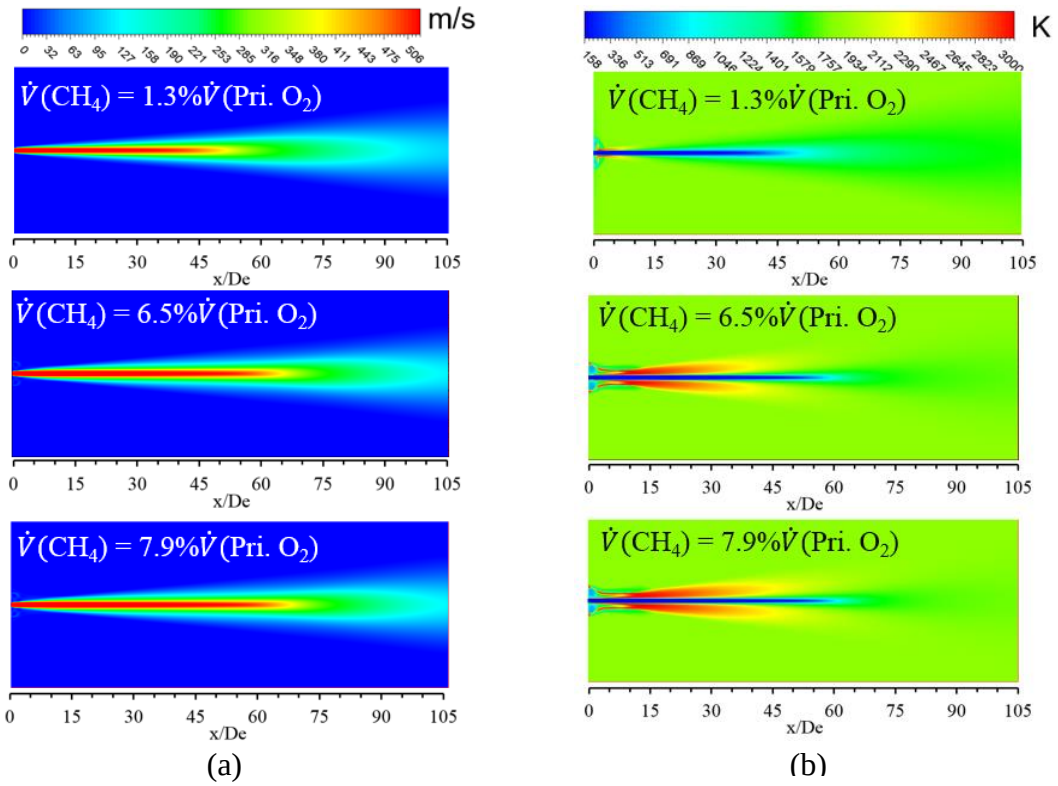

Figure 96. Coherent jet velocity and temperature contours under different fuel input, (a) Velocity, (b) Temperature.

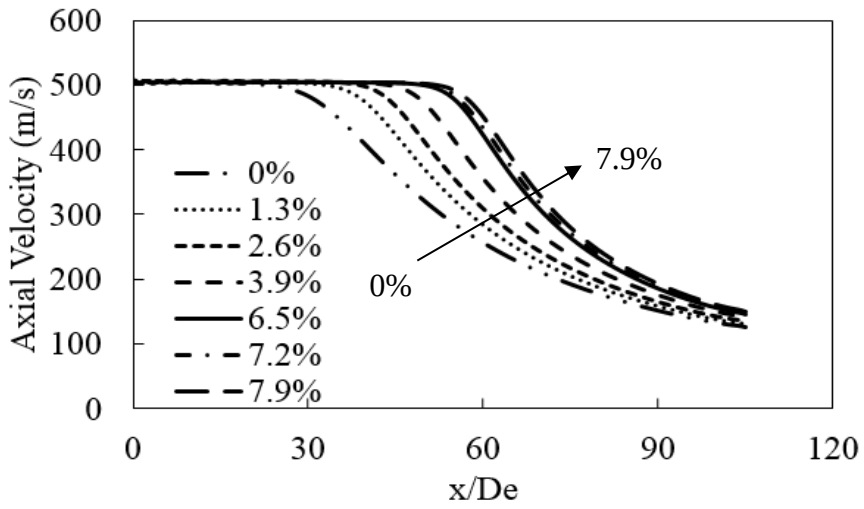

Figure 97. Effects of fuel input on the coherent jet axial velocity profiles.

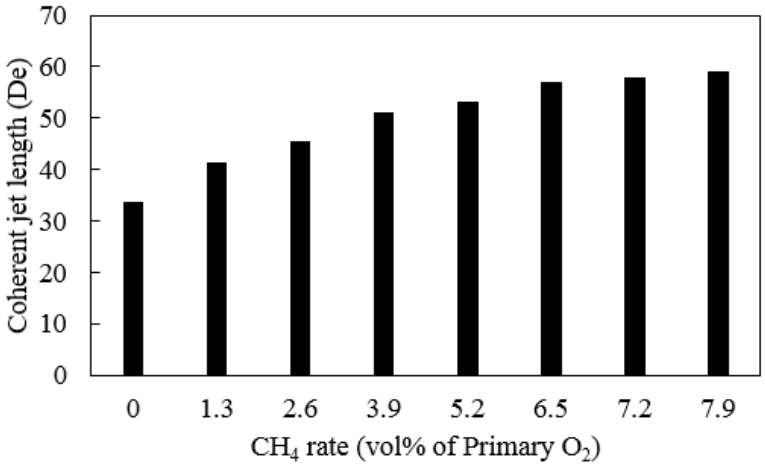

Figure 98. Effects of fuel input on the coherent jet length.

The coherent jet axial velocity profiles under seven different fuel/primary oxygen volume flow rate ratios are shown in Figure 97. It can be seen that the decrease of fuel input from baseline case condition will lead to the significantly earlier decline of coherent jet axial velocity, which will reduce the coherent jet length accordingly, while an increase in the fuel input will not delay the coherent axial velocity decline greatly. As shown in Figure 98, the coherent jet length increases slightly when the fuel/primary oxygen volume flow rate ratio exceeds 6.5%, while reducing the fuel input from the baseline conditions will decrease the coherent jet length significantly. Therefore, the fuel input can play a significant role in coherent jet potential core length under high ambient temperature conditions. Without sufficient fuel input to form a stable combustion flame, the coherent jet length will be reduced dramatically.

Effects of fuel type

The uses of three commonly used gas fuel in the steel industry, such as blast furnace gas (BFG), coke oven gas (COG), and natural gas (NG) as the shrouding fuel for coherent jet have been studied. Due to the availability of BFG and COG in a steel plant, the potential usage for EAF coherent jet could reduce the overall operation cost. Under the same shrouding fuel mass flow rate as shown in Table 17, simulations of the coherent jet flow characteristics using BFG, COG, and NG were conducted. The BFG, COG and NG compositions and heating values were obtained from the steel industry are listed in Table 21 [138]. Generally, the species in BFG are mostly CO_2 and CO. However, CH_4 and H_2 are highly concentrated in the COG. In terms of the volume average

molecular weight in the gas, the BFG is higher than the COG. The effects of shrouding gas on supersonic jet flow characteristics have been studied by Zhao et al. [139,140]. Three different shrouding gases, H_2, O_2, CO_2 for conventional supersonic jet were used. The simulation results indicated that the use of H_2 and CO_2 as the shrouding gases provide the longest and the shortest supersonic jet length, respectively. The rate of ambient gas entrainment can be expressed as Equation (101) [81,141]. The M_a/M_o is the ratio of the mass of ambient gas being entrained to the mass of the original gas jet. The ρ_a is the ambient gas density. The ρ_o is the original gas jet density. The $x/d_e$is the axial distance from the nozzle exit divided by the nozzle diameter. It is expected to obtain different supersonic gas jet potential core length by using different shrouding gases as the density of the shrouding gas played an important role in the entrainment rate. By using higher density ambient gas, obtain the same mass of gas entrainment takes less axial distance. By using the gas compositions listed in Table 21, the flow properties of the coherent jet with different fuel was studied. The effects of fuel type on the oxy-fuel combustion is shown in Figure 99. The coherent jet axial velocity predicted by the CFD model using different fuel types is shown in Figure 100.

$$\frac{M_a}{M_o} = 0.32 \left(\frac{\rho_a}{\rho_o}\right)^{0.5} \frac{x}{d_e} \tag{101}$$

Table 21. Fuel compositions (vol%) [138].

Species	BFG Inlet	COG Inlet	NG Inlet
O_2		0.004	
N_2	0.47	0.04	
C_2H_6		0.008	0.029
C_2H_4		0.022	
CH_4		0.253	0.944
CO_2	0.25	0.026	0.027
CO	0.22	0.05	
H_2	0.06	0.597	

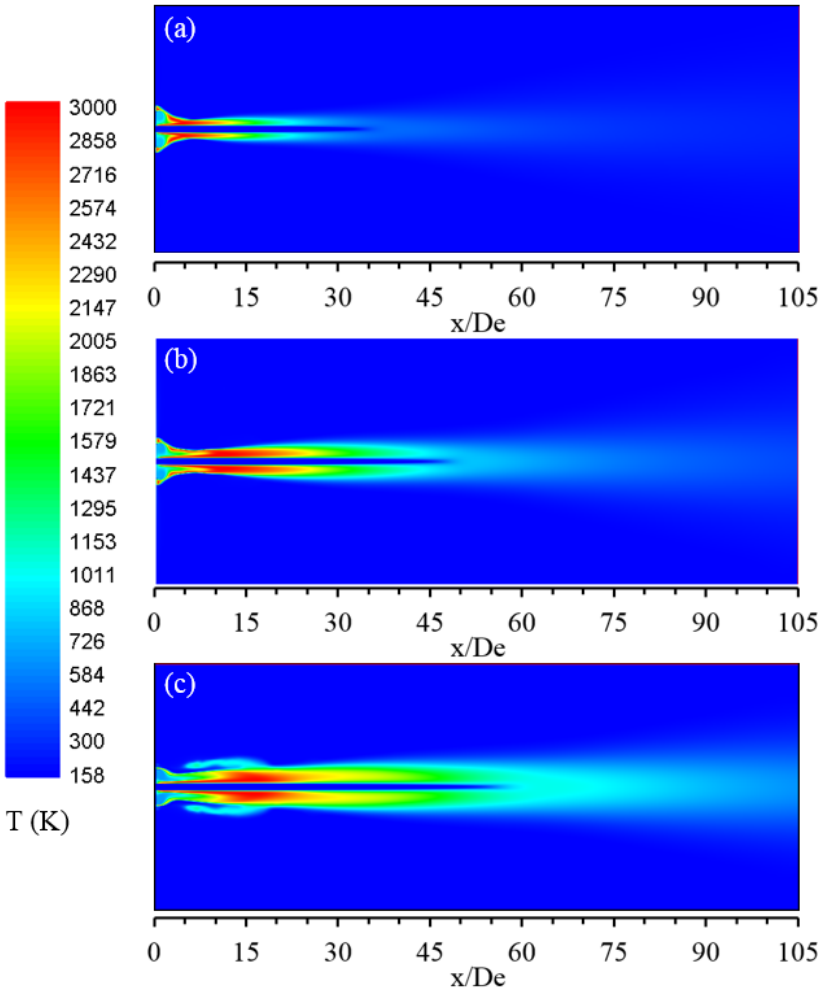

Figure 99. Effects of fuel type on the combustion in coherent oxygen jet, (a) BFG, (b) NG, (c) COG.

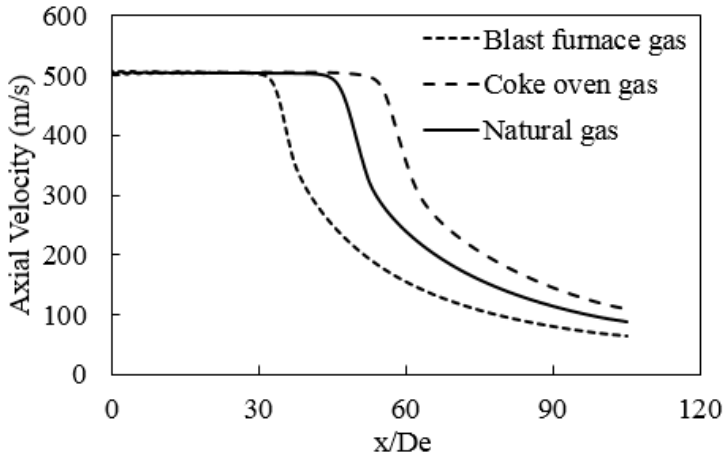

Figure 100. Effects of fuel type on the coherent oxygen jet axial velocity.

According to Figure 99, the BFG combustion formed the shortest flame, while the COG combustion formed the longest flame. The supersonic jet (center jet) entrained the combustion flue gases through turbulence mixing and then dispersed into a subsonic jet. The combustion flue gases are in different densities due to the fuel composition listed in Table 21. The COG combustion flue gas density is the lowest compared to BFG and NG due to the composition H_2. Therefore, the coherent jet using COG as the shrouding fuel has the longest jet length as indicated in Figure 100. Therefore, reduce the shrouding fuel molecular weight or gas density will increase coherent jet length.

Effects of the combustion model

The combustion is the key factor that defines the coherent jet. The formation of combustion flame shroud for the supersonic oxygen jet extended the jet potential core length significantly longer. Accurately modeling of combustion is a critical step to obtain correct jet velocity profiles. Most of the coherent jet numerical models applied the EDC combustion model to simulate the combustion with detailed kinetics. For combustion mechanisms, both simplified one-step reaction [53] and complicated 325-step reaction mechanisms in GRI-Mech 3.0 [85] are used. It is computationally cheap to use the simplified one-step CH_4-O_2 combustion mechanism compared to the complicated 325-step reaction mechanism. However, the flame temperature predicted by the simplified one-step reaction is generally higher than the complicated 325-step reaction mechanism. Although the computing power is becoming stronger nowadays, it is still computationally expensive to simulate the industrial coherent jet using full three-dimensional geometry and complicated 325-step reaction mechanism. In this study, a 28-step combustion reaction mechanism is proposed to achieve high computational efficiency and model accuracy. In order to study the effects of reaction mechanism selection on the coherent jet profile, five different reaction mechanisms are studied: 1-step global reaction, 2-step global reaction, revised WD, revised JL and 28-step reaction mechanisms. The combustion flame temperatures predicted using three different reaction mechanisms are shown in Figure 101. The axial velocity profiles using the three different reaction mechanisms are shown in Figure 102.

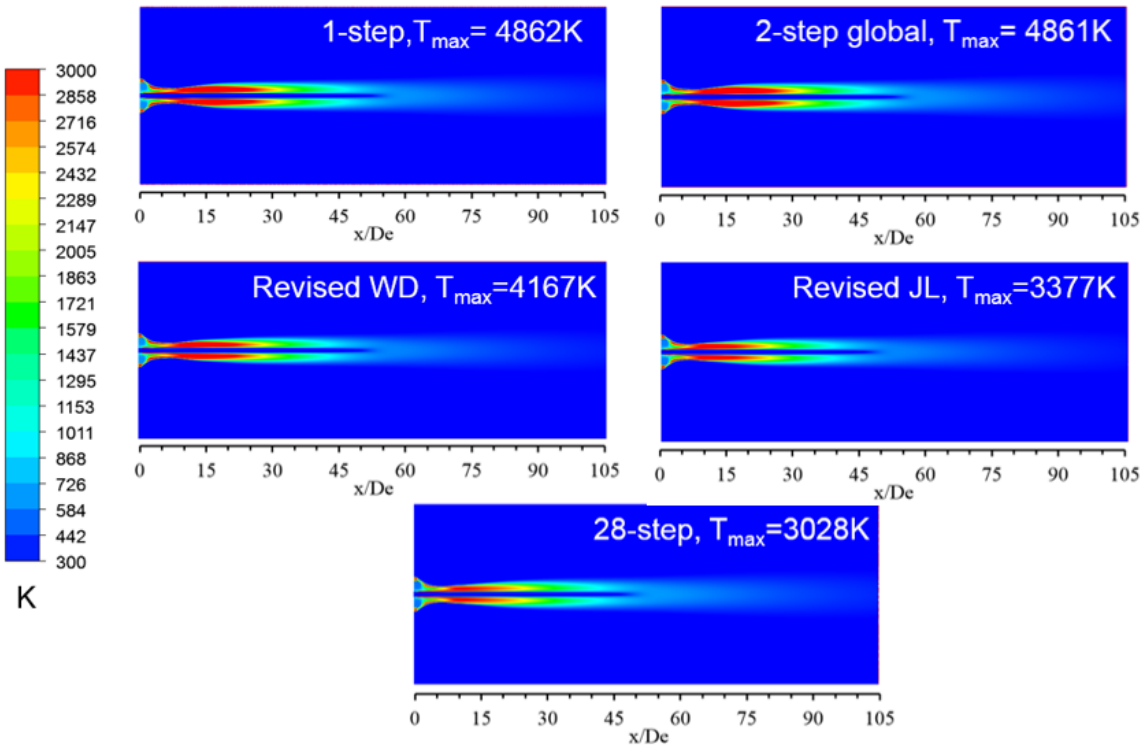

Figure 101. Coherent jet combustion flame temperature using different mechanisms.

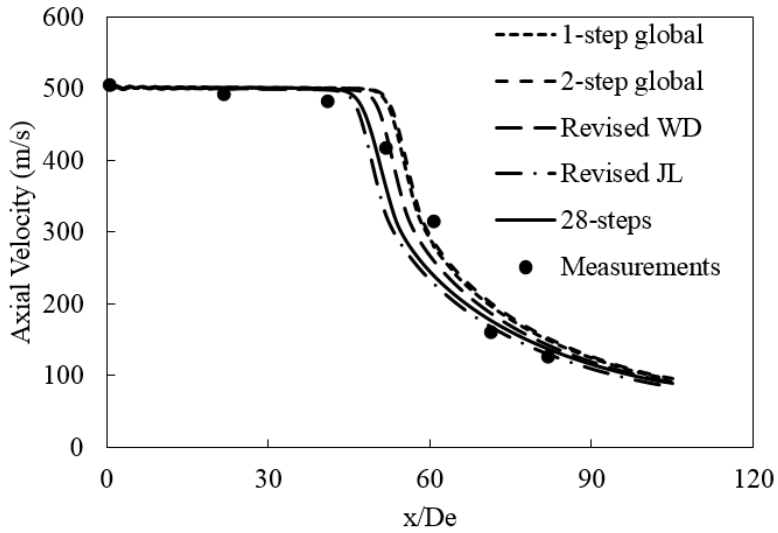

Figure 102. Effects of combustion mechanisms on the coherent jet axial velocity profiles.

According to Figure 101, different combustion reaction mechanisms predict different high-temperature zone locations and different flame temperatures. Similar temperature field was predicted by using the 1-step and the 2-step global chemical reaction mechanisms. In general, the

highest temperatures predicted by the 1-step and 2-step global chemical reaction mechanisms are higher than that predicted by the 28-step chemical reaction mechanism. The combustion temperature is lower by using the 28-step chemical reaction mechanism due to more intermediate species such as CH_3, CH_2O, OH, that are generated in the reactions. Both the one-step and two-step reaction mechanisms predict the highest flame temperature as being over 4800 K, which is over-predicted compared to the GRI-Mech 3.0 prediction [83,85]. The over-prediction of the temperature is caused by the use of chemical reaction kinetics and radiation model for natural gas-air combustion instead of natural gas-oxygen combustion [100,126]. By using the 28-step reaction mechanism, the highest flame temperature is approximately 3028 K, which is lower than the natural gas-oxygen combustion adiabatic flame temperature [104]. Andersen et al. [121] proposed revised WD and revised JL chemical reaction mechanisms for the oxy-natural gas combustion. The highest flame temperature predicted by using the revised WD and revised JL reaction mechanisms are 4167K and 3077K, respectively. As shown in Figure 102, combustion mechanisms also have effects on the coherent jet axial velocity profile. For the three points in the supersonic speed zone, the 28-step and the revised WD reaction mechanisms predict the closest results compared to the 1-step global, 2-step global and the revised JL reaction mechanisms. In the turbulence mixing region of the coherent jet, higher shrouding gas temperature gradients will decrease the turbulence mixing and therefore extend high jet velocity for a longer distance. Due to the over-prediction of combustion temperature, both the 1-step global and 2-step global chemical reaction mechanisms over-predict the axial velocity of the coherent jet. Therefore, selection of the combustion mechanism is important in the coherent jet simulation. The current model using the 28-step reaction mechanism is able to achieve both accuracy and efficiency. The revised WD reaction mechanism is also suggested for a quick test of numerical models during model development since it can also predict the jet axial velocity profile well compared to experimental work.

In summary, a coherent jet CFD model has been developed with detailed consideration of compressible gas flow properties and combustion effects. A modified k-epsilon turbulence model was applied to consider the effects of both compressibility and temperature gradient on the flow properties. The combustion was modeled using the EDC model with a 28-step chemical reaction mechanism for methane-oxygen combustion. A CFD model validation shows that the CFD model

prediction on the jet axial velocity profiles has a good agreement with the experimental measurements for both inclusion and absence of the flame shroud. It is indicated that by adding the flame shroud, the coherent jet length increases from 18 De to 48 De. The coherent jet flow properties and the combustion flame shape were investigated using the validated CFD model. The following conclusions are drawn on based on this study:

1. The coherent jet length increases linearly with the ambient temperature in the range of 300 K to 1922 K.
2. At high-temperature steelmaking conditions, the effects of fuel input on the coherent jet length have been investigated. The results indicate that fuel input can play a significant role in coherent jet length. The results showed that when the fuel input exceeds 6.5% of the primary oxygen volume flow rate, the potential core length of the coherent jet will not increase significantly. Without sufficient fuel input to form a stable combustion flame, the coherent jet potential core length will be reduced dramatically.
3. The study of using different fuel for coherent jet combustion indicates that reduce the shrouding fuel molecular weight or gas density will increase coherent jet potential core length.

5.4 Summary

Numerical modeling on steel scrap melting in bath has been conducted. The CFD model consists of two different sub-models, melting in bath model and coherent jet model. The heat transfer from the electric arc was treated as heat flux. The melting in bath and coherent jet sub-models are carefully developed and validated. The melting in bath model uses the enthalpy-porosity method to describe the scrap melting process and the VOF method is used to describe the multiphase flow in the bath. Useful information about the effects of steel scrap porosity on the melting time is provided. The coherent jet model was developed with detailed consideration of compressible gas flow properties and combustion effects. Various operating conditions for the coherent jet have been investigated.

CHAPTER 6. CONCLUSIONS AND FUTURE RESEARCH

6.1 Conclusions

A comprehensive CFD model involving turbulence interacting flow, combustion, heat transfer, and a dynamic operating condition were developed for an industrial walking beam slab reheating furnace. The CFD model offers detailed descriptions of the complicated combustion and heat transfer processes. The furnace temperature was properly predicted based on actual operating boundary conditions, and the model was validated by an instrumented slab trial and the operating online model. The current model is capable of predicting the temperature distribution inside the reheating furnace and also the temperature distribution inside a slab being heated. The model provides reasonable predictions and can be used to identify potential production issues and to optimize the furnace operation.

A comprehensive two-dimensional (2D) numerical heat transfer model for slab reheating in a walking beam furnace was developed using the finite difference method. The model is capable of predicting slab temperature evolution during a reheating process based on real-time furnace conditions and steel physical properties. The model was validated by using mill instrumented slab trials and production data. The results show that the temperature evolution predicted by the model is in good agreement with that measured by the thermocouples embedded in the instrumented slab. Compared with 3D CFD simulation of a reheating process, this 2D heat transfer model used for predicting slab temperature evolution requires less computing power and can provide results in a few seconds. This is a very convenient and user-friendly tool which can be used easily by mill metallurgists in troubleshooting and process optimization.

The steel slab reheating CFD model was then extended to the steel scrap heating and melting model. A three-dimensional CFD model has been developed with detailed consideration of furnace geometry, oxy-fuel burner configuration, natural gas combustion, gas scrap heat transfer, and scrap oxidation. The model has been validated against the experimental and numerical simulation done by Mandal [59]. This model was applied to an industrial EAF to study the effects of using the oxy-fuel burner to preheat the steel scraps before the arcing process. The simulation results show that

the average scrap temperature would increase about 400 K during a 20-minute preheating using 4MW burner power with five burners in the EAF. This model will be further developed for scrap melting by modeling both oxy-fuel burners and the electric arc.

In addition, a 3-D CFD model has been developed with detailed consideration of fluid flow and heat transfer in the steel bar melting in bath process. A CFD model for steel melting in multiphase flow system was developed. The CFD model uses the enthalpy-porosity method and the VOF method can describe the important phenomena during the scrap melting in bath process. The overall validation shows good agreement against the experimental measurements on both melting time and steel bar diameters. The results also indicate that,

1. Increase the steel initial temperature will reduce the formed shell thickness and increase the melting efficiency
2. The small spacing between steel bars or steel scraps will increase the melting time due to steel iceberg phenomena.
3. Increase steel scrap porosity to larger than 0.77 in bath to avoid significant agglomeration is suggested.

A coherent jet CFD model has been developed with detailed consideration of compressible gas flow properties and combustion effects. A modified k-epsilon turbulence model was applied to consider the effects of both compressibility and temperature gradient on the flow properties. The combustion was modeled using the EDC model with a 28-step chemical reaction mechanism for methane-oxygen combustion. A CFD model validation shows that the CFD model prediction on the jet axial velocity profiles has a good agreement with the experimental measurements for both inclusion and absence of the flame shroud. It is indicated that by adding the flame shroud, the coherent jet length increases from 18 De to 48 De. The coherent jet flow properties and the combustion flame shape were investigated using the validated CFD model. The following conclusions are drawn on based on this study:

1. The coherent jet length increases linearly with the ambient temperature in the range of 300 K to 1922 K.
2. At high-temperature steelmaking conditions, the effects of fuel input on the coherent jet length have been investigated. The results indicate that fuel input can play a significant role

in coherent jet length. The results showed that when the fuel input exceeds 6.5% of the primary oxygen volume flow rate, the potential core length of the coherent jet will not increase significantly. Without sufficient fuel input to form a stable combustion flame, the coherent jet potential core length will be reduced dramatically.

3. The study of using different fuel for coherent jet combustion indicates that reduce the shrouding fuel molecular weight or gas density will increase coherent jet potential core length.

Based on the sub-models, a 3-D CFD model can be further developed with detailed consideration of fluid flow and heat transfer for the scrap melting process in industrial EAF. The flow characteristics, temperature field and scrap melting process in the steel bath during the EAF operation can be revealed.

6.2 Future Research

The state-of-the-art numerical modeling for steel slab reheating process has been conducted. This study was focused on modeling combustion and heat transfer in a specific steel reheating furnace. Both the developed CFD model and the application can be further studied to broad the impact of this modeling process. Future research on steel slab reheating process modeling is listed below:

1. Model development:
    a. Refine the combustion model by using more complicated combustion mechanisms for natural gas combustion.
    b. And scale formation model to take into account the effect of scale formation on heat transfer.
2. Model application:
    a. Investigate the effects of various operating parameters on the slab reheating process including hot charge, steel grades, slab geometry, travel speed, fuel input, recuperator efficiency, burner failure, etc.
    b. Trouble-shooting slab temperature non-uniformity.
    c. Optimize industrial operation using the 2D heat transfer model by design optimal charging process for different steel grades.

Numerical simulation on the scrap preheating process in industrial EAF is first-time studied. The steel scrap preheating CFD model is developed using real EAF operation with various assumptions. Future work for the steel scrap preheating model has been identified and listed as the following:

1. Model development:
    a. Refine the current model with more detailed scrap charging profiles.
    b. Refine the current model with detailed descriptions of hydrocarbon combustion, liquid steel dripping, and scrap movement.
    c. Identify a better treatment of hot heel and the charged molten iron in the current model.
2. Model application:
    a. Investigate the different scrap charging profiles on the heat transfer efficiency.
    b. Conduct model validation on the current CFD model using industrial measurements.

Numerical simulation on the scrap melting in bath process in industrial EAF is studied. The steel scrap melting in bath CFD model is developed with two important sub-models, the melting in bath model and the coherent jet model. Research on steel scrap melting in bath has not reached the real application stage yet. The future work on the scrap melting in bath model is listed below:

1. Model development:
    a. Add on electric arc model to the current model to consider heat transfer from electrodes more accurately.
    b. Add the porous medium in the bath to represent the scraps.
2. Model application:
    a. Investigate the different stirring power on the scrap melting efficiency.
    b. Conduct model validation.

Besides the three model developed in this dissertation, future research work in the EAF area are also listed as the following:

1. Model the scrap melting above bath process. It is currently very challenging to simulate the scrap melting above bath process due to the complexity of modeling the physical phenomena such as the heat transfer between the electric arc and the steel scraps, the scrap movement, and liquid steel dripping. The extensive study should be pursued to understand the detailed physics.

2. Model the steel refining stage using CFD. Steel refining process in current EAF operation determines the operational efficiency and final product quality. Both multiphase flow and chemical reactions need to be considered.
3. Model integration. To represent the EAF operation process, four different models are needed. The model integration should be performed to ensure the developed CFD model has the capability to investigate the industrial EAF batch process.

REFERENCES

[1]. J. Stubbes, "Energy Use in the U.S. Steel Industry: an Historical Perspective and Future," Technical report, U.S. Department of Energy, Washington, DC, 2000.

[2]. Steel Statistical Yearbook, World Steel Association, 2017.

[3]. 2018 AIST Electric Arc Furnace Roadmap, *Iron Steel Technol.*, vol. 15, no. 1, pp. 154–157, 2018

[4]. G. Tang, B. Wu, D. Bai, Y. Wang, R. Bodnar, and C. Zhou, "Numerical Simulation of a Walking Beam Slab Reheating Furnace," *Iron Steel Technol.*, vol. 14, no. 3, pp. 78–88, 2017.

[5]. S. H. Han, S. W. Baek, and M. Y. Kim, "Transient Radiative Heating Characteristics of Slabs in a Walking Beam Type Reheating Furnace," *Int. J. Heat Mass Transf.*, vol. 52, pp. 1005–1011, 2009.

[6]. S. H. Han, D. Chang, and C. Y. Kim, "A Numerical Analysis of Slab Heating Characteristics in a Walking Beam Type Reheating Furnace," *Appl. Therm. Eng.*, vol. 53, pp. 3855–3861, 2010.

[7]. M. Gu, G. Chen, X. Liu, C. Wu, and H. Chu, "Numerical Simulation of Slab Heating Process in a Regenerative Walking Beam Reheating Furnace," *Int. J. Heat Mass Transf.*, vol. 76, pp. 405–410, 2014.

[8]. S. H. Han and D. Chang, "Optimum Residence Time Analysis for a Walking Beam Type Reheating Furnace," *Int. J. Heat Mass Transf.*, vol. 55, no. 15–16, pp. 4079–4087, 2012.

[9]. S. H. Han, D. Chang, and C. Huh, "Efficiency Analysis of Radiative Slab Heating in a Walking-Beam-Type Reheating Furnace," *Energy*, vol. 36, no. 2, pp. 1265–1272, 2011.

[10]. F. A. D. Oliveira, J. A. Carvalho, P. M. Sobrinho, and A. de Castro, "Analysis of Oxy-fuel Combustion as an Alternative to Combustion with Air in Metal Reheating Furnaces," *Energy*, vol. 78, pp. 290–297, 2014.

[11]. M. T. Johansson, "Bio-synthetic Batural Gas as Fuel in Steel Industry Reheating Furnaces - A Case Study of Economic Performance and Effects on Global CO_2 Emissions," *Energy*, vol. 57, pp. 699–708, 2013.

[12]. J. H. Jang, D. E. Lee, M. Y. Kim, and H. G. Kim, "Investigation of the Slab Heating Characteristics in a Reheating Furnace with the Formation and Growth of Scale on the Slab Surface," *Int. J. Heat Mass Transf.*, vol. 53, no. 19–20, pp. 4326–4332, 2010.

[13]. S. K. Dubey and P. Srinivasan, "Development of Three Dimensional Transient Numerical Heat Conduction Model with Growth of Oxide Scale for Steel Billet Reheat Simulation,"

Int. J. Therm. Sci., vol. 84, pp. 214–227, 2014.

[14]. J. G. Kim, K. Y. Huh, and I. T. Kim, "Three-dimensional Analysis of the Walking-Beam-Type Slab Reheating Furnace in Hot Strip Mills," *Numer. Heat Transf. Part A Appl.*, vol. 38, no. 6, pp. 589–609, 2000.

[15]. C. T. Hsieh, M. J. Huang, S. T. Lee, and C. H. Wang, "Numerical Modeling of a Walking-Beam-Type Slab Reheating Furnace," *Numer. Heat Transf. Part A Appl.*, vol. 53, no. 9, pp. 966–981, 2008.

[16]. M. Y. Kim, "A Heat Transfer Model for the Analysis of Transient Heating of the Slab in a Direct-fired Walking Beam Type Reheating Furnace," *Int. J. Heat Mass Transf.*, vol. 50, no. 19–20, pp. 3740–3748, 2007.

[17]. V. K. Singh, P. Talukdar, and P. J. Coelho, "Performance Evaluation of Two Heat Transfer Models of a Walking Beam Type Reheat Furnace," *Heat Transf. Eng.*, vol. 36, no. 1, pp. 91–101, 2015.

[18]. J. H. Jang, D. E. Lee, C. Kim, and M. Y. Kim, "Prediction of Furnace Heat Transfer and Its Influence on the Steel Slab Heating and Skid Mark Formation in a Reheating Furnace," *ISIJ Int.*, vol. 48, no. 10, pp. 1325–1330, 2008.

[19]. J. G. Kim and K. Y. Huh, "Prediction of Transient Slab Temperature Distribution in the Reheating Furnace of a Walking-Beam Type for Rolling of Steel Slabs," *ISIJ Int.*, vol. 40, no. 11, pp. 1115–1123, 2000.

[20]. Y. J. Y. Jang and S. W. S. Kim, "An Estimation of a Billet Temperature during Reheating Furnace Operation," *Int. J. Control Autom. Syst.*, vol. 5, no. 1, pp. 43-50, 2007.

[21]. M. J. Huang, C. T. Hsieh, S. T. Lee, and C. H. Wang, "A Coupled Numerical Study of Slab Temperature and Gas Temperature in the Walking-Beam-Type Slab Reheating Furnace," *Numer. Heat Transf. Part A Appl.*, vol. 54, no. 6, pp. 625–646, 2008.

[22]. J. Y. Jang and J. B. Huang, "Optimization of a Slab Heating Pattern for Minimum Energy Consumption in a Walking-Beam Type Reheating Furnace," *Appl. Therm. Eng.*, vol. 85, pp. 313–321, 2015.

[23]. S. H. Han, Y. S. Lee, J. R. Cho, and K. H. Lee, "Efficiency Analysis of Air-fuel and Oxy-Fuel Combustion in a Reheating Furnace," *Int. J. Heat Mass Transf.*, vol. 121, pp. 1364–1370, 2018.

[24]. B. Mayr, R. Prieler, M. Demuth, and C. Hochenauer, "Modelling of High Temperature Furnaces under Air-fuel and Oxygen Enriched Conditions," *Appl. Therm. Eng.*, vol. 136, pp. 492–503, 2018.

[25]. Y. Hu, C. K. Tan, J. Broughton, and P. A. Roach, "Development of a First-principles Hybrid Model for Large-scale Reheating Furnaces," *Appl. Energy*, vol. 173, pp. 555–566, 2016.

[26]. T. Morgado, P. J. Coelho, and P. Talukdar, "Assessment of Uniform Temperature Assumption in Zoning on the Numerical Simulation of a Walking Beam Reheating Furnace," *Appl. Therm. Eng.*, vol. 76, pp. 496–508, 2015.

[27]. C. K. Tan, J. Jenkins, J. Ward, J. Broughton, and A. Heeley, "Zone Modelling of the Thermal Performances of a Large-scale Bloom Reheating Furnace," *Appl. Therm. Eng.*, vol. 50, no. 1, pp. 1111–1118, 2013.

[28]. J. M. Casal, J. Porteiro, J. L. Míguez, and A. Vázquez, "New Methodology for CFD Three-dimensional Simulation of a Walking Beam Type Reheating Furnace in Steady State," *Appl. Therm. Eng.*, vol. 86, pp. 69–80, 2015.

[29]. Emadi, A. Saboonchi, M. Taheri, and S. Hassanpour, "Heating Characteristics of Billet in a Walking Hearth Type Reheating Furnace," *Appl. Therm. Eng.*, vol. 63, no. 1, pp. 396–405, 2014.

[30]. S. Chen, S. Abraham, and D. Poshard, "Modification of Reheat Furnace Practices through Comprehensive Process Modeling," *Iron Steel Technol.*, vol. 5, no. 8, pp. 66–79, 2008.

[31]. Jaklič, F. Vode, and T. Kolenko, "Online Simulation Model of the Slab-reheating Process in a Pusher-type Furnace," *Appl. Therm. Eng.*, vol. 27, no. 5–6, pp. 1105–1114, 2007.

[32]. J. Oda, K. Akimoto, and T. Tomoda, "Long-term Global Availability of Steel Scrap," *Resour. Conserv. Recycl.*, vol. 81, pp. 81–91, 2013.

[33]. V. Logar, D. Dovzan, and I. Škrjanc, "Mathematical Modeling and Experimental Validation of an Electric Arc Furnace," *ISIJ Int.*, vol. 51, no. 3, pp. 382–391, 2011.

[34]. Annual Energy Outlook 2016, with projections to 2040, U.S. Energy Information Administration, pp. 36, 2016.

[35]. J. Madias, A. Bilancieri, and S. Hornby, "The Influence of Metallics and EAF Design," *Steel Times Int.*, pp. 35-40, 2017.

[36]. J. Madias, "Electric Furnace Steelmaking," pp. 271-300, 2014.

[37]. Technology Roadmap Research Program for the Steel Industry, Final Report, December, 2010, American Iron and Steel Institute.

[38]. H. J. Odenthal, A. Kemminger, F. Krause, L. Sankowski, N. Uebber, and N. Vogl, "Review on Modeling and Simulation of the Electric Arc Furnace (EAF)," *Steel Res. Int.*, vol. 89, no. 1, p. 1700098, 2018.

[39]. C. Wang, M. Brämming, and M. Larsson, "Numerical Model of Scrap Blending in BOF with Simultaneous Consideration of Steel Quality, production cost, and energy use," *Steel Res. Int.*, vol. 84, no. 4, pp. 387–394, 2013.

[40]. F. Memoli, J. A. T. Jones, F. Picciolo, and N. Palamini, "The Use of DRI in a Consteel®

EAF Process," *Iron Steel Technol.*, vol. 12, no. 1, pp. 72–80, 2015.

[41]. J. Maiolo, M. Boutazakhti, C. W. Li, and C. Williams, "Developments Towards an Intelligent Electric Arc Furnace at CMC texas using Goodfellow EFSOP technology," AISTech 2017 conference, Nashville, TN, USA, 2017.

[42]. R. D. M. MacRosty and C. L. E. Swartz, "Dynamic Modeling of an Industrial Electric Arc Furnace," *Ind. Eng. Chem. Res.*, vol. 44, no. 21, pp. 8067–8083, 2005.

[43]. V. Logar, D. Dovzan, and I. Skrjanc, "Modeling and Validation of an Electric Arc Furnace: Part 1, Heat and Mass Transfer," *ISIJ Int.*, vol. 52, no. 3, pp. 402–412, 2012.

[44]. V. Logar and I. Skrjanc, "Modeling and Validation of the Radiative Heat Transfer in an Electric Arc Furnace," *ISIJ Int.*, vol. 52, no. 7, pp. 1225–1232, 2012.

[45]. N. Arzpeyma, O. Widlund, M. Ersson, and P. Jönsson, "Mathematical Modeling of Scrap Melting in an EAF using Electromagnetic Stirring," *ISIJ Int.*, vol. 53, no. 1, pp. 48–55, 2013.

[46]. J. Li and N. Provatas, "Kinetics of Scrap Melting in Liquid Steel: Multipiece Scrap Melting," *Metall. Mater. Trans. B*, vol. 39, no. 2, pp. 268–279, 2008.

[47]. B. Zhou, Y. Yang, M. A. Reuter, and U. M. J. Boin, "Modelling of Aluminium Scrap Melting in a Rotary Furnace," *Miner. Eng.*, vol. 19, no. 3, pp. 299–308, 2006.

[48]. Y. Kim, A. Hossain, and Y. Nakamura, "Numerical Study of Melting of a Phase Change Material (PCM) Enhanced by Deformation of a Liquid-gas Interface," *Int. J. Heat Mass Transf.*, vol. 63, pp. 101–112, 2013.

[49]. M. Carmona and C. Cortés, "Numerical Simulation of a Secondary Aluminum Melting Furnace Heated by a Plasma Torch," *J. Mater. Process. Technol.*, vol. 214, no. 2, pp. 334–346, 2014.

[50]. O. J. P. Gonzalez, M. A. RamíRez-Argáez, and A. N. Conejo, "Effect of Arc Length on Fluid Flow and Mixing Phenomena in AC Electric Arc Furnaces," *ISIJ Int.*, vol. 50, no. 1, pp. 1–8, 2010.

[51]. Y. Li and R. J. Fruehan, "Computational Fluid Dynamics Simulation of Postcombustion in the Electric Arc Furnace," *Metall. Mater. Trans. B*, vol. 34, no. 3, pp. 333–343, 2003.

[52]. C. Yigit, G. Coskun, E. Buyukkaya, U. Durmaz, and H. R. Güven, "CFD Modeling of Carbon Combustion and Electrode Radiation in an Electric Arc Furnace," *Appl. Therm. Eng.*, vol. 90, pp. 831–837, 2015.

[53]. M. Alam, J. Naser, G. Brooks, and A. Fontana, "Computational Fluid Dynamics Modeling of Supersonic Coherent Jets for Electric Arc Furnace Steelmaking Process," *Metall. Mater. Trans. B*, vol. 41, no. 6, pp. 1354–1367, 2010.

[54]. S. C. Chen, R. Zhu, J. S. Li, C. L He, and M. Lu, "Three-phase Fluid Numerical Simulation and Water Modeling Experiment of Supersonic Oxygen Jet Impingement on Molten Bath in EAF," *J. Iron Steel Res. Int.*, vol. 21, no. 6, pp. 589–595, 2014.

[55]. C. L. He, R. Zhu, K. Dong, Y. Q. Qiu, and K. M. Sun, "Modeling of an Impinging Oxygen Jet on Molten Bath Surface in 150 t EAF," *J. Iron Steel Res. Int.*, vol. 18, no. 9, pp. 13–20, 2011.

[56]. E. Khodabandeh, A. Rahbari, M. A. Rosen, Z. N. Ashrafi, O. A. Akbari, and A. M. Anvari, "Experimental and Numerical Investigations on Heat Transfer of a Water- cooled Lance for Blowing Oxidizing Gas in an Electrical Arc Furnace," *Energy Convers. Manag.*, vol. 148, pp. 43–56, 2017.

[57]. K. Mandal and G. A. Irons, "A Study of Scrap Heating By Burners . Part I : Experiments," *Metall. Mater. Trans. B*, vol. 44B, no. 1, pp. 184-195, 2013.

[58]. K. Mandal and G. A. Irons, "A Study of Scrap Heating by Burners: Part II: Numerical Modeling," *Metall. Mater. Trans. B*, vol. 44, no. 1, pp. 196–209, 2013.

[59]. K. Mandal, "Modeling of Scrap Heating By Burners," Ph.D. Dissertation, Mcmaster University, 2010.

[60]. J. C. Gruber, T. Echterhof, and H. Pfeifer, "Investigation on the Influence of the Arc Region on Heat and Mass Transport in an EAF Freeboard using Numerical Modeling," *Steel Res. Int.*, vol. 87, no. 1, pp. 15–28, 2016.

[61]. M. Alam, J. Naser, and G. Brooks, "Computational Fluid Dynamics Simulation of Supersonic Oxygen Jet Behavior at Steelmaking Temperature," *Metall. Mater. Trans. B*, vol. 41, no. 3, pp. 636–645, 2010.

[62]. T. Bhattacharya, L. Zhan, and B. Chukwulebe, "A Numerical Test Bench for Supersonic Oxygen Nozzles and Its Application to the BOF Process," *Iron Steel Technol.*, vol. 12, no. 4, pp. 51–60, 2015.

[63]. C. Giavani, E. Malfa, and V. Battaglia "The Evolution of the Consteel ® EAF," The SEAISI Quarterly (South East Asia Iron and Steel Institute) conference, 2012.

[64]. Y. N. Toulouevski, I. Y. Zinurov, "Fuel Arc Furnace (FAF) for Effective Scrap Melting, from EAF to FAF," ISBN 978-981-10-5885-1, Springer Nature, Singapore, 2017.

[65]. J. Li, G. A. Brooks, and N. Provatas, "Phase-field Modeling of Steel Scrap Melting in a Liquid Steel Bath," *AISTech - Iron Steel Technol. Conf. Proc.*, vol. 1, pp. 833–843, 2004.

[66]. V. R. Voller and C. Prakash, "A Fixed Grid Numerical Modelling Methodology for Convection Diffusion Mushy Region Phase Change Problems," *Int. J. Heat Mass Transf.*, vol. 30, no. 8. pp. 1709–1719, 1987.

[67]. D. Brent, V. R. Voller, and K. J. Reid, "Enthalpy-porosity Technique for Modeling

Convection-diffusion Phase Change: Application to the Melting of a Pure Metal," *Numer. Heat Transf.*, vol. 13, no. 3, pp. 297–318, 1988.

[68]. E. M. Sparrow, S. V. Patankar and S. Ramadhyani, "Analwsis of Melting in the Presence of Natural Confection in the Melt Region," *J. Heat Transfer*, vol. 99, no. 4, pp. 520-526, 1977.

[69]. J. Szekely and P. S. Chhabra, "The Effect of Natural Convection on the Shape and Movement of the Melt-solid Interface in the Controlled Solidification of Lead," *Metall. Mater. Trans. B*, vol. 1, no. 5, pp. 1195–1203, 1970.

[70]. J. Jeong, N. Goldenfeld, and J. A. Dantzig, "Phase Field Model for Three-dimensional Dendritic Growth with Fluid Flow," *Phys. Rev. E*, vol. 64, no. 4, pp. 1–14, 2001.

[71]. J. J. Gonzalez, F. Lago, P. Freton, M. Masquère, and X. Franceries, "Numerical Modelling of an Electric Arc and Its Interaction with the Anode: Part II. The Three-dimensional model-influence of External Forces on the Arc Column," *J. Phys. D. Appl. Phys.*, vol. 38, no. 2, pp. 306–318, 2005.

[72]. F. Lago, J. J. Gonzalez, P. Freton, and A. Gleizes, "A Numerical Modelling of an Electric Arc and Its Interaction with the Anode: Part I. The Two-dimensional Model," *J. Phys. D. Appl. Phys.*, vol. 37, no. 6, pp. 883–897, 2004.

[73]. P. Freton, J. J. Conzalez, and A. Gleizes, "Comparison Between a Two- and a Three-dimensional Arc Plasma," *J. Phys. D. Appl. Phys.*, vol. 33, no. 19, pp. 2442–2452, 2000.

[74]. P. Freton, J. J. Gonzalez, A. Gleizes, F. C. Peyret, G. Caillibotte, and M. Delzenne, "Numerical and Experimental Study of a Plasma Cutting Torch," *J. Phys. D. Appl. Phys.*, vol. 35, pp. 115–131, 2002.

[75]. Q. Zhou, H. Li, F. Liu, S. Guo, W. Guo, and P. Xu, "Effects of Nozzle Length and Process Parameters on Highly Constricted Oxygen Plasma Cutting Arc," *Plasma Chem. Plasma Process.*, vol. 28, no. 6, pp. 729–747, 2008.

[76]. H. Nishiyama, T. Sawada, H. Takana, M. Tanaka, and M. Ushio, "Computational Simulation of Arc Melting Process with Complex Interactions," *ISIJ Int.*, vol. 46, no. 5, pp. 705–711, 2006.

[77]. C. Rehmet, F. Fabry, V. Rohani, F. Cauneau, and L. Fulcheri, "Unsteady State Analysis of Free-burning Arcs in a 3-Phase AC Plasma Torch: Comparison Between Parallel and Coplanar Electrode Configurations," *Plasma Sources Sci. Technol.*, vol. 23, no. 6, pp. 1-12, 2014.

[78]. C. Rehmet, V. rohani, F. Cauneau, and L. Rulcheri, "3D Unsteady State MHD Modeling of a 3-Phase AC Hot Graphite Electrodes Plasma Torch," *Plasma Chem. Plasma Process.*, vol. 33, pp. 491–515, 2013.

[79]. M. Kirschen, L. Voj, and H. Pfeifer, "NOx Emission from Electric Arc Furnace in Steel

Industry : Contribution from Eelectric Arc and Co-combustion Reactions," *Clean Techn. Environ. Policy*, vol. 7, pp. 236–244, 2005.

[80]. P. Mathur and C. Messina, "Praxair CoJet^{TM} Technology – Principles and Actual Results from Recent Installations," *AISE Steel Technol.*, vol. 78, no. 5, pp. 21–25, 2001.

[81]. J.E. Anderson and D.R. Farrenkopf, US Patent 5 823 762, 1998.

[82]. G. Wei, R. Zhu, K. Dong, G. Ma, and T. Cheng, "Research and Analysis on the Physical and Chemical Properties of Molten Bath with Bottom-Blowing in EAF Steelmaking Process," *Metall. Mater. Trans. B*, vol. 47, no. 5, pp. 3066–3079, 2016.

[83]. G. Wei, R. Zhu, X. Wu, L. Yang, K. Dong, T. Cheng, and T. Tang, "Study on the Fluid Flow Characteristics of Coherent Jets with CO_2 and O_2 Mixed Injection in Electric Arc Furnace Steelmaking Processes," *Metall. Mater. Trans. B*, vol. 49, no. 3, pp. 1405–1420, 2018.

[84]. G. Wei, R. Zhu, T. Cheng, K. Dong, and R. Liu, "Modelling on the Penetration Depth of the Coherent Supersonic Jet in EAF Steelmaking," *Ironmaking Steelmaking*, vol. 45, no. 9, pp. 828-838, 2018.

[85]. F. Liu, R. Zhu, K. Dong, and S. Hu, "Flow Field Characteristics of Coherent Jet with Preheating Oxygen under Various Ambient Temperatures," *ISIJ Int.*, vol. 56, no. 9, pp. 1519–1528, 2016.

[86]. F. Liu, R. Zhu, K. Dong, and S. Hu, "Effect of Ambient and Oxygen Temperature on Flow Field Characteristics of Coherent Jet," *Metall. Mater. Trans. B*, vol. 47, no. 1, pp. 228–243, 2016.

[87]. F. Liu, D. Sun, R. Zhu, R. Su, and X. Wang, "Effect of Shrouding CH_4 Flow Rate on Flow Field and Stirring Ability of Coherent Jet in Steelmaking Process," *Springerplus*, vol. 5, no. 1, pp. 1-14, 2016.

[88]. Z. Li and D. Cang, "Numerical Simulation of Supersonic Oxygen Jets at High Ambient Temperature," *Steel Res. Int.*, vol. 88, no. 4, p. 1600209, 2017.

[89]. T. H. Shih, W. W. Liou, A. Shabbir, Z. Yang, and J. Zhu, "A New k-ε eddy Viscosity Model for High Reynolds Number Turbulent Flows," *Compurers Fluids*, vol. 24, no. 3, pp. 227–238, 1995.

[90]. J. C. Chai, H. S. Lee, and S. V. Patankar, "Finite Volume Method for Radiation Heat Transfer," *J. Thermophys. Heat Transf.*, vol. 8, no. 3, pp. 419–425, 1994.

[91]. M. Landfahrer, R. Prieler, B. Mayr, H. Gerhardter, R. Schongrundner, J. Klarner, and C. Hochenauer, "Development of a Numerically Efficient CFD Model to Predict Transient Temperature Distribution of Mother Tubes Moving Translative and Rotative through a Gas Fired Furnace," *Appl. Therm. Eng.*, vol. 123, pp. 290–300, 2017.

[92]. B. Mayr, R. Prieler, M. Demuth, M. Potesser, and C. Hochenauer, "CFD and Experimental Analysis of a 115 kW Natural Gas Fired Lab-scale Furnace under Oxy-fuel and Air-fuel Conditions," *Fuel*, vol. 159, pp. 864–875, 2015.

[93]. ANSYS, FLUENT 15.0, Theory Guide, FLUENT, Inc.

[94]. M. Graça, A. Duarte, P. J. Coelho, and M. Costa, "Numerical Simulation of a Reversed Flow Small-scale Combustor," *Fuel Process. Technol.*, vol. 107, pp. 126–137, 2013.

[95]. J. Y. Murthy and S. R. Mathur, "Finite Volume Method for Radiative Heat Transfer Using Unstructured Meshes," *J. Thermophys. Heat Transf.*, vol. 12, no. 3, pp. 313–321, 1998.

[96]. T. F. Smith, Z. F. Shen, J. N. Friedman, "Evaluation of Coefficients for the Weighted Sum of Gray Gases Model," *J. Heat Transfer*, vol. 104, no. 4, pp. 602-608, 1982.

[97]. Coppalle and P. Vervisch, "The Total Emissivities of High-Temperature Flames," *Combust. Flame*, vol. 49, no. 1-3, pp. 101–108, 1983.

[98]. ANSYS, "ANSYS, FLUENT 15.0, User Guide, FLUENT, Inc." 2015.

[99]. H.K. Versteeg, W. Malalasekera, "An introduction to Computational Fluid Dynamics, the finite volume method," Prentice Hall, 2nd edition, 2007.

[100]. C. Yin, L. C. R. Johansen, L. A. Rosendahl, and S. K. Kær, "New Weighted Sum of Gray Gases Model Applicable to Computational Fluid Dynamics (CFD) Modeling of Oxy - Fuel Combustion : Derivation , Validation , and Implementation," *Energy Fuels*, vol. 24, no. 12, pp. 6275-6282, 2010.

[101]. S. Ergun, "Pressure Drop in Blast Furnace and in Cupola," *Ind. Eng. Chem.*, vol. 45, no. 2, pp. 477-485, 1953.

[102]. X. Chen, X. L. Xia, C. Sun, and X. W. Yan, "Transient Thermal Analysis of the Coupled Radiative and Convective Heat Transfer in a Porous Filled Tube Exchanger at High Temperatures," *Int. J. Heat Mass Transf.*, vol. 108, pp. 2472–2480, 2017.

[103]. J. C. Chen. and S. W. Churchill, "Radiant Heat Transfer in Packed Beds," *AIChE J.*, vol. 9, no. 1, pp. 35-41, 1963.

[104]. C. Yin, L. A. Rosendahl, and S. K. Kær, "Chemistry and Radiation in Oxy-fuel Combustion : A Computational Fluid Dynamics Modeling Study," *Fuel*, vol. 90, no. 7, pp. 2519–2529, 2011.

[105]. R. Johansson, B. Leckner, K. Andersson, and F. Johnsson, "Account for Variations in the H_2O to CO_2 Molar Ratio when Modelling Gaseous Radiative Heat Transfer with the Weighted-sum-of-grey-gases Model," *Combust. Flame*, vol. 158, no. 5, pp. 893–901, 2011.

[106]. C. Wang, W. Ge, M. F. Modest, and B. He, "A Full-spectrum k -distribution Look-up Table for Radiative Transfer in Nonhomogeneous Gaseous Media," *J. Quant. Spectrosc. Radiat.*

Transfer, vol. 168, pp. 46–56, 2016.

[107]. L. Yan, G. Yue, and B. He, "Development of an Absorption Coefficient Calculation Method Potential for Combustion and Gasification Simulations," *Int. J. Heat Mass Transf.*, vol. 91, pp. 1069–1077, 2015.

[108]. C. Yin, "Prediction of Air-fuel and Oxy-fuel Combustion through a Generic Gas Radiation Property Model," *Appl. Energy*, vol. 189, pp. 449–459, 2017.

[109]. N. Wakao, S. Kaguei, and T. Funazkri, "Effect of Fluid Dispersion Coefficients on Particle-to-fluid Heat Transfer Coefficients in Packed Beds. Correlation of Nusselt Numbers," *Chem. Eng. Sci.*, vol. 34, no. 3, pp. 325–336, 1979.

[110]. S. Hjartstam, F. Normann, K. Andersson, and F. Johnsson, "Oxy-Fuel Combustion Modeling: Performance of Global Reaction Mechanisms," *Ind. Eng. Chem. Res.*, vol. 51, no. 31, pp. 10327–10337, 2012.

[111]. H. T. Abuluwefa, R. I. L. Guthrie, and F. Ajersch, "Oxidation of Low Carbon Steel in Multicomponent Gases : Part II . Reaction Mechanisms during Reheating," vol. 28, no. 8, pp. 1643-1651, 1997.

[112]. V. H. J. Lee, B. Gleeson, and D. J. Young, "Scaling of Carbon Steel in Simulated Reheat Furnace Atmospheres," *Oxid. Met.*, vol. 63, no.112, pp. 15-31, 2005.

[113]. D. Fu, Y. Chen, and C. Q. Zhou, "Numerical Methods for Simulating the Reduction of Iron Ore in Blast Furnace Shaft," *J. Therm. Sci. Eng. Appl.*, vol. 6, no. 2, pp. 1–9, 2014.

[114]. D.C. Wilcox, "Turbulence Modelling for CFD", DCW Industries, La Canada, CA, 1998.

[115]. S. Sarkar and B. Lakshmanan, "Application of a Reynolds-Stress Turbulence Model to the Compressible Shear Layer," *AIAA J.*, vol. 29, no. 5, pp. 743-749, 1991.

[116]. K. S. Abdol-Hamid, S. P. Pao, S. J. Massey and A. Elmiligui, "Temperature Corrected Turbulence Model for High Temperature Jet Flow," *J. Fluids Eng.*, vol. 126, no. 5. pp. 844-850, 2004.

[117]. B. F. Magnussen. "On the Structure of Turbulence and a Generalized Eddy Dissipation Concept for Chemical Reaction in Turbulent Flow," The 19th Aerospace Sciences meeting, St. Louis 1981.

[118]. M. Jazbec, D. F. Fletcher, and B. S. Haynes, "Simulation of the Ignition of Lean Methane Mixtures using CFD Modelling and a Reduced Chemistry Mechanism," *Appl. Math. Model.*, vol. 24, no. 8-9, pp. 689–696, 2000.

[119]. G. Tang, A. Saavedra, B. Wu, T. Okosun, D. Bai, Y. Wang, R. Bodnar, and C. Q. Zhou, "Modeling of Steel Slab Reheating Process in a Walking Beam Reheating Furnace," in *Proceedings of ASME 2016 Summer Heat Transfer Conference, Washington, DC.*, 2013, vol. 1, no. 1, pp. 108–112.

[120]. D. Lindholm, "A Finite Element Method for Solution of the Three-demensional Time-dependent Heat-conduction Equation with Application for Heating of Steels in Reheating Furnaces," *Numer. Heat Transf. Part A Appl.*, vol. 35, pp. 155-172, 1999.

[121]. J. Andersen, C. L. Rasmussen, T. Giselsson, and P. Glarborg, "Global Combustion Mechanisms for Use in CFD Modeling under Oxy-Fuel Conditions," *Energy Fuels*, vol. 23, no. 3, pp. 1379–1389, 2009.

[122]. C. K. Westbrook and F. L. Dryer, "Simplified Reaction Mechanisms for the Oxidation of Hydrocarbon Fuels in Flames," *Combust. Sci. Technol.*, vol. 27, pp. 31-43, 1981.

[123]. W. P. Jones, R. P. Lindstedt, "Global Reaction Schemes for Hydrocarbon Combustion," *Combust. Flame*, vol. 73, no. 3, pp. 233-249, 1988.

[124]. R. Johansson, K. Andersson, B. Leckner, and H. Thunman, "Models for Gaseous Radiative Heat Transfer Applied to Oxy-fuel Conditions in Boilers," *Int. J. Heat Mass Transf.*, vol. 53, no. 1–3, pp. 220–230, 2010.

[125]. L. Yan, G. Yue, and B. He, "Application of an Efficient Exponential Wide Band Model for the Natural Gas Combustion Simulation in a 300 kW BERL Burner Furnace," *Appl. Therm. Eng.*, vol. 94, pp. 209–220, 2016.

[126]. C. Yin, S. Singh, and S. S. Romero, "A Gas Radiation Property Model Applicable to General Combustion CFD and Its Demonstration in Oxy-fuel Combustion Simulation," *Energy Procedia*, vol. 120, pp. 564–571, 2017.

[127]. N. Lallemant, F. Breussin, R. Weber, "Flame Structure, Heat Transfer and Pollutant Emissions Characteristics of Oxy-natural Gas Flames in the 0.7-1 MW Thermal Input Range," *J. Energy Inst.*, vol. 73, no. 496, pp. 169-182, 2000.

[128]. F. Memoli, C. Mapelli, P. Ravanelli, and M. Corbella, "Simulation of Oxygen Penetration and Decarburisation in EAF Using Supersonic Injection System," *ISIJ Int.*, vol. 44, no. 8, pp. 1342–1349, 2004.

[129]. Y. Chen, A.K. Silaen, and C.Q. Zhou, "Numerical Simulation of Fluid Flow During the Steel Refining Process in an Electric Arc Furnace," MS&T 2018, October, 14 -18, Columbus, Ohio, USA, 2018.

[130]. J. Li, G. Brooks, and N. Provatas, "Steel Scrap Melting in Liquid Steel Bath in EAF," *Metall. Mater. Trans. B*, vol. 36B, pp. 293–302, 2005.

[131]. G. Li and B. G. Thomas, "Transient Thermal Model of the Continuous Single-wheel Thin-Strip Casting Process," *Metall. Mater. Trans. B*, vol. 27, no. 3, pp. 509–525, 1996.

[132]. I. Sumi, Y. Kishimoto, Y. Kikuchi, and H. Igarashi, "Effect of High-temperature Field on Supersonic Oxygen Jet Behavior," *ISIJ Int.*, vol. 46, no. 9, pp. 1312–1317, 2006.

[133]. S. Ito and I. Muchi, "Transport Phenomena of Supersonic Jet in Oxygen Top Blowing

Converter," *Tetsu-to-Hagane*, vol. 55, no. 13, pp. 1152–1163, 1969.

[134]. B. Allemand, P. Bruchet, C. Champinot, S. Melen, and F. Porzucek, "Theoretical and Experimental Study of Supersonic Oxygen Jets – Industrial Application in EAF," *Rev. Met. Paris*, vol. 98, no. 6, pp. 571-587, 2002.

[135]. C.E. Baukal, "The John Zink Hamworthy Combustion Handbook: Volume 1 - Fundamentals," 2nd ed., Taylor&Francis Group. LLC, 2013.

[136]. S. Sarkar, "The Pressure–dilatation Correlation in Compressible Flows," *Phys. Fluids A*, vol. 4, no. 12, pp. 2674-2682, 1992.

[137]. O. Zeman, "Dilatation Dissipation: The Concept and Application in Modeling Compressible Mixing Layers," *Phys. Fluids A*, Vol. 2, no. 2, pp. 178-188, 1990.

[138]. G. Tang, B. Wu, K. Johnson, A. Kirk, D. Fu, and C. Q. Zhou, "Numerical Study of a Tangentially Fired Boiler for Reducing Steam Tube Overheating," *Appl. Therm. Eng.*, vol. 102, pp. 261–271, 2016.

[139]. F. Zhao, D. Sun, R. Zhu, and L. Yang, "Effect of Shrouding Gas Parameters on Characteristics of Supersonic Coherent Jet," *Metall. Mater. Trans. B*, vol. 48, no. 3, pp. 1807–1816, 2017.

[140]. F. Liu, D. Sun, R. Zhu, and Y. Li, "Effect of Shrouding Gas Temperature on Characteristics of a Supersonic Jet Flow Field with a Shrouding Laval Nozzle Structure," *Metall. Mater. Trans. B*, vol. 49, no. 4, pp. 2050–2062, 2018.

[141]. F.P. Ricou, D.B. Spalding, "Measurements of Entrainment by Axisymmetrical Turbulent Jets," *J. Fluid Mech.*, vol. 9, no. 1, pp. 21-32, 1961.

VITA

Guangwu Tang was born in Lu'an, Anhui, China. He received a Bachelor of Science in Metallurgical Engineering in June of 2011 from Anhui University of Technology, in Maanshan, Anhui, China. He obtained a Master of Science in Mechanical Engineering in December of 2013 from Purdue University Northwest (formerly Calumet), in Hammond, IN, USA. He then obtained a Master of Modeling, Simulation and Visualization in December of 2014 from Purdue University Northwest, in Hammond, IN. He joined the research group at the Center for Innovation through Visualization and Simulation (CIVS), directed by Professor Chenn Q. Zhou at Purdue University Northwest in 2011. He began work on his Ph.D. in Mechanical Engineering at Purdue University in West Lafayette in Spring 2015. He expects to be granted his Doctor of Philosophy in Mechanical Engineering in May of 2019.

Through the course of his studies, he has written ten journal papers, five of them are directly based on this thesis research. Four of them are published in the *Applied Thermal Engineering, International Journal of Heat and Mass Transfer, JOM,* and *Steel Research International.* One of them is submitted to *Applied Thermal Engineering* and currently under revision (November 2018). Additionally, he has published and presented nine conference papers based on this research at the AISTech 2016, 2017, 2018 (Iron and Steel Technology Conference), STEELSIM Conference (2017), ASME Summer Heat Transfer Conference (2016), ESTAD Conference (2017), ASME IMECE Conference (2017) and TMS (2019). A list of his selected publications during his Ph.D. study is included on the following pages. Publications based directly on this research have won the AISTech 2017 Computer Application Best Paper Award (Awarded to: Numerical Simulation of a Walking Beam Type Steel Slab Reheating Furnace).

PUBLICATIONS

[1] Tang, G., Chen, Y., Silaen, A.K., Krotov, Y., Riley, M., Zhou, C.Q., "Effects of Fuel Input on Coherent Jet Potential Core Length at High Ambient Temperature" *Appl. Therm. Eng.*. (1st revision)

[2] Tang, G., Chen, Y., Silaen, A.K., Wang, T., Zhou, C.Q., "Investigation of Supersonic Oxygen Jet Potential Core Length at Various Ambient Temperature" *JOM*. (In press)

[3] G. Tang, B. Wu, D. Bai, Y. Wang, R. Bodnar, C.Q. Zhou, "CFD Modeling and Validation of Dynamic Slab Heating Process in an Industrial Walking Beam Reheating Furnace," *Appl. Therm. Eng.*, vol. 132, pp. 779-789, 2018.

[4] G. Tang, B. Wu, D. Bai, Y. Wang, R. Bodnar, C.Q. Zhou, "Modeling of the Slab Heating Process in a Walking Beam Reheating Furnace for Process Optimization," *Int. J. Heat Mass Transf.*, vol. 113, pp. 1142-1151, 2017.

[5] G. Tang, A.K. Silaen, B. Wu, D. Fu, C.Q. Zhou, D. Agnello-Dean, J. Wilson, Q. Meng, and S. Khanna, "Numerical Simulation and Optimization of an Industrial Fluid Catalytic Cracking Regenerator", *Appl. Therm. Eng.*, vol. 112, pp. 750-760, 2017.

[6] G. Tang, A.K. Silaen, B. Wu, D. Fu, C.Q. Zhou, D. Agnello-Dean, J. Wilson, Q. Meng, and S. Khanna, "Numerical Simulation of an FCC Regenerator Hydrodynamics", *Powder Technol.*, vol. 305, pp. 662-672, 2017.

[7] G. Tang, B. Wu, K. Johnson, A. Kirk, and C.Q. Zhou, "Numerical Study of a Tangentially Fired Boiler Firing Metallurgical Gases: Reducing Water Pipe Overheating", *Appl. Therm. Eng.*, vol. 102, pp. 261-271, 2016.

[8] G. Tang, Y. Chen, A.K. Silaen, Y. Krotov, M. Riley, C.Q. Zhou, "Investigation of Coherent Jet Potential Core Length in an Electric Arc Furnace", *Steel Res. Int.*, 2018. (In press)

[9] G. Tang, A.K. Silaen, B. Wu, C.Q. Zhou, D. Agnello-Dean, J. Wilson, Q. Meng, and S. Khanna, "Numerical Simulation of and Industrial Fluid Catalytic Cracking Regenerator", *J. Thermal Sci. Eng. Appl.*, 7(2), pp. 021012-021012-10, 2015.

[10] G. Tang, B. Wu, K. Johnson, A. Kirk, and C.Q. Zhou, "Simulation of an Industrial Tangentially Fired Boiler Firing Metallurgical Gases", *J. Thermal Sci. Eng. Appl.*, 7(1), pp. 011003-011003-11, 2014.

[11] G. Tang, B. Wu, L. Gong, A.K. Silaen, J. Lash, E.K. Borges, C.Q. Zhou, "Numerical Study of a Basic Oxygen Process Hydrodynamics", *Iron Steel Technol.*, pp. 52-59, April 2016.

[12] G. Tang, B. Wu, D. Bai, Y. Wang, R. Bodnar, C.Q. Zhou, "Numerical Simulation of a Walking Beam Type Steel Slab Reheating Furnace," *Iron Steel Technol.*, pp. 78-88, March 2017.

[13] G. Tang, Y. Chen, A.K. Silaen, A. Spencer, Y. Krotov, C.Q. Zhou, "Modeling of Scrap Preheating by Oxy-fuel Combustion in an Electric Arc Furnace", *Iron Steel Technol.*, January 2019. (In press)

[14] C.Q. Zhou, G. Tang, J. Wang, D. Fu, B. Wu, A.K. Silaen, T. Okosun, "Comprehensive Numerical Modeling of the Blast Furnace Ironmaking Process", *JOM*, vol. 68, no. 5, pp. 1353-1362, 2016.

[15] D. Fu, G. Tang, Y. Zhao, J. D'Alessio, C.Q. Zhou, "Integration of Tuyere, Raceway and Shaft Models for Predicting Blast Furnace Process", *JOM*, vol. 70, no. 6, pp. 951-957, 2018.

[16] D. Fu, G. Tang, Y. Zhao, J. D'Alessio, C.Q. Zhou, "Modeling of Iron Ore Reactions in Blast Furnace", *Int. J. Heat Mass Transf.*, vol. 103, pp. 77-86, 2017.

[17] B. Wu, G. Tang, X. Chen, C.Q. Zhou, P.C. Colella, T. Okosun, "Optimization of a Urea Decomposition Chamber using CFD and VR", *Appl. Therm. Eng.*, vol. 70, pp. 827-837, 2014.

[18] C.Q. Zhou, J. Wang, G. Tang, J. Moreland, D. Fu, B. Wu, "Integration of Advanced Simulation and Visualization for Manufacturing Process Optimization", *JOM*, vol. 68, no. 5, pp. 1363-1369, 2016.

[19] X. Liu, B. Worl, G. Tang, A.K. Silaen, J. Cox, K. Johnson, R. Bodnar, C.Q. Zhou, "Numerical Simulation of Heat Transfer and Scale Formation in a Reheat Furnace", *Steel Res. Int.*, 2018. (In press)

[20] X. Liu, B. Worl, G. Tang, A.K. Silaen, J. Cox, K. Johnson, C.Q. Zhou, "A Numerical Model to Predict Scale Formation in an Industrial Reheat Furnace," *Iron Steel Technol.*, December 2018. (In press)